UNIVERSITY OF SOUTHAMPTON

FACULTY OF ENGINEERING AND THE ENVIRONMENT
INSTITUTE OF SOUND AND VIBRATION RESEARCH

Far-Field Microphone Array Techniques for Acoustic Characterisation of Aerofoils

by

Fabio Casagrande Hirono

Thesis for the degree of Doctor of Philosophy

October 2018

Declaration of Authorship

I, FABIO CASAGRANDE HIRONO, declare that this thesis titled "*Far-Field Microphone Array Techniques for Acoustic Characterisation of Aerofoils*" and the work presented in it are my own. I confirm that:

- This work was done wholly or mainly while in candidature for a research degree at this University.
- Where any part of this thesis has previously been submitted for a degree or any other qualification at this University or any other institution, this has been clearly stated.
- Where I have consulted the published work of others, this is always clearly attributed.
- Where I have quoted from the work of others, the source is always given. With the exception of such quotations, this thesis is entirely my own work.
- I have acknowledged all main sources of help.
- Where the thesis is based on work done by myself jointly with others, I have made clear exactly what was done by others and what I have contributed myself.
- Parts of this work have been published as:
  - F. Casagrande Hirono, P. F. Joseph, F. M. Fazi, *"Aerofoil Source Estimation from Nearfield Array Measurements"*, in 23rd AIAA/CEAS Aeroacoustics Conference, AIAA AVIATION Forum, Denver, USA, 2017.
  - F. Casagrande Hirono, P. F. Joseph, F. M. Fazi, *"Wavenumber-Domain Method for Source Reconstruction from Far-Field Array Measurements in Flow"*, in 7th Berlin Beamforming Conference (BeBeC), Berlin, Germany, 2018.
  - F. Casagrande Hirono, P. F. Joseph, F. M. Fazi, *"Aerofoil Surface Pressure Reconstruction from Far-Field Array Measurements"*, in 24th AIAA/CEAS Aeroacoustics Conference, AIAA AVIATION Forum, Atlanta, USA, 2018.

Signed: _____

Date: _____

UNIVERSITY OF SOUTHAMPTON

Abstract

Faculty of Engineering and Environment
Institute of Sound and Vibration Research

Doctor of Philosophy

Far-Field Microphone Array Techniques for Acoustic Characterisation of Aerofoils

by Fabio Casagrande Hirono

This Thesis is concerned with the acoustic characterisation of flat plate aerofoils interacting with turbulent flows, and the use of microphone array methods as an experimental tool to assess these characteristics. The main equations describing acoustic propagation and radiation in a moving medium are described, covering plane waves, point sources and distributed sources. The geometric far-field approximation, introduced here as the *Fraunhofer approximation*, is shown to relate the acoustic field seen by a distant observer to the Spatial Fourier Transform of the source distribution evaluated within the so-called "radiation ellipse" in the wavenumber domain. The Amiet model for turbulence-flat plate interaction noise is presented, and its surface pressure and acoustic radiation characteristics for single- and multiple-gust responses are discussed from a wavenumber-domain perspective. Three sources of near-field effects were identified in a flat plate: the fundamental dipole hydrodynamic near-field, considered significant contributor to the acoustic field at low frequecies; the geometric near-field, considered significant at high frequencies; and the response to subcritical gusts, considered significant at low frequencies for a finite-span aerofoil. The prediction model was validated via microphone array acoustic measurements of a flat plate in a wind tunnel, showing a good agreement between the predicted and the measured acoustic fields, particularly regarding the coherence between microphones. The same set of signals was processed with conventional beamforming and CLEAN-SC, and again a good agreement was observed between prediction and measurements. Finally, a far-field inversion method was proposed by inverting the above mentioned Fourier relationship between the far-field pressure and the source wavenumber spectrum; two formulations were proposed, and it was shown that the estimated source is effectively a band-passed version of the original source and thus lacks fine spatial detail. This band-passing phenomenon in the far-field radiation effectively smears out the original source distribution, and the estimated source becomes larger than the physical source. It is shown that both forms have very similar formulations to frequency-domain delay-and-sum beamforming.

Acknowledgements

First and foremost, I would like to express my most sincere love and gratitude to my parents, Edilene and Marcelo, for their unending love and support.

I would also like to thank my supervisors, Dr. Filippo Fazi and Prof. Phil Joseph, for their continued support and friendship during this period. Many thanks to Dr. Chaitanya Paruchuri for his help setting up the experiments and for our very insightful discussions, and very special thanks to Dr. Pieter Sijtsma and Prof. Philip Nelson for their thorough examination of this work.

Throughout the years I was lucky enough to meet some wonderful friends in Southampton. Their love was essential to help me maintain my sanity during the hard times, and I'm very grateful to all of them.

This PhD candidature was sponsored under the "*Science Without Borders*" programme of the National Council for Scientific and Technological Development (CNPq) of the Federal Government of Brazil, to whom I am very grateful for the financial support.

Contents

List of Figures

List of Tables

Abbreviations

ADAT	**A**lesis **D**igital **A**udio **T**ape (Lightpipe)
B&K	**B**rüel and **K**jær
CLEAN-SC	**CLEAN** based on **S**patial **C**oherence
COP	**C**oherent **O**utput **M**ethod
CSD	**C**ross-power **S**pectral **D**ensity
CSM	**C**ross **S**pectral **M**atrix
DARP	**D**efence and **A**erospace **R**esearch **P**artnership
DAMAS	**D**econvolution **A**pproach for the **M**apping of **A**coustic **S**ources
DFT	**D**iscrete **F**ourier **T**ransform
FF	**F**ar-**F**ield
ISVR	**I**nstitute of **S**ound and **V**ibration **R**esearch
KHI	**K**irchhoff-**H**elmholtz **I**ntegral
LE	**L**eading **E**dge
MADI	**M**ultichannel **A**udio **D**igital **I**nterface
NACA	**N**ational **A**dvisory **C**ommittee for **A**eronautics
NF	**N**ear-**F**ield
PSD	**P**ower **S**pectral **D**ensity
PSF	**P**oint **S**pread **F**unction
RMS	**R**oot **M**ean **S**quare
STFT	**S**hort-**T**ime **F**ourier **T**ransform
SVD	**S**ingular **V**alue **D**ecomposition
TE	**T**railing **E**dge
USB	**U**niversal **S**erial **B**us

Physical Constants

Speed of sound at 1 atm and 0° C	$c_0(T_C = 0)$	=	331.5 m/s
Density of air	ρ_0	=	1.2 kg/m^3

Symbols

A	Surface pressure decay (in decibels)	
b	Aerofoil semichord	$b = c/2$
c	Aerofoil chord	$c = 2b$
c_0	Speed of sound as a function of temperature T_C	$c_0(T_C) = c_0(0)\sqrt{\frac{T_C+273.15}{273.15}}$
d	Aerofoil semispan	$d = L/2$
$\frac{D}{Dt}\{.\}$	Total derivative	$\frac{D}{Dt}\{.\} = \frac{\partial}{\partial t}\{.\} + U_x\frac{\partial}{\partial x}\{.\}$
D	Dirichlet boundary condition at surface S; largest dimension of planar source	
erf	Error function	$\mathrm{erf}(x) = \frac{2}{\sqrt{\pi}}\int_0^x e^{-t^2}\,\mathrm{d}t$
f	Temporal frequency	
f_s	Sampling frequency	
g^{LE}	Flat plate response function	
G	Green's function	
j	Imaginary unit	$j^2 = -1$
k_0	Acoustic wavenumber	$k_0 = \frac{2\pi}{\lambda_0} = \frac{\omega}{c_0}$
k_χ	Chordwise hydrodynamic wavenumber	
k_ψ	Spanwise hydrodynamic wavenumber	
$\mathbf{k}$	Acoustic wavenumber vector	$\mathbf{k} = (k_x, k_y, k_z)$
$\hat{\mathbf{k}}$	Observer-dependent wavenumber vector	$\hat{\mathbf{k}} = (\hat{k}_x, \hat{k}_y, \hat{k}_z)$ $= \left(k_0\left(\frac{x-M_x\sigma_{\mathbf{r}}}{\beta^2\sigma_{\mathbf{r}}}\right), k_0\frac{y}{\sigma_{\mathbf{r}}}, k_0\frac{z}{\sigma_{\mathbf{r}}}\right)$
$\breve{k}_i$	Half-chord normalised trace wavenumber	$\breve{k}_i = k_i b$
L	Aerofoil span	$L = 2d$
M_x	Mach number	$M_x = U_x/c_0$
$\mathbf{n}$	Outwards-pointing normal vector at surface S	$\mathbf{n} = (n_x, n_y, n_z)$
$\mathbf{n}_s$	Unit normal vector pointing in the $+x$ direction	$\mathbf{n}_x = (1, 0, 0)$

N	Neumann boundary condition at surface S; number of points	
p	Acoustic pressure	
q	Source strength distribution in spatial domain	
$\tilde{q}$	Estimated source strength distribution	
Q	Source strength in wavenumber domain; volumetric source distribution	
$\tilde{Q}$	Estimated source strength wavenumber spectrum	
r	Source-observer distance	$r = \|\mathbf{r} - \mathbf{r}_s\|$
$\mathbf{r}$	Position vector	$\mathbf{r} = (x, y, z)$
$\overline{\mathbf{r}}$	Flow-transformed position vector	$\overline{\mathbf{r}} = (\overline{x}, \overline{y}, \overline{z}) = \left(\frac{x}{\beta^2}, \frac{y}{\beta}, \frac{z}{\beta}\right)$
R	Observer distance from source centre	$R = \|\mathbf{r}\|$
R_{FF}	Fraunhofer far-field distance limit	$R_{FF} = \frac{2D^2}{\lambda}$
S	Boundary surface of V	
$S_{pp'}(x, x')$	Cross-power Spectral Density	$S_{xx'} = \lim_{T\to\infty} \frac{\pi}{T} \mathrm{E}\left\{p(x)p^*(x')\right\}$
$S_{pp}(x)$	Power Spectral Density	$S_{xx} = \lim_{T\to\infty} \frac{\pi}{T} \mathrm{E}\left\{p(x)p^*(x)\right\}$
t	Time	
T	Measurement duration	
T_i	Turbulence intensity (in percentage)	$T_i = \sqrt{\overline{u^2}}/U_x$
T_C	Air temperature (in Celsius)	
U_x	Mean flow velocity in x direction	
$\mathbf{u}$	Acoustic particle velocity vector	$\mathbf{u} = (u_x, u_y, u_z)$
v	Surface velocity	
V	Control volume	
w	Turbulent gust vertical velocity	
W_{dip}	Dipole-associated wavenumber-domain window function	
$\breve{x}$	Half-chord normalised position	$\breve{x} = x/b$
α	Term within far-field-approximated distance r	$\alpha = 2\frac{\overline{\mathbf{r}}\cdot\overline{\mathbf{r}}_s}{\|\overline{\mathbf{r}}\|^2}$
β	Prandtl-Glauert factor	$\beta^2 = 1 - M_x^2$
γ	Angle between source and observer	$\cos(\gamma) = \frac{\mathbf{r}\cdot\mathbf{r}_s}{\|\mathbf{r}\|\|\mathbf{r}_s\|}$
γ^2	Coherence-squared function	$\gamma^2(x, x') = \frac{\|S_{xx'}\|^2}{S_{xx}S_{x'x'}}$

Γ	Gamma function	$\Gamma(z) = \int_0^\infty x^{z-1}e^{-x}\,\mathrm{d}x$
δ	Dirac Delta function	
Δp	Aerofoil surface pressure jump	
Δk_ψ^{ML}	Sinc function null-to-null main lobe width in k_ψ domain	
ΔS_m	Equivalent area in wavenumber domain	
θ	Polar angle	
Θ_G	Graham's parameter	$\Theta_G = \frac{k_\chi M_x}{k_\psi \beta}$
κ_χ	Particular chordwise hydrodynamic wavenumber	$\kappa_\chi = \frac{\omega}{U_x}$
κ_ψ	Particular spanwise hydrodynamic wavenumber	$\kappa_\psi = k_0 \frac{y}{\sigma_\mathbf{r}}$
λ_0	Acoustic wavelength	$\lambda_0 = \frac{c_0}{f}$
Λ	Integral length scale	
μ_a	Acoustic reduced frequency	$\mu_a = \frac{\breve{k}_\chi M_x}{\beta^2}$
ρ	Acoustic medium density	
$\sigma_\mathbf{r}$	Convection-corrected observer radius	$\sigma_\mathbf{r} = \sqrt{x^2 + \beta^2(y^2+z^2)} = \beta^2 \left\|\bar{\mathbf{r}}\right\|$
$\sigma_{\mathbf{r},\mathbf{r}_s}$	Convection-corrected distance	$\sigma_{\mathbf{r},\mathbf{r}_s} = \sqrt{(x-x_s)^2 + \beta^2[(y-y_s)^2 + (z-z_s)^2]}$
τ	Propagation time in a convected medium	$\tau = \frac{-(x-x_s)M_x + \sigma_{\mathbf{r},\mathbf{r}_s}}{c_0\beta^2}$
ϕ	Azimuthal angle	
Φ	Wavenumber spectral density of turbulent gust velocity	
ω	Angular frequency	
$\mathcal{F}$	Fresnel integral	$\mathcal{F}(\zeta) = \frac{1}{2\pi}\int_0^\zeta \frac{e^{jz}}{\sqrt{z}}\,\mathrm{d}z$
$\mathcal{F}^*$	Complex-conjugate Fresnel integral	$\mathcal{F}^*(\zeta) = \frac{1}{2\pi}\int_0^\zeta \frac{e^{-jz}}{\sqrt{z}}\,\mathrm{d}z$
$\mathcal{L}$	Effective lift function	
$\frac{\partial}{\partial \mathbf{n}}$	Normal derivative in direction $\mathbf{n}$	$\frac{\partial}{\partial \mathbf{n}}\{.\} = \mathbf{n}\cdot\nabla\{.\}$

Chapter 1

Introduction

This Thesis investigates the acoustic characteristics of turbulence-flat plate interaction noise, and the use of microphone arrays for experimentally assessing these characteristics. Aerofoil interaction noise is an important source of broadband noise in many industrial applications, and has been the topic of considerable research in the past decades. As a distributed, partially-coherent source immersed in a moving medium, it presents significant challenges from a microphone array signal processing perspective, and as such it is an interesting test case for source estimation methods.

A literature review on analytical models for aerofoil interaction noise has identified a gap regarding the description of the aerofoil acoustic *near-field*. As further discussed below, most recent studies on aerofoil interaction noise apply the *far-field approximation*, and investigate the effects of different aerofoil geometries or experimental conditions on the far-field sound only. Little, if any, discussion has been made on under which conditions the far-field approximation is valid, or what are the acoustic characteristics observed in the aerofoil near-field. Therefore, we propose to investigate the far-field and near-field characteristics as observed for an aerofoil interacting with a turbulent flow as part of the original contributions of this Thesis.

Microphone array signal processing methods have become the norm for aeroacoustic measurements in recent years. Most popular array methods - such as conventional beamforming [1], or deconvolution methods such as DAMAS [2] and CLEAN-SC [3] - can estimate the spatial distribution of source powers, but are not used to estimate the source phase or coherence structure. Given the random nature of most aeroacoustic phenomena, estimating the source coherence as well as the source power distribution would paint a much more complete picture

of the noise sources. We then propose a source estimation framework based on the far-field approximation and the Spatial Fourier Transform as part of the Thesis original contributions, and demonstrate how this method can be used to estimate the acoustic source power distribution and its coherence structure.

The remainder of the Thesis describes the steps taken to develop these contributions. The next section covers the literature review of analytical models for aerofoil interaction noise, and on aerofoil measurements with microphone arrays. This is followed by a list of the Thesis original contributions, and a description of the Thesis structure.

1.1 Literature Review

The interaction of a turbulent gust with a solid lifting surface, commonly termed "turbulence-aerofoil interaction noise" or "leading edge noise", is a large contributor to noise in many applications, such as turbomachinery [4] and wind turbines [5], and as such is subject to a substantial body of research. Recent research efforts in aerofoil interaction noise can be broadly divided into three areas: numerical methods, analytical methods and experimental methods. The next paragraphs attempt to describe their main characteristics and distinctions.

Numerical methods attempt to directly simulate the interaction of the turbulent flow with a solid surface using computational techniques. These methods are computationally-intensive, time-consuming [6], and usually aimed at describing the tiniest details of the sound generation mechanism and reproducing it as closely as possible [7]. While computational resources are becoming more powerful every year, some particular cases of Reynolds and Mach numbers are still out of reach of current numerical methods [7], and the computational cost makes them prohibitive for some applications.

Analytical methods, on the other hand, model a known mechanism of noise generation and attempt to obtain an approximate analytical solution. Such solutions are often reached at the cost of assuming drastic simplifications of the flow features or problem geometry: for example, Amiet's model for turbulence-aerofoil interaction [8] is derived for a flat-plate aerofoil immersed in an isotropic, uniform turbulent flow. Real experimental conditions frequently differ from such assumptions, and a significant body of work has been done recently to extend the existing models to more realistic conditions.

While less accurate than their numerical counterparts, analytical methods are much cheaper and faster, and thus are still very important for preliminary engineering design and identifying trends for known physical mechanisms [7, 9]. Given the current relevance of analytical methods, and given that numerical methods require specific skills and training, we will not discuss numerical methods in this work.

In contrast to the previous two, *experimental methods* focus on experimentally assessing characteristics of the radiated sound in terms of measurable quantities such as acoustic spectra and directivity functions. Since experiments must by design reproduce the physical phenomenon under study, such methods are much closer to the "real" problem to be tackled, and experimental results are thus often used to validate numerical and analytical results. Current aerofoil interaction noise measurement methods can vary from single-microphone power spectral density (PSD) measurements, used to observe the far-field sound radiated by the aerofoil as a whole, to microphone array beamforming methods, used to separate and quantify multiple sources simultaneously.

The next sections will cover a brief review of analytical and experimental methods recently applied to aerofoil interaction noise, point some limitations of the current methods, and describe how the work developed during this research project fits within these gaps in the literature.

1.1.1 Analytical Methods for Aerofoil-Turbulence Interaction Noise Prediction

For aerofoil interaction noise predictions, the Amiet model [8, 10] is perhaps the most established and forms the basis of many methodologies currently in use [6]. A very good overview of the Amiet model can be found in Roger and Moreau [9], where the authors also tackle trailing edge noise and vortex shedding noise using a similar mathematical formulation.

The Amiet model assumes a flat, rectangular plate as a simplified aerofoil model. This flat plate is subject to an incoming turbulent flow, which is described as a Fourier sum of incoherent hydrodynamic plane waves moving at the mean flow velocity towards the aerofoil. The flat plate unsteady aerodynamic response is calculated for each gust from linearised potential theory, resulting in an analytical expression for the unsteady lift forces over the aerofoil surface; the total unsteady lift force is obtained by integrating over all gusts' responses. Finally, the sound field is calculated from the unsteady lift using an acoustic analogy: the unsteady force

distribution is equivalent to a distribution of point dipole sources over the aerofoil planform area, and the sound field is given by integrating the contribution of all sources.

Most recent research efforts on turbulence-interaction analytical models have focused in developing extensions towards more realistic experimental conditions: for example, we can find attempts to predict interaction noise for spanwise-varying conditions [11] and the inclusion of realistic aerofoil geometries (i.e. thickness and camber) in the formulation [12]. Other works have discussed the mean flow distortion generated by aerofoil thickness and its impact on the assumed turbulence model [13], and an increased low-frequency extension [6].

The model is also used by researchers working on new aerofoil designs aiming at reducing their acoustic radiation. There has been a strong interest in extending the existing models to include the effects of leading edge serrations [4, 14, 15], and extensions to porous leading edges have also been investigated [14].

1.1.1.1 Limitations of Current Analytical Methods

Because many applications of interaction noise come from the aviation industry and aim to reduce noise levels perceived by the general population, research efforts are often focused on the *far-field* noise emmited by the aerofoil. Assuming the observer is in the far-field allows significant simplifications of the analytical formulation, resulting in a much more tractable closed form expression for the far-field sound. The use of the far-field assumption is also reinforced by the nonexistence of analytical solutions for the near-field sound of most types of acoustic sources. It is therefore not surprising that all papers referenced so far in this Section assume far-field conditions and do not consider near-field effects.

However, it has not been established in these references what the conditions are for the far-field approximation to be valid, whether the approximation is applicable to typical aerofoil measurement situations, or what errors should be expected if the approximation is applied incorrectly. Therefore, we propose to investigate the far-field approximation, determine its conditions of validity and attempt to provide some physical interpretation.

The absence of studies describing near-field characteristics of aerofoil interaction noise also complicates the design of a microphone array geometry optimised for this particular source type, since the acoustic characteristics in the near-field region are not well established. We thus propose a more thorough investigation of the source characteristics for this research project,

including the identification of the origins of near-field effects and to what extent they might affect the measurements.

1.1.2 Aerofoil-Turbulence Interaction Noise Measurements

Recent efforts in aerofoil noise measurements often focus on microphone arrays and deconvolution methods; however, it is interesting to go briefly through other methods used in the literature. Bahr et al. [16] presented an interesting analysis of trailing edge noise measurement techniques, most of which have also been applied to leading edge measurements as well and therefore are of interest. They listed, in increasing sensor count: single-microphone measurements, two- and three-microphones Coherent Output Method (COP), microphone arcs and linear arrays for directivity measurements, and microphone array beamforming.

Many authors have used single-microphone measurements, where the main variable of interest is the microphone signal spectrum as a proxy for the aerofoil radiated noise [13, 14]. These are clearly the simplest method to implement, but might not be representative of the aerofoil radiation towards different directions and are easily contaminated by extraneous noise. Other authors have compared single-microphone spectra with array measurements [17–19], often indicating a good agreement between both methods and noting the favourable noise rejection capabilities of array measurements.

Two- and three-microphone Coherent Output Power (COP) methods use microphones located at opposite sides of the aerofoil surface and explore the dipole nature of aerofoil radiation to reject external noise sources [16, 20]. Such methods have had limited use in interaction noise measurements, possibly due to the popularisation of microphone array signal processing methods and their improved noise rejection capabilities.

Microphone arcs or linear arrays are often used for directivity measurements [16, 21]. In this setup, the microphone spectra are plotted as a function of the observation angle, and the resulting plot is interpreted as a directivity measurement of the source under study. These are a popular alternative due to their simplicity, but often require complex installation setups such as arcs of microphones suspended above the aerofoil [15].

In recent years, perhaps the most popular method for interaction noise measurement is microphone array beamforming. Frequency-domain conventional beamforming consists of applying a phase shift and summing the microphone signals so that signals originated from a given

spatial location sum up coherently and are amplified, while signals originated from other locations and incoherent noise sum up incoherently and are attenuated. The beamformer outputs an estimate of the source strength at a target location, and steering the beamformer over multiple locations yield the so-called "source map" containing the estimated source strength distribution over a region of interest. A very thorough review of conventional beamforming methods for aeroacoustic measurements can be found in Sijtsma [22]

Despite being more resource-intensive than the previous methods and having results that might be more difficult to interpret [16], recent increases in computational power have helped popularise the method: many authors have reported conventional beamforming measurements of aerofoil interaction noise [17–19, 23, 24] in recent years. Even more recently, the use of deconvolution methods seem to have become the de facto standard in aeroacoustic measurements and have also been reported extensively; of those, the most popular methods are the CLEAN-SC method [18, 23, 25, 26] and the DAMAS method [19, 20, 24].

1.1.2.1 Limitations of Current Measurement Methods

Conventional beamforming measurements have well-known limitations in the form of limited, frequency-dependent spatial resolution and sidelobes. It is well established in the literature that these limitations can be mitigated through careful microphone array design [27] and the adoption of deconvolution methods in the post-processing stage [2, 3].

However, we would like to point a less studied limitation of beamforming methods: even though they can be said to reconstruct the source distribution, most aeroacoustic applications of beamforming focus on recovering only the source powers, but not the source coherence characteristics. It is known that for sources with random characteristics, a full description of the source powers and mutual coherences at a single frequency is given by the source strength cross-spectral matrix (CSM).

From a measurement perspective, it is then desireable to estimate the source cross-spectral matrix from the acoustic measurements; this capability would enable researchers to investigate the source coherence structure, thus yielding more information about the physics of the problem.

1.2 Original Contributions of this Thesis

The original contributions of this Thesis are summarised below:

- A link between the radiated acoustic pressure at a far-field observer and a single wavenumber component of the source Spatial Fourier Transform is demonstrated via the Fraunhofer far-field approximation. While this link is well-known in the acoustics literature [28–30], it is derived through a systematic Fourier-based framework, generalized to distributions of either monopole or dipole sources, in steady or subsonic convected media, and its conditions of validity are established.

- A review of the flat plate interaction noise model by Amiet [8] is presented, with emphasis in describing the flat plate surface pressure and cross-spectrum characteristics in the spatial and in the wavenumber domain. Examples of single-gust and multiple-gust surface pressure responses are shown in the wavenumber domain, and interpreted in terms of their corresponding far-field radiation via the previously introduced Fourier framework.

- Three sources of near-field effects are identified on the flat plate radiation model: the hydrodynamic dipole near-field, considered a significant contributor to the radiated sound at low frequencies; the geometric near-field, considered significant at high frequencies; and the aerofoil response to subcritical gusts, considered significant at low frequencies for finite-span aerofoils.

- An experimental validation of Amiet model using a microphone array in an open-jet wind tunnel experiment is presented. The predicted and measured acoustic field cross-spectra at the microphone locations are compared, and source maps obtained with conventional beamforming and CLEAN-SC from predicted and measured data are compared.

- A Fourier-based far-field inversion method for planar sources in flow is proposed in two formulations. The first starts from an arbitrary microphone array geometry and obtains an irregular wavenumber-domain sampling, while the second imposes a uniform wavenumber-domain sampling and defines the microphone array geometry in a second step. The second method can be considered an extension of that proposed by Kim and Nelson [31] for monopole sources in a steady medium, as here it is formulated for dipole sources in a subsonic moving medium.

1.3 Thesis Structure

Chapter 1 presents a brief literature review of the recent advances on aerfoil interaction noise prediction methods and measurement methods. We report two gaps in the current literature: a detailed description of turbulence-aerofoil interaction noise characteristics as an acoustic source, with emphasis on the description of near-field effects; and an experimental method to estimate the source strength CSM in aerofoil interaction noise measurements.

Chapter 2 reviews sound radiation and propagation, including expressions for plane waves in a homogeneous convected medium, acoustic radiation from point sources and boundary sources in an inhomogeneous convected medium, and shear layer diffraction effects. We also formally introduce the Fraunhofer geometric far-field approximation, show its inherent assumptions and limitations, and observe it can be interpreted as a plane wave approximation of the sound field as seen far from the source. Finally, we show the relationship between the acoustic far-field of a distributed source and the Spatial Fourier Transform of the source strength distribution via the Fraunhofer far-field approximation.

Chapter 3 outlines an analytical method for predicting turbulence-flat plate interaction noise surface pressure and acoustic radiation. We present the analytical model including near-field effects, and show how the model simplifies under far-field (i.e. the Fraunhofer far-field approximation) and infinite-span assumptions. We also describe the flat plate surface pressure response characteristics in both spatial and wavenumber domain, for both single-gust and multiple-gusts interactions.

Chapter 4 describes acoustic radiation predictions obtained with the interaction noise model from Chapter 3 for representative cases of both single-gust and multiple-gusts interaction. We compare the different forms of the prediction model with "far-field" experimental results, where we predict near-field effects should be apparent for single-gust radiation at high frequencies, even in "far-field" experimental setup. We identify three possible sources of near-field effects in the leading edge noise model: the dipole hydrodynamic field, the radiation from subcritical gusts, and the geometric near-field. These effects are assessed in terms of how they affect measurements performed in the near-field, where we show that subcritical gusts are significant contributors of sound at low frequencies and will have a propagating (i.e. non-evanescent) acoustic response for finite-span aerofoils. Finally, we predict that geometric near-field effects

are not apparent when considering multiple-gusts interaction noise, although they become apparent when investigating single-gust interaction noise.

Chapter 5 describes the experiments performed in the ISVR open jet wind tunnel with both a far-field microphone arc and a near-field planar microphone array. We compare the predicted and measured acoustic PSD, cross-PSD phase and coherence for the microphone array elements, and obtain a good agreement for the phase and coherence but poor agreement for the PSD estimation. We then use the interaction noise model to explain trends in coherence as a function of frequency and microphone location, with good agreement between the predictions and measurements.

Chapter 6 reviews microphone array signal processing methods for source estimation. Conventional beamforming and CLEAN-type deconvolution algorithms are described in detail, with some simulated test cases used for illustrative purposes. We then predict the performance of these methods when analysing synthesized microphone array data generated from the interaction noise model, and obtain good agreement with experimental results. We also apply beamforming and CLEAN-SC for measurements made with different aerofoils, and discuss the results.

Chapter 7 proposes a source estimation method for planar sound sources in a moving medium from far-field measurements. The method is based on inverting the Fourier relationship between source in wavenumber domain and radiated far-field in a convected medium, described in Chapter 2. The method is presented in two slightly different approaches: arbitrary wavenumber-domain sampling, and uniform wavenumber-domain sampling. We show that an acoustic source will lose the finer details in its spatial characteristics when estimated from the far-field, due to the loss of high spatial frequencies - i.e. large magnitude wavenumbers. We also show that the proposed method holds strong similarities to frequency-domain delay-and-sum beamforming.

Chapter 8 provides a summary of the Thesis contributions, and proposes some topics for future work.

Chapter 2

Sound Propagation and Radiation in a Moving Medium

In this Chapter we analyse the fundamentals of sound propagation and radiation in a convected medium. We consider the propagation of plane waves in homogeneous media with a subsonic mean flow, and obtain relationships describing their behaviour and conditions for existence. This is followed by a section covering the acoustics of inhomogeneous media, where we use Green's function to describe the radiation of point sources and distributed sources, such as an aerofoil in a turbulent flow.

The Fraunhofer geometric far-field approximation is extensively used in this work and is presented in detail in the following section, including its derivation and conditions of validity. We then merge the three topics discussed above and present a far-field approximation to the radiation of distributed sources, where the acoustic field seen by a distant observer is interpreted as a plane wave and is related to the Spatial Fourier Transform of the source strength distribution. This approximation is identical to the one used by Amiet [8] in his far-field model of leading edge radiation, and forms the basis of our proposed source estimation method from far-field measurements in flow.

Finally, we present a brief discussion on the effects of sound propagation through a shear layer, as observed in open-jet wind tunnel experiments. We propose a simplified model for the refraction of acoustic rays moving propagating through an infinitesimally thin shear layer, which is later used to both predict and compensate for shear layer effects in simulated and experimental data, respectively.

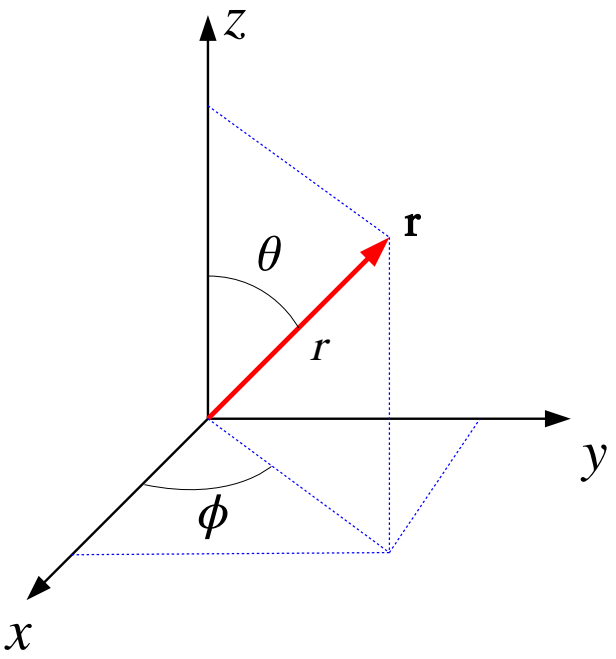

Figure 2.1: Position vector $\mathbf{r}$ in Cartesian (x, y, z) and spherical (r, θ, ϕ) coordinate system.

All analyses presented in this document assume a three-dimensional space. A vector $\mathbf{r}$ can be written in a Cartesian coordinate system as $\mathbf{r} = (x, y, z)$ and in a spherical coordinate system as $\mathbf{r} = (r, \theta, \phi)$, as shown in Figure 2.1. These coordinate systems are related through the following relations:

$$\begin{cases} x = r\sin(\theta)\cos(\phi) \\ y = r\sin(\theta)\sin(\phi) \\ z = r\cos(\theta), \end{cases} \qquad \begin{cases} r = \|\mathbf{r}\| = \sqrt{x^2 + y^2 + z^2} \\ \theta = \arccos(z/r) \\ \phi = \arctan(y/x). \end{cases} \tag{2.1}$$

2.1 Acoustics of Homogeneous Convected Media

The equations describing acoustic waves in a three-dimensional space can be derived from the linearised equations for conservation of mass and conservation of momentum in a fluid, as shown below. However, since aeroacoustic noise is generated by fluid motion, the effects of convection must be included when describing the propagation of acoustic waves.

Let us assume the acoustic medium is subject to a mean flow of velocity $\mathbf{U} = (U_x, 0, 0)$ in the positive-x direction. The uppercase letter denotes a steady value, in opposition to lowercase

letters denoting unsteady (i.e. acoustic) values. The mean flow Mach number is written $M_x = U_x/c_0$, where c_0 is the speed of sound in a quiescent medium.

While generally assumed constant, the speed of sound has a dependence on the air temperature T_C in Celsius and can be calculated as [32]

$$c_0(T_C) = c_0(0)\sqrt{\frac{T_C + 273.15}{273.15}}, \tag{2.2}$$

where the speed of sound at $T_C = 0°\text{C}$ is $c_0(0) = 331.5$ m/s [32].

We define the *total derivative* (or *material derivative*) $Df(\mathbf{r},t)/Dt$ of a function $f(\mathbf{r},t)$, representing the rate of change of the function in a frame of reference that moves with the fluid particles [30]:

$$\frac{Df(\mathbf{r},t)}{Dt} = \frac{\partial f(\mathbf{r},t)}{\partial t} + \mathbf{U}\cdot\nabla f(\mathbf{r},t) \tag{2.3}$$

$$= \frac{\partial f(\mathbf{r},t)}{\partial t} + U_x\frac{\partial f(\mathbf{r},t)}{\partial x}. \tag{2.4}$$

2.1.1 The Homogeneous Convected Wave Equation

In a uniformly moving medium with no sources, the linearised equation of conservation of mass can be written as [30, 33]

$$\frac{D\rho(\mathbf{r},t)}{Dt} + \rho_0\nabla\cdot\mathbf{u}(\mathbf{r},t) = 0, \tag{2.5}$$

where ρ is the acoustic medium density, ρ_0 is the mean fluid density, and $\mathbf{u} = (u_x, u_y, u_z)$ is the acoustic particle velocity. The divergence operator of a vector field is denoted as $\nabla\cdot\{.\} = \partial\{.\}/\partial x + \partial\{.\}/\partial y + \partial\{.\}/\partial z$.

The linearised equation of conservation of momentum is written as

$$\rho_0\frac{D\mathbf{u}(\mathbf{r},t)}{Dt} + \nabla p(\mathbf{r},t) = 0, \tag{2.6}$$

where p is the acoustic pressure, and the gradient operator of a scalar field is denoted as $\nabla\{.\} = (\partial\{.\}/\partial x, \partial\{.\}/\partial y, \partial\{.\}/\partial z)$

These two equations, combined with the isentropic relationship $p(\mathbf{r},t) = c_0^2\rho(\mathbf{r},t)$ [34], give rise to the *homogeneous convected wave equation*

$$\left(\nabla^2 - \frac{1}{c_0^2}\frac{D^2}{Dt^2}\right) p(\mathbf{r},t) = 0. \tag{2.7}$$

The wave equation can be simplified for sources and fields that display time-harmonic behaviour. We will use the real part of the complex exponential $e^{+j\omega t}$ to denote time-harmonic behaviour at the angular frequency ω:

$$p(\mathbf{r},t) = \mathrm{Re}\left\{p(\mathbf{r},\omega)e^{j\omega t}\right\}, \tag{2.8}$$

and leave the notation $\mathrm{Re}\left\{[.]e^{j\omega t}\right\}$ implicit from here onwards. Alternatively, we could obtain a frequency representation $p(\mathbf{r},\omega)$ of the time-domain signal $p(\mathbf{r},t)$ by applying a Temporal Fourier Transform:

$$p(\mathbf{r},\omega) = \frac{1}{2\pi}\int_{-\infty}^{+\infty} p(\mathbf{r},t)e^{-j\omega t}\,\mathrm{d}t. \tag{2.9}$$

For a time-harmonic sound field, the convected wave equation can be rewritten as [33]

$$\left(\nabla^2 + \left[k_0 - jM_x\frac{\partial}{\partial x}\right]^2\right) p(\mathbf{r},\omega) = 0, \tag{2.10}$$

where $k_0 = \omega/c_0$ is the acoustic wavenumber.

The conservation of momentum equation can also be simplified under a time-harmonic assumption to give the *convective Euler's equation* [33], relating the acoustic particle velocity and the acoustic pressure gradient:

$$\rho_0\left(j\omega + U_x\frac{\partial}{\partial x}\right)\mathbf{u}(\mathbf{r},\omega) + \nabla p(\mathbf{r},\omega) = 0. \tag{2.11}$$

2.1.2 Plane Wave Solutions in Convected Media

In the following chapters we will rely heavily on approximating sound fields as plane waves, so let us consider plane wave solutions to the convected wave equation in more detail. In later sections we will be considering only the acoustic field radiated to the space above the sources, which are assumed to be located at the $z = 0$ plane; hence, we restrict our current analysis to $z \geq 0$ coordinates only.

A plane wave represents a separable solution to the homogeneous Helmholtz equation in a Cartesian coordinate system; a unitary-amplitude plane wave is denoted as

$$p(\mathbf{r}, \omega) = e^{-jk_x x} e^{-jk_y y} e^{-jk_z z} \tag{2.12}$$

$$= e^{-j\mathbf{k}\cdot\mathbf{r}}, \tag{2.13}$$

where $\mathbf{k} = (k_x, k_y, k_z)$ is the wavenumber vector, with magnitude $k = \|\mathbf{k}\|$ and pointing in the direction of propagation (θ_p, ϕ_p) of the plane wave. Its Cartesian components k_x, k_y, k_z are called *trace wavenumbers* in the x, y, z directions, respectively. The wavenumber vector can also be represented in polar coordinates as (k, θ_p, ϕ_p), where

$$\begin{cases} k_x = k\sin(\theta_p)\cos(\phi_p) \\ k_y = k\sin(\theta_p)\sin(\phi_p) \\ k_z = k\cos(\theta_p), \end{cases} \qquad \begin{cases} k = \|\mathbf{k}\| = \sqrt{k_x^2 + k_y^2 + k_z^2} \\ \theta_p = \arccos(k_z/k) \\ \phi_p = \arctan(k_y/k_x). \end{cases} \tag{2.14}$$

The wavenumber vector magnitude k is related to the wavelength λ and phase speed c_p of the plane wave, observed in the direction of propagation, through the expression

$$k = \frac{\omega}{c_p} = \frac{2\pi}{\lambda}. \tag{2.15}$$

Note the absence of the subscript $\{.\}_0$ in the above variables, indicating they are not necessarily identical to the acoustic wavenumber k_0, the acoustic wavelength $\lambda_0 = 2\pi/k_0$ and the speed of sound c_0 in a quiescent medium.

We can insert Eq. 2.13 into Eq. 2.10 and obtain the dispersion relation for a uniformly moving medium:

$$k_x^2 + k_y^2 + k_z^2 = (k_0 - M_x k_x)^2 \tag{2.16}$$

$$= k_0^2 - 2k_0 M_x k_x + M_x^2 k_x^2. \tag{2.17}$$

Note that the wavenumber vector magnitude is not a constant, but instead a function of the streamwise trace wavenumber k_x. In other words, it will vary with the relative angle between the wavenumber vector $\mathbf{k}$ and the mean flow velocity $\mathbf{U} = (U_x, 0, 0)$. As a consequence, plane waves propagating in a uniformly moving medium will also have varying phase velocity c_p and wavelength λ, depending on their direction of propagation relative to the mean flow.

Let us now assume the trace wavenumbers k_x and k_y are independent variables and can be chosen arbitrarily. The process of obtaining the k_z component of the wavenumber vector from its trace components (k_x, k_y) is equivalent to calculating a three-dimensional sound field $p(\mathbf{r}, \omega)$ from its trace $p(x, y, \omega)$ in the $z = 0$ plane only; this process is used in later sections to obtain the acoustic radiation of planar sources [7]. A k_z that satisfies Eq. 2.17 for a given (k_x, k_y) pair can be found as

$$k_z = \pm\sqrt{(k_0 - M_x k_x)^2 - k_x^2 - k_y^2} \tag{2.18}$$

$$= \pm\sqrt{k_0^2 - (1 - M_x^2)k_x^2 - 2k_0 M_x k_x - k_y^2}. \tag{2.19}$$

In later sections we will consider sources on the plane $z = 0$ radiating into the half-space $z > 0$, so we consider only positive-valued solutions of Eq. 2.19 as representing waves radiated from these sources.

For positive-, real-valued k_z, the dispersion relation for a convected medium represents half the surface of an ellipsoid, shown in Figure 2.2. The intersection of the ellipsoid surface with the $k_z = 0$ plane forms an ellipse, indicated by the dash-dotted line. Both the ellipsoid and the ellipse become stretched towards negative k_x values with increasing Mach number M_x, and revert respectively into a sphere and a circle of radius k_0 and centred at $(k_x, k_y) = (0, 0)$ for a quiescent medium ($M_x = 0$) [29].

For a given pair of trace wavenumbers (k_x, k_y) located inside the ellipse, the corresponding k_z component that satisfies the dispersion relation (Eq. 2.19) is real-valued and given by the

height of the ellipsoid above the (k_x, k_y) point, as indicated in Fig. 2.2. The acoustic field $p(\mathbf{r}, \omega) = e^{-j\mathbf{k}\cdot\mathbf{r}}$ evaluated from this wavenumber vector $\mathbf{k} = (k_x, k_y, k_z)$ represents a plane wave propagating in physical space $(x, y, z \geq 0)$ in the direction (θ_p, ϕ_p), as described in Eq. 2.14.

On the other hand, trace wavenumbers (k_x, k_y) located outside the ellipse cannot have a corresponding real-valued k_z that obeys the dispersion relation (Eq. 2.19), and hence cannot represent a propagating plane wave at the chosen angular frequency ω and Mach number M_x. In these cases, k_z is purely imaginary, and the resulting acoustic field is an evanescent wave decaying exponentially in the $+z$ direction:

$$k_z = \pm j\sqrt{(1 - M_x^2)k_x^2 + 2k_0 M_x k_x + k_y^2 - k_0^2} \tag{2.20}$$

$$= \pm j k_z', \tag{2.21}$$

where k_z' is positive- and real-valued. We will again consider only positive-valued solutions of Eq. 2.21 from now onwards. The resulting evanescent field in the $z > 0$ space is expressed as

$$p(\mathbf{r}, \omega) = e^{-jk_x x} e^{-jk_y y} e^{-k_z' z}. \tag{2.22}$$

The boundary between propagating and non-propagating waves is obtained for trace wavenumbers (k_x, k_y) located over the ellipse, where $k_z = 0$, and represent acoustic waves propagating in a direction parallel to the $z = 0$ plane. This curve in the (k_x, k_y) plane is called the *radiation ellipse* [35]; for a quiescent medium $(M_x = 0)$, the radiation ellipse reverts to the *radiation circle* [29].

We can obtain an expression for the radiation ellipse by setting $k_z = 0$ and rearranging Eq. 2.17:

$$\frac{(k_x + k_{x1})^2}{k_{r1}^2} + \frac{k_y^2}{k_{r2}^2} = 1, \tag{2.23}$$

where

$$k_{x1} = \frac{k_0 M_x}{\beta^2}, \quad k_{r1} = \frac{k_0}{\beta^2}, \quad k_{r2} = \frac{k_0}{\beta}, \quad \beta^2 = 1 - M_x^2. \tag{2.24}$$

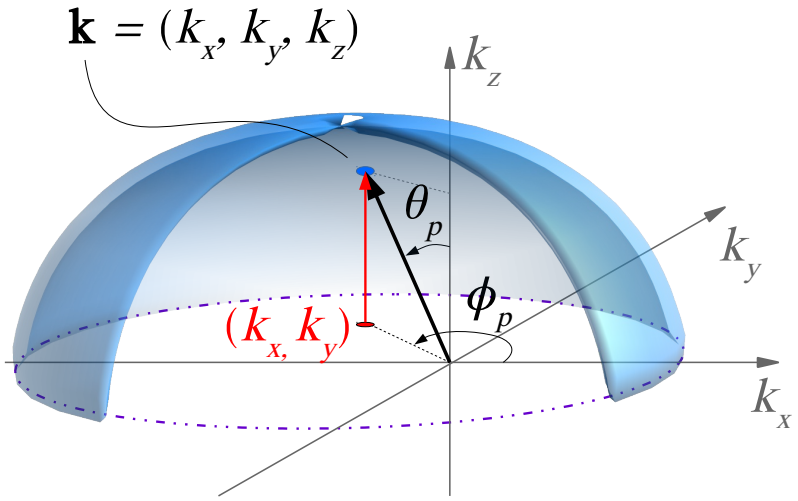

Figure 2.2: Three-dimensional diagram of the radiation ellipsoid in wavenumber domain. The vector $\mathbf{k} = (k_x, k_y, k_z)$ is located over the surface of the ellipsoid and represents a propagating plane wave in the direction (θ_p, ϕ_p). Note that $\mathbf{k} = (k, \theta_p, \phi_p)$ in polar coordinates.

Equation 2.23 describes an ellipse centred at $(-k_{x1}, 0)$, with a semimajor axis k_{r1} and a semiminor axis k_{r2} [35]. The ellipse is shown in Figure 2.3 for $M_x = 0.5$, with the radiation circle for $M_x = 0$ at the same angular frequency ω for comparison. The ellipse has its area proportional to frequency: at low frequencies, the ellipse will contain only wavenumbers with small magnitude, while at higher frequencies the ellipse will increase in size and contain wavenumbers with larger magnitude.

From Equation 2.23, we can obtain an expression for the streamwise wavenumbers k_x on the right half of the ellipse (i.e. $k_x \geq -k_{x1}$) as a function of the wavenumber k_y:

$$k_x = \frac{1}{\beta^2}\left(\sqrt{k_0^2 - (k_y\beta)^2} - k_0 M_x\right), \qquad (k_x, k_y) \in \text{Rad. Ellipse.} \tag{2.25}$$

Equation 2.25 will be used later when discussing the response functions of flat plate aerofoils to a single turbulent gust in Section 3.2.2.

Since $\|\mathbf{k}\| = k$ is strictly non-negative, Equation 2.17 can be simplified to yield the wavenumber vector magnitude as

$$k = k_0 - M_x k_x. \tag{2.26}$$

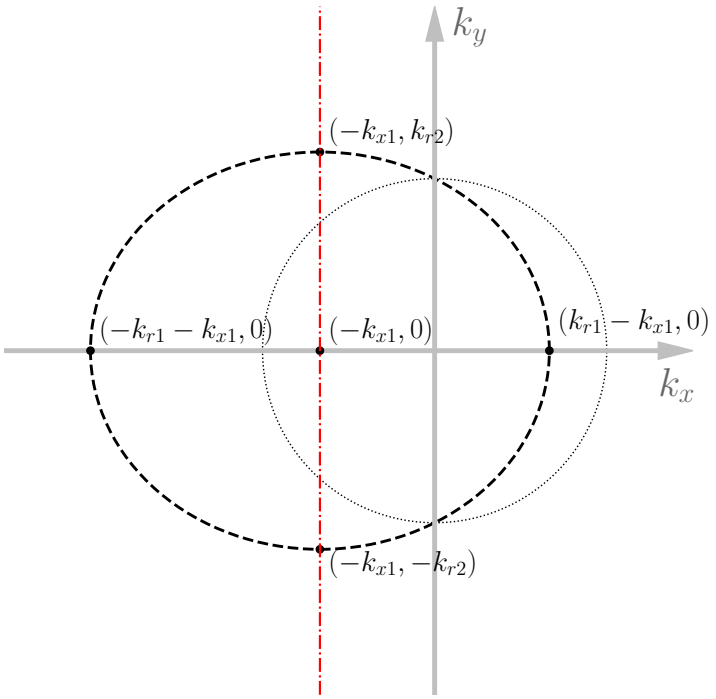

Figure 2.3: Radiation Ellipse for a mean flow in the positive-x direction ($M_x = 0.5$).

This allows us to use Equation 2.14 to obtain explicit expressions for the propagation angles (θ_p, ϕ_p) as a function of the trace wavenumbers (k_x, k_y):

$$\begin{cases} \theta_p = \arccos\left(\dfrac{\sqrt{(k_0 - M_x k_x)^2 - k_x^2 - k_y^2}}{k_0 - M_x k_x}\right) \\ \phi_p = \arctan\left(k_y / k_x\right). \end{cases} \tag{2.27}$$

2.1.2.1 Example: Single-k_x Pressure Distribution in Varying Mach Number Flow

As an example, consider a pressure distribution composed of a single k_x term over the infinite $z = 0$ plane. For different flow conditions, there can be different plane waves on the three-dimensional space above the plane that share the same trace wavenumber k_x. For simplicity, we will look into the $y = 0$ plane; this is identical to assuming $k_y = 0$ [29], and shows how a single pressure distribution can correspond to different acoustic fields in the medium above it under different propagation conditions.

Figure 2.4 shows four examples of a fixed k_x trace wavenumber (see (k_x, k_z) wavenumber diagram in the left-hand side of the Figure) and their corresponding acoustic plane wave solutions in a quiescent ($M_x = 0$, middle of the Figure) and in a convected medium ($M_x = 0.5$,

right-hand side of the Figure). Note how the induced wavenumber vector magnitude and direction of propagation change between the two different media. The exception is the wave propagating perpendicular to the flow (Figure 2.4b), where the wavenumber vector is the same in both cases.

It is shown that the presence or absence of a mean flow can drastically alter the acoustic field: note in Figure 2.4d how a disturbance that propagates to the far-field in a quiescent medium can become evanescent in a convected medium, for example. Although not shown here, it is also possible for a negative k_x component to represent an evanescent wave in quiescent medium and a propagating wave in a convected medium.

2.1.2.2 Plane Wave Representations of Sound Fields

Since plane waves are a solution to the wave equation, and since the wave equation is linear, any field composed of a sum of plane waves will also be a solution to the wave equation. From Fourier Theory, it is possible to synthesize an arbitrary three-dimensional field as a sum of plane wave [1, 29]. Note that, in this context, the term *plane waves* is used to denote both propagating waves and evanescent waves [29].

This relationship can be expressed via the *Spatiotemporal Fourier Transform*, defined as

$$p(\mathbf{k},\omega) = \frac{1}{(2\pi)^4}\int_t\int_{\mathbf{r}} p(\mathbf{r},t)\; e^{j\mathbf{k}\cdot\mathbf{r}}e^{-j\omega t}\,\mathrm{d}\mathbf{r}\,\mathrm{d}t. \tag{2.28}$$

Therefore, there is a complex-valued spectrum $p(\mathbf{k},\omega)$ which describes a spatiotemporal field $p(\mathbf{r},t)$ in the wavenumber-frequency domains.

We also define the *Inverse Spatiotemporal Fourier Transform* as

$$p(\mathbf{r},t) = \int_\omega\int_{\mathbf{k}} p(\mathbf{k},\omega)\; e^{-j\mathbf{k}\cdot\mathbf{r}}e^{j\omega t}\,\mathrm{d}\mathbf{k}\,\mathrm{d}\omega. \tag{2.29}$$

Hence, a three-dimensional, time-varying field $p(\mathbf{r},t)$ can be expressed as a Fourier sum of time-harmonic plane waves, whose spectrum $p(\mathbf{k},\omega)$ denote the complex amplitudes of each plane wave term.

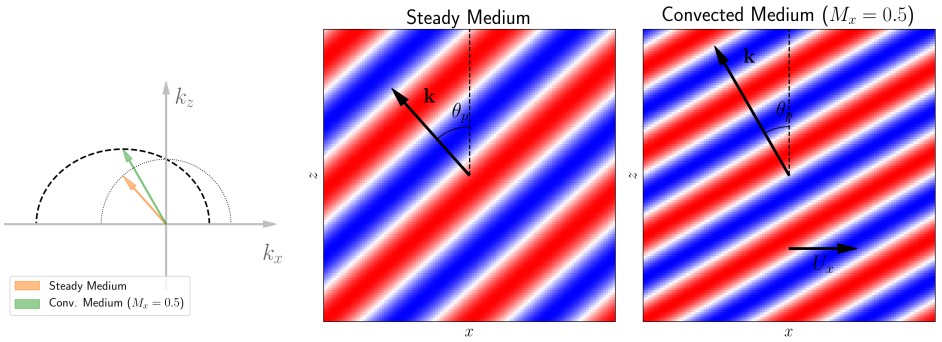

(a)

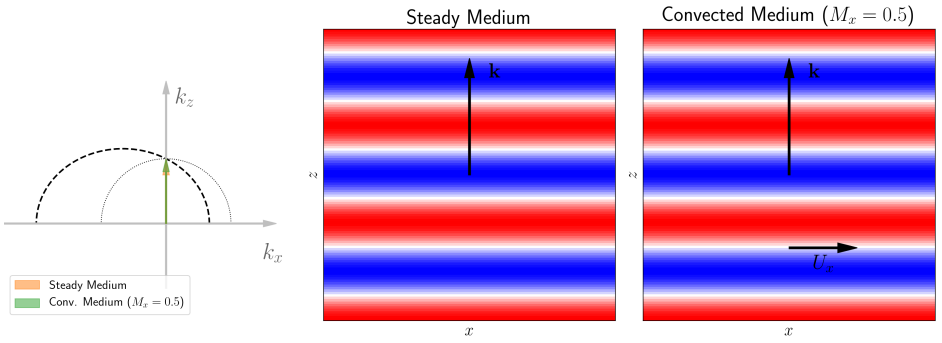

(b)

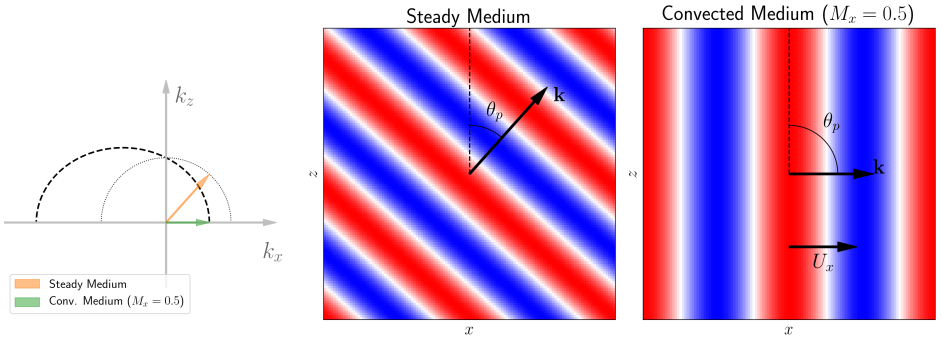

(c)

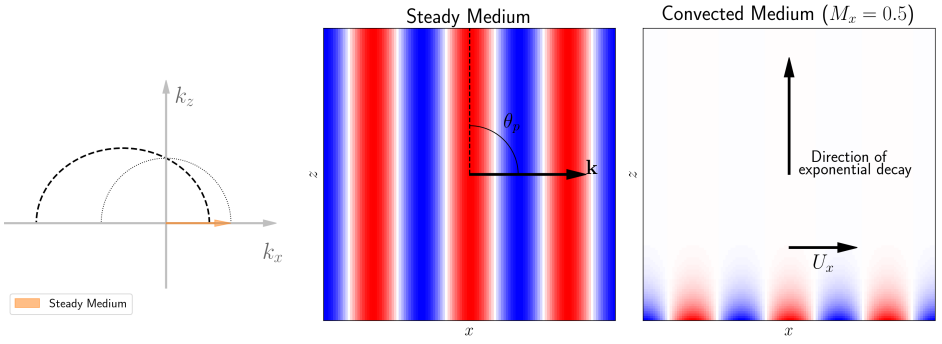

(d)

Figure 2.4: Examples of plane wave propagation in the xz-plane for a quiescent and a moving medium ($M_x = 0.5$), as induced by a single disturbance with trace wavenumbers $(k_x, k_y = 0)$: (a) $k_x < 0$; (b) $k_x = 0$; (c) $0 < k_x < k_0$; (d) $k_x = k_0$.

2.2 Green's Functions and the Inhomogeneous Convected Wave Equation

While plane waves offer a convenient solution to the homogeneous wave equation, they are not the most adequate form in the presence of inhomogeneities. This limitation can be too restrictive for some cases, and therefore we need to consider different solutions to the Helmholtz equation.

A general solution for second-order linear differential equations - such as the wave equation - can be obtained through the well-established method of Green's functions [36, 37]. Green's functions are solutions for a case that is homogeneous everywhere except at a single point; the solution for a particular inhomogeneity distribution is then expressed as an integration in terms of Green's functions [37].

We will now obtain a general solution to the inhomogeneous convected Helmholtz equation using the method of Green's functions. Let us assume an arbitrary source distribution of the form $Q(\mathbf{r}_s, \omega)$, such that the inhomogeneous convected Helmholtz equation is written as

$$\left(\nabla^2 + \left[k_0 - jM_x\frac{\partial}{\partial x}\right]^2\right) p(\mathbf{r}_s, \omega) = -Q(\mathbf{r}_s, \omega). \tag{2.30}$$

The term $Q(\mathbf{r}_s, \omega)$ is a general term describing a distribution of sources inside a volume V, as shown in Figure 2.5. We denote the volume V as being bounded by a surface S; in the particular example shown in Figure 2.5, $S = S_1 \cup S_2$. Surfaces S_1 and S_2 can represent either mathematical abstractions created to facilitate the problem, or actual physical boundaries in the volume V. Note as well that the unitary normal vectors $\mathbf{n}$ point *outwards* of the volume V.

2.2.1 Boundary Conditions

When present, the surface S interacts with the acoustic field $p(\mathbf{r}, \omega)$ through the *boundary conditions* prescribed on S. The Green's function describes how sound propagates through the domain of interest [38], and hence it must include the effects of any particular boundary conditions present in the problem of interest.

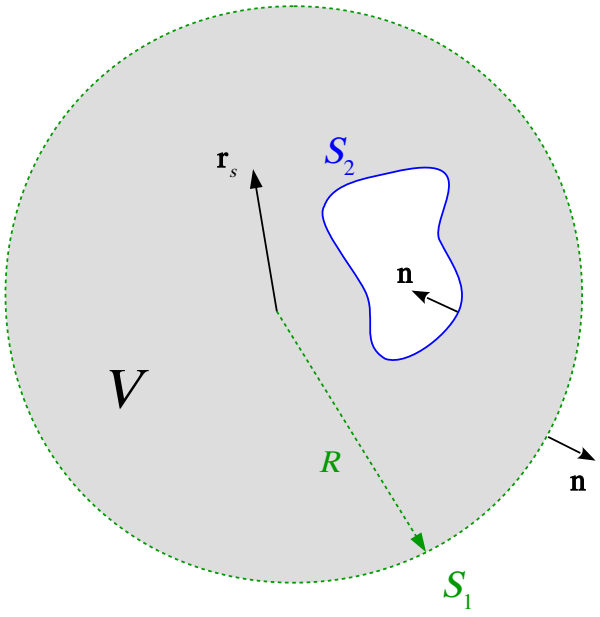

Figure 2.5: Schematic of the problem used to derive the free-field Green's Function and the Kirchhoff-Helmholtz Integral formulation.

Boundary conditions can be physically interpreted as a distribution of equivalent acoustic sources placed infinitesimally close to the surface [37]. In order to underscore this dualism between acoustic sources and boundary conditions, we will use the adjectives *homogeneous* and *inhomogeneous* when describing boundary conditions as well. We define:

- *Homogeneous* boundary conditions: when it is required that the acoustic field (or its normal gradient) be identically zero at the surface S;
- *Inhomogeneous* boundary conditions: when it is required that the acoustic field (or its normal gradient) be a given non-zero function at the surface S.

The most fundamental boundary conditions used in acoustics are: the *Dirichlet boundary condition*, where the boundary conditions are imposed on the complex amplitude of the acoustic field at the boundary; the *Neumann boundary condition*, where the boundary conditions are imposed on the normal gradient of the acoustic field at the boundary; and the *Sommerfeld radiation condition*, where it is imposed that the acoustic field is composed solely of waves outgoing towards infinity.

2.2.1.1 The Dirichlet Boundary Condition

The Dirichlet boundary condition is given by

$$p(\mathbf{r}_s, \omega) = D(\mathbf{r}_s, \omega), \quad \mathbf{r}_s \in S, \tag{2.31}$$

where $D(\mathbf{r}_s, \omega)$ is a prescribed acoustic pressure at the boundary S. The *inhomogeneous* Dirichlet condition is given by $D_I(\mathbf{r}_s, \omega) \neq 0$, while the *homogeneous* Dirichlet condition is given by $D_H(\mathbf{r}_s, \omega) = 0$. A Green's Function that satisfies the Dirichlet boundary condition is named a *Dirichlet Green's Function* [38].

Physically, the homogeneous Dirichlet boundary condition can be interpreted as modeling a boundary that has zero acoustic impedance, where any wave propagating outwards of the volume V will have its acoustic pressure forced to zero at the boundary: this situation occurs when sound propagating underwater reaches a water-air boundary, for example. The inhomogeneous Dirichlet boundary condition denotes a prescribed pressure over a given surface: for example, an aerofoil interacting with a turbulent gust in a mean flow will block the gusts components normal to the aerofoil, causing a pressure jump to develop over the aerofoil surface.

2.2.1.2 The Neumann Boundary Condition

The Neumann boundary condition is given by

$$\frac{\partial}{\partial \mathbf{n}} p(\mathbf{r}_s, \omega) = N(\mathbf{r}_s, \omega), \quad \mathbf{r}_s \in S, \tag{2.32}$$

where $\partial\{.\}/\partial\mathbf{n} = \mathbf{n} \cdot \nabla$ is the derivative in the direction of the outwards normal vector $\mathbf{n}$, and $N(\mathbf{r}_s, \omega)$ is the prescribed pressure gradient normal to the boundary. The *inhomogeneous* Neumann condition is given by $N_I(\mathbf{r}_s, \omega) \neq 0$, while the *homogeneous* Neumann condition is given by $N_H(\mathbf{r}_s, \omega) = 0$. A Green's Function that satisfies the Neumann boundary condition is named a *Neumann Green's Function* [38].

Note, however, that the normal gradient of the acoustic pressure $\partial p(\mathbf{r}_s, \omega)/\partial \mathbf{n}$ is directly related to the acoustic particle velocity $u_n(\mathbf{r}_s, \omega)$ normal to the surface and its streamwise derivative $\partial u_n(\mathbf{r}_s, \omega)/\partial x$ through Eq. 2.11, rewritten here for the normal component only:

$$\frac{\partial p(\mathbf{r}_s, \omega)}{\partial \mathbf{n}} = -j\rho_0 \omega u_n(\mathbf{r}_s, \omega) - \rho_0 U_x \frac{\partial}{\partial x_s} u_n(\mathbf{r}_s, \omega). \tag{2.33}$$

For no-flow conditions, the term containing the streamwise derivative $\partial/\partial x$ vanishes, and Neumann boundary conditions can then be interpreted as imposing an acoustic particle velocity distribution normal to a surface S.

Physically, homogeneous Neumann boundary conditions can be interpreted as having the surface S being impenetrable and stationary, such that there will be no acoustic particle velocity across it. Equivalently, the inhomogeneous Neumann boundary condition can arise from a vibrating surface, where we assume the normal surface velocity $\partial v/\partial \mathbf{n}$ at S imposes an identical normal acoustic particle velocity $\mathbf{u}_n$ on the fluid.

2.2.1.3 The Sommerfeld Radiation Condition

When considering acoustic sources in the absence of boundaries - i.e. in free-field conditions - it is common to describe this condition as having the volume V of interest surrounded by a spherical or hemispherical boundary - such as surface S_1 in Figure 2.5 - and then take the limit of R going to infinity. As S_1 gets further away, any prescribed boundary conditions on S_1 cease to affect the volume V due to the sheer distance between them; alternatively, it can be said that any solution to a free-field problem must consist solely of acoustic waves travelling away from the sources and towards infinity (i.e. *outgoing* waves), and not otherwise (*incoming* waves).

These equivalent conditions, named *Sommerfeld radiation condition*, can be denoted as a boundary condition on S_1 and written for a quiescent medium as [39]

$$\lim_{r \to \infty} r \left(\frac{\partial p(\mathbf{r}, \omega)}{\partial r} + jk_0 p(\mathbf{r}, \omega) \right) = 0. \tag{2.34}$$

If free-field conditions are assumed, the Green's function is assumed to satisfy the Sommerfeld radiation condition [40] - i.e. there can only exist waves outgoing from a source.

2.2.2 General Solution to the Inhomogeneous Convected Wave Equation

Let us now obtain the general solution to the acoustic radiation problem for an arbitrary source distribution and boundary conditions in a convected medium, as posed on Equation 2.30, using the method of Green's functions. Such general solution has been previously presented by Wu and Lee [41] using the weighted residual method, and more recently by Mancini et al. [42] using integral theorems and vector algebra manipulation; we will describe an approach similar to the latter.

We define a convected Green's function $G_{U_x}(\mathbf{r}|\mathbf{r}_s, \omega)$, corresponding to the acoustic field observed at $\mathbf{r}$ generated by a time-harmonic point monopole source at $\mathbf{r}_s$ in a convected medium; such function must satisfy the inhomogeneous convected Helmholtz equation when the singularity on the right-hand side is a Dirac Delta at the monopole location:

$$\left(\nabla^2 + \left[k_0 - jM_x\frac{\partial}{\partial x}\right]^2\right) G_{U_x}(\mathbf{r}|\mathbf{r}_s, \omega) = -\delta(\mathbf{r} - \mathbf{r}_s). \tag{2.35}$$

The Green's function represents the spatial field generated by a time-harmonic point source at the point $\mathbf{r}_s$, subject to any prescribed boundary conditions on the surface S.

The Green's function for a quiescent medium is reciprocal, such that $G(\mathbf{r}|\mathbf{r}_s, \omega) = G(\mathbf{r}_s|\mathbf{r}, \omega)$, as long as the two points $\mathbf{r}, \mathbf{r}_s$ are inside the volume V where the Helmholtz equation is satisfied. However, in a convected medium, reciprocity also requires that the flow direction is reversed [30], which is expressed as

$$G_{U_x}(\mathbf{r}|\mathbf{r}_s, \omega) = G_{-U_x}(\mathbf{r}_s|\mathbf{r}, \omega). \tag{2.36}$$

We then rewrite Eq. 2.35 for the reciprocal case; note that the flow direction has been reversed, leading to a change in the sign of the $\partial/\partial x$ operator inside the square brackets:

$$\left(\nabla^2 + \left[k_0 + jM_x\frac{\partial}{\partial x}\right]^2\right) G_{-U_x}(\mathbf{r}_s|\mathbf{r}, \omega) = -\delta(\mathbf{r}_s - \mathbf{r}). \tag{2.37}$$

We multiply Eq. 2.30 by $G_{-U_x}(\mathbf{r}_s|\mathbf{r}, \omega)$, multiply Eq. 2.37 by $p(\mathbf{r}_s, \omega)$ and subtract the latter from the former to obtain:

$$\begin{aligned}
&\left[G_{-U_x}(\mathbf{r}_s|\mathbf{r},\omega)\nabla^2 p(\mathbf{r}_s,\omega) - p(\mathbf{r}_s,\omega)\nabla^2 G_{-U_x}(\mathbf{r}_s|\mathbf{r},\omega)\right]\ldots \\
&\qquad \ldots + \left[G_{-U_x}(\mathbf{r}_s|\mathbf{r},\omega)\left(k_0 - jM_x\frac{\partial}{\partial x}\right)^2 p(\mathbf{r}_s,\omega) - p(\mathbf{r}_s,\omega)\left(k_0 + jM_x\frac{\partial}{\partial x}\right)^2 G_{-U_x}(\mathbf{r}_s|\mathbf{r},\omega)\right] \\
&\quad = -Q(\mathbf{r}_s,\omega)G_{-U_x}(\mathbf{r}_s|\mathbf{r},\omega) + \delta(\mathbf{r}_s - \mathbf{r})p(\mathbf{r}_s,\omega). \qquad (2.38)
\end{aligned}$$

We can now integrate both sides of Eq. 2.38 over a volume V defined in the coordinates $\mathbf{r}_s$ and surrounding the source region; integrating the right-hand side and exchanging $G_{-U_x}(\mathbf{r}_s|\mathbf{r},\omega)$ with $G_{U_x}(\mathbf{r}|\mathbf{r}_s,\omega)$, we obtain

$$\begin{aligned}
&-\int_V Q(\mathbf{r}_s,\omega)G_{U_x}(\mathbf{r}|\mathbf{r}_s,\omega)\,\mathrm{d}V(\mathbf{r}_s) + \int_V \delta(\mathbf{r}_s - \mathbf{r})p(\mathbf{r}_s,\omega)\,\mathrm{d}V(\mathbf{r}_s) \\
&\qquad = -\int_V Q(\mathbf{r}_s,\omega)G_{U_x}(\mathbf{r}|\mathbf{r}_s,\omega)\,\mathrm{d}V(\mathbf{r}_s) + \begin{cases} p(\mathbf{r},\omega), & \mathbf{r}\in V \\ p(\mathbf{r},\omega)/2, & \mathbf{r}\in\partial V \\ 0, & \mathbf{r}\notin V \end{cases}. \qquad (2.39)
\end{aligned}$$

Integrating the left-hand side of Eq. 2.38, we obtain

$$\begin{aligned}
&\int_V \left[G_{-U_x}(\mathbf{r}_s|\mathbf{r},\omega)\nabla^2 p(\mathbf{r}_s,\omega) - p(\mathbf{r}_s,\omega)\nabla^2 G_{-U_x}(\mathbf{r}_s|\mathbf{r},\omega)\right]\,\mathrm{d}V(\mathbf{r}_s)\ldots \\
&\quad + \int_V \left[G_{-U_x}(\mathbf{r}_s|\mathbf{r},\omega)\left(k_0 - jM_x\frac{\partial}{\partial x}\right)^2 p(\mathbf{r}_s,\omega)\right. \\
&\qquad \left. -p(\mathbf{r}_s,\omega)\left(k_0 + jM_x\frac{\partial}{\partial x}\right)^2 G_{-U_x}(\mathbf{r}_s|\mathbf{r},\omega)\right]\mathrm{d}V(\mathbf{r}_s). \qquad (2.40)
\end{aligned}$$

The first term of Eq. 2.40 can be simplified by exchanging $G_{-U_x}(\mathbf{r}_s|\mathbf{r},\omega)$ with $G_{U_x}(\mathbf{r}|\mathbf{r}_s,\omega)$ and using Green's Theorem:

$$\begin{aligned}
&\int_V \left[G_{U_x}(\mathbf{r}|\mathbf{r}_s,\omega)\nabla^2 p(\mathbf{r}_s,\omega) - p(\mathbf{r}_s,\omega)\nabla^2 G_{U_x}(\mathbf{r}|\mathbf{r}_s,\omega)\right]\,\mathrm{d}V(\mathbf{r}_s) \\
&\qquad = \int_S \left[G_{U_x}(\mathbf{r}|\mathbf{r}_s,\omega)\frac{\partial}{\partial\mathbf{n}}p(\mathbf{r}_s,\omega) - p(\mathbf{r}_s,\omega)\frac{\partial}{\partial\mathbf{n}}G_{U_x}(\mathbf{r}|\mathbf{r}_s,\omega)\right]\,\mathrm{d}S(\mathbf{r}_s), \qquad (2.41)
\end{aligned}$$

where the surface $S(\mathbf{r}_s)$ is the boundary of the volume $V(\mathbf{r}_s)$, the vector $\mathbf{n} = (n_x, n_y, n_z)$ is the outward-pointing normal to the surface S at $\mathbf{r}_s$, and $\partial/\partial\mathbf{n}$ is the normal derivative to the

surface S in the outward direction; thus, we have transformed the volume integral in V in a surface integral in S.

The second integral in Eq. 2.40 can be rewritten by exchanging $G_{-U_x}(\mathbf{r}_s|\mathbf{r},\omega)$ for $G_{U_x}(\mathbf{r}|\mathbf{r}_s,\omega)$ and expanding the terms in parenthesis as

$$\begin{aligned}\int_V \Bigg[& G_{U_x}(\mathbf{r}|\mathbf{r}_s,\omega)\left(k_0^2 - 2jk_0M_x\frac{\partial}{\partial x} - M_x^2\frac{\partial^2}{\partial x^2}\right)p(\mathbf{r}_s,\omega)\ldots \\ & -p(\mathbf{r}_s,\omega)\left(k_0^2 + 2jk_0M_x\frac{\partial}{\partial x} - M_x^2\frac{\partial^2}{\partial x^2}\right)G_{U_x}(\mathbf{r}|\mathbf{r}_s,\omega)\Bigg]\,\mathrm{d}V(\mathbf{r}_s) \qquad (2.42)\\ = \int_V \Bigg[& k_0^2\overbrace{\Big(G_{U_x}(\mathbf{r}|\mathbf{r}_s,\omega)p(\mathbf{r}_s,\omega) - p(\mathbf{r}_s,\omega)G_{U_x}(\mathbf{r}|\mathbf{r}_s,\omega)\Big)}^{=0}\ldots \\ & -2jk_0M_x\Big(G_{U_x}(\mathbf{r}|\mathbf{r}_s,\omega)\frac{\partial}{\partial x}p(\mathbf{r}_s,\omega) + p(\mathbf{r}_s,\omega)\frac{\partial}{\partial x}G_{U_x}(\mathbf{r}|\mathbf{r}_s,\omega)\Big)\ldots \\ & -M_x^2\Big(G_{U_x}(\mathbf{r}|\mathbf{r}_s,\omega)\frac{\partial^2}{\partial x^2}p(\mathbf{r}_s,\omega) - p(\mathbf{r}_s,\omega)\frac{\partial^2}{\partial x^2}G_{U_x}(\mathbf{r}|\mathbf{r}_s,\omega)\Big)\Bigg]\,\mathrm{d}V(\mathbf{r}_s). \qquad (2.43)\end{aligned}$$

The first term in Eq. 2.43 is identically zero, as indicated, while the second term can be simplified by considering the following identities:

$$G_{U_x}(\mathbf{r}|\mathbf{r}_s,\omega)\frac{\partial}{\partial x}p(\mathbf{r}_s,\omega) = G_{U_x}(\mathbf{r}|\mathbf{r}_s,\omega)\nabla\cdot[p(\mathbf{r}_s,\omega)\mathbf{n}_x]\,, \qquad (2.44)$$

$$p(\mathbf{r}_s,\omega)\frac{\partial}{\partial x}G_{U_x}(\mathbf{r}|\mathbf{r}_s,\omega) = [p(\mathbf{r}_s,\omega)\mathbf{n}_x]\cdot\nabla G_{U_x}(\mathbf{r}|\mathbf{r}_s,\omega), \qquad (2.45)$$

where $\mathbf{n}_x = (1,0,0)$ is a unit vector pointing in the positive-x direction and the term $p(\mathbf{r}_s,\omega)\mathbf{n}_x$ in square brackets is treated as a vector field. We can then rewrite the second term in Eq. 2.43 as

$$\begin{aligned}
&\int_V \left[G_{U_x}(\mathbf{r}|\mathbf{r}_s,\omega)\frac{\partial}{\partial x}p(\mathbf{r}_s,\omega) + p(\mathbf{r}_s,\omega)\frac{\partial}{\partial x}G_{U_x}(\mathbf{r}|\mathbf{r}_s,\omega)\right] \mathrm{d}V(\mathbf{r}_s) \\
&\quad = \int_V \Big(G_{U_x}(\mathbf{r}|\mathbf{r}_s,\omega)\nabla\cdot[p(\mathbf{r}_s,\omega)\mathbf{n}_x] + [p(\mathbf{r}_s,\omega)\mathbf{n}_x]\cdot\nabla G_{U_x}(\mathbf{r}|\mathbf{r}_s,\omega)\Big)\,\mathrm{d}V(\mathbf{r}_s) && (2.46)\\
&\quad = \int_V \nabla\cdot\Big(G_{U_x}(\mathbf{r}|\mathbf{r}_s,\omega)\,[p(\mathbf{r}_s,\omega)\mathbf{n}_x]\Big)\,\mathrm{d}V(\mathbf{r}_s) && (2.47)\\
&\quad = \int_S G_{U_x}(\mathbf{r}|\mathbf{r}_s,\omega)\,([p(\mathbf{r}_s,\omega)\mathbf{n}_x]\cdot\mathbf{n})\,\mathrm{d}S(\mathbf{r}_s) && (2.48)\\
&\quad = \int_S \left[G_{U_x}(\mathbf{r}|\mathbf{r}_s,\omega)p(\mathbf{r}_s,\omega)n_x\right]\mathrm{d}S(\mathbf{r}_s), && (2.49)
\end{aligned}$$

where n_x is the x component of the normal vector $\mathbf{n} = (n_x, n_y, n_z)$; the passage from the volume integral to the surface integral comes from the divergence theorem.

The third term in Eq. 2.43 can be simplified by considering the following identity:

$$\begin{aligned}
&G_{U_x}(\mathbf{r}|\mathbf{r}_s,\omega)\frac{\partial^2}{\partial x^2}p(\mathbf{r}_s,\omega) - p(\mathbf{r}_s,\omega)\frac{\partial^2}{\partial x^2}G_{U_x}(\mathbf{r}|\mathbf{r}_s,\omega) \\
&\qquad = \nabla\cdot\left[\left(G_{U_x}(\mathbf{r}|\mathbf{r}_s,\omega)\frac{\partial}{\partial x}p(\mathbf{r}_s,\omega) - p(\mathbf{r}_s,\omega)\frac{\partial}{\partial x}G_{U_x}(\mathbf{r}|\mathbf{r}_s,\omega)\right)\mathbf{n}_x\right], && (2.50)
\end{aligned}$$

where $\mathbf{n}_x = (1,0,0)$. Hence, we can once again use the divergence theorem and rewrite the third term in Eq. 2.43 as

$$\begin{aligned}
&\int_V \left[G_{U_x}(\mathbf{r}|\mathbf{r}_s,\omega)\frac{\partial^2}{\partial x^2}p(\mathbf{r}_s,\omega) - p(\mathbf{r}_s,\omega)\frac{\partial^2}{\partial x^2}G_{U_x}(\mathbf{r}|\mathbf{r}_s,\omega)\right]\mathrm{d}V(\mathbf{r}_s) \\
&\qquad = \int_V \nabla\cdot\left[\left(G_{U_x}(\mathbf{r}|\mathbf{r}_s,\omega)\frac{\partial}{\partial x}p(\mathbf{r}_s,\omega) - p(\mathbf{r}_s,\omega)\frac{\partial}{\partial x}G_{U_x}(\mathbf{r}|\mathbf{r}_s,\omega)\right)\mathbf{n}_x\right]\mathrm{d}V(\mathbf{r}_s) \\
&\qquad = \int_S \left[\left(G_{U_x}(\mathbf{r}|\mathbf{r}_s,\omega)\frac{\partial}{\partial x}p(\mathbf{r}_s,\omega) - p(\mathbf{r}_s,\omega)\frac{\partial}{\partial x}G_{U_x}(\mathbf{r}|\mathbf{r}_s,\omega)\right)\mathbf{n}_x\right]\cdot\mathbf{n}\;\mathrm{d}S(\mathbf{r}_s) && (2.51)\\
&\qquad = \int_S \left(G_{U_x}(\mathbf{r}|\mathbf{r}_s,\omega)\frac{\partial}{\partial x}p(\mathbf{r}_s,\omega) - p(\mathbf{r}_s,\omega)\frac{\partial}{\partial x}G_{U_x}(\mathbf{r}|\mathbf{r}_s,\omega)\right)n_x\;\mathrm{d}S(\mathbf{r}_s). && (2.52)
\end{aligned}$$

Now, we can join and rearrange Eqs. 2.39, 2.41, 2.49 and 2.52, and obtain the following form:

$$
\begin{aligned}
&\int_V Q(\mathbf{r}_s,\omega) G_{U_x}(\mathbf{r}|\mathbf{r}_s,\omega)\,\mathrm{d}V(\mathbf{r}_s) \\
&\quad + \int_S \Bigg[\left(G_{U_x}(\mathbf{r}|\mathbf{r}_s,\omega)\frac{\partial}{\partial \mathbf{n}} p(\mathbf{r}_s,\omega) - p(\mathbf{r}_s,\omega)\frac{\partial}{\partial \mathbf{n}} G_{U_x}(\mathbf{r}|\mathbf{r}_s,\omega) \right) \\
&\qquad\quad -2jk_0 M_x \Big(G_{U_x}(\mathbf{r}|\mathbf{r}_s,\omega) p(\mathbf{r}_s,\omega) \Big) n_x \\
&\qquad\quad -M_x^2 \left(G_{U_x}(\mathbf{r}|\mathbf{r}_s,\omega)\frac{\partial}{\partial x} p(\mathbf{r}_s,\omega) - p(\mathbf{r}_s,\omega)\frac{\partial}{\partial x} G_{U_x}(\mathbf{r}|\mathbf{r}_s,\omega) \right) n_x \Bigg]\,\mathrm{d}S(\mathbf{r}_s) \\
&= \begin{cases} p(\mathbf{r},\omega), & \mathbf{r} \in V \\ p(\mathbf{r},\omega)/2, & \mathbf{r} \in S \\ 0, & \mathbf{r} \notin V \end{cases} .
\end{aligned}
\tag{2.53}
$$

Equation 2.53 is the general solution for the inhomogeneous convected Helmholtz equation [41, 42]. The acoustic pressure inside the volume V depends on an arbitrary volumetric source distribution $Q(\mathbf{r}_s,\omega)$ and on the boundary conditions $p(\mathbf{r}_s,\omega)$ and $\partial p(\mathbf{r}_s,\omega)/\partial \mathbf{n}$ at the boundary surface S.

This is the most general form for the solution of the inhomogeneous wave equation, and from it we can derive a few special cases:

- The acoustic field generated by a prescribed source distribution in an *unbounded* medium, termed here the *"free-field radiation problem"*;
- The acoustic field generated by a prescribed source distribution in a *bounded* medium, which require the use of a *tailored Green's function*;
- The acoustic field generated by a prescribed source distribution and scattered by a body inside V with prescribed *homogeneous* boundary conditions on its surface, termed here *"scattering problem"*;
- The acoustic field in a source-free medium with prescribed *inhomogeneous* boundary conditions, termed here the *"Kirchhoff-Helmholtz Integral"*.

In this document we will describe the free-field radiation problem and the Kirchhoff-Helmholtz Integral formulation; the tailored Green's function problems and scattering problems will not be described, although they can be tackled using the same formalism.

The key to understand how a single method can be used to obtain the solutions to these seemingly different problems is well described by Morse and Feshbach [37]: *"The Green's function is therefore a solution for a case which is homogeneous everywhere except at one point. When the point is on the boundary, the Green's function may be used to satisfy inhomogeneous boundary conditions; when it is out in space, it may be used to satisfy the inhomogeneous equation."*

2.2.3 General Solution for Point Sources in Free-Field

Let us now assume a volumetric distribution of sources $Q(\mathbf{r}_s, \omega)$ in free-field. To obtain the free-field solution, we assume the spherical boundary surface S surrounding the source region is at an infinite distance from the source region and from the observer location $\mathbf{r}$; hence, from the Sommerfeld radiation condition, the contributions from the boundary will have decayed to zero by the time they reach the observer location, and can be discarded. In such case, the general solution for the inhomogeneous convected Helmholtz equation becomes

$$\int_V Q(\mathbf{r}_s, \omega) G_{U_x}(\mathbf{r}|\mathbf{r}_s, \omega)\, \mathrm{d}V(\mathbf{r}_s) = p(\mathbf{r}, \omega). \tag{2.54}$$

We consider the solutions to two types of point sources: convected monopoles and convected dipoles. Such solutions can be obtained via Lorentz-type transformations of the well-established non-convective monopole and dipole transfer functions [43]; however, the derivations will not be shown, and we will refer only to the final solutions shown below.

2.2.3.1 Convected Monopole Transfer Function

The acoustic transfer function between a monopole source located at $\mathbf{r}_s$ and an observer located at $\mathbf{r}$ in a uniform flow and free-field conditions can be obtained by assuming a unitary magnitude point volume source, denoted as

$$Q(\mathbf{r}_s, \omega) = \delta(\mathbf{r} - \mathbf{r}_s). \tag{2.55}$$

The convected monopole transfer function is defined by the convected Green's function

$$G_{U_x}(\mathbf{r}|\mathbf{r}_s,\omega) = \frac{e^{-jk_0\overline{r}}}{4\pi\beta^2\overline{r}} e^{jk_0 M_x\left(\overline{\overline{x}}-\overline{\overline{x}}_s\right)}, \tag{2.56}$$

where the overline represents flow-transformed variables [43]:

$$\overline{\mathbf{r}} = \left(\overline{\overline{x}},\overline{y},\overline{z}\right) = \left(\frac{x}{\beta^2},\frac{y}{\beta},\frac{z}{\beta}\right), \quad \overline{r} = \left\|\overline{\mathbf{r}}-\overline{\mathbf{r}}_s\right\|, \quad \beta = \sqrt{1-M_x^2}. \tag{2.57}$$

Under no-flow conditions, $r = \|\mathbf{r}-\mathbf{r}_s\|$ and the Green's function reduces to the usual point monopole transfer function:

$$G(\mathbf{r}|\mathbf{r}_s,\omega) = \frac{e^{-jk_0 r}}{4\pi r}. \tag{2.58}$$

Figure 2.6 shows a slice at the plane $y = 0$ of the three-dimensional acoustic fields radiated by a point monopole in a quiescent medium (Fig. 2.6a) and in a moving medium with Mach number $M_x = 0.5$ (Fig. 2.6b).

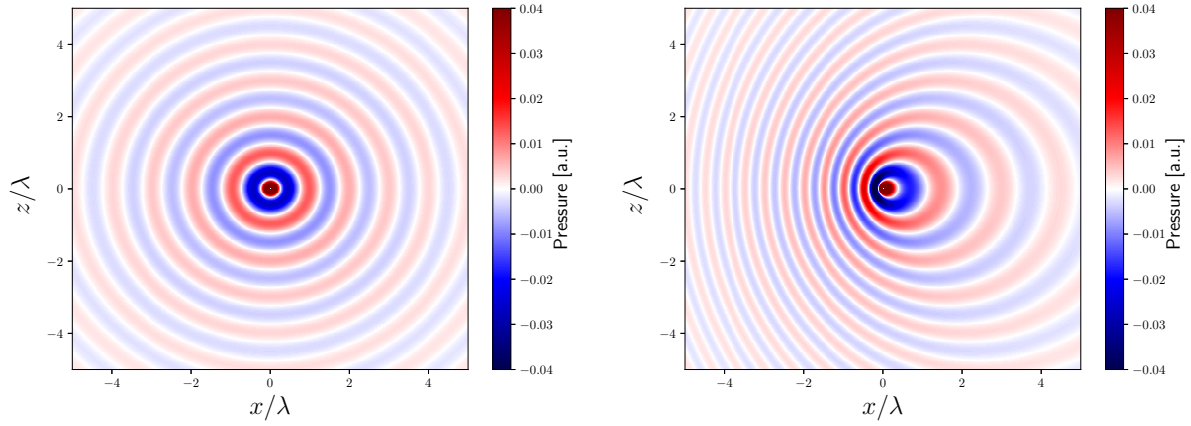

Figure 2.6: Acoustic field radiated by a point monopole: (a) in a quiescent medium; (b) in a moving medium ($M_x = 0.5$).

2.2.3.2 Convected Dipole Transfer Function

The acoustic transfer function between a dipole source located at $\mathbf{r}_s$ and with its acoustic axis aligned in the $+z$ direction and an observer located at $\mathbf{r}$ in a uniform flow and free-field

conditions can be obtained by assuming a unitary magnitude point force source aligned with the dipole acoustic axis; this is denoted as [28]

$$Q(\mathbf{r}_s, \omega) = \nabla \cdot (\delta(\mathbf{r} - \mathbf{r}_s)\mathbf{n}_z). \tag{2.59}$$

The dipole transfer function is defined by the spatial derivative of the convected Green's function in the direction of application of the force. This transfer function is given by

$$\frac{\partial}{\partial z_s} G_{U_x}(\mathbf{r}|\mathbf{r}_s, \omega) = \left(jk_0 + \frac{1}{\overline{r}}\right) \frac{(\overline{z} - \overline{z}_s)}{\beta \overline{r}} \frac{e^{-jk_0 \overline{r}}}{4\pi\beta^2 \overline{r}} e^{jk_0 M_x (\overline{\overline{x}} - \overline{\overline{x}}_s)}, \tag{2.60}$$

where the overline represents the same flow-transformed variables previously defined in Eq. 2.57. For no-flow conditions, $r = \|\mathbf{r} - \mathbf{r}_s\|$ and the above function reduces to the standard dipole transfer function:

$$\frac{\partial}{\partial z_s} G(\mathbf{r}|\mathbf{r}_s, \omega) = \left(jk_0 + \frac{1}{r}\right) \frac{(z - z_s)}{r} \frac{e^{-jk_0 r}}{4\pi r}. \tag{2.61}$$

Figure 2.7 shows a slice at the plane $y = 0$ of the three-dimensional acoustic fields radiated by a point dipole in a quiescent medium (Fig. 2.7a) and in a moving medium with Mach number $M_x = 0.5$ (Fig. 2.7b). The dipole has its acoustic axis oriented in the $+z$ direction; note, as a consequence, the null acoustic field over the plane $z = 0$.

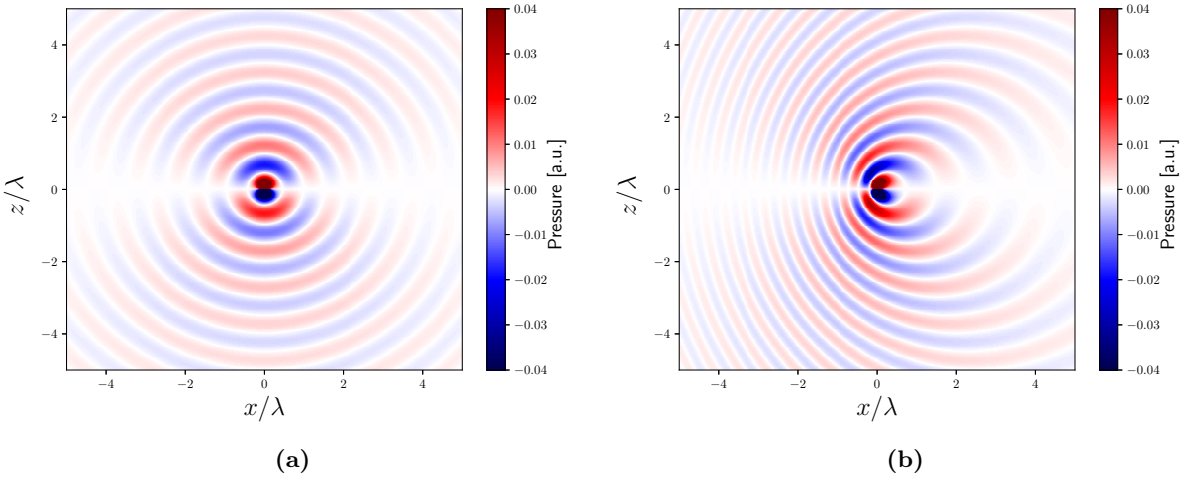

Figure 2.7: Acoustic field radiated by a point dipole: (a) in a quiescent medium; (b) in a moving medium ($M_x = 0.5$).

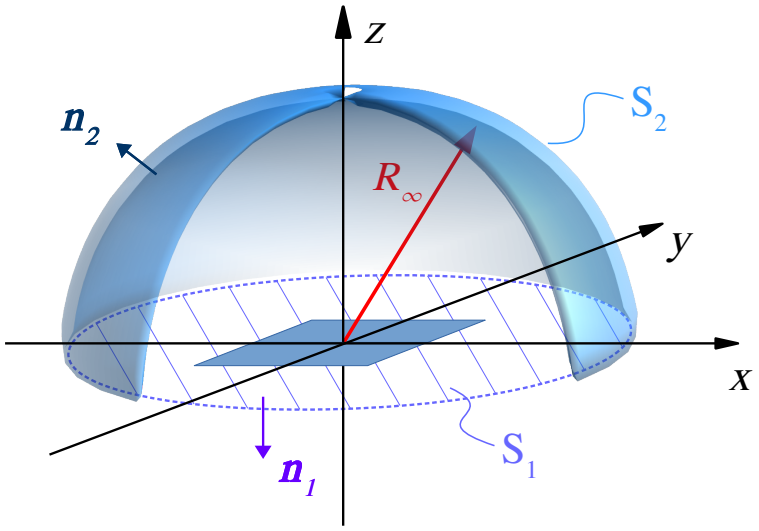

Figure 2.8: Geometry for planar radiator located at the (x, y) plane; the surface $S = S_1 + S_2$ bounds the volume V of interest, and the normal vectors $\mathbf{n}_1$ and $\mathbf{n}_2$ point outwards of the volume V.

2.2.4 General Solution for Boundary Sources: Kirchhoff-Helmholtz Integral

Let us now adapt the general solution for the particular case of inhomogeneous boundary conditions with no volumetric distribution of sources inside the volume V. We will consider a planar radiator located over the $z = 0$ plane, and look into the acoustic field $p(\mathbf{r}, \omega)$ in the half space above the planar radiator ($z \geq 0$).

Figure 2.8 shows the proposed geometry. The surface $S = S_1 + S_2$ defines the boundary of the region V: the surface S_1 is the $z = 0$ plane up to a distance R_∞, and the surface S_2 is a hemisphere of radius R_∞ over the surface S_1. We now consider the limit of $R_\infty \to \infty$, and invoke the Sommerfeld radiation condition to discard the contribution of the boundary terms on the surface S_2. Hence, we can consider the surface S_1 only.

Note, however, that if the surface S_1 is parallel to the flow direction, then the outwards-pointing normal vector to this surface can be written as $\mathbf{n}_1 = (n_x, n_y, n_z) = (0, 0, -1)$. Since this normal vector does not have a component in the x direction (i.e. $n_x = 0$), the second and third terms inside the surface integral in Eq. 2.53 - the terms proportional to M_x and M_x^2 - vanish [33]; another consequence is that the normal derivatives $\partial/\partial\mathbf{n}$ simplify to $-\partial/\partial z$. Therefore, Equation 2.53 simplifies to

$$\int_{S_1} \left(p(\mathbf{r}_s,\omega)\frac{\partial}{\partial z_s} G_{U_x}(\mathbf{r}|\mathbf{r}_s,\omega) - G_{U_x}(\mathbf{r}|\mathbf{r}_s,\omega)\frac{\partial}{\partial z_s} p(\mathbf{r}_s,\omega) \right) \mathrm{d}S(\mathbf{r}_s) = \begin{cases} p(\mathbf{r},\omega), & \mathbf{r} \in V \\ p(\mathbf{r},\omega)/2, & \mathbf{r} \in S \\ 0, & \mathbf{r} \notin V \end{cases}, \tag{2.62}$$

which is known as *Kirchhoff-Helmholtz Integral* (KHI) equation for a convected medium.

This Equation describes the acoustic field above a plane using a distribution of convected monopole and dipole sources on the surface S_1, with the monopole strength being proportional to the normal acoustic pressure gradient at the surface and the dipole strength proportional to the acoustic pressure at the surface.

Its format is similar to the Kirchhoff-Helmholtz Integral for a quiescent medium [29, 39, 40], but using the convective Green's function $G_{U_x}(\mathbf{r}|\mathbf{r}_s,\omega)$ and its normal derivative in the formulation. For no-flow conditions, we can simply replace them by the standard Green's function (Eq. 2.58) and its derivative (Eq. 2.61) and obtain the classical KHI formulation.

If we now assume particular boundary conditions over the surface S_1, we can obtain tailored forms of the Green's functions and simplify Equation 2.62 even further, as shown below.

2.2.4.1 Planar Vibrating Surfaces

Let us now consider the surface S_1 is vibrating with normal velocity $v_z(\mathbf{r}_s,\omega)$; we assume the surface velocity at a point is identically transmitted to the acoustic particles immediately above it, and hence the normal acoustic particle velocity $u_z(\mathbf{r}_s,\omega)$ at a point will be equal to the surface velocity at the same point:

$$u_z(\mathbf{r}_s,\omega) = v_z(\mathbf{r}_s,\omega). \tag{2.63}$$

This condition is equivalent to assuming inhomogeneous Neumann boundary conditions over the vibrating surface, allowing us to adopt a Neumann Green's function. Such function has the property that $\partial G_N(\mathbf{r}|\mathbf{r}_s,\omega)/\partial z_s = 0$ at all points over the surface except at $\mathbf{r}_s$, and hence Neumann boundary conditions are sometimes referred to as "hard wall boundary conditions". The KHI formula then simplifies to

$$-\int_{S_1} G_N(\mathbf{r}|\mathbf{r}_s,\omega)\frac{\partial}{\partial z_s}p(\mathbf{r}_s,\omega)\,\mathrm{d}S(\mathbf{r}_s) = \begin{cases} p(\mathbf{r},\omega), & \mathbf{r}\in V \\ p(\mathbf{r},\omega)/2, & \mathbf{r}\in S \\ 0, & \mathbf{r}\notin V \end{cases}, \tag{2.64}$$

where $\partial p(\mathbf{r}_s,\omega)/\partial z_s$ is related to the normal velocity at the surface and acts as a source strength term.

By imposing homogeneous Neumann boundary conditions on the remainder of the $z = 0$ plane, one can use the method of images to obtain a Neumann Green's function which is equal to twice the free-field Green's function (Eq. 2.56) [44]:

$$G_N(\mathbf{r}|\mathbf{r}_s,\omega) = 2G_{U_x}(\mathbf{r}|\mathbf{r}_s,\omega), \tag{2.65}$$

Thus, the Neumann Green's function displays a monopole-like behaviour; consequently, so does a point velocity source acting at the boundary of a moving medium.

We now use the convective Euler's equation (Eqs. 2.11 and 2.33) to link the normal acoustic particle velocity to the gradient of the acoustic pressure; however, in the convective case, the dependence is on both the normal velocity and the normal velocity gradient along the flow direction [33]. The final formulation for the acoustic field generated by a planar vibrating surface with normal velocity $v_z(\mathbf{r}_s,\omega)$ in a convected medium has the form

$$2\int_{S_1} G_{U_x}(\mathbf{r}|\mathbf{r}_s,\omega)\left(j\rho\omega v_z(\mathbf{r}_s,\omega) + U_x\frac{\partial}{\partial x}v_z(\mathbf{r}_s,\omega)\right)\mathrm{d}S(\mathbf{r}_s) = \begin{cases} p(\mathbf{r},\omega), & \mathbf{r}\in V \\ p(\mathbf{r},\omega)/2, & \mathbf{r}\in S \\ 0, & \mathbf{r}\notin V \end{cases}. \tag{2.66}$$

2.2.4.2 Planar Pressure Surfaces

For surfaces that support a prescribed pressure distribution, we can assume inhomogeneous Dirichlet boundary conditions at the boundary, allowing us to use a Dirichlet Green's function; such function has the property that $G_D(\mathbf{r}|\mathbf{r}_s,\omega) = 0$ over the surface at all points except $\mathbf{r}_s$, and thus the KHI equation simplifies to

$$\int_{S_1} p(\mathbf{r}_s,\omega)\frac{\partial}{\partial z_s}G_D(\mathbf{r}|\mathbf{r}_s,\omega)\,\mathrm{d}S(\mathbf{r}_s) = \begin{cases} p(\mathbf{r},\omega), & \mathbf{r}\in V \\ p(\mathbf{r},\omega)/2, & \mathbf{r}\in S \\ 0, & \mathbf{r}\notin V \end{cases}, \tag{2.67}$$

where $p(\mathbf{r}_s,\omega)$ is the imposed pressure distribution at the surface, and acts as a source strength term.

By imposing homogeneous Dirichlet boundary conditions on the plane, one can use the method of images to obtain a Dirichlet Green's function whose normal derivative is equal to twice the normal derivative of the free-field Green's function (Eq. 2.60) [44]:

$$\frac{\partial}{\partial z_s}G_D(\mathbf{r}|\mathbf{r}_s,\omega) = 2\frac{\partial}{\partial z_s}G_{U_x}(\mathbf{r}|\mathbf{r}_s,\omega). \tag{2.68}$$

Thus, the normal derivative of the Dirichlet Green's function displays a dipole-like behaviour; consequently, so does a point pressure source acting at the boundary of a moving medium.

The final formulation for the acoustic field generated by a planar pressure distribution $p(\mathbf{r}_s,\omega)$ in a convected medium has the form

$$2\int_{S_1} p(\mathbf{r}_s,\omega)\frac{\partial}{\partial z_s}G_{U_x}(\mathbf{r}|\mathbf{r}_s,\omega)\,\mathrm{d}S(\mathbf{r}_s) = \begin{cases} p(\mathbf{r},\omega), & \mathbf{r}\in V \\ p(\mathbf{r},\omega)/2, & \mathbf{r}\in S \\ 0, & \mathbf{r}\notin V \end{cases}, \tag{2.69}$$

2.3 Far-Field Approximation

In the previous section, we obtained equations for determining the acoustic pressure field generated by a variety of acoustic sources, including spatial distribution of sources in free-field, and planar sources at boundaries. While the resulting equations are exact, they often do not have closed-form analytical solutions available for any source distribution; however, one can obtain approximate closed-form solutions when the observer is geometrically distant from the source; such approximation is generally referred to as (geometric) *far-field approximation*.

The far-field approximation is widely known and used in acoustics [28, 30, 32], optics [45] and electromagnetic antennas [46, 47], to cite a few areas; most of this section is based on the above mentioned references.

However, not many authors in the acoustics community refer to it as the *Fraunhofer approximation*, as it is usually named in the optics community [45] and used for describing some types of diffraction. The same approximation ends up often being written in different forms, with little or no discussion on the similarities of the many forms; hence, we have decided to adopt the name "Fraunhofer approximation" in an effort to highlight these similarities. Little thought is generally given to the conditions under which the approximation can be considered valid, so we discuss it as well in the next sections.

Figure 2.9 shows a geometrical representation of the problem. Let us assume a planar acoustic source at $z = 0$, with $\mathbf{r}_s = (x_s, y_s, 0)$ denoting a point over the source surface and $\mathbf{r} = (x, y, z)$ denoting the location of an observer; the origin of the coordinate system is located at the source centre. Let the source largest dimension be given by D, and r denote the distance between the source point $\mathbf{r}_s$ and the observer point $\mathbf{r}$; the Fraunhofer far-field approximation consists of approximating the actual source-to-observer distance r as

$$r = \|\mathbf{r} - \mathbf{r}_s\| \approx \|\mathbf{r}\| - \frac{\mathbf{r} \cdot \mathbf{r}_s}{\|\mathbf{r}\|} \tag{2.70}$$

$$= \|\mathbf{r}\| - \|\mathbf{r}_s\| \cos(\gamma), \tag{2.71}$$

where γ is the angle between the observer location vector $\mathbf{r}$ and the source location vector $\mathbf{r}_s$.

2.3.1 Derivation of Fraunhofer Far-Field Approximation

We will now discuss how to obtain the approximation shown in Equation 2.70 and what the conditions are under which the approximation is valid. We will assume a convected medium and use flow-transformed variables (defined in Eq. 2.57); equivalent results can be obtained for a quiescent medium by setting $M_x = 0$.

We start by rewriting $\overline{r}$ as

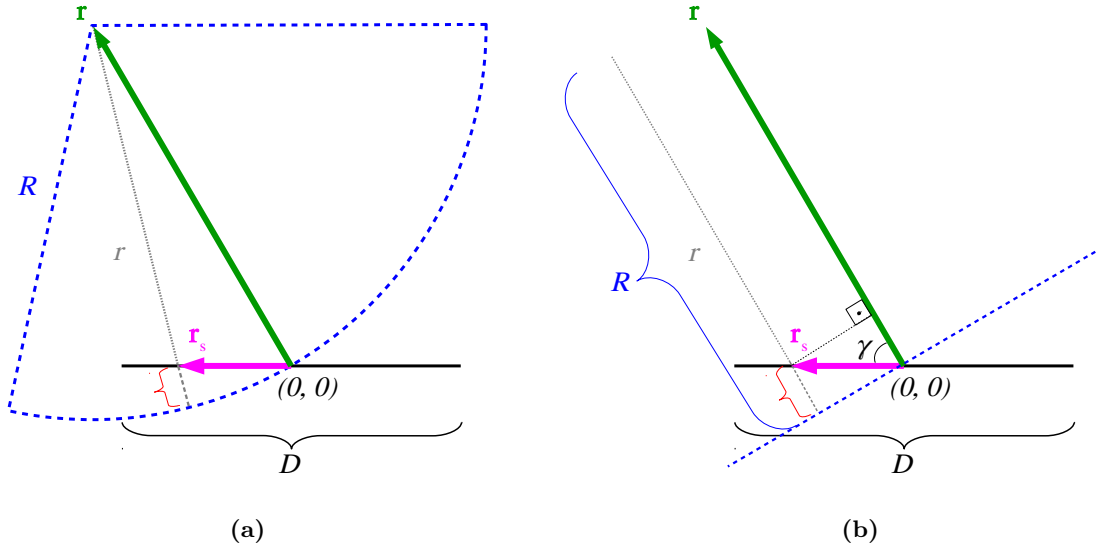

Figure 2.9: Estimating the source-observer distance r: (a) the actual distance $r = \|\mathbf{r} - \mathbf{r}_s\|$ between observer and source; (b) the approximated distance $r \approx \|\mathbf{r}\| - \|\mathbf{r}_s\| \cos(\gamma)$ using the Fraunhofer far-field approximation.

$$\overline{r} = \left(\|\overline{\mathbf{r}}\|^2 - 2\overline{\mathbf{r}} \cdot \overline{\mathbf{r}}_s + \|\overline{\mathbf{r}}_s\|^2 \right)^{1/2} \tag{2.72}$$

$$= \|\overline{\mathbf{r}}\| \left(1 - 2\frac{\overline{\mathbf{r}} \cdot \overline{\mathbf{r}}_s}{\|\overline{\mathbf{r}}\|^2} + \frac{\|\overline{\mathbf{r}}_s\|^2}{\|\overline{\mathbf{r}}\|^2} \right)^{1/2}. \tag{2.73}$$

Here we make our first assumption: the observer is many source lengths away from the origin, which we can write as $\|\overline{\mathbf{r}}_s\|^2 / \|\overline{\mathbf{r}}\|^2 \ll 1$. We can then rewrite the remaining expression as

$$\overline{r} \approx \|\overline{\mathbf{r}}\| (1 - \alpha)^{1/2}, \qquad \alpha = 2\frac{\overline{\mathbf{r}} \cdot \overline{\mathbf{r}}_s}{\|\overline{\mathbf{r}}\|^2}. \tag{2.74}$$

We can now approximate the square root term using the binomial series [47] :

$$(1 - \alpha)^{1/2} = 1 - \frac{\alpha}{2} - \frac{\alpha^2}{8} - \ldots, \tag{2.75}$$

where we retain the first two terms of the series for our final expression:

$$\overline{r} \approx \|\overline{\mathbf{r}}\| \left(1 - \frac{\alpha}{2} \right) = \|\overline{\mathbf{r}}\| - \frac{\overline{\mathbf{r}} \cdot \overline{\mathbf{r}}_s}{\|\overline{\mathbf{r}}\|} \tag{2.76}$$

Equation 2.76 is the *Fraunhofer far-field approximation* [45].

It is interesting to note that the Fraunhofer approximation implicitly assumes the acoustic signals emitted by all points in the source will travel parallel to each other on their paths towards the observer in the far-field [46], as shown in Figure 2.9. This is not immediately obvious from the initial assumptions, but it gives an intuitive idea of how far the observer must be from the source for the approximation to be considered valid.

2.3.1.1 Far-Field Approximation Error and Region of Validity

It is possible to obtain an estimate for the error committed in the Fraunhofer approximation, which we can use to obtain the conditions under which the approximation can be deemed satisfactory. The discarded terms of the binomial series (Eq. 2.75) can be interpreted as a second-order estimate of the distance error committed when making the Fraunhofer approximation; let us rewrite the absolute value of the third term (the leading order term of the discarded part, proportional to α^2) as

$$\|\overline{r}_{error}\| = \|\overline{\mathbf{r}}\| \left(\frac{\alpha^2}{8}\right) = \frac{\|\overline{\mathbf{r}}\|}{8} \left(2\frac{\overline{\mathbf{r}} \cdot \overline{\mathbf{r}}_s}{\|\overline{\mathbf{r}}\|^2}\right)^2 \tag{2.77}$$

$$= \frac{1}{2R} \|\overline{\mathbf{r}}_s\|^2 \cos^2(\gamma). \tag{2.78}$$

The error $\|\overline{r}_{error}\|$ is maximized when $\cos^2(\gamma) = 1$ and $\|\overline{\mathbf{r}}_s\|$ takes its maximum value - assumed here to be half of the largest source dimension D (i.e. $\|\overline{\mathbf{r}}_s\|_{max} = D/2$), leading to

$$\|\overline{r}_{error}\|_{max} = \frac{D^2}{8R}. \tag{2.79}$$

The argument so far has been purely geometrical; however, it should not be controversial to state the important factor is not the absolute distance error - say, in metres - but instead how this error compares to the acoustic wavelength of interest. Of course, a distance error can also be associated with a phase error $k_0\overline{r}_{error}$ in the complex exponential $e^{jk_0\overline{r}}$.

From the antenna literature [46, 47], the Fraunhofer approximation is assumed to be accurate for a value of $\|\overline{r}_{error}\|_{max} < \lambda_0/16$; this suggests the far-field approximation is valid for distances

$$R > \frac{2D^2}{\lambda_0}. \tag{2.80}$$

Equation 2.80 is possibly one of the most popular definitions for the geometrical far-field. For a fixed observer distance R, we can then assume the Fraunhofer far-field approximation is valid for frequencies such that

$$f < \frac{Rc_0}{2D^2}. \tag{2.81}$$

Hence, for a fixed observer distance from the source centre, there is a *high frequency bound* to the far-field approximation.

It must be noted that the rule proposed in Equation 2.80 provides only a rough estimate for the validity of the approximation. By considering accuracy values other than $\lambda_0/16$, one can derive alternative formulations with different multiplying constants instead of the number 2; for example, Goodman [45] derives the Fraunhofer far-field approximation as a limiting case of the Fresnel near-field approximation (not discussed here), and arrives at the slightly different formulation

$$R > \frac{\pi D^2}{\lambda_0} \tag{2.82}$$

for the far-field approximation limit. This formulation is stricter than the one proposed by Equation 2.80; it can be interpreted as bounding the maximum distance error (Eq. 2.79) to be less than the more stringent limit of $\lambda_0/(8\pi)$, despite being obtained through a different derivation.

It must be mentioned that few authors - such as Sarkar et al. [47], for example - point out that the proposed accuracy limit of $\lambda_0/16$ is fairly arbitrary, and we have not been able to identify its origin. Many other expressions for the far-field limit exist, most being proportional to D^2/λ_0 but using different multiplying constants; such expressions can be interpreted as assuming accuracy limits other than $\lambda_0/16$.

As an example, see Table 1 of Capps [48], where the author compiled more than 15 different definitions of the near-field/far-field boundary as used by antenna engineers. This variety of

results can yield conflicting information on ranges and frequencies of validity for the approximation, which might help explain why the Fraunhofer distance limit is not widely used in the engineering community for categorical statements regarding geometrical near- and far-field regions.

2.3.1.2 Source Compactness and the Fraunhofer Approximation

For a source with characteristic length D, the Helmholtz number $k_0 D$ can be used to determine the degree of *source compactness* [49]: for frequencies where $k_0 D \ll 1$ (i.e. the Helmholtz number is "very small") the source is considered *compact*, and will behave as a point source on the scale of a large region surrounding it. For higher frequencies, the source is considered *non-compact*, and the observer will be subject to significant variations in phase shift from different regions over the source. As a consequence, non-compact sources might present strong interference effects - both constructive and destructive - between their different regions, while such effects are not observed to the same extent for compact sources.

One can relate the source compactness to the Fraunhofer far-field distance limit in a fairly direct manner; Eq. 2.82 can be rewritten as a function of the Helmholtz number:

$$R > \frac{\pi D^2}{\lambda_0} = \frac{1}{2}(k_0 D)D. \tag{2.83}$$

From Equation 2.83, it can be said that the extent of the near-field region of a source will be proportional to the source characteristic length D and to the degree of source compactness, given by the Helmholtz number $k_0 D$; therefore, a compact source ($k_0 D \ll 1$) will have a near-field region extent that is *much shorter* than its characteristic length D, while a non-compact source will have a near-field region extent that is *much longer* than its length D.

Clearly, the above statement should be taken carefully, since in order to obtain the Fraunhofer approximation we had to assume the observer distance is much larger than the source length, which contradicts the first part of the above sentence. However, the above expression does point to a link between near-field extent and the degree of source compactness.

2.3.2 Far-Field Approximation of Convected Monopole

Extended sources are often modelled using distributions of point sources. As such, before we investigate distributed sources, let us consider a single point monopole source in a convected medium, with its location $\mathbf{r}_s$ close to but not exactly at the origin. We would now like to approximate the acoustic field as seen far from this source by applying the Fraunhofer approximation to the convected monopole transfer function (Eq. 2.56). We use a similar procedure in Section 2.3.3 to obtain an approximation to the far-field radiation of point dipole sources, and in Section 2.3.4 we use these results to investigate the acoustic far-field of extended sources by modelling them as distribution of point sources around the origin.

The convected monopole transfer function in Eq. 2.56 presents a few dependencies on the exact flow-transformed source-to-observer distance $\overline{r} = \|\overline{\mathbf{r}} - \overline{\mathbf{r}}_s\|$ that we would like to approximate. The term in the denominator describes an amplitude decay as a function of distance, and can be reasonably approximated by

$$\frac{1}{\beta^2 \overline{r}} \approx \frac{1}{\sigma_{\mathbf{r}}}, \tag{2.84}$$

where $\sigma_{\mathbf{r}}$ is the convection-corrected observer radius:

$$\sigma_{\mathbf{r}} = \sqrt{x^2 + \beta^2 \left(y^2 + z^2\right)} = \beta^2 \left\|\overline{\mathbf{r}}\right\|. \tag{2.85}$$

However, the exponential term $e^{-jk_0\overline{r}}$ is an oscillating function with range $\overline{r}$, and requires a more accurate approximation. By assuming far-field conditions, we can use Eq. 2.70 in flow-transformed coordinates to approximate $\overline{r}$ inside the complex exponential of the convected Green's function (Eq. 2.56). The far-field-approximated Green's function is

$$G_{FF}(\mathbf{r}|\mathbf{r}_s, \omega) = \frac{e^{-jk_0\|\overline{\mathbf{r}}\|} e^{jk_0 \frac{\overline{\mathbf{r}}\cdot\overline{\mathbf{r}}_s}{\|\overline{\mathbf{r}}\|}}}{4\pi\sigma_{\mathbf{r}}} e^{jk_0 M_x\left(\overline{\overline{x}} - \overline{\overline{x}}_s\right)} \tag{2.86}$$

$$= \frac{1}{4\pi\sigma_{\mathbf{r}}} e^{-j\hat{\mathbf{k}}\cdot(\mathbf{r}-\mathbf{r}_s)}, \tag{2.87}$$

where the term $\hat{\mathbf{k}} = \left(\hat{k}_x,\ \hat{k}_y,\ \hat{k}_z\right)$ is a wavenumber vector dependent on the observer position and on the Mach number of the form

$$\hat{\mathbf{k}}(\mathbf{r}, M_x) = \left(k_0 \left(\frac{x - M_x \sigma_{\mathbf{r}}}{\beta^2 \sigma_{\mathbf{r}}} \right),\ k_0 \frac{y}{\sigma_{\mathbf{r}}},\ k_0 \frac{z}{\sigma_{\mathbf{r}}} \right) \tag{2.88}$$

$$= \Big(k \sin(\theta_p) \cos(\phi_p),\ k \sin(\theta_p) \sin(\phi_p),\ k \cos(\theta_p) \Big), \tag{2.89}$$

and (θ_p, ϕ_p) are the direction of propagation and k is the wavenumber vector magnitude of a plane wave, as discussed in Chapter 2. The mapping between observer location $\mathbf{r}$ and wavenumber vector $\hat{\mathbf{k}}$ in Eq. 2.88 is an injective function: every observer location over a hemisphere in the far-field has a unique corresponding wavenumber vector. However, there are wavenumber vectors that do not correspond to any physically possible observer location, as described further below.

Equation 2.87 can be interpreted in the following manner: the acoustic field generated by a point monopole source at $\mathbf{r}_s$ is perceived by an observer at $\mathbf{r}$ in the far-field as a plane wave of the form $e^{-j\hat{\mathbf{k}}\cdot\mathbf{r}}$, with complex amplitude $e^{j\hat{\mathbf{k}}\cdot\mathbf{r}_s}/(4\pi\sigma_{\mathbf{r}})$. The effects of the mean flow on the phase of the acoustic field were absorbed into the wavenumber vector $\hat{\mathbf{k}}$, allowing us to express the complex exponential in Eq. 2.87 using physical space variables $\mathbf{r} = (x, y, z)$ instead of flow-transformed variables $\bar{\mathbf{r}} = (\overline{x}, \overline{y}, \overline{z})$.

As it represents a (perceived) plane wave propagating in a subsonic convected medium, the wavenumber vector $\hat{\mathbf{k}}$ will follow all the properties previously described for plane wave solutions: it exists on the surface of an ellipsoid in wavenumber domain, its magnitude is associated with the angle between the observer direction and the mean flow direction, and its polar angles (θ_p, ϕ_p) represent the direction of propagation of the plane wave.

As Eq. 2.88 allows us to determine the trace wavenumbers corresponding to a known observer location, it is also possible to determine the observer location on a hemisphere of radius $R = \|\mathbf{r}\|$ that will correspond to a known pair of trace wavenumbers $(\hat{k}_x, \hat{k}_y)$. First, it is necessary to calculate the corresponding $\hat{k}_z$ through Eq. 2.19 (assumed real-valued for points inside the radiation ellipse). We can then obtain the observer coordinates $\mathbf{r} = (x, y, z)$ individually and in sequence through the following expressions:

$$\begin{cases} |x(\hat{\mathbf{k}}, M_x)| = \dfrac{R}{\sqrt{1+\left(\frac{\hat{k}_y}{\beta^2\left(\hat{k}_x+k_{x1}\right)}\right)^2+\left(\frac{\hat{k}_z}{\beta^2\left(\hat{k}_x+k_{x1}\right)}\right)^2}}, \quad \operatorname{sgn}\left(x(\hat{\mathbf{k}}, M_x)\right) = \operatorname{sgn}\left(\hat{k}_x + k_{x1}\right), \\ y(\hat{\mathbf{k}}, M_x) = \dfrac{\hat{k}_y}{\beta^2\left(\hat{k}_x + k_{x1}\right)} x(\hat{\mathbf{k}}, M_x), \\ z(\hat{\mathbf{k}}, M_x) = \dfrac{\hat{k}_z}{\beta^2\left(\hat{k}_x + k_{x1}\right)} x(\hat{\mathbf{k}}, M_x). \end{cases} \tag{2.90}$$

However, for streamwise wavenumbers $\hat{k}_x = -k_{x1}$, the corresponding chordwise observer coordinate becomes $x = 0$ and the other coordinates cannot be determined. In such cases, we must obtain the remaining coordinates as

$$\begin{cases} y(\hat{\mathbf{k}}, M_x)|_{x=0} = \dfrac{R}{\sqrt{1+\left(\frac{\hat{k}_z}{\hat{k}_y}\right)^2}}, \\ z(\hat{\mathbf{k}}, M_x)|_{x=0} = \dfrac{\hat{k}_z}{\hat{k}_y} y. \end{cases} \tag{2.91}$$

Finally, if $\hat{k}_x = -k_{x1}$ and the spanwise wavenumber $\hat{k}_y = 0$, then the observer location must be given by $\mathbf{r} = (0, 0, R)$.

2.3.2.1 Quiescent Medium Case ($M_x = 0$)

Figure 2.10 shows this approximation to a monopole source in a quiescent medium and in a moving medium. In the case of a quiescent medium, $M_x = 0$ and the wavenumber vector $\hat{\mathbf{k}}$ has the form

$$\hat{\mathbf{k}}(\mathbf{r}, 0) = \left(k_0 \frac{x}{R},\ k_0 \frac{y}{R},\ k_0 \frac{z}{R}\right) \tag{2.92}$$

$$= \Big(k_0 \sin(\theta_{geo}) \cos(\phi_{geo}),\ k_0 \sin(\theta_{geo}) \sin(\phi_{geo}),\ k_0 \cos(\theta_{geo})\Big), \tag{2.93}$$

where $R = \|\mathbf{r}\|$ is the observer distance from the source centre, and $(\theta_{geo}, \phi_{geo})$ is the observer geometrical angle. The perceived plane wave points out of the source centre (the origin of the coordinate system) and towards the observer direction - that is, $(\theta_p, \phi_p) = (\theta_{geo}, \phi_{geo})$.

This is represented schematically for a source and observer on the plane $y = 0$ in Figure 2.10a. It can be seen that the acoustic field inside the red dashed circle around the observer generated by the point source (in the left-hand side) is well approximated by the plane wave (in the right-hand side). As can be expected, the further the observer is from the source, the better the plane wave will approximate the point source wavefront curvature.

2.3.2.2 Moving Medium Case ($0 < M_x < 1$)

The wavenumber vector direction in the far-field approximation behaves differently in a moving medium, where the convection effects change the apparent wavefront direction of propagation as seen by the observer. The perceived plane wave does not point out of the source centre and towards the observer location $\mathbf{r}$; instead, it points out of an apparent source location $\mathbf{r}'_s$ that is further downstream from the real source location, as seen in Figure 2.10b, and towards the observer location $\mathbf{r}$. The apparent source location is given by

$$\mathbf{r}'_s = \mathbf{r}_s + (U_x\tau, 0, 0), \tag{2.94}$$

where τ is the time taken for an acoustic signal to propagate from the actual source location $\mathbf{r}_s$ to the observer location $\mathbf{r}$ in a moving medium [50]:

$$\tau = \frac{-(x - x_s)M_x + \sigma_{\mathbf{r},\mathbf{r}_s}}{c_0\beta^2}, \tag{2.95}$$

and $\sigma_{\mathbf{r},\mathbf{r}_s}$ is a convection-corrected source-to-observer distance:

$$\sigma_{\mathbf{r},\mathbf{r}_s} = \sqrt{(x - x_s)^2 + \beta^2\left[(y - y_s)^2 + (z - z_s)^2\right]}. \tag{2.96}$$

Hence, the apparent source location depends on the observer position.

This is represented schematically for a source and observer in the $y = 0$ plane in Figure 2.10b. The acoustic field inside the red dashed circle around the observer generated by the point source (in the left-hand side) is again well approximated by the plane wave (in the right-hand side). And again, the further the observer is from the source, the better the approximation will be.

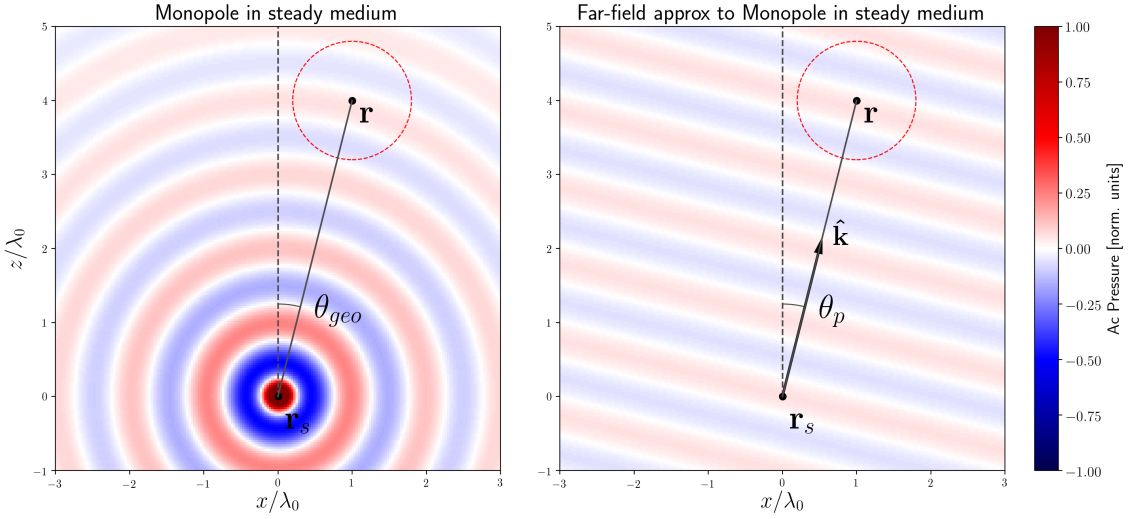

(a)

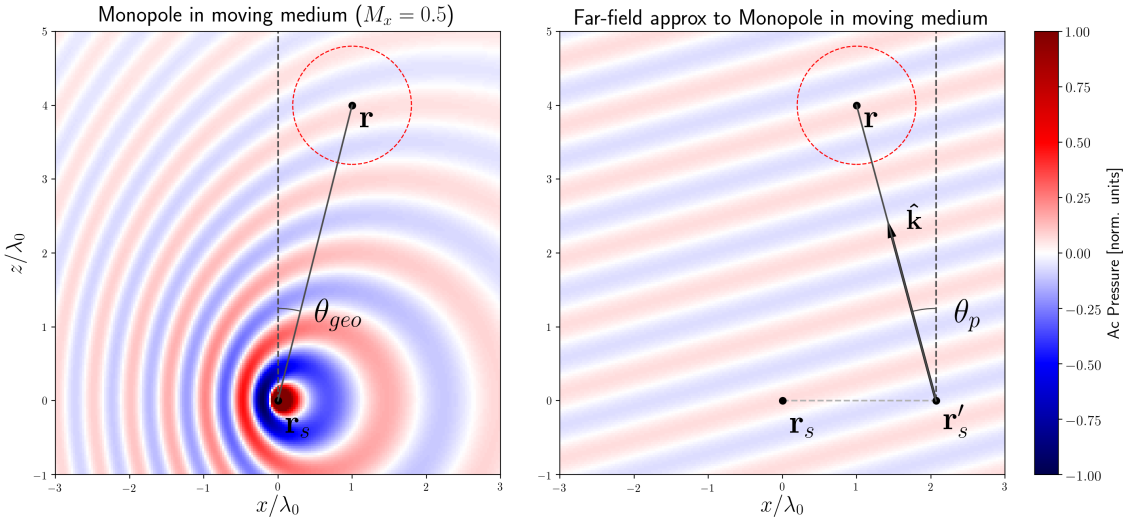

(b)

Figure 2.10: Far-field approximation of point monopole source (left-hand side) interpreted as a plane wave (right-hand side): (a) propagation in a quiescent medium; (b) propagation in a moving medium with $M_x = 0.5$. Source position is given by $\mathbf{r}_s$, observer position by $\mathbf{r}$ and apparent source position for moving medium case by $\mathbf{r}'_s$; angles are assumed positive in the clockwise direction from the vertical axis.

In order to showcase the effects of the mean flow on the far-field approximation, the relationship between the geometrical angle θ_{geo} and the perceived plane wave direction of propagation angle θ_p can be traced for different Mach numbers (assuming both source and observer are at the plane $y = 0$ - i.e. $\phi = 0$). Figure 2.11 shows this distortion in the apparent wavefront direction of propagation; the relationship is a unit slope line (i.e. $\theta_p = \theta_{geo}$) for $M_x = 0$, while an increase in the mean flow velocity "pushes" the perceived plane wave angle θ_p towards values lower than θ_{geo}.

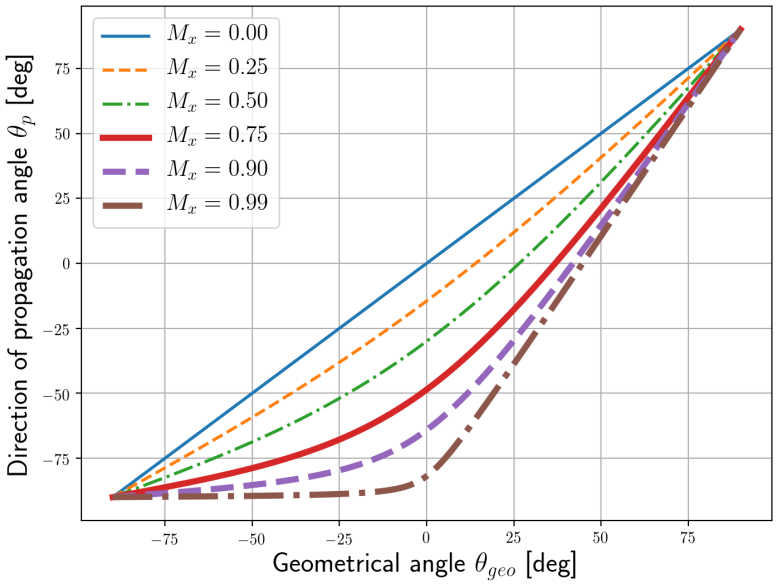

Figure 2.11: Plane wave propagation angle as a function of geometrical angle for different Mach numbers; see Figure 2.10 for a geometrical interpretation. Both source and observer are assumed to be over the plane $y = 0$. Angles are assumed positive in the clockwise direction from the vertical (z) axis, so $+90°$ represents downstream.

2.3.3 Far-Field Approximation of Convected Dipole

The far-field approximation for a point dipole follows a similar rationale to the point monopole case, but requires a few extra steps. When compared to the convected monopole (Eq. 2.56), the extra terms in Eq. 2.60 can be approximated in the far-field as

$$\left(jk_0 + \frac{1}{\overline{r}}\right)\frac{(\overline{z} - \overline{z}_s)}{\beta\overline{r}} \approx jk_0\frac{z}{\sigma_{\mathbf{r}}}, \tag{2.97}$$

where we express the dipole directivity as $z/\sigma_{\mathbf{r}}$ and remove the near-field term $1/\overline{r}$. The remaining terms in the dipole transfer function are approximated as for the convected monopole response; the final convected dipole response is

$$\frac{\partial}{\partial z_s} G_{FF}(\mathbf{r}|\mathbf{r}_s, \omega) = \frac{jk_0}{4\pi\sigma_{\mathbf{r}}} \left(\frac{z}{\sigma_{\mathbf{r}}}\right) e^{-j\hat{\mathbf{k}}\cdot(\mathbf{r}-\mathbf{r}_s)}. \tag{2.98}$$

The dipole acoustic field can also be approximated as a plane wave of the type $e^{-j\hat{\mathbf{k}}\cdot\mathbf{r}}$, and its complex amplitude is $jk_0(z/\sigma_{\mathbf{r}})(e^{-j\hat{\mathbf{k}}\cdot\mathbf{r}_s}/4\pi\sigma_{\mathbf{r}})$ in the far-field. Plane waves propagating at directions almost parallel to the xy-plane will be attenuated by the dipole directivity factor $z/\sigma_{\mathbf{r}}$; this indicates a limitation of dipole-type sources of generating plane waves at such directions, which will be further discussed when modelling planar sources with a distributions of point dipoles.

Here we note another type of near-field effect: the dipole near-field term, often described as *dipole hydrodynamic near-field*, is a textbook example of near-field [32], and is generally ignored for $k_0\overline{r} \gg 1$. This is also a frequency-dependent relationship, and assuming a fixed observer distance R can be rewritten as

$$f \gg \frac{c_0}{2\pi R}. \tag{2.99}$$

Hence, for a fixed observer distance, the dipole hydrodynamic near-field imposes a *lower frequency bound* to the far-field assumption. Note that this is the opposite to the geometrical near-field, which imposes a *high frequency bound*.

As a final comment on the far-field approximation to the dipole acoustic field, we note that Eq. 2.98 can be rewritten as

$$\frac{\partial}{\partial z_s} G_{FF}(\mathbf{r}|\mathbf{r}_s) = \frac{jk_0 z}{4\pi\sigma_{\mathbf{r}}^2} e^{jk_0\left(\frac{M_x x - \sigma_{\mathbf{r}}}{\beta^2}\right)} e^{jk_0\left(\frac{x - M_x\sigma_{\mathbf{r}}}{\sigma_{\mathbf{r}}\beta^2}\right)x_s} e^{jk_0\left(\frac{y}{\sigma_{\mathbf{r}}}\right)y_s}, \tag{2.100}$$

which is the expression used by Amiet [8] when considering the acoustic far-field radiation of an aerofoil interacting with a turbulent gust. This expression will be used in the next chapter when discussing Amiet's model.

2.3.4 Far-Field Approximation of Planar Sources

2.3.4.1 Distribution of Monopoles

We will now look into the acoustic field generated by a distributed planar source as seen by an observer in the far-field. Let us consider an observer at position $\mathbf{r}$, at a radius R from the source centre. Assuming convected monopole radiation and propagation, a continuous source distribution of strength $q(\mathbf{r}_s, \omega)$ and located on the plane $z_s = 0$ will generate an acoustic field at the observer location of the form

$$p(\mathbf{r}, \omega) = \int_{y_s} \int_{x_s} q(\mathbf{r}_s, \omega) G_{U_x}(\mathbf{r}|\mathbf{r}_s, \omega) \ \mathrm{d}x_s \, \mathrm{d}y_s. \tag{2.101}$$

By assuming far-field conditions, we can use the far-field approximation to the Green's function (Eq. 2.87) into Eq. 2.101 and obtain

$$p(\mathbf{r}, \omega) \approx \frac{e^{-j\hat{\mathbf{k}}\cdot\mathbf{r}}}{4\pi\sigma_{\mathbf{r}}} \int_{y_s} \int_{x_s} q(\mathbf{r}_s, \omega) e^{j\hat{\mathbf{k}}\cdot\mathbf{r}_s} \, \mathrm{d}x_s \, \mathrm{d}y_s. \tag{2.102}$$

Note that while the convected Green's function in Eq. 2.101 must be evaluated over flow-transformed spatial coordinates, Eq. 2.102 is expressed in non-transformed space coordinates. As previously described, the far-field approximation allows us to express some convection effects in the wavenumber domain instead of the spatial domain.

From the Spatiotemporal Fourier Transform defined in Eq. 2.28, the double integral term in Eq. 2.102 can be related to the two-dimensional Spatial Fourier Transform $Q(\hat{\mathbf{k}}, \omega)$ of the source strength distribution evaluated at the source-dependent wavenumber vector $\hat{\mathbf{k}} = (\hat{k}_x, \ \hat{k}_y)$. This can be demonstrated by rewriting the above equation as

$$p(\mathbf{r}, \omega) \approx \frac{e^{-j\hat{\mathbf{k}}\cdot\mathbf{r}}}{4\pi\sigma_{\mathbf{r}}} \int_{y_s} \int_{x_s} q(\mathbf{r}_s, \omega) \left[\int_{k_y} \int_{k_x} e^{j\mathbf{k}\cdot\mathbf{r}_s} \delta(\mathbf{k} - \hat{\mathbf{k}}) \, \mathrm{d}k_x \, \mathrm{d}k_y \right] \mathrm{d}x_s \, \mathrm{d}y_s \tag{2.103}$$

$$= \frac{e^{-j\hat{\mathbf{k}}\cdot\mathbf{r}}}{4\pi\sigma_{\mathbf{r}}} \int_{k_y} \int_{k_x} \left[\int_{y_s} \int_{x_s} q(\mathbf{r}_s, \omega) e^{j\mathbf{k}\cdot\mathbf{r}_s} \, \mathrm{d}x_s \, \mathrm{d}y_s \right] \delta(\mathbf{k} - \hat{\mathbf{k}}) \, \mathrm{d}k_x \, \mathrm{d}k_y \tag{2.104}$$

$$= \frac{e^{-j\hat{\mathbf{k}}\cdot\mathbf{r}}}{4\pi\sigma_{\mathbf{r}}} \int_{k_y} \int_{k_x} \left[(2\pi)^2 Q(\mathbf{k}, \omega) \right] \delta(\mathbf{k} - \hat{\mathbf{k}}) \, \mathrm{d}k_x \, \mathrm{d}k_y \tag{2.105}$$

$$= \frac{e^{-j\hat{\mathbf{k}}\cdot\mathbf{r}}}{4\pi\sigma_{\mathbf{r}}} (2\pi)^2 Q\left(\hat{k}_x, \hat{k}_y, \omega\right), \tag{2.106}$$

where $\delta(.)$ is the Dirac Delta function. Thus, the acoustic far-field is seen by the observer as a plane wave of the type $e^{-j\hat{\mathbf{k}}\cdot\mathbf{r}}$, with complex amplitude given by $(2\pi)^2 Q(\hat{k}_x, \hat{k}_y, \omega)/(4\pi\sigma_{\mathbf{r}})$. As the amplitude and phase of the perceived plane wave is proportional to the source wavenumber spectrum at the observer-dependent wavenumber $(\hat{k}_x, \hat{k}_y)$, it can be said the far-field observer "samples" the source wavenumber spectrum at this particular wavenumber value.

2.3.4.2 Distribution of Dipoles

When the planar source under consideration is modelled as a distribution of dipoles with their dipole axes in the $+z$ direction, the expressions become slightly different. For simplicity, we will maintain the notation for the source strength distribution as $q(\mathbf{r}_s, \omega)$ for the dipole case as well. The radiation integral is then written as

$$p(\mathbf{r}, \omega) = \int_{y_s} \int_{x_s} q(\mathbf{r}_s, \omega) \frac{\partial}{\partial z_s} G_{U_x}(\mathbf{r}|\mathbf{r}_s, \omega) \; \mathrm{d}x_s \, \mathrm{d}y_s. \tag{2.107}$$

By assuming far-field conditions, we can insert the far-field approximation to the dipole transfer function (Eq. 2.98) into Eq. 2.107 and obtain

$$p(\mathbf{r}, \omega) \approx jk_0 \left(\frac{z}{\sigma_{\mathbf{r}}}\right) \frac{e^{-j\hat{\mathbf{k}}\cdot\mathbf{r}}}{4\pi\sigma_{\mathbf{r}}} \int_{y_s} \int_{x_s} q(\mathbf{r}_s, \omega) e^{j\hat{\mathbf{k}}\cdot\mathbf{r}_s} \, \mathrm{d}x_s \, \mathrm{d}y_s, \tag{2.108}$$

$$= jk_0 \left(\frac{z}{\sigma_{\mathbf{r}}}\right) \frac{e^{-j\hat{\mathbf{k}}\cdot\mathbf{r}}}{4\pi\sigma_{\mathbf{r}}} (2\pi)^2 Q\left(\hat{k}_x, \hat{k}_y, \omega\right). \tag{2.109}$$

Once again, the acoustic far-field radiated by a distributed source is proportional to the Spatial Fourier Transform of the source distribution evaluated at an observer-dependent wavenumber $\hat{\mathbf{k}}$. The overall analysis is very similar to the monopole case, except in this particular instance we note the additional frequency factor jk_0 and directivity factor $(z/\sigma_{\mathbf{r}})$ due to the dipole nature of the source elements.

However, we will show that we can alternatively interpret the directivity term $(z/\sigma_{\mathbf{r}})$ as a wavenumber window function $W_{dip}(k_x, k_y)$. From Eq. 2.88, we write

$$\frac{z}{\sigma_{\mathbf{r}}} = \frac{\hat{k}_z}{k_0} \tag{2.110}$$

$$= \frac{1}{k_0}\sqrt{(k_0 - M_x\hat{k}_x)^2 - \hat{k}_x^2 - \hat{k}_y^2} \tag{2.111}$$

$$= W_{dip}\left(\hat{k}_x, \hat{k}_y, \omega\right). \tag{2.112}$$

The wavenumber window function $W_{dip}\left(\hat{k}_x, \hat{k}_y, \omega\right)$, being essentially proportional to $\hat{k}_z$, is always real- and positive-valued for $(\hat{k}_x, \hat{k}_y)$ inside the radiation ellipse, and assumes zero value for $(\hat{k}_x, \hat{k}_y)$ located on the radiation ellipse.

We can now write the far-field as

$$p(\mathbf{r}, \omega) \approx jk_0\frac{e^{-j\hat{\mathbf{k}}\cdot\mathbf{r}}}{4\pi\sigma_{\mathbf{r}}}(2\pi)^2\left[Q\left(\hat{k}_x, \hat{k}_y, \omega\right)W_{dip}\left(\hat{k}_x, \hat{k}_y, \omega\right)\right] \tag{2.113}$$

$$= jk_0\frac{e^{-j\hat{\mathbf{k}}\cdot\mathbf{r}}}{4\pi\sigma_{\mathbf{r}}}(2\pi)^2 Q_{win}\left(\hat{k}_x, \hat{k}_y, \omega\right), \tag{2.114}$$

where $Q_{win}\left(\hat{k}_x, \hat{k}_y, \omega\right)$ corresponds to a windowed wavenumber transform of the source strength distribution.

Therefore, the acoustic far-field as generated by a planar distribution of dipole sources can also be determined from the Spatial Fourier Transform of the source distribution evaluated inside the radiation ellipse; however, the dipole directivity imposes a windowing function that essentially tapers out the contribution of wavenumbers near the radiation ellipse, and the acoustic field is even further spatially low-passed than with monopole sources. This effect must be taken into account when attempting to recover the source wavenumber spectrum from the pressure readings.

2.3.4.3 Proof of Equivalence between Observer Hemisphere and Radiation Ellipse

By tracing the relationship between all possible observer locations over a hemisphere surrounding the acoustic source and their perceived far-field wavenumber vectors, we obtain the "acoustic domain" [51] of the wavenumber spectrum. This domain corresponds to all wavenumbers (k_x, k_y) contained inside the radiation ellipse (Eq. 2.23), as we demonstrate below.

All the points on a hemisphere of radius $R = \|\mathbf{r}\|$ can be projected to the area inside a circle of radius R in (x, y) space; hence, for any observer located on this hemisphere, its coordinates must satisfy

$$\frac{x^2}{R^2} + \frac{y^2}{R^2} \leq 1. \tag{2.115}$$

We now demonstrate that all observer locations spanned by Eq. 2.115 map to points inside the radiation ellipse (Eq. 2.23) via the perceived wavenumber vector $\hat{\mathbf{k}}$: if $\hat{\mathbf{k}}$ is constrained to be inside the radiation ellipse, we can insert Eq. 2.88 into Eq. 2.23 and obtain

$$\frac{\left(k_0\left(\frac{x-M_x\sigma_\mathbf{r}}{\beta^2\sigma_\mathbf{r}}\right)+\frac{k_0M_x}{\beta^2}\right)^2}{\left(\frac{k_0}{\beta^2}\right)^2} + \frac{\left(k_0\frac{y}{\sigma_\mathbf{r}}\right)^2}{\left(\frac{k_0}{\beta}\right)^2} \leq 1, \tag{2.116}$$

which can be simplified to

$$\left(\frac{x}{\sigma_\mathbf{r}}\right)^2 + \left(\beta\frac{y}{\sigma_\mathbf{r}}\right)^2 \leq 1, \tag{2.117}$$

and finally, to

$$x^2 + \beta^2 y^2 \leq \sigma_\mathbf{r}^2. \tag{2.118}$$

Given that $\sigma_\mathbf{r}^2 = x^2 + \beta^2(y^2 + z^2)$, the last expression must always be true for all observer positions considered in Eq. 2.115. Hence, the space spanned by all observers located on a hemisphere around the source will correspond to the space spanned inside the radiation ellipse in wavenumber domain (when Eqs. 2.115 and 2.118 assume a strict inequality), and observers at the edge of the hemisphere will correspond to wavenumbers exactly on the radiation ellipse (when Eqs. 2.115 and 2.118 assume a strict equality).

Figure 2.12 represents the mapping between points in the hemisphere around the source in $\mathbf{r} = (x, y, z)$ physical space and the radiation ellipse in $\mathbf{k} = (k_x, k_y)$ wavenumber domain for a mean flow at $M_x = 0.5$, with regions that are mapped through Eq. 2.88 shown with the same colour in both spaces. Note this is a one-to-one relationship between observer position and perceived wavenumber.

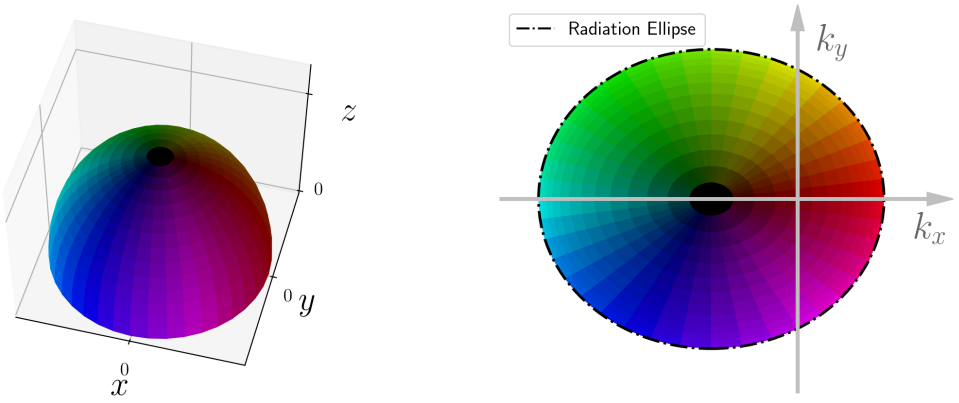

Figure 2.12: Figure denoting the mapping between points in the hemisphere around the source in $\mathbf{r} = (x, y, z)$ physical space and the radiation ellipse in $\mathbf{k} = (k_x, k_y)$ wavenumber domain for a mean flow at $M_x = 0.5$. Regions in the hemisphere surface are mapped to regions with the same color in the wavenumber domain.

2.3.5 Far-Field Power Spectral Estimation

The above analysis allow the determination of the acoustic far-field as estimated from a deterministic source distribution. However, when the sources present random behaviour, it is necessary to work in the cross-spectral domain. From Eq. 2.106, we denote the cross-power spectral density $S_{pp'}(\mathbf{r}, \mathbf{r}', \omega)$ of the acoustic far field radiated by a planar source as

$$S_{pp'}(\mathbf{r}, \mathbf{r}', \omega) = \frac{\pi}{T} \mathrm{E}\left\{p(\mathbf{r}, \omega) p^*(\mathbf{r}', \omega)\right\} \tag{2.119}$$

$$\approx \frac{\pi}{T} \mathrm{E}\left\{\left(\frac{e^{-j\hat{\mathbf{k}}\cdot\mathbf{r}}}{4\pi\sigma_{\mathbf{r}}}(2\pi)^2 Q\left(\hat{\mathbf{k}}, \omega\right)\right)\left(\frac{e^{-j\hat{\mathbf{k}}'\cdot\mathbf{r}'}}{4\pi\sigma_{\mathbf{r}'}}(2\pi)^2 Q\left(\hat{\mathbf{k}}', \omega\right)\right)^*\right\} \tag{2.120}$$

$$= \frac{\pi}{T}\frac{e^{-j\left(\hat{\mathbf{k}}\cdot\mathbf{r} - \hat{\mathbf{k}}'\cdot\mathbf{r}'\right)}}{(4\pi)^2\sigma_{\mathbf{r}}\sigma_{\mathbf{r}'}}(2\pi)^4 \ \mathrm{E}\left\{Q\left(\hat{\mathbf{k}}, \omega\right) Q^*\left(\hat{\mathbf{k}}', \omega\right)\right\} \tag{2.121}$$

$$= \frac{e^{-j\left(\hat{\mathbf{k}}\cdot\mathbf{r} - \hat{\mathbf{k}}'\cdot\mathbf{r}'\right)}}{(4\pi)^2\sigma_{\mathbf{r}}\sigma_{\mathbf{r}'}}(2\pi)^4 \ S_{QQ'}\left(\hat{\mathbf{k}}, \hat{\mathbf{k}}', \omega\right). \tag{2.122}$$

Therefore, the cross-power spectral density of the acoustic pressure at two observer locations $\mathbf{r}, \mathbf{r}'$ is associated with the cross-power spectral density of the source strength in wavenumber domain, evaluated at two wavenumbers $\hat{\mathbf{k}}, \hat{\mathbf{k}}'$ and multiplied by an extra amplitude and phase term that depends on both observer locations and wavenumber vectors.

Similarly, the (auto) power spectral density $S_{pp}(\mathbf{r}, \omega)$ can be approximated in the far-field as

$$S_{pp}(\mathbf{r},\omega) = \frac{\pi}{T}\mathrm{E}\left\{p(\mathbf{r},\omega)p^*(\mathbf{r},\omega)\right\} \tag{2.123}$$

$$\approx \frac{\pi}{T}\mathrm{E}\left\{\left(\frac{e^{-j\hat{\mathbf{k}}\cdot\mathbf{r}}}{4\pi\sigma_{\mathbf{r}}}(2\pi)^2 Q\left(\hat{\mathbf{k}},\omega\right)\right)\left(\frac{e^{-j\hat{\mathbf{k}}\cdot\mathbf{r}}}{4\pi\sigma_{\mathbf{r}}}(2\pi)^2 Q\left(\hat{\mathbf{k}},\omega\right)\right)^*\right\} \tag{2.124}$$

$$= \frac{\pi}{T}\frac{1}{(4\pi\sigma_{\mathbf{r}})^2}(2\pi)^4\ \mathrm{E}\left\{Q\left(\hat{\mathbf{k}},\omega\right)Q^*\left(\hat{\mathbf{k}},\omega\right)\right\} \tag{2.125}$$

$$= \frac{1}{(4\pi\sigma_{\mathbf{r}})^2}(2\pi)^4\ S_{QQ}\left(\hat{\mathbf{k}},\omega\right), \tag{2.126}$$

where $S_{QQ}\left(\hat{\mathbf{k}},\omega\right)$ is the power spectral density of the source strength in the wavenumber domain at the particular wavenumber $\hat{\mathbf{k}}$.

2.4 Shear Layer Effects and Correction

The above analysis was performed considering the acoustic sources are completely surrounded by a uniformly convecting medium; however, it is not uncommon to encounter cases where the surrounding medium is convecting only within a region, and quiescent outside. This occurs in open-jet wind tunnel experiments, for example: a shear layer will develop in the interface between the two regions, and sound waves propagating through this shear layer will be refracted. This effect will change the direction of propagation of the sound waves, affecting both their amplitude and travel time, and must be taken into account when using source reconstruction algorithms such as beamforming.

An open-jet wind tunnel with a rectangular nozzle was used for the experiments described in Chapter 5, represented in Figure 2.13, and thus will be the assumed problem geometry for our analysis. The air in front of the tunnel nozzle is being convected in the $+x$ direction at a velocity U_x; the convecting region is represented in the lower part of the image. A point source is located inside the flow at $\mathbf{r}_s = (x_s, y_s, z_s)$, and a microphone is located outside the flow at $\mathbf{r}_m = (x_m, y_m, z_m)$. The shear layer is assumed to be a plane surface of zero thickness, and is thus represented as a plane at height $z = z_l$. It is implicitly required that z_l must be located between z_s and z_m.

Let us assume an acoustic ray being emitted by the source and reaching the microphone; the acoustic ray path does not follow a straight line between the source and microphone,

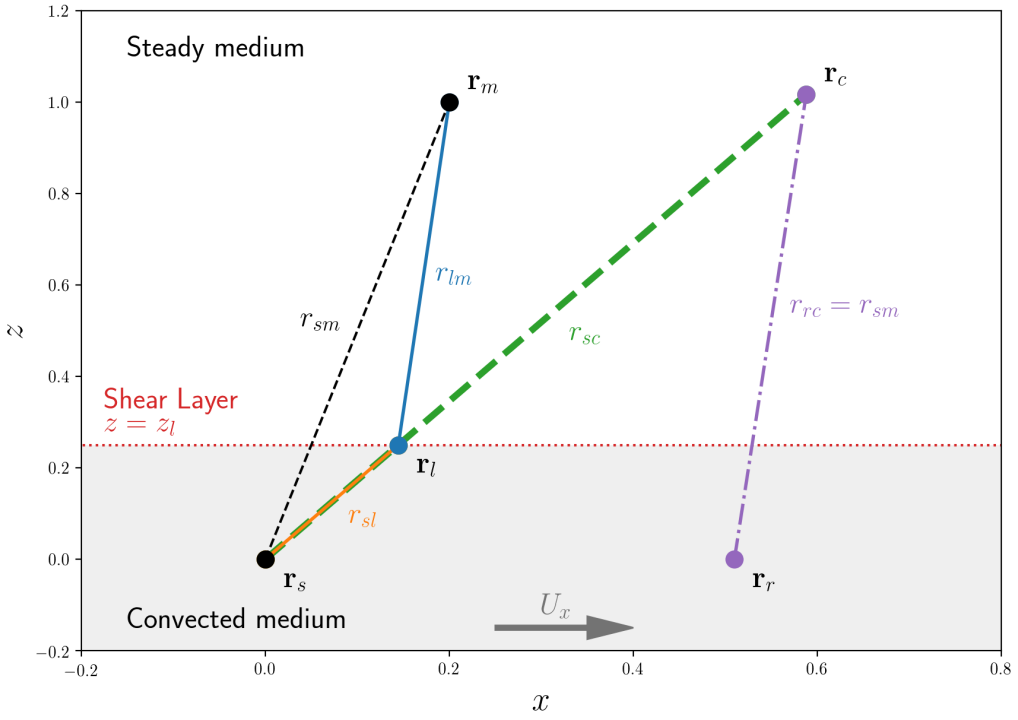

Figure 2.13: Cross-section in the xz plane of an acoustic ray trajectory across a shear layer.

but instead crosses the shear layer at the point $\mathbf{r}_l = (x_l, y_l, z_l)$, where it is refracted and changes direction, before reaching the microphone at $\mathbf{r}_m$. The path r_{sl} occurs inside the flow, and hence must obey the convected wave equation; meanwhile, the path r_{lm} occurs in the quiescent medium region, and thus must obey the standard wave equation.

For a given pair of source and observer positions, we are then interested in determining two variables: the total propagation time taken by the acoustic ray to travel from the source through the shear layer and to the microphone; and the total propagation distance covered by the acoustic ray during its propagation time. With a complete prediction model for both the amplitude and the phase seen by an observer in the out-of-stream region, both effects can be incorporated into the propagation matrix used to estimate the sound radiation by the acoustic sources; similarly, knowledge of these effects allow them to be taken into account when applying source estimation methods.

We propose a simplified analytical model for describing the propagation time and amplitude decay of an acoustic ray moving through a shear layer. For completeness, we also describe the widely used Amiet's model for shear layer correction [52]; although not explicitly compared

here, the proposed method and Amiet's method yield very similar results and are considered equivalent.

2.4.1 Total Propagation Time

The total propagation time allows us to determine the phase shift of the acoustic ray in its path from the source to the microphone location. The Fermat's Principle of least travel time [53] can be used to determine the shear layer crossing point $\mathbf{r}_l$: this point will be such that minimizes the total propagation time τ_{sm} from source to microphone. Koop et al. [54] adopted the same principle (where it is named as Huygens' Principle) to find the shear layer crossing point in a 2D case, but the method can be easily extended to 3D geometry, as show below. A similar approach has also been used by Bahr et al. [55, 56], and the same equations are presented in the Appendix of Amiet [52].

For clarity, let us redefine a convection-corrected distance σ_{ab} between two points $\mathbf{r}_a$ and $\mathbf{r}_b$ as

$$\sigma_{ab} = \sqrt{(x_b - x_a)^2 + \beta^2 \left[(y_b - y_a)^2 + (z_b - z_a)^2\right]}. \tag{2.127}$$

As described above, an acoustic ray propagating inside the mean flow must obey the convected wave equation. The time taken for the ray to propagate from the source $\mathbf{r}_s$ to the shear layer crossing point $\mathbf{r}_l$ is given by [50]

$$\tau_{sl} = \frac{-(x_l - x_s)M_x + \sigma_{sl}}{c_0 \beta^2}. \tag{2.128}$$

Outside the mean flow, the acoustic ray must obey the standard wave equation and move with the speed of sound c_0 in any direction. The time taken for the ray to propagate from the shear layer crossing point $\mathbf{r}_l$ to the microphone $\mathbf{r}_m$ is then written as

$$\tau_{lm} = \frac{r_{lm}}{c_0}. \tag{2.129}$$

The total propagation time is then given by the sum of the two intermediate times:

$$\tau_{sm} = \tau_{sl} + \tau_{lm}. \tag{2.130}$$

We can now take the partial derivatives of Equation 2.130 with respect to the shear layer coordinates x_l and y_l, leading to the following system of equations [52, 54, 55]:

$$\begin{cases} \left(\dfrac{x_l - x_s}{\sigma_{sl}}\right) - \beta^2 \left(\dfrac{x_m - x_l}{r_{lm}}\right) - M_x = 0, \\ \left(\dfrac{y_l - y_s}{\sigma_{sl}}\right) - \left(\dfrac{y_m - y_l}{r_{lm}}\right) = 0. \end{cases} \tag{2.131}$$

These equations present constraints on the shear layer crossing point in the x and y axes; the z_l coordinate is already constrained to be on the shear layer plane.

The approach adopted in this work is to numerically calculate the shear layer crossing point $\mathbf{r}_l$ that minimises the acoustic ray total travel time (Eq. 2.130), subject to the constraints on each spatial dimension given by Eq. 2.131. We use the minimization function from the SciPy package [57] with the aforementioned constraints; if necessary, an initial guess can be given as the point where a straight line between the source and the observer intersects the shear layer plane, which can easily be obtained from geometric analysis. Once the point $\mathbf{r}_l$ is found, the total propagation time is determined through Equation 2.130.

2.4.2 Amplitude Decay

It is known from ray acoustics theory that the acoustic pressure squared is proportional to the cross-sectional area of a "ray tube" (or "ray bundle") [58]. Therefore, the refraction of the acoustic rays crossing the shear layer will affect the area of the ray tube before and after refraction, and hence its amplitude. A few other effects beyond refraction are also associated with the interaction of sound with a shear layer, such as reflection of sound waves back into the convecting region [52] and turbulent scattering of waves crossing a thick, turbulent shear layer [59]. These effects can be studied in more detail by using full ray acoustics theory or computational aeroacoustics methods [60], for example; these are not described because they require significantly more information about the shear layer characteristics, and their level of accuracy is not considered necessary for this work.

We propose a simplified analytical model, partially based on ray acoustics, for approximating the amplitude decay of the sound waves across the shear layer. For a point monopole source, the acoustic pressure $p(\mathbf{r}_1, \omega)$ observed at a point $\mathbf{r}_1$ by a source with strength $q(\mathbf{r}_s, \omega)$ at a point $\mathbf{r}_s$ is written as

$$p(\mathbf{r}_1, \omega) = q(\mathbf{r}_s, \omega) \frac{e^{-jk_0 r_1}}{4\pi r_1}, \tag{2.132}$$

where $r_1 = \|\mathbf{r}_1 - \mathbf{r}_s\|$ is the source-to-observer distance. The acoustic pressure $p(\mathbf{r}_2, \omega)$ at a point $\mathbf{r}_2$ geometrically aligned with the point $\mathbf{r}_1$ but further away is written as

$$p(\mathbf{r}_2, \omega) = q(\mathbf{r}_s, \omega) \frac{e^{-jk_0 r_2}}{4\pi r_2} \tag{2.133}$$

$$= \underbrace{\left[q(\mathbf{r}_s, \omega) \frac{e^{-jk_0 r_1}}{4\pi r_1} \right]}_{= p(\mathbf{r}_1, \omega)} \frac{r_1}{r_2} e^{-jk_0 (r_2 - r_1)}, \tag{2.134}$$

where it is shown that one can estimate the acoustic pressure $p(\mathbf{r}_2, \omega)$ from the pressure $p(\mathbf{r}_1, \omega)$ and the distances between the source and both observation points. The correction terms determine the amplitude decay due to spherical spreading over the larger distance r_2 and the phase shift over the extra distance difference $r_2 - r_1$.

Therefore, we can incorporate an extra step to determine the acoustic pressure at a point x_m in the out-of-stream region for a source at x_s: first, we determine the shear layer crossing point x_l for an acoustic ray leaving the source and reaching the observer, as described above. The incident acoustic pressure at the shear layer is computed using the convected Green's function, and we then estimate the acoustic pressure at x_m from the pressure at the shear layer as described above. A similar shear layer amplitude correction method is described by Bahr et al. [56], but we will adopt a slightly different approach by considering convection effects on the amplitude of the incident acoustic pressure.

2.4.2.1 Shear Layer Amplitude Decay for Monopole Source

Let us use Eq. 2.56 for a convected monopole to describe an acoustic ray propagating from the source towards the shear layer crossing point, and let us divide this expression into an amplitude term and a complex exponential term containing the phase:

$$G_{U_x}(\mathbf{r}_l | \mathbf{r}_s, \omega) = \frac{e^{-jk_0 \left[\overline{r}_{sl} - M_x (\overline{\overline{x}}_l - \overline{\overline{x}}_s) \right]}}{4\pi \beta^2 \overline{r}_{sl}} \tag{2.135}$$

$$= \frac{1}{4\pi \sigma_{sl}} e^{-j\omega \tau_{sl}}. \tag{2.136}$$

Once the ray is refracted and propagates within the quiescent medium region, it assumes a simple monopole-like propagation from the shear layer up to the observer position:

$$G(\mathbf{r}_m|\mathbf{r}_l,\omega) = \frac{e^{-jk_0 r_{lm}}}{4\pi r_{lm}} \tag{2.137}$$

$$= \frac{1}{4\pi r_{lm}} e^{-j\omega\tau_{lm}}. \tag{2.138}$$

By combining the two effects, the total propagation equation will then become:

$$G(\mathbf{r}_m|\mathbf{r}_s,\omega) = \left[G_{U_x}(\mathbf{r}_l|\mathbf{r}_s,\omega)\right] \frac{\sigma_{sl}}{\sigma_{sl}+r_{lm}} e^{-j\omega\tau_{lm}} \tag{2.139}$$

$$= \left[\frac{e^{-j\omega\tau_{sl}}}{4\pi\sigma_{sl}}\right] \frac{\sigma_{sl}}{\sigma_{sl}+r_{lm}} e^{-j\omega\tau_{lm}} \tag{2.140}$$

$$= \frac{e^{-j\omega(\tau_{sl}+\tau_{lm})}}{4\pi(\sigma_{sl}+r_{lm})}. \tag{2.141}$$

Figure 2.14 shows the predicted acoustic field for a point monopole source located in the convected region and near a shear layer; the dashed line indicates the shear layer location, and the Mach number is $M_x = 0.5$ in the convected region. The convection effects are clearly visible in the lower part of the Figure, but note that the (originally spherical) wavefronts are distorted after passing through the shear layer.

Note as well the acoustic field presents a discontinuity at the shear layer location for x coordinates upstream of the source location. This discontinuity appears because our model does not account for reflections at the shear layer; however, as acoustic measurements in open jet wind tunnels are generally performed in the quiescent region, this is considered to be a secondary effect for our purposes. Our model is otherwise representative of the general effects observed in shear layer flows over acoustic fields.

2.4.2.2 Shear Layer Amplitude Decay for Dipole Source

Let us use Equation 2.60 for a point dipole in a moving medium to describe an acoustic ray propagating from a point dipole source towards the shear layer crossing point, and let us divide this expression into an amplitude term and a complex exponential term containing the phase:

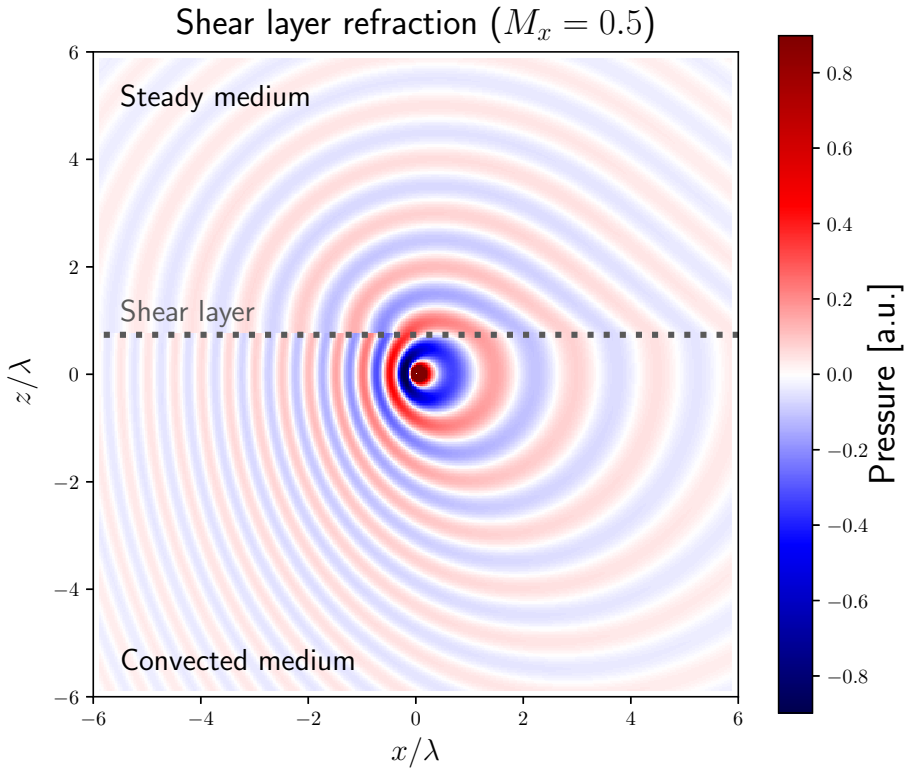

Figure 2.14: Cross-section in the xz-plane of the acoustic field across a shear layer generated by a monopole source; the Mach number for the convected region is $M_x = 0.5$.

$$G(\mathbf{r}_l|\mathbf{r}_s,\omega) = \left(jk_0 + \frac{1}{\overline{r}_{sl}}\right)\frac{(\overline{z}_l - \overline{z}_s)}{\overline{r}_{sl}\beta}\frac{e^{-jk_0\left[\overline{r}_{sl} - M(\overline{\overline{x}}_l - \overline{\overline{x}}_s)\right]}}{4\pi\beta^2\overline{r}_{sl}} \tag{2.142}$$

$$= \left(jk_0 + \frac{1}{\overline{r}}\right)\frac{(z_l - z_s)}{\sigma_{sl}}\frac{1}{4\pi\sigma_{sl}}e^{-j\omega\tau_{sl}}. \tag{2.143}$$

Note that the equation contains three different terms affecting the acoustic ray amplitude: the first contains the dipole hydrodynamic near field, the second contains the dipole directivity, and the third contains the spherical amplitude decay with distance, all of them evaluated over transformed variables.

We now make the assumption that the first and third terms (the dipole near-field and the spherical spreading amplitude decay) will continue to change after the acoustic ray goes through the shear layer, but the second term (the dipole directivity) will remain unmodified. The hypothesis behind this assumption is that the directivity function is a property inherent to the angle of propagation of the acoustic ray when leaving the source, and not to the acoustic ray propagation distance; thus, the directivity function will affect the ray amplitude as the ray

is emitted from the source, but it ceases to have an effect it once the ray has been emitted. The resulting expression for the dipole field across a shear layer is then

$$G(\mathbf{r}_m|\mathbf{r}_m,\omega) = \left(jk_0 + \frac{1}{\overline{r}_{sl}+r_{lm}}\right)\frac{(z_l-z_s)}{\sigma_{sl}}\frac{e^{-j\omega(\tau_{sl}+\tau_{lm})}}{4\pi(\sigma_{sl}+r_{lm})}. \tag{2.144}$$

2.4.3 Amiet Shear Layer Correction Procedure

In the 1970s, Amiet [52] proposed an analytical method for shear layer correction. His method consists in calculating an equivalent microphone position $\mathbf{r}_c$, such that the acoustic ray that reaches $\mathbf{r}_m$ in the presence of the shear layer would instead reach $\mathbf{r}_c$ in the absence of the shear layer, as shown in Figure 2.13. Note that, as the equivalent case assumes no shear layer, $\mathbf{r}_c$ is geometrically aligned with the shear layer crossing point $\mathbf{r}_l$ and with the source location $\mathbf{r}_s$.

We can associate the corrected position $\mathbf{r}_c$ to a retarded source position $\mathbf{r}_r$, which corresponds to the centre of the convected spherical wavefront that would reach the corrected microphone position $\mathbf{r}_c$ in the absence of the shear layer. This retarded position corresponds to an apparent source location, as discussed in previous sections. Note that the distance r_{sc} also corresponds to the sound propagation inside the hypothetical flow beyond the shear layer height, and thus sound propagation through this path must also obey the convected wave equation.

In principle, any other point located in the same direction could be used as corrected microphone position; however, we adopt the definition originally proposed by Amiet [52] and choose the point of equal retarded radius - i.e. the radius between the retarded source position $\mathbf{r}_r$ and the corrected microphone position $\mathbf{r}_c$ is the same as the distance between the actual source $\mathbf{r}_s$ and the actual microphone $\mathbf{r}_m$. It should be mentioned that this choice of corrected microphone position does not lead to the same propagation time as seen by the real microphone.

In order to determine the corrected position $\mathbf{r}_c$, we first determine the acoustic ray propagation velocity inside the flow by $c_{ray} = r_{sl}/\tau_{sl}$. We then consider that, in the absence of a shear layer, a spherical wavefront generated by the source at $\mathbf{r}_s$ will expand outwards with the speed of sound c_0 while at the same time being convected in the positive-x direction; therefore, when the wavefront reaches the corrected microphone position $\mathbf{r}_c$ at time τ_{sc}, its centre (the apparent source location, or retarded source location $\mathbf{r}_r$) will be located at $\mathbf{r}_s + (U_x\tau_{sc}, 0, 0)$, and the wavefront radius to its centre will be $r_{rc} = c_0\tau_{sc}$. However, since by definition we assume

$r_{rc} = r_{sm}$, we can then write $\tau_{sc} = r_{sm}/c_0$. Finally, the corrected source position $\mathbf{r}_c$ can be obtained by "propagating" the acoustic ray in its original direction during a time interval τ_{sc}, or $\mathbf{r}_c = \mathbf{r}_s + (\mathbf{r}_l / \|\mathbf{r}_l\|) c_{ray} \tau_{sc}$.

In some simplified test cases, the proposed shear layer correction model and the Amiet model yielded very similar results, and hence are treated as being equivalent for our purposes.

Chapter 3

Characteristics of Leading Edge Noise Surface Pressure on a Flat Plate

This section investigates the surface pressure, near-field and far-field noise characteristics due to a flat plate leading edge interacing with a turbulent flow. The flat plate model is due to Amiet [8], and it is shown that the classical Amiet far-field formulation can be directly obtained from the far-field approximation for planar sources discussed in the previous chapter. Amiet's effective chordwise lift and spanwise sinc-like directivity can, therefore, be interpreted as the Spatial Fourier Transform of the aerofoil source distribution evaluated over the flat plate surface.

We make an in-depth analysis of the aerofoil response function, including its representation in the wavenumber domain, considering the surface pressure and the acoustic field characteristics for both single- and multiple-gust cases. As established in Chapter 2, the wavenumber-domain representation within the radiation ellipse is directly linked to the radiated acoustic far-field.

The sections covering the presentation of the method are heavily based on the work related to the Amiet model by Reboul [61], Roger [7] and de Santana [62].

3.1 Aerofoil Response to a Turbulent Gust

The Amiet model [8, 10] describes the acoustic surface pressure and radiation created by the interaction of a turbulent velocity field with the leading edge of a flat-plate aerofoil. The flat plate has chord $c = 2b$ and span $L = 2d$. The origin of the coordinate system is placed at the centre of the aerofoil, as shown in Figure 3.1.

We assume that the incoming turbulent field moves with a uniform convection velocity of Mach number $M_x = U_x/c_0$ in the positive x-direction. The incoming field is modelled by an integration of sinusoidal gusts, denoted by a pair of streamwise and spanwise wavenumbers (k_χ, k_ψ). The gusts are hydrodynamic (i.e. vortical) waves, and have an essentially different nature from acoustic waves; we reinforce this difference by denoting acoustic wavenumbers as (k_x, k_y) - i.e. with different subscripts.

The angle ζ of incidence of the gust refers to the gust direction of propagation (i.e. the direction normal to the wavefronts) with respect to the aerofoil chord, and is given by

$$\tan(\zeta) = k_\psi/k_\chi. \tag{3.1}$$

Gusts with $k_\psi = 0$ will therefore have an angle of incidence $\zeta = 0$; however, its wavefronts will be parallel to the aerofoil leading edge, and hence such gusts are often called *parallel* gusts. On the other hand, gusts with $k_\psi \neq 0$ are called *oblique* or *skewed* gusts.

3.1.1 Aerofoil Surface Pressure

We define a "frozen" turbulent gust in the plane of the flat plate ($z = 0$) moving with the flow speed U_x in the $+x$ direction. The gust vertical velocity $w(x, y, t)$ in this plane can be written as an integration over all gust wavenumber components

$$w(x, y, t) = \int_{-\infty}^{+\infty} \int_{-\infty}^{+\infty} \hat{w}(k_\chi, k_\psi)\ e^{-j[k_\chi(x - U_x t) + k_\psi y]}\, \mathrm{d}k_\chi\, \mathrm{d}k_\psi, \tag{3.2}$$

where $\hat{w}(k_\chi, k_\psi)$ is the turbulence wavenumber spectrum. The spectrum can be obtained by calculating the double Spatial Fourier Transform of $w(x, y)$. A single incoming harmonic gust with amplitude $\hat{w}_0(k_\chi, k_\psi)$ will have the form

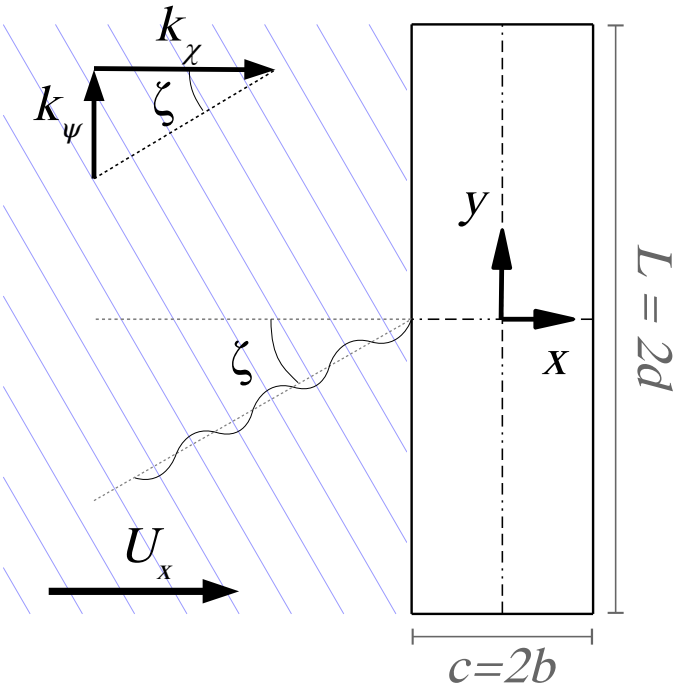

Figure 3.1: Oblique gust with wavenumbers (k_χ, k_ψ) inciding at an angle ζ with flow velocity U_x over the leading edge of an aerofoil.

$$w(x, y, t) = \hat{w}_0(k_\chi, k_\psi) e^{-j\left[k_\chi(x - U_x t) + k_\psi y\right]}. \tag{3.3}$$

The pressure jump $\Delta p(x_s, y_s, t)$ developed over the aerofoil surface as induced by a single gust will assume the form

$$\Delta p(x_s, y_s, t) = 2\pi\rho_0 U_x \hat{w}_0(k_\chi, k_\psi) g^{LE}(x_s, k_\chi, k_\psi)\ e^{-j(k_\psi y_s - k_\chi U_x t)}, \tag{3.4}$$

where $g^{LE}(x_s, k_\chi, k_\psi)$ is the aerofoil response function that couples the chordwise pressure jump to the particular hydrodynamic gust that excites it; these are detailed in Section 3.1.4. Note that the *chordwise* surface pressure jump is determined by the aerofoil response function, while the *spanwise* pressure jump will follow the the spanwise gust component $e^{-jk_\psi y_s}$.

We can then integrate the above equation over all gusts wavenumber components to obtain the total pressure jump $\Delta p(x_s, y_s, t)$:

$$\Delta p(x_s, y_s, t) = 2\pi\rho_0 U_x \int_{-\infty}^{+\infty}\int_{-\infty}^{+\infty} \hat{w}(k_\chi, k_\psi)\; g^{LE}(x_s, k_\chi, k_\psi) e^{-j(k_\psi y_s - k_\chi U_x t)}\,\mathrm{d}k_\chi\,\mathrm{d}k_\psi. \quad (3.5)$$

We now apply the Temporal Fourier Transform to Equation 3.5 to obtain the aerofoil pressure jump $\Delta p(x_s, y_s, \omega)$ in the frequency domain:

$$\Delta p(x_s, y_s, \omega) = 2\pi\rho_0 \int_{-\infty}^{+\infty} \hat{w}(\kappa_\chi, k_\psi)\; g^{LE}(x_s, \kappa_\chi, k_\psi) e^{-jk_\psi y_s}\,\mathrm{d}k_\psi, \quad (3.6)$$

where from the Fourier Transform we obtain $\kappa_\chi = \omega/U_x$. Thus, all turbulence-leading edge interaction noise generated at a temporal frequency ω is related to one particular value κ_χ of the chordwise hydrodynamic wavenumber k_χ.

However, turbulence is a random phenomenon, and can only be analysed in a statistical sense. Let us assume that the turbulent velocity field has a finite extent in the chordwise direction $x \in [-X, X]$; since the turbulence is moving with the flow velocity U_x in the $+x$ direction, there will be an associated time length $T = X/U_x$ such that the turbulence will only interact with the aerofoil during a time interval $t \in [-T, T]$. We can now consider the limit of both X and T going to infinity to define the PSD and the CSD of the turbulence quantities [8].

The cross-power spectral density of the surface pressure jump can be defined as

$$S_{\Delta p\Delta p'}(x_s, x'_s, y_s, y'_s, \omega) = \lim_{T\to\infty}\left[\frac{\pi}{T}\mathrm{E}\left\{\Delta p(x_s, y_s, \omega)\Delta p^*(x'_s, y'_s, \omega)\right\}\right] \quad (3.7)$$

$$= \lim_{T\to\infty}\left[(2\pi\rho_0)^2\frac{\pi}{T}\int_{-\infty}^{+\infty}\int_{-\infty}^{+\infty}\mathrm{E}\left\{w(\kappa_\chi, k_\psi)w^*(\kappa_\chi, k'_\psi)\right\}\ldots\right.$$
$$\left.\ldots\, g^{LE}(x_s, \kappa_\chi, k_\psi) g^{LE*}(x'_s, \kappa_\chi, k'_\psi) e^{-j(k_\psi y_s - k'_\psi y'_s)}\,\mathrm{d}k_\psi\,\mathrm{d}k'_\psi\right]. \quad (3.8)$$

Hydrodynamic gusts with different wavenumbers are assumed orthogonal in homogeneous turbulence [8]; this is denoted as

$$\lim_{T\to\infty}\left[\frac{\pi}{T}\mathrm{E}\left\{w(\kappa_\chi, k_\psi)w^*(\kappa_\chi, k'_\psi)\right\}\right] = U_x\delta(k_\psi - k'_\psi)\Phi_{ww}(\kappa_\chi, k_\psi), \quad (3.9)$$

where $\Phi_{ww}(\kappa_\chi, k_\psi)$ is the wavenumber spectral density of the turbulent gust velocity. The cross-PSD of the surface pressure jump can then be rewritten as

$$S_{\Delta p\Delta p'}(x_s, x_s', y_s, y_s', \omega) = (2\pi\rho_0)^2 U_x \int_{-\infty}^{+\infty} \Phi_{ww}(\kappa_\chi, k_\psi) \dots \\ \dots g^{LE}(x_s, \kappa_\chi, k_\psi) g^{LE*}(x_s', \kappa_\chi, k_\psi) e^{-jk_\psi(y_s - y_s')} \, \mathrm{d}k_\psi. \quad (3.10)$$

Note the appearance of the extra U_x factor when calculating the cross-spectrum of the aerofoil surface pressure jump.

Here we point out that it is common to express the cross-spectral density in the temporal frequency f instead of the angular frequency $\omega = 2\pi f$, which leads to the alternative expression for the CSD:

$$S_{\Delta p\Delta p'}(x_s, x_s', y_s, y_s', f) = 2\pi S_{\Delta p\Delta p'}(x_s, x_s', y_s, y_s', \omega). \quad (3.11)$$

It should also be observed that while all expressions for PSD in this chapter define double-sided spectra, it is more convenient to calculate single-sided spectra in order to compare simulations with experimental measurements. When calculating a single-sided spectrum, an extra multiplying factor of 2 must be included in the equations.

3.1.2 Aerofoil Acoustic Radiation

The acoustic pressure radiated by the aerofoil can be obtained from the Ffowcs-Williams and Hawkings acoustic analogy [63]. The surface pressure jump can be interpreted as a surface distribution of point dipole sources normal to the flat plate. The total radiated acoustic pressure $p(\mathbf{r}, \omega)$ seen by an observer located at $\mathbf{r} = (x, y, z)$ is the surface integration over the dipole source distribution:

$$p(\mathbf{r}, \omega) = \int_{-d}^{d} \int_{-b}^{b} \Delta p(x_s, y_s, \omega) \frac{\partial}{\partial z_s} G(\mathbf{r}|\mathbf{r}_s, \omega) \, \mathrm{d}x_s \, \mathrm{d}y_s, \quad (3.12)$$

where $\partial G / \partial z_s$ is the transfer function for a point dipole in a convected medium (Eq. 2.60):

$$\frac{\partial}{\partial z_s} G_{U_x}(\mathbf{r}|\mathbf{r}_s, \omega) = \left(jk_0 + \frac{1}{\overline{r}} \right) \frac{(\overline{z} - \overline{z}_s)}{\beta \overline{r}} \frac{e^{-jk_0 \overline{r}}}{4\pi\beta^2 \overline{r}} e^{jk_0 M_x (\overline{\overline{x}} - \overline{\overline{x}}_s)}.$$

The cross-power spectral density $S_{pp'}(\mathbf{r}, \mathbf{r}', \omega)$ between the acoustic pressure at two observer points $\mathbf{r}$ and $\mathbf{r}'$ is:

$$S_{pp'}(\mathbf{r}, \mathbf{r}', \omega) = \lim_{T\to\infty}\left[\frac{\pi}{T}\mathrm{E}\left\{p(\mathbf{r}, \omega)p^*(\mathbf{r}', \omega)\right\}\right] \tag{3.13}$$

$$= \int_{-d}^{+d}\int_{-b}^{+b}\int_{-d}^{+d}\int_{-b}^{+b} S_{\Delta p\Delta p'}(\mathbf{r}_s, \mathbf{r}'_s, \omega)\frac{\partial}{\partial z_s}G(\mathbf{r}|\mathbf{r}_s, \omega)\ldots$$
$$\ldots\frac{\partial}{\partial z'_s}G^*(\mathbf{r}'|\mathbf{r}'_s, \omega)\,\mathrm{d}x_s\,\mathrm{d}y_s\,\mathrm{d}x'_s\,\mathrm{d}y'_s. \tag{3.14}$$

Equation 3.14 is the "complete" Amiet model for interaction noise prediction, including near-field effects.

3.1.3 Far-Field Formulation

The complete Amiet model shown in Equation 3.14, while tractable via numerical methods, is clearly a complex and cumbersome calculation to be dealt with analytically. In order to obtain a more manageable formulation, Amiet assumed the observer is in the far-field of the source. We have identified Amiet's approximation as being exactly the Fraunhofer far-field approximation, which was extensively discussed in Chapter 2. All discussions regarding the Fraunhofer approximation, such as its range of validity and interpretation as a plane wave approximation, are thus applicable in the present context.

3.1.3.1 Far-Field, Finite Span Formulation

The first step is to adopt the far-field formulation for the dipole acoustic radiation; the formulation adopted by Amiet is presented in Eq. 2.100. The far-field acoustic pressure radiated by an aerofoil (Eq. 3.12) is then approximated as

$$p(\mathbf{r}, \omega) \approx \int_{-d}^{d}\int_{-b}^{b}\left[2\pi\rho_0\int_{-\infty}^{+\infty} w(\kappa_\chi, k_\psi)\; g^{LE}(x_s, \kappa_\chi, k_\psi)e^{-jk_\psi y_s}\,\mathrm{d}k_\psi\right]\ldots$$
$$\ldots\left[\frac{jk_0 z}{4\pi\sigma_{\mathbf{r}}^2}e^{jk_0\left(\frac{M_x x-\sigma_{\mathbf{r}}}{\beta^2}\right)}e^{jk_0\left(\frac{x-M_x\sigma_{\mathbf{r}}}{\sigma_{\mathbf{r}}\beta^2}\right)x_s}e^{jk_0\left(\frac{y}{\sigma_{\mathbf{r}}}\right)y_s}\right]\mathrm{d}x_s\,\mathrm{d}y_s \tag{3.15}$$

$$= \rho_0\frac{jk_0 bz}{2\sigma_{\mathbf{r}}^2}e^{jk_0\left(\frac{M_x x-\sigma_{\mathbf{r}}}{\beta^2}\right)}\int_{-\infty}^{+\infty} w(\kappa_\chi, k_\psi)\mathcal{L}^{LE}(x, \kappa_\chi, k_\psi)\frac{(2d)\sin\left((k_\psi-\kappa_\psi)\,d\right)}{(k_\psi-\kappa_\psi)\,d}\,\mathrm{d}k_\psi, \tag{3.16}$$

where $\kappa_\psi = k_0 y/\sigma_{\mathbf{r}}$, and $\mathcal{L}^{LE}(x, k_\chi, k_\psi)$ is the effective lift [64] for a single turbulent gust (k_χ, k_ψ):

$$\mathcal{L}^{LE}(x, k_\chi, k_\psi) = \frac{1}{b}\int_{-b}^{b} g^{LE}(x_s, k_\chi, k_\psi) e^{jk_0\left(\frac{x - M_x\sigma_{\mathbf{r}}}{\sigma_{\mathbf{r}}\beta^2}\right)x_s}\,\mathrm{d}x_s. \tag{3.17}$$

Assuming far-field conditions allows the separation of the source integration into the x_s and y_s components and to treat them as Spatial Fourier Transforms, as previously discussed in Section 2.3.4. The term $k_0(x - M_x\sigma_{\mathbf{r}})/(\sigma_{\mathbf{r}}\beta^2)$ in Eq. 3.17 is identical to the first component of the far-field acoustic wavenumber vector $\hat{\mathbf{k}} = (\hat{k}_x, \hat{k}_y, \hat{k}_z)$ in Eq. 2.88. The effective lift function in Eq. 3.17 can then be interpreted as a normalised Spatial Fourier Transform of the chordwise surface pressure jump evaluated over the (acoustic) wavenumber $\hat{k}_x$:

$$\mathcal{L}^{LE}(x, k_\chi, k_\psi) = \frac{1}{b}\int_{-b}^{b} g^{LE}(x_s, k_\chi, k_\psi) e^{j\hat{k}_x x_s}\,\mathrm{d}x_s \tag{3.18}$$

$$= \frac{2\pi}{b} g^{LE}(\hat{k}_x, k_\chi, k_\psi), \tag{3.19}$$

The relationship between the observer chordwise position x and the chordwise acoustic wavenumber $\hat{k}_x$ has an implicit dependence on the flow-corrected chordwise observer angle $x/\sigma_{\mathbf{r}}$; consequently, the effective lift function describes the aerofoil acoustic directivity for chordwise angles. There are known closed-form solutions available for the effective lift function [7, 61], as shown in Section 3.1.4.3.

In Eq. 3.16, the spanwise integration of the aerofoil noise results in a sinc function in $k_\psi (= \hat{k}_y)$, with a main lobe of height of $2d$, null-to-null width $\Delta k_\psi^{ML} = 2\pi/d$ and centred at $\kappa_\psi = k_0 y/\sigma_{\mathbf{r}}$. This function is the Spatial Fourier Transform of a rectangular window of length $L = 2d$ and behaves as a bandpass filter in k_ψ centred on κ_ψ.

The relationship between the observer spanwise position y and the acoustic wavenumber $\hat{k}_y$ has a dependence on the flow-corrected observer spanwise angle $y/\sigma_{\mathbf{r}}$, and hence the sinc function also defines an acoustic directivity as a function of spanwise observer angle. The sinc function main lobe will sift a particular spanwise gust wavenumber towards a specific span angle, indicating that most of the acoustic radiation reaching an observer at an angle $y/\sigma_{\mathbf{r}}$ is due to a gust at the specific hydrodynamic wavenumber $\kappa_\psi = \hat{k}_y = k_0 y/\sigma_{\mathbf{r}}$. For example, an

observer located at mid-span ($y = 0$) will be exposed mostly to the acoustic radiation induced by the gust with spanwise hydrodynamic wavenumber $\kappa_\psi = 0$.

For an observer aligned with the y axis (i.e. $x = z = 0$), the sifted spanwise wavenumber simplifies to $\kappa_\psi = \kappa_x M_x/\beta$. Gusts with hydrodynamic spanwise wavenumber inside the interval $k_\psi \in [-\kappa_x M_x/\beta, \kappa_x M_x/\beta]$ will display strong acoustic radiation towards a unique spanwise angle in the interval $\theta \in [-\pi/2, \pi/2]$, while gusts outside that range will not have a preferred spanwise radiation direction. It is shown in Section 3.1.4.1 (see p. 74) that the aerofoil response function assumes different forms for hydrodynamic gusts inside and outside of this range: gusts inside this range are called *supercritical* gusts, while gusts outside this range are called *subcritical* gusts.

In the case of multiple gusts, the acoustic cross-power spectral density $S_{pp'}(\mathbf{r}, \mathbf{r}', \omega)$ for the far-field, finite-span model can be written as:

$$S_{pp'}(\mathbf{r}, \mathbf{r}', \omega) = \left(\frac{\rho_0 k_0 b}{2}\right)^2 \left(\frac{z}{\sigma_{\mathbf{r}}^2}\right)\left(\frac{z'}{\sigma_{\mathbf{r}}'^2}\right) U_x \int_{-\infty}^{+\infty} \Phi(\kappa_x, k_\psi)\mathcal{L}^{LE}(x, \kappa_x, k_\psi)\mathcal{L}^{LE*}(x', \kappa_x, k_\psi)\ldots$$
$$\ldots \frac{(2d)\sin\left(\left(k_\psi - \kappa_\psi\right)d\right)}{\left(k_\psi - \kappa_\psi\right)d} \frac{(2d)\sin\left(\left(k_\psi - \kappa_\psi'\right)d\right)}{\left(k_\psi - \kappa_\psi'\right)d}\,\mathrm{d}k_\psi, \tag{3.20}$$

while the acoustic power spectral density of the far-field sound $S_{pp}(\mathbf{r}, \omega)$ can be written as

$$S_{pp}(\mathbf{r}, \omega) = \left(\frac{\rho_0 k_0 b z}{2\sigma_{\mathbf{r}}^2}\right)^2 U_x \int_{-\infty}^{+\infty} \Phi_{ww}(\kappa_\chi, k_\psi) \left\|\mathcal{L}^{LE}(x, \kappa_\chi, k_\psi)\right\|^2 \left\|\frac{(2d)\sin\left(\left(k_\psi - \kappa_\psi\right)d\right)}{\left(k_\psi - \kappa_\psi\right)d}\right\|^2 \mathrm{d}k_\psi. \tag{3.21}$$

3.1.3.2 Far-Field, Infinite Span Formulation

As discussed above, the spanwise integration gives rise to a sinc function in the k_ψ domain, as shown in Equation 3.16. In the limit of the aerofoil span becoming large (i.e. $d \to \infty$), the sinc function will tend to behave as a Dirac Delta function inside the k_ψ integration; see Appendix A on how this can be demonstrated. We denote this as:

$$\lim_{d\to\infty} \frac{(2d)\sin\left(\left(k_\psi - \kappa_\psi\right)d\right)}{\left(k_\psi - \kappa_\psi\right)d} = 2\pi\delta\left(k_\psi - \kappa_\psi\right). \tag{3.22}$$

The integration over the k_ψ wavenumbers coupled with the Delta function will effectively sift the spanwise turbulence wavenumber, so that only $\kappa_\psi = k_0 y/\sigma_{\mathbf{r}}$ contributes to the observation point $y/\sigma_{\mathbf{r}}$ in the far field. Therefore, the infinite-span, far field pressure $p(\mathbf{r},\omega)$ can be approximated by the acoustic field generated by a single gust with hydrodynamic wavenumbers $(\kappa_\chi, \kappa_\psi)$:

$$p(\mathbf{r},\omega) \approx \rho_0 \frac{j\pi k_0 bz}{\sigma_{\mathbf{r}}^2} e^{jk_0\left(\frac{M_x x - \sigma_{\mathbf{r}}}{\beta^2}\right)} w(\kappa_\chi,\kappa_\psi)\mathcal{L}^{LE}(x,\kappa_\chi,\kappa_\psi). \tag{3.23}$$

In this limit, for an observer directly above the aerofoil ($y = 0$), only the normal incidence gust $k_\psi = 0$ will contribute to the observed acoustic pressure; all oblique gusts ($k_\psi \neq 0$) will cancel along the span and will not radiate towards the observer direction.

The far-field, infinite-span (single-gust) power spectral density $S_{pp}(\mathbf{r},\omega)$ has to be formulated in a slightly different form, because the convergence of the sinc-squared function is not the same as the square of the convergence of the sinc function. As discussed in Appendix A, we must write

$$\lim_{d\to\infty} \frac{1}{2d}\left[\frac{(2d)\sin\left(\left(k_\psi - \frac{k_0 y}{\sigma_{\mathbf{r}}}\right)d\right)}{\left(k_\psi - \frac{k_0 y}{\sigma_{\mathbf{r}}}\right)d}\right]^2 = 2\pi\delta\left(k_\psi - \frac{k_0 y}{\sigma_{\mathbf{r}}}\right). \tag{3.24}$$

And hence, the far-field, infinite-span (single gust) PSD can be derived from Equation 3.21 as

$$S_{pp}(\mathbf{r},\omega) = \left(\frac{\rho_0 k_0 bz}{2\sigma_{\mathbf{r}}^2}\right)^2 U_x \int_{-\infty}^{+\infty} \Phi_{ww}(\kappa_\chi,k_\psi)\left\|\mathcal{L}^{LE}(x,\kappa_\chi,k_\psi)\right\|^2 \ldots \\ \ldots (2d)\frac{1}{2d}\left\|\frac{(2d)\sin\left(\left(k_\psi - \frac{k_0 y}{\sigma_{\mathbf{r}}}\right)d\right)}{\left(k_\psi - \frac{k_0 y}{\sigma_{\mathbf{r}}}\right)d}\right\|^2 \mathrm{d}k_\psi. \tag{3.25}$$

Performing the integration results in

$$S_{pp}(\mathbf{r},\omega) = \left(\frac{\rho_0 k_0 bz}{\sigma_{\mathbf{r}}^2}\right)^2 U_x \pi d\ \Phi_{ww}(\kappa_\chi,\kappa_\psi)\ \left\|\mathcal{L}^{LE}(x,\kappa_\chi,\kappa_\psi)\right\|^2. \tag{3.26}$$

3.1.4 Aerofoil Response Functions

3.1.4.1 Supercritical and Subcritical Gusts

Implementing the interaction noise model using a numerical method requires calculating the aerofoil response to individual gusts; Graham [65] described how the response of an infinite-span aerofoil subject to a subsonic, oblique gust can assume two forms, depending on the value of the parameter

$$\Theta_G = \frac{k_\chi M_x}{k_\psi \beta}. \tag{3.27}$$

A gust is termed *supercritical* when $\|\Theta_G\| \geq 1$. The aerofoil response to a supercritical gust is similar to the response to a compressible, normal incidence gust. In this case, it my be shown that the intersection point between the gust and the aerofoil leading edge moves supersonically relative to the fluid [8], and the aerofoil is an efficient radiator of sound to the far-field.

A gust is termed *subcritical* when $\|\Theta_G\| < 1$. The aerofoil response to a subcritical gust is similar to the response to an incompressible, oblique gust. In this case, the intersection point between the gust and the aerofoil leading edge moves subsonically relative to the fluid, and the aerofoil is an inefficient radiator of sound. More specifically, a subcritical gust response by an infinite-span aerofoil will induce an evanescent acoustic field, which decays exponentially away from the aerofoil and does not reach the far field [7].

For a fixed temporal frequency - and hence fixed k_χ - we can define the critical value of k_ψ such that $\Theta_G = 1$ as

$$k_\psi^{crit} = \frac{k_\chi M_x}{\beta}. \tag{3.28}$$

Thus, all k_ψ integrations can be described as a superposition of the subcritical gusts contribution for $|k_\psi| > k_\psi^{crit}$, plus the supercritical gusts contribution for $|k_\psi| \leq k_\psi^{crit}$. As a consequence of this duality, the aerofoil response function $g^{LE}(x_s, k_\chi, k_\psi)$ assume different forms for supercritical and subcritical gusts [7, 61].

Note that the critical spanwise hydrodynamic wavenumber k_ψ^{crit} has been previously identified in Section 3.1.3.1 (see p. 70), where it was shown that supercritical gusts will radiate strongly in a given spanwise direction, while subcritical gusts do not have a preferred radiation direction.

3.1.4.2 Aerofoil Response Functions

The analytical formulation for compressible gusts used in this Thesis are based on Amiet's proposed solution based on the Schwarzschild technique [9], which consists of calculating the solution for an infinite-chord aerofoil with no trailing edge (that is, infinite downstream of the leading edge) to model the leading edge scattering of the hydrodynamic gusts, and then applying a correction factor for an infinite-chord aerofoil with no leading edge (that is, infinite upstream of the trailing edge) to consider the trailing edge scattering of the aerofoil surface pressure response. As the model is based on linearised potential theory [9], the solutions can be added directly. In principle this is an iterative procedure, but Amiet states that the first two iterations are enough for practical problems.

The first two terms of the aerofoil response function have the form

$$g^{LE}(x_s, k_\chi, k_\psi) = g_1(x_s, k_\chi, k_\psi) + g_2(x_s, k_\chi, k_\psi), \tag{3.29}$$

where g_1 and g_2 represent the leading edge scattering and the trailing edge backscattering of sound, respectively. In the formulations for g_1 and g_2, all quantities will be normalised by the half-chord b, which is denoted using a "breve" ($\breve{\cdot}$) symbol:

$$\breve{x} = \frac{x}{b}, \qquad \breve{k}_i = k_i b,$$

and the acoustic reduced frequency is denoted as $\mu_a = \breve{k}_\chi M_x / \beta^2$.

For supercritical gusts ($\Theta_G \geq 1$), we write [61]

$$\kappa^2 = \mu_a^2 - \left(\frac{\breve{k}_\psi}{\beta}\right)^2 = \mu_a^2 \left(1 - \frac{1}{\Theta_G^2}\right), \tag{3.30}$$

$$g_1(x_s, k_\chi, k_\psi) = e^{-j\pi/4} \frac{e^{-j[(\kappa - \mu_a M_x)(\breve{x}_s + 1)]}}{\pi\sqrt{\pi(\breve{x}_s + 1)(\breve{k}_\chi + \beta^2\kappa)}}, \tag{3.31}$$

$$g_2(x_s, k_\chi, k_\psi) = -e^{-j\pi/4} \frac{e^{-j[(\kappa - \mu_a M_x)(\breve{x}_s + 1)]}}{\pi\sqrt{2\pi(\breve{k}_\chi + \beta^2\kappa)}} \left\{1 - (1+j)\ \mathcal{F}^*\left[2\kappa(1 - \breve{x}_s)\right]\right\}, \tag{3.32}$$

where $\mathcal{F}^*[.]$ is the complex conjugate of the Fresnel integral $\mathcal{F}[.]$. The latter is defined as

$$\mathcal{F}(\zeta) = \frac{1}{\sqrt{2\pi}} \int_0^\zeta \frac{e^{jz}}{\sqrt{z}}\, \mathrm{d}z, \tag{3.33}$$

and therefore the former is defined as

$$\mathcal{F}^*(\zeta) = \frac{1}{\sqrt{2\pi}} \int_0^\zeta \frac{e^{-jz}}{\sqrt{z}}\, \mathrm{d}z. \tag{3.34}$$

For subcritical gusts ($\Theta_G < 1$), we have [61]

$$\kappa'^2 = -\kappa^2 \tag{3.35}$$

$$= \left(\frac{\breve{k}_\psi}{\beta}\right)^2 - \mu_a^2 = \mu_a^2 \left(\frac{1}{\Theta_G^2} - 1\right), \tag{3.36}$$

and write $g^{LE} = g'_1 + g'_2$, with

$$g'_1(x_s, k_\chi, k_\psi) = e^{-j\pi/4} \frac{e^{[(-\kappa' + j\mu_a M_x)(\breve{x}_s + 1)]}}{\pi\sqrt{\pi(\breve{x}_s + 1)(\breve{k}_\chi - j\beta^2\kappa')}}, \tag{3.37}$$

$$g'_2(x_s, k_\chi, k_\psi) = -e^{-j\pi/4} \frac{e^{[(-\kappa' + j\mu_a M_x)(\breve{x}_s + 1)]}}{\pi\sqrt{2\pi(\breve{k}_\chi - j\beta^2\kappa')}} \left\{1 - \mathrm{erf}\left[\sqrt{2\kappa'(1 - \breve{x}_s)}\right]\right\}, \tag{3.38}$$

where erf[.] is the error function:

$$\mathrm{erf}(x) = \frac{2}{\sqrt{\pi}} \int_0^x e^{-t^2}\, \mathrm{d}t. \tag{3.39}$$

Note that the above equations are not defined for critical gusts ($k_\psi = k_\psi^{crit}$); therefore, the critical gust response is numerically interpolated from responses slightly above and slightly below criticality in order to obtain a smooth transition, as previously commented by Roger [7].

3.1.4.3 Effective Lift Functions

From these formulations for the aerofoil response functions, we can write the respective effective lift functions $\mathcal{L}^{LE}(x, k_\chi, k_\psi)$ defined in Eq. 3.17. For supercritical gusts ($\Theta_G \geq 1$), we write

$$\mathcal{L}_1(x, k_\chi, k_\psi) = \frac{1}{\pi}\sqrt{\frac{2}{(\breve{k}_\chi + \beta^2\kappa)H_1}}\mathcal{F}^*(2H_1)e^{jH_2} \tag{3.40}$$

and

$$\begin{aligned}\mathcal{L}_2(x, k_\chi, k_\psi) = \frac{e^{jH_2}}{\pi H_1\sqrt{2\pi\left(\breve{k}_\chi + \beta^2\kappa\right)}}\Bigg\{ & j\left(1 - e^{-j2H_1}\right)\ldots \\ & \ldots + (1-j)\left[\mathcal{F}^*(4\kappa) - \sqrt{\frac{2\kappa}{\kappa + \mu_a x/\sigma}}e^{-j2H_1}\mathcal{F}^*\big(2(\kappa + \mu_a x/\sigma_{\mathbf{r}})\big)\right]\Bigg\},\end{aligned} \tag{3.41}$$

where $H_1 = \kappa - \mu_a x/\sigma_{\mathbf{r}}$ and $H_2 = \mu_a(M_x - x\sigma_{\mathbf{r}}) - \pi/4$ [9, 61].

Note that the term H_1 becomes negative when evaluated for certain gusts near criticality at some frequencies and observer locations, which in turn yield innacurate results in the evaluation of $\mathcal{L}_1(x, k_\chi, k_\psi)$.

For subcritical gusts ($\Theta_G < 1$), we write

$$\mathcal{L}_1'(x, k_\chi, k_\psi) = \frac{1}{\pi}\sqrt{\frac{2}{\left(\breve{k}_\chi - j\beta^2\kappa'\right)(j\kappa' - \mu_a x/\sigma_{\mathbf{r}})}}\mathcal{F}\big(2(j\kappa' - \mu_a x/\sigma_{\mathbf{r}})\big)e^{jH_2} \tag{3.42}$$

and

$$\mathcal{L}_2'(x,k_\chi,k_\psi)=\frac{je^{jH_2}}{\pi H_3\sqrt{2\pi\left(\breve{k}_\chi-j\beta^2\kappa'\right)}}\Bigg\{1-e^{-2H_3}-\operatorname{erf}\left(\sqrt{4\kappa'}\right)\ldots$$
$$\ldots+2e^{-2H_3}\sqrt{\frac{\kappa'}{j\kappa'+\mu_a x/\sigma_{\mathbf{r}}}}\mathcal{F}\big(2(j\kappa'-\mu_a x/\sigma_{\mathbf{r}})\big)\Bigg\}, \quad (3.43)$$

where $H_3=\kappa'-j\mu_a x/\sigma_{\mathbf{r}}$ [9, 61].

Note that the supercritical formulations require the calculation of the complex conjugate of the Fresnel integral, written as $\mathcal{F}^*[.]$ (Eq. 3.34), while the subcritical formulations require the Fresnel integral without complex conjugation, written as $\mathcal{F}[.]$ (Eq. 3.33).

3.1.5 Turbulent Velocity Wavenumber Spectrum

In order to match the experimental conditions, we adopted the von Karman wavenumber energy spectrum [8] for homogeneous, isotropic turbulence. This model describes the velocity spectrum vertical to the flat plate $\Phi_{ww}(k_\chi,k_\psi)$ as a function of hydrodynamic wavenumbers (k_χ,k_ψ). It is defined in terms of the mean-squared velocity $\overline{u^2}$ and the integral length scale Λ as

$$\Phi_{ww}(k_\chi,k_\psi)=\frac{4}{9\pi}\frac{\overline{u^2}}{k_e^2}\frac{\breve{k}_\chi^2+\breve{k}_\psi^2}{\left(1+\breve{k}_\chi^2+\breve{k}_\psi^2\right)^{7/3}}, \quad (3.44)$$

$$k_e=\frac{\sqrt{\pi}}{\Lambda}\frac{\Gamma(5/6)}{\Gamma(1/3)}, \quad (3.45)$$

where $\breve{k}_i=k_i/k_e$ and $\Gamma(\cdot)$ is the Gamma function.

3.2 Aerofoil Surface Pressure Characteristics

We will now discuss in more depth the aerofoil surface pressure jump characteristics as induced by turbulence-leading edge interaction to understand what information it yields about the acoustic radiation. It will also serve as a background for what is expected in the proposed source reconstruction scheme using microphone arrays.

The next sections show some numerical computations based on a general experimental setup often used for interaction noise measurements in the ISVR's anechoic open jet wind tunnel (see, for example, Clair et al. [15]). A flat plate with chord $c = 0.15$ m and span $L = 0.45$ m (the aspect ratio is $L/c = 3$) is positioned in the potential core of the wind tunnel. The flow speed is $U_x = 60$ m/s, the turbulence intensity is $T_i = \sqrt{{u_{rms}}^2/U_x^2} = 0.025$ and the integral length scale is $\Lambda = 0.007$ m.

3.2.1 Aerofoil Surface Discretisation

Equations 3.31 and 3.37 suggests that the gust-leading edge interaction pressure jump for a flat-plate aerofoil exhibits a $1/\sqrt{x}$ singularity at the leading edge, which requires extra care when evaluating the aerofoil surface pressure near the leading edge. A non-uniform discretisation scheme is therefore adopted in the chordwise direction, similar to the one used by Clair et al. [15]. The chord sampling points $x_s[n] \in (-b, b]$ are calculated via

$$x_s[n] = \left(\frac{e^{l[n]} - e^{-L_{exp}/2}}{e^{+L_{exp}/2} - e^{-L_{exp}/2}} \right) (2b) - b, \tag{3.46}$$

where $l[n]$ contains N_x+1 points uniformly sampled over the non-dimensional interval $[-L_{exp}/2, L_{exp}/2]$. The first sample of $x_s[n]$, located exactly at the leading edge, is then removed from the grid. The exponential function, when evaluated over the negative values around $-L_{exp}/2$, provides a finer discretisation for the points close to the leading edge. Shorter interval lengths L_{exp} provide a sampling scheme that is closer to uniform sampling, while larger values provide a more non-uniform sampling; throughout this work, we adopted $L_{exp} = 2$.

The spanwise sampling is uniform, with N_y points in the range $y_s \in [-d, d]$. Note that the spanwise sampling interval Δy_s is identical over the flat plate span, while the chordwise sampling interval Δx_s is non-uniform and becomes smaller closer to the leading edge. Care must therefore be taken when numerically integrating the surface pressure to consider the correct corresponding sample width.

Figure 3.2 shows an example of the proposed discretisation with $(N_x, N_y) = (50, 101)$ points, used for illustration purposes; a denser grid of $(N_x, N_y) = (100, 101)$ was adopted for the actual numerical calculations to achieve convergence.

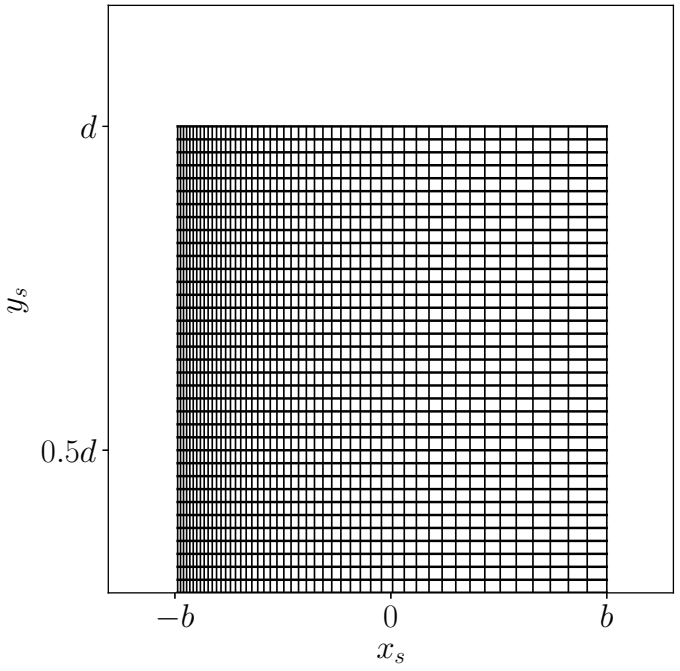

Figure 3.2: Example of flat-plate aerofoil surface discretisation mesh around the span tip; this aerofoil surface is uniformly discretised with 101 points in the spanwise direction, and non-uniformly discretised with 50 points in the chordwise direction.

3.2.2 Wavenumber Analysis of Single-Gust Response Functions

We will start discussing the surface pressure response to a single gust, which is fully coherent over the entire $z = 0$ plane.

3.2.2.1 Supercritical Gusts

The leading edge scattering term is described by Equation 3.31 for supercritical gusts, and can be rewritten in terms of a travelling wave modulated by an envelope function and a constant phase shift of $-\pi/4$:

$$g_1(x_s, k_\chi, k_\psi) = g_1^{env}(x_s, k_\chi, k_\psi)\ e^{-jk_x^{sup}(x_s+b)}\ e^{-j\pi/4}, \tag{3.47}$$

where the envelope function is

$$g_1^{env}(x_s, k_\chi, k_\psi) = \frac{1}{\pi\sqrt{\pi(\breve{x}_s + 1)(\breve{k}_\chi + \beta^2\kappa)}} \tag{3.48}$$

and k_x^{sup} is a purely real wavenumber term of the form

$$k_x^{sup} = \frac{1}{b}\left(\kappa - \mu_a M_x\right) \tag{3.49}$$

$$= \frac{1}{\beta^2}\left(\sqrt{k_0^2 - (k_\psi \beta)^2} - k_0 M_x\right). \tag{3.50}$$

Note that, for spanwise wavenumbers $k_\psi = k_y$ in the supercritical range, this wavenumber component will be located over the radiation ellipse in (k_x, k_y) domain (compare with Eq. 2.25). As k_ψ increases (i.e. as the gusts become more oblique), k_x^{sup} decreases.

Returning to the total aerofoil surface pressure jump for single-gust excitation (Eq. 3.6), each gust with spanwise hydrodynamic wavenumber k_ψ will induce a spanwise phase variation of the type $e^{-jk_\psi y_s}$ over the aerofoil surface. A supercritical single-gust excitation will therefore induce a response similar to a travelling wave of the type $e^{-j\left[k_x^{sup}(x_s+b)+k_\psi y_s\right]}$. In the wavenumber domain, this aerofoil response will be centred at the acoustic wavenumber (k_x^{sup}, k_ψ), located over the right-hand-side half of the radiation ellipse. A sample of these wavenumbers are indicated in Figure 3.3 with circles.

The aerofoil response function can then be interpreted as an acoustic wave propagating over the aerofoil surface in the (x_s, y_s) plane, in the direction given by the acoustic wavenumbers (k_x^{sup}, k_ψ) and at the velocity of sound in a moving medium. These conclusions will be illustrated in the next sections.

3.2.2.2 Subcritical Gusts

A similar analysis can be performed for the subcritical gust response function (Eq. 3.37), which can be rewritten as

$$g_1'(x_s, k_\chi, k_\psi) = g_1^{'env}(x_s, k_\chi, k_\psi)\; e^{-jk_x^{sub}(x_s+b)}\; e^{-j\pi/4}, \tag{3.51}$$

where the envelope function is

$$g_1^{'env}(x_s, k_\chi, k_\psi) = \frac{1}{\pi\sqrt{\pi(\breve{x}_s + 1)(\breve{k}_\chi - j\beta^2\kappa')}}. \tag{3.52}$$

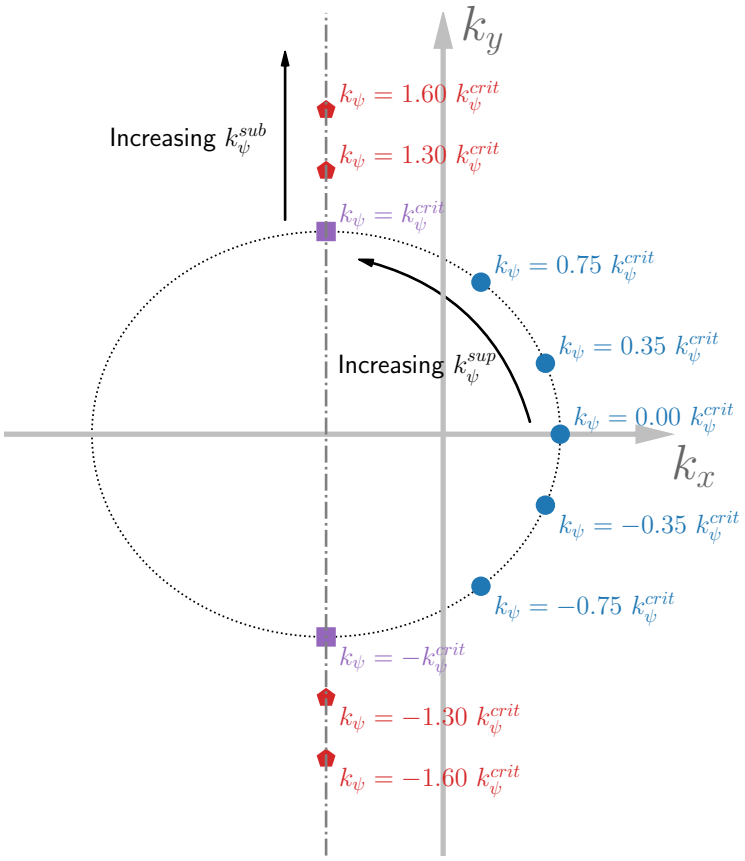

Figure 3.3: Diagram displaying in acoustic wavenumber space (k_x, k_y) the location of the main wavenumber component of the aerofoil response function $g^{LE}(x_s, k_\chi, k_\psi)$ for different hydrodynamic spanwise wavenumbers k_ψ; supercritical gusts responses are indicated with a circle, critical gusts responses are indicated with a square, and subcritical gusts responses are indicated with pentagons.

Again, the response can be decomposed into: a complex-valued envelope function; a complex exponential, that can be interpreted as a wave propagating along the chord in the streamwise direction; and a constant phase shift of $-\pi/4$. The wavenumber term k_x^{sub} can be written as the sum of a propagating and a decaying part as

$$k_x^{sub} = \frac{1}{b}(-j\kappa' - \mu_a M_x) \tag{3.53}$$

$$= \left(-\frac{k_0 M_x}{\beta^2}\right) + j\left(-\frac{1}{\beta^2}\sqrt{(k_\psi\beta)^2 - k_0^2}\right). \tag{3.54}$$

Hence, the subcritical chordwise wavenumber contains a real and an imaginary part. The real part corresponds to a travelling wave component in the downstream direction, while the imaginary part is negative and corresponding to an exponential decay component in the downstream direction. Note that as k_ψ increases (i.e. as the gusts become more oblique), the

real component remains the same, but the imaginary component increases in magnitude and the aerofoil response quickly decays in amplitude in x_s.

In wavenumber space, the travelling wave component will correspond to a point $(-\frac{k_0 M_x}{\beta^2}, k_\psi)$ that moves in a straight line away from the radiation ellipse for increasing k_ψ. Representative examples of these wavenumbers are indicated with pentagons in Figure 3.3. Hence, the travelling wave component of the aerofoil response will generate an evanescent acoustic wave into the acoustic medium.

3.2.2.3 Gust Integration Limit for Surface Pressure Calculations

Due to their exponential decay, subcritical gusts will only affect a certain portion of the aerofoil chord around the leading edge and up to a given chord point x_s. For a fixed chordwise coordinate x_s, therefore, there will be a maximum subcritical gust spanwise wavenumber $k_\psi^{[A]}(x_s)$ below which the evanescent character of the aerofoil response will attenuate the surface pressure distribution by less than A decibels (say, -20 dB). This relationship can be obtained by setting the magnitude of the evanescent component at that chord point to be equal to A dB:

$$20\log_{10}\left(e^{-\left[\frac{1}{\beta^2}\sqrt{(k_\psi^{[A]}\beta)^2-k_0^2}\right](x_s+b)}\right)=A, \tag{3.55}$$

from which we can derive the following expression for the maximum spanwise gust limit:

$$k_\psi^{[A]}\left(x_s, M_x, k_0\right)=k_\psi^{crit}\sqrt{\left[-\frac{\beta^2\ln\left(10^{\frac{A}{20}}\right)}{k_0(x_s+b)}\right]^2+1}. \tag{3.56}$$

Hence, at a given chord position x_s, subcritical gusts with spanwise wavenumbers $|k_\psi| < k_\psi^{[A]}$ are considered significant contributors to the surface pressure response at that point, while gusts with spanwise wavenumbers $|k_\psi| > k_\psi^{[A]}$ will induce a response with a magnitude below A dB at that chord point. Their contribution to the surface pressure response at that point can therefore be ignored. Note that the maximum spanwise gust wavenumber increases as $1/(x_s+b)$ for points approaching the leading edge ($x_s=-b$).

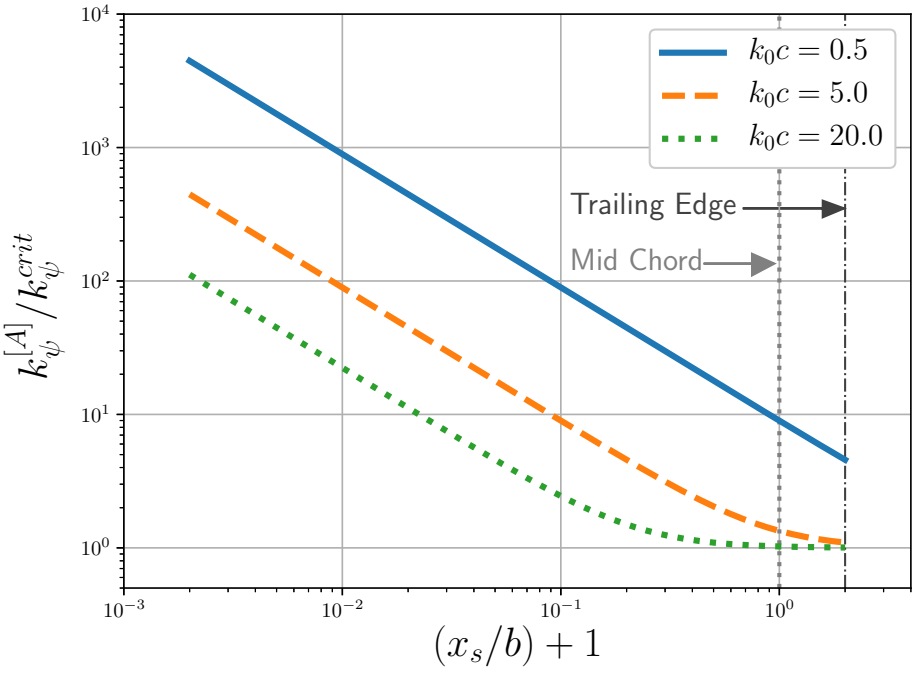

Figure 3.4: Evanescent gust spanwise wavenumber $k_\psi^{[A]}$, with evanescent response at $A = -20$ dB at each chord point x_s, in double-logarithmic plot, for chordwise normalised frequencies $k_0c = [0.5, 5, 20]$.

Figure 3.4 shows the maximum subcritical gust spanwise wavenumber $k_\psi^{[A]}$ for $A = -20$ dB as a function of x_s for three chordwise reduced frequencies $k_0c = [0.5, 5, 20]$. It can be seen that as x_s moves downstream, the less the aerofoil response is affected by subcritical gusts, which can then be ignored in the analysis. Conversely, if x_s moves upstream towards the leading edge - and if one observes the aerofoil response at lower frequencies - than it is necessary to consider a much larger range of subcritical gusts in order to correctly estimate the aerofoil response.

We have tested the convergence of the surface pressure cross-spectral density $S_{\Delta p \Delta p'}(\mathbf{r}_s, \mathbf{r}'_s, \omega)$ as a function of maximum spanwise gust integration, and have found that $k_\psi^{[-20]}$ is a sufficient integration limit to achieve convergence in the cross-spectrum for a wide range of frequencies. This limit will be adopted later on when computing the aerofoil response to multiple gusts.

3.2.3 Single-Gust Surface Pressure Characteristics

Let us now demonstrate the aerofoil response to single gusts at different reduced frequencies ($k_0c = 0.5$, $k_0c = 5$ and $k_0c = 20$). We consider a flow Mach number $M_x \approx 0.17$ to match the experimental conditions.

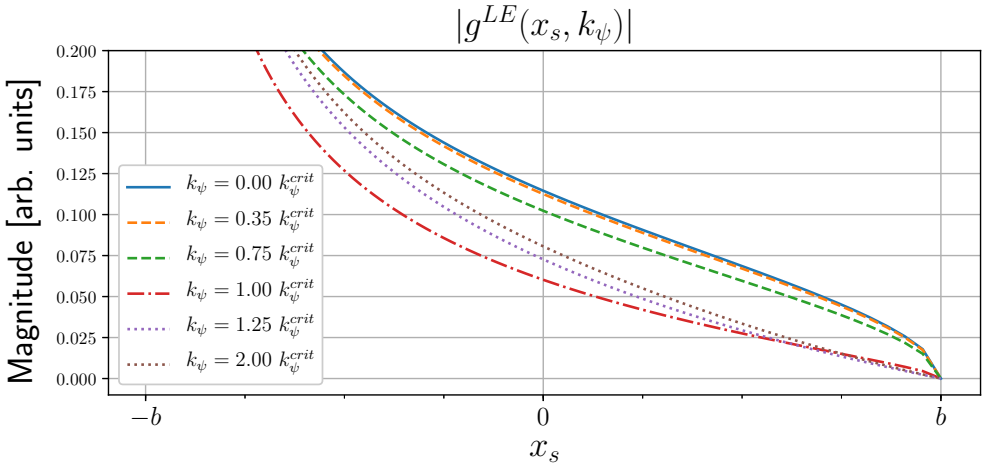

Figure 3.5: Typical aerofoil response function chordwise magnitude for different range of gusts, shown in arbitrary units. The solid line denotes a normal incidence gust (supercritical); the dashed lines denote oblique supercritical gusts; the dash-dotted line denotes a critical gust; and the dotted lines denote subcritical gusts; $k_0 c = 0.5$, $M_x \approx 0.17$. [Modified from Roger [7]]

3.2.3.1 Example: Low Frequency Response ($k_0 c = 0.5$)

Consider a low frequency example at $k_0 c = 0.5$, in which the aerofoil is a compact source (i.e. much smaller than the acoustic wavelength), and radiates effectively as a single, point dipole source [30]. Figure 3.5 shows the magnitude of the chordwise aerofoil response function for normal-incidence (supercritical), oblique supercritical, critical and subcritical gusts. This Figure illustrates how at low frequencies, all types of gust load the aft portions of the aerofoil surface.

Figure 3.6 shows the real part of the surface pressure jump. The surface loading in this example is almost entirely in phase over the entire surface, except for small areas of phase change for subcritical gusts at relatively high spanwise wavenumber value. It can also be observed how the surface loading is very similar for all gusts, indicating that at low frequencies even subcritical gusts should be as efficient radiators of sound to the far-field as supercritical gusts.

Figure 3.7 shows the magnitude (in dB) of the Spatial Fourier Transform of the surface pressure distributions for the 6 examples shown in Figure 3.6; the white traces represent the radiation ellipse. Very little variations inside the radiation ellipse region in the wavenumber domain, denoting an almost uniform acoustic radiation to the far-field at all angles for all gusts. No particular main lobe or sidelobes are visible at this frequency range.

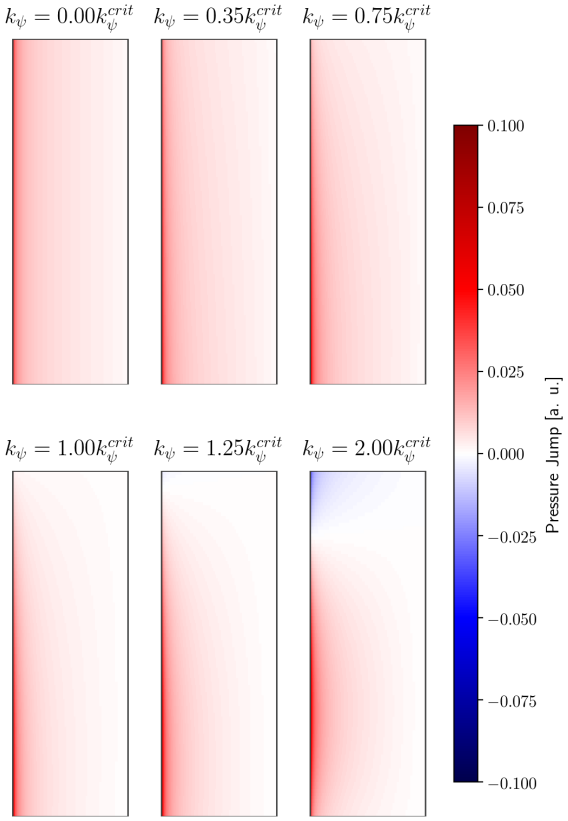

Figure 3.6: Typical aerofoil surface pressure jump (real part) for different range of supercritical and subcritical gusts; $k_0 c = 0.5$, $M_x \approx 0.17$.

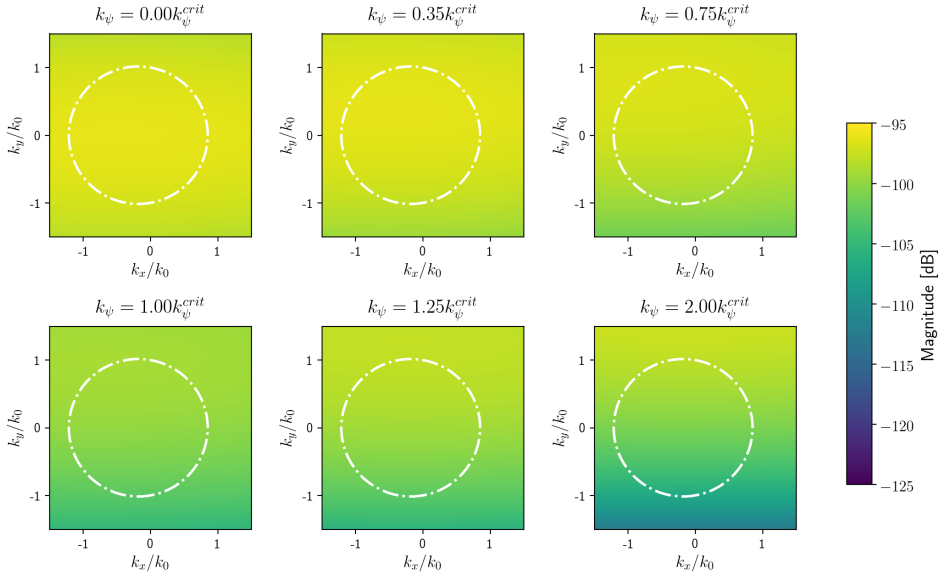

Figure 3.7: Wavenumber Transform of aerofoil surface pressure jump for different range of supercritical and subcritical gusts; $k_0 c = 0.5$, $M_x \approx 0.17$.

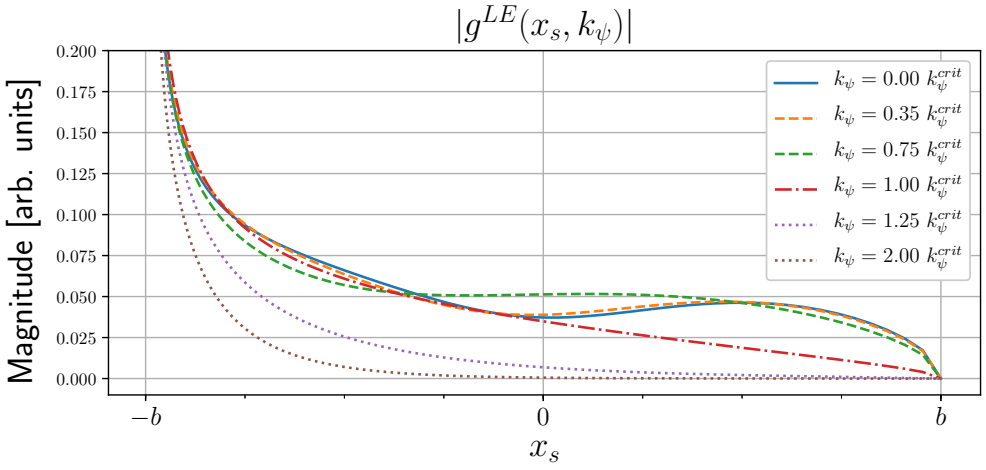

Figure 3.8: Typical aerofoil response function chordwise magnitude for different range of gusts, shown in arbitrary units. The solid line denotes a normal incidence gust (supercritical); the dashed lines denote oblique supercritical gusts; the dash-dotted line denotes a critical gust; and the dotted lines denote subcritical gusts; $k_0 c = 5$, $M_x \approx 0.17$. [Modified from Roger [7]]

3.2.3.2 Example: Medium Frequency Response ($k_0 c = 5$)

Figure 3.8 shows the absolute value of the aerofoil response function for the previously discussed set of supercritical and subcritical gusts. All gust responses present the singularity at the leading edge, but it can be seen that supercritical gusts load more significantly the aerofoil surface as a whole, while for subcritical gusts the loading is more concentrated at the leading edge and decay exponentially towards the trailing edge.

Figure 3.9 shows the surface pressure jump for parallel-incidence and oblique gusts excitation at medium frequency ($k_0 c = 5$). It can be clearly seen how the aerofoil response wavefronts move from towards the downstream direction for a parallel-incidence gust, to towards the spanwise direction for oblique gusts. It can also be seen how supercritical gusts load most of the aerofoil surface, while the loading due to subcritical gusts is concentrated close to the leading edge.

The magnitude (in dB) of the Spatial Fourier Transform of the aerofoil surface pressure responses are shown on Figure 3.10. A series of sidelobes can be seen in the k_y direction due to the aerofoil finite span. Some weak sidelobes are also present in the k_x direction, although these are much broader due to the aerofoil chord being smaller than the span. As previously discussed, the wavenumber component of maximum pressure are concentrated along the radiation ellipse for supercritical gusts, and moves in a vertical line away from the ellipse for subcritical gusts, as previously shown in Figure 3.3.

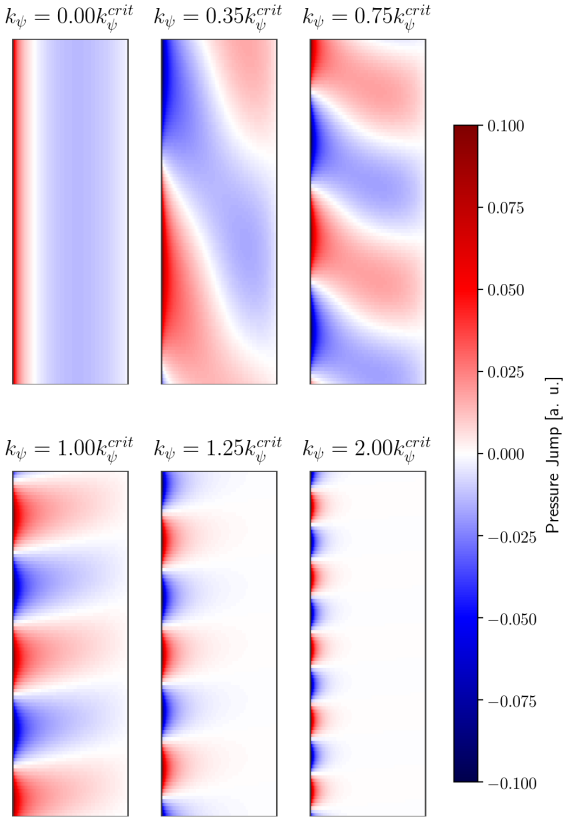

Figure 3.9: Typical single-gust aerofoil surface pressure jump (real part) for different range of supercritical and subcritical gusts; $k_0 c = 5$, $M_x \approx 0.17$.

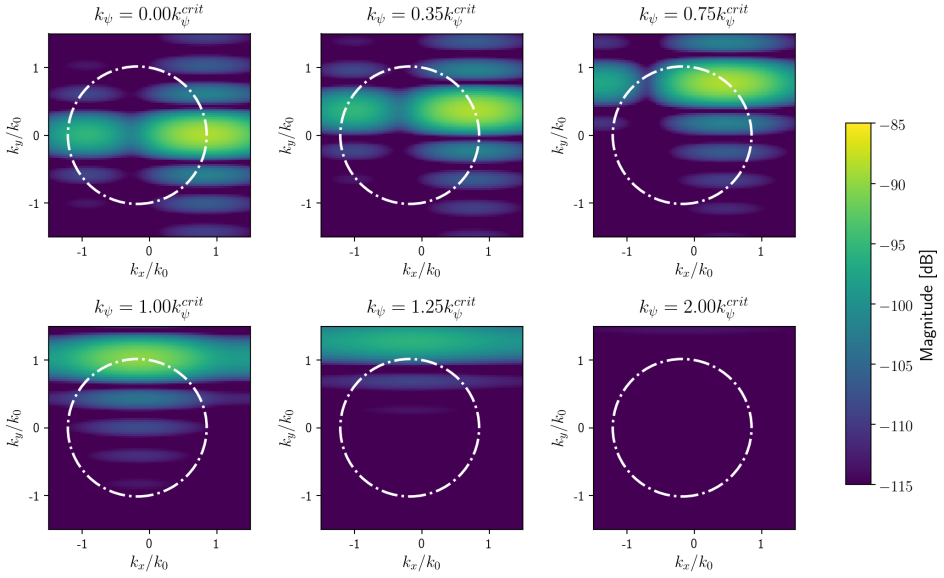

Figure 3.10: Wavenumber Transform of single-gust aerofoil surface pressure jump for different range of supercritical and subcritical gusts; $k_0 c = 5$, $M_x \approx 0.17$.

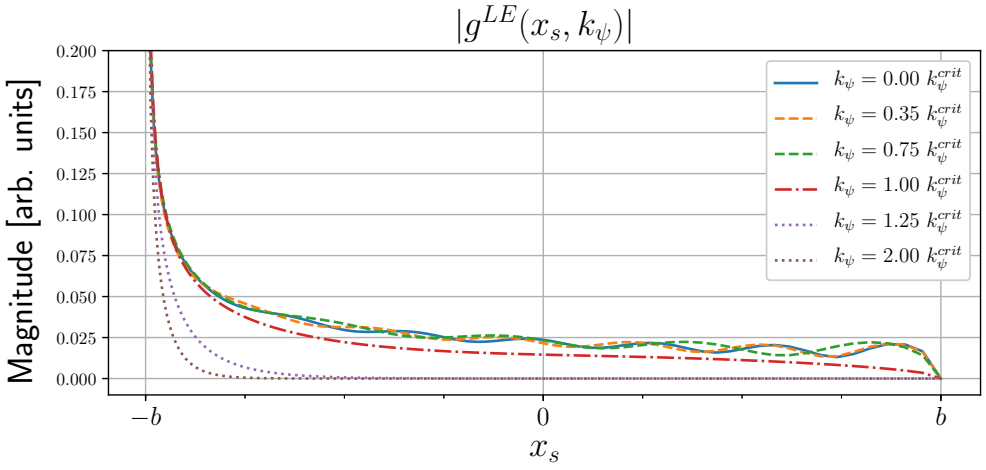

Figure 3.11: Typical aerofoil response function chordwise magnitude for different range of gusts, shown in arbitrary units. The solid line denotes a normal incidence gust (supercritical); the dashed lines denote oblique supercritical gusts; the dash-dotted line denotes a critical gust; and the dotted lines denote subcritical gusts; $k_0 c = 20$, $M_x \approx 0.17$. [Modified from Roger [7]]

3.2.3.3 Example: High Frequency Response ($k_0 c = 20$)

Figure 3.11 shows the aerofoil response magnitude at high frequencies ($k_0 c = 20$), where overall magnitudes are lower than the medium and low frequency cases. The exponential decay for the subcritical gusts is more pronounced at this higher frequency. Figure 3.12 shows the real part of the surface pressure jump over the aerofoil surface. Note, however, that the levels displayed in this Figure are 5 times lower than that shown for low and medium frequencies (note the colorbar scale). Once again, the wave-like characteristics of the surface pressure are apparent, with the change in direction of the wavefronts as the gust spanwise wavenumber k_ψ increases clearly observable. Note also the severe attenuation of the subcritical gusts responses when compared to previous cases.

Figure 3.13 shows the Spatial Fourier Transform of the surface pressure distributions shown in the previous Figure. The main lobe of the supercritical response functions is clearly positioned on top of the radiation ellipse, moving around it as the hydrodynamic spanwise gust wavenumber changes, and clearly departing from the radiation ellipse for subcritical gusts. One can also observe how only the sidelobes are inside the radiation ellipse for the critical gust response, indicating an inefficient acoustic radiation to the far-field.

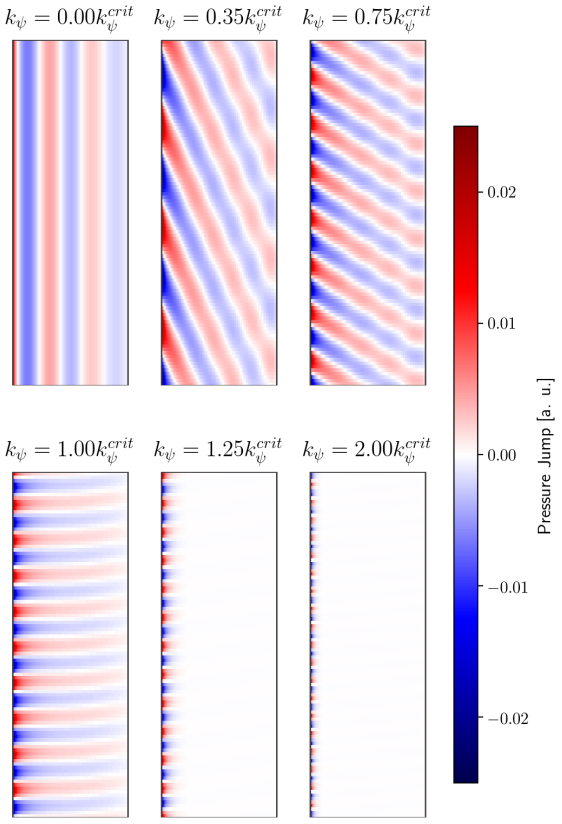

Figure 3.12: Typical aerofoil surface pressure jump (real part) for different range of supercritical and subcritical gusts; note that the levels displayed in this figure are 5 times lower than the ones shown previously for low and medium frequencies. $k_0 c = 20$, $M_x \approx 0.17$.

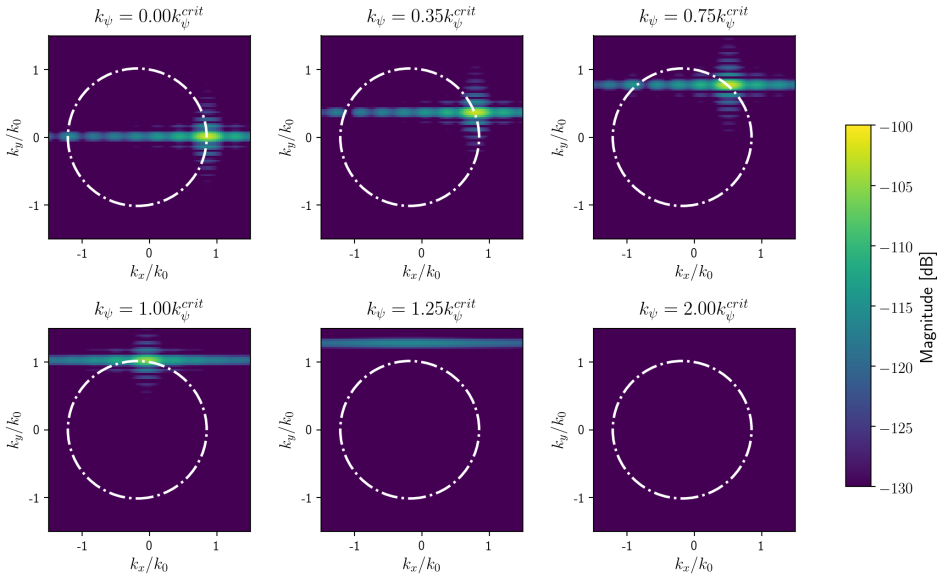

Figure 3.13: Wavenumber Transform of aerofoil surface pressure jump for different range of supercritical and subcritical gusts; $k_0 c = 20$, $M_x \approx 0.17$.

3.2.4 Multiple-Gust Surface Pressure Characteristics

This Section considers the simultaneous contribution of multiple mutually incoherent vortical gusts, representative of an isotropic turbulent flow. From Eq. 3.10, the total surface pressure jump over the aerofoil is obtained by integrating multiple gusts responses, each one inducing a fully-coherent surface pressure distribution:

$$S_{\Delta p\Delta p'}(x_s, x'_s, y_s, y'_s, \omega) = (2\pi\rho_0)^2 U_x \int_{-\infty}^{+\infty} \Phi_{ww}(\kappa_\chi, k_\psi) \dots \\ \dots g^{LE}(x_s, \kappa_\chi, k_\psi) g^{LE*}(x'_s, \kappa_\chi, k_\psi) e^{-jk_\psi(y_s - y'_s)} \, \mathrm{d}k_\psi.$$

As the flat plate surface pressure jump corresponds to the source strength distribution in the acoustic analogy, a thorough investigation of the pressure jump characteristics will yield information about the radiated acoustic field.

We choose some reference points $\mathbf{r}_s^{ref}$ on the aerofoil surface and investigate the cross-spectrum magnitude, phase and coherence against these references. Figure 3.14 shows the three reference points in the mid-span: 1% chord (i.e. near the leading edge), 10% chord, and 50% chord (i.e. at mid-chord).

The coherence function, defined from classical Signal Processing [66] as

$$\gamma^2(\mathbf{r}_{ref}, \mathbf{r}_s, \omega) = \frac{|S_{\Delta p\Delta p'}(\mathbf{r}_s^{ref}, \mathbf{r}_s, \omega)|^2}{S_{\Delta p\Delta p}(\mathbf{r}_s^{ref}, \omega) \; S_{\Delta p\Delta p}(\mathbf{r}_s, \omega)}, \tag{3.57}$$

determines the degree of linear association between the surface pressure at the two points. Regions where the surface pressure is coherent will generate sound fields that interfere constructively and behave as a single larger, more efficient acoustic radiator. Meanwhile, incoherent regions will not generate constructively interfering sound fields and are less efficient sound sources when viewed as a whole.

3.2.4.1 Surface Pressure Characteristics

Figures 3.15 to 3.17 show the aerofoil surface pressure cross-spectrum magnitude and phase, and the surface pressure coherence, evaluated over the entire aerofoil surface for each case: at frequencies $k_0 c \in [0.5, 5, 20]$ and reference points at 1% chord (Fig. 3.15), 10% chord (Fig.

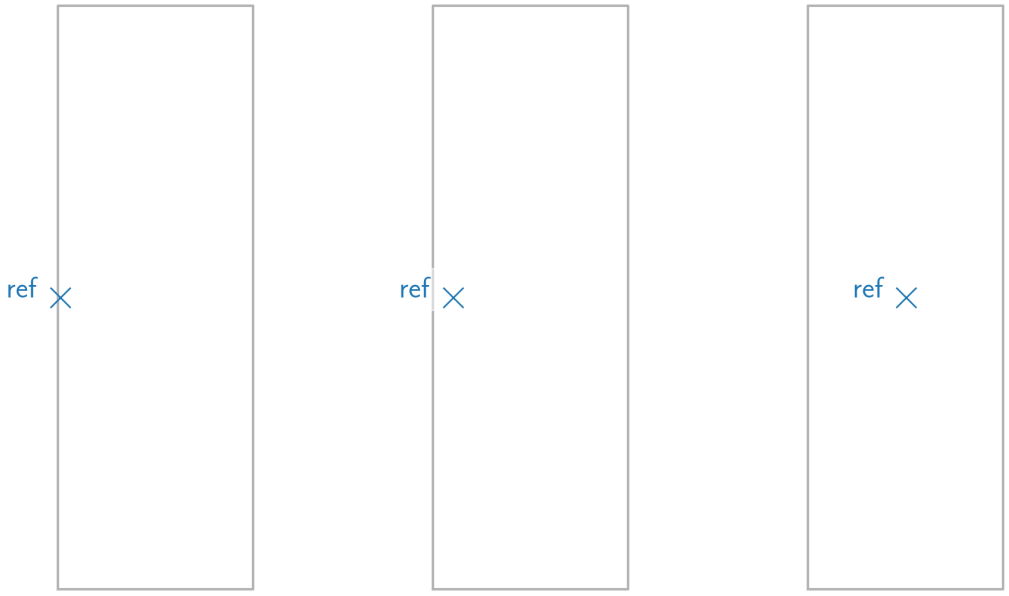

Figure 3.14: Mid-span reference points. (a) 1% chord; (b) 10% chord; (c) 50% chord.

3.16) and 50% chord (Fig. 3.17). We have empirically obtained convergent results using a gust wavenumber sampling of 4 samples per sinc function null-to-null main lobe width Δk_ψ (see Section 3.1.3.1), and adopting a gust integration limit of $k_\psi^{[-20]}$.

Some general trends relative to the surface pressure coherence can be inferred from these Figures. In Fig. 3.15, with the reference at 1% chord, it can be observed that points near the leading edge have a very short coherence length in the chordwise direction and shorter in the spanwise direction. As described in Section 3.2.2.3, it is necessary to consider a large range of gust wavenumbers to obtain convergence at this reference point - i.e. $k_\psi^{[-20]}$ is large. While high wavenumber gusts do not affect the aft section of the aerofoil, they can still load the leading edge and impose a shorter spanwise coherence length. The chordwise coherence is longer than the spanwise coherence, and the coherence length is slightly longer at lower frequencies, but the differences are very small.

In Figure 3.16, with the reference positioned at 10% chord, the coherence lengths are longer than in the previous case. The difference between the different frequencies is now clearer, with higher frequencies having shorter coherence lengths. The chordwise coherence length is also observed to be longer than the spanwise coherence length. It can also be noted that

the coherence decreases slightly for points upstream of the reference (i.e. towards the leading edge).

Finally, in Figure 3.17, with the reference at 50% chord, the coherence lengths become significantly longer in the spanwise direction.

These results indicate that, despite the pressure jump singularity, the leading edge might be an inefficient radiator of sound due to the highly incoherent nature of the surface pressure near that region at all frequencies. On the other hand, the surface pressure on the aft regions display longer coherence lengths and might be more efficient radiators of sound, particularly at lower frequencies.

Note as well the variation in cross-spectrum phase relative to the references: points located downstream of the references (i.e. towards the trailing edge) tend to be positive, while points upstream of the references tend to be negative. This effect might be related to how the single-gust flat plate response functions can be described as a travelling wave over the aerofoil surface, as discussed in Section 3.2.2.

Cross-Spectrum and Coherence ref. 1% Chord

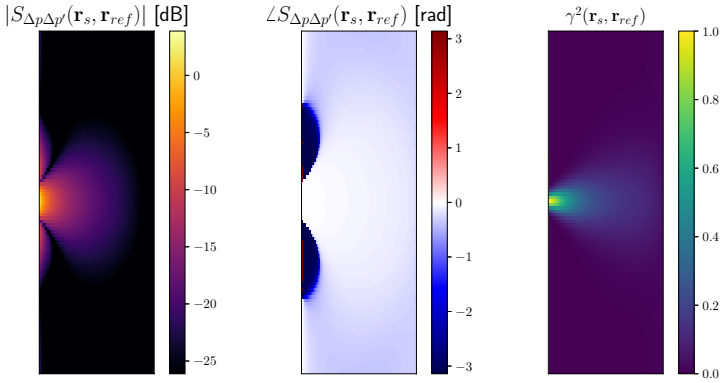

(a)

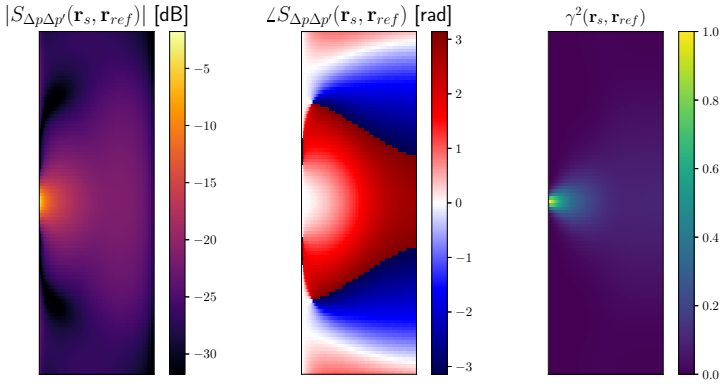

(b)

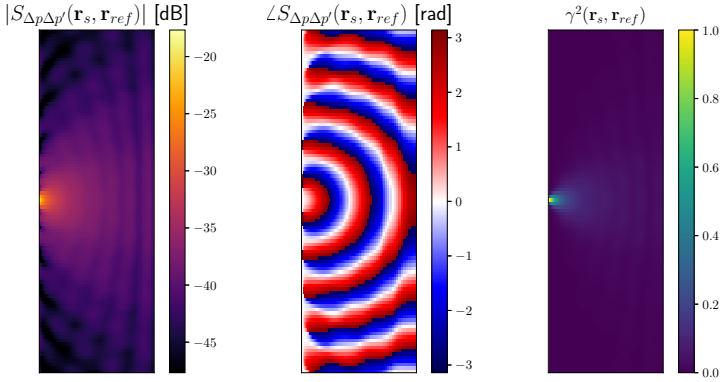

(c)

Figure 3.15: Cross-spectral density magnitude and phase, and coherence, for reference point 1% chord: (a) low frequency ($k_0 c = 0.5$); (b) medium frequency ($k_0 c = 5$); (c) high frequency ($k_0 c = 20$).

Cross-Spectrum and Coherence ref. 10% Chord

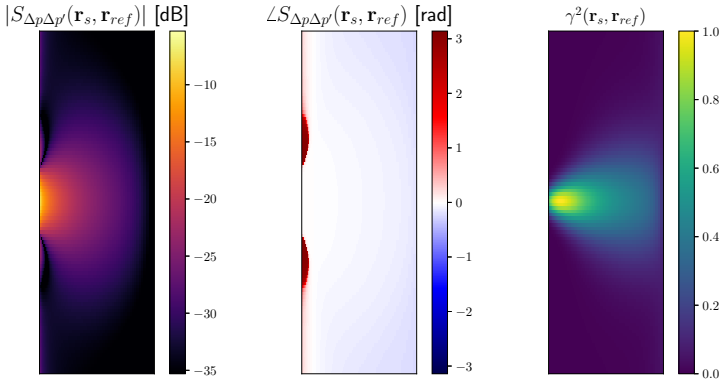

(a)

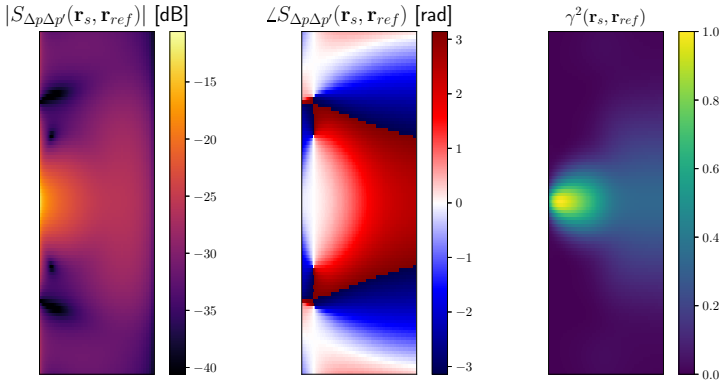

(b)

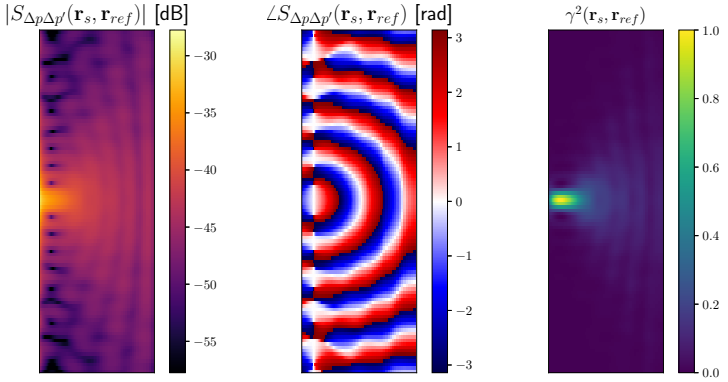

(c)

Figure 3.16: Cross-spectral density magnitude and phase, and coherence, for reference point 10% chord: (a) low frequency ($k_0 c = 0.5$); (b) medium frequency ($k_0 c = 5$); (c) high frequency ($k_0 c = 20$).

Cross-Spectrum and Coherence ref. 50% Chord

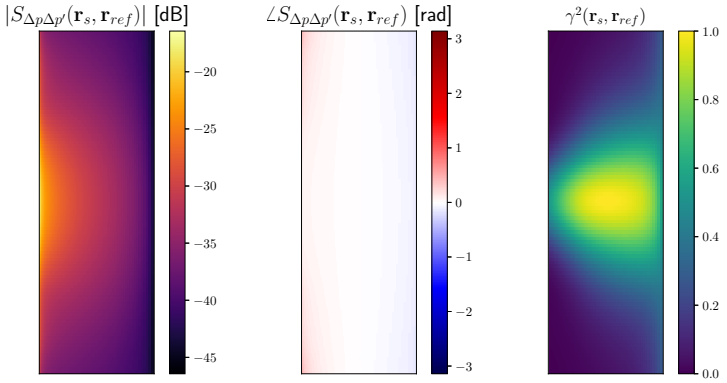

(a)

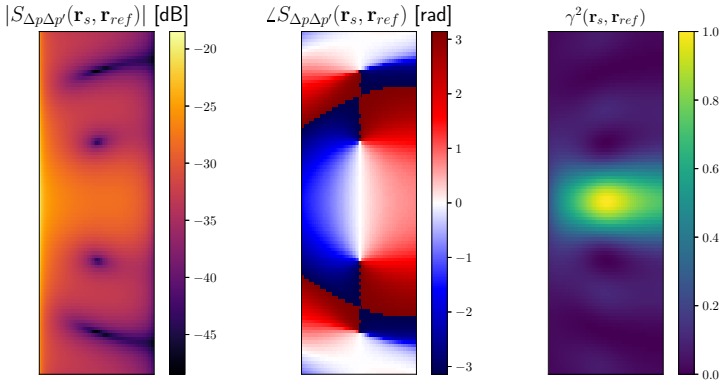

(b)

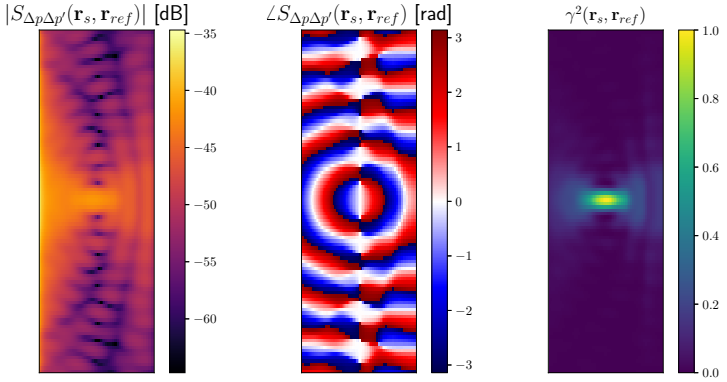

(c)

Figure 3.17: Cross-spectral density magnitude and phase, and coherence, for reference point 50% chord: (a) low frequency ($k_0c = 0.5$); (b) medium frequency ($k_0c = 5$); (c) high frequency ($k_0c = 20$).

3.2.4.2 Total Wavenumber Power Spectra Characteristics

In previous Sections, we considered the Spatial Fourier Transform of the fully coherent surface pressure response to single vortical gust components. In practice, turbulence contains a continuum of wavenumber components that are mutually uncorrelated, and requires a cross-spectral density analysis. We can obtain a surface pressure cross-spectrum in the wavenumber domain by calculating

$$S_{\Delta p \Delta p'}(\mathbf{k}, \mathbf{k}', \omega) = \frac{1}{(2\pi)^4} \int \int S_{\Delta p \Delta p'}(\mathbf{r}_s, \mathbf{r}'_s, \omega) e^{j(\mathbf{k}\cdot\mathbf{r}_s - \mathbf{k}'\cdot\mathbf{r}'_s)} \, \mathrm{d}\mathbf{r}_s \, \mathrm{d}\mathbf{r}'_s. \tag{3.58}$$

We plot in Figure 3.18 the auto-power spectral density (in dB) in wavenumber domain (k_x, k_y) at frequencies $k_0 c \in [0.5, 5, 20]$, representing the amount of "energy" contained in each wavenumber component of the surface pressure jump. This Figure can be interpreted as the incoherent sum of the wavenumber spectra of the single-gust responses previously shown in Figures 3.7, 3.10 and 3.13, where each single gust response has its main wavenumber component located over the radiation ellipse. As a consequence, the energy in the wavenumber autospectrum is visibly concentrated along the radiation ellipse for medium and high frequencies.

The wavenumber spectra inside the radiation ellipse can be related to the acoustic far-field radiated by the source, as established in Sections 2.3.4 and 2.3.5, and is associated to the source far-field directivity. At low frequencies, the energy is uniformly distributed inside the ellipse, indicating an almost omnidirectional far-field response by the aerofoil. However, the radiation ellipse occupies a relatively small area in wavenumber domain at this frequency, and the energy can be seen to spread across wavenumbers both inside and outside the ellipse; thus, only a small portion of the surface pressure energy will radiate as far-field sound. This indicates that a far-field-based source reconstruction method will not be able to recover a significant amount of highy energetic wavenumber components, and will likely underestimate the source distribution at this frequency.

At higher frequencies it tends to concentrate towards the ellipse and form multiple radiation lobes and nulls, while for wavenumbers outside the radiation ellipse the energy can be seen to decay. Therefore, at such frequencies, a significant amount of the energy contained in the aerofoil surface pressure will radiate as far-field sound. We can also observe the appearance of radiation lobes and nulls inside the ellipse: at medium frequency, only one null is observed within the radiation region, while at high frequency multiple nulls can be observed.

Note that sources composed of distribution of dipoles have an extra wavenumber factor $W_{dip}(k_x, k_y, \omega)$ (Eq. 2.112) when associating their wavenumber spectrum to the radiated far-field, as discussed in Section 2.3.4.2. This windowing function will attenuate the contributions to the far-field of wavenumbers towards the radiation ellipse, while maintaining the contribution of wavenumbers near the centre of the ellipse. Since most of the energy in the surface pressure jump developed over an aerofoil interacting with a turbulent gust is contained in wavenumbers located over the radiation ellipse, therefore these same wavenumbers do not radiate effectively to the far-field.

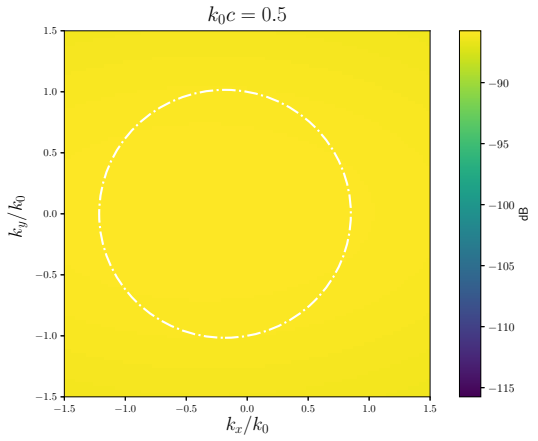

(a)

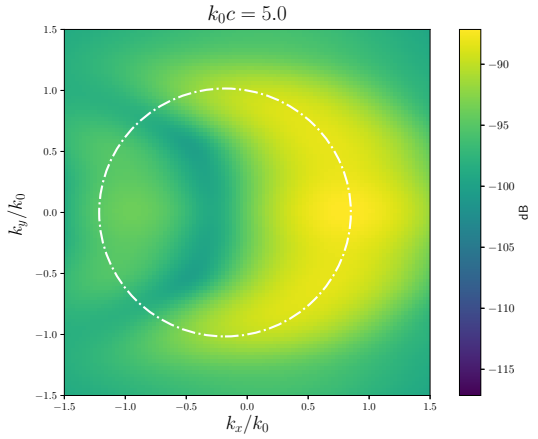

(b)

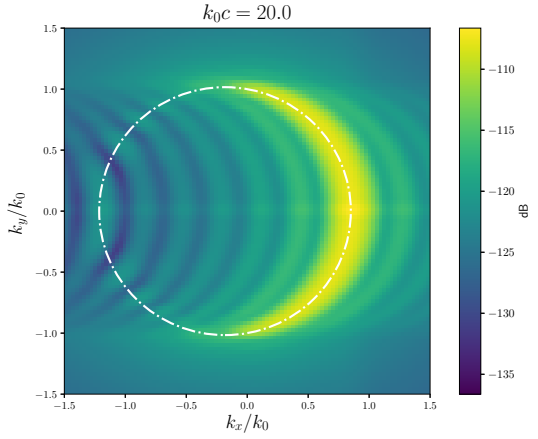

(c)

Figure 3.18: Auto-power spectral density magnitude in wavenumber domain: (a) low frequency ($k_0c = 0.5$); (b) medium frequency ($k_0c = 5$); (c) high frequency ($k_0c = 20$).

Chapter 4

Leading Edge Noise Radiation from a Flat Plate

In this Chapter we consider the acoustic field radiated by an aerofoil in a turbulent flow. The characteristics of the flat plate source distribution have been discussed in the previous chapter, and we now investigate the resulting acoustic radiation for single- and multiple-gust responses.

Repeating Equation 3.14, the cross-power spectral density $S_{pp'}(\mathbf{r}, \mathbf{r}', \omega)$ of the radiated acoustic field is related to the cross-power spectral density $S^{\Delta}_{qq'}(\mathbf{r}_s, \mathbf{r}'_s, \omega)$ of the surface pressure jump via the convected dipole transfer function $\partial G(\mathbf{r}|\mathbf{r}_s, \omega)/\partial z_s$:

$$S_{pp'}(\mathbf{r}, \mathbf{r}', \omega) = \int_{-d}^{+d}\int_{-b}^{+b}\int_{-d}^{+d}\int_{-b}^{+b} S_{\Delta p \Delta p'}(\mathbf{r}_s, \mathbf{r}'_s, \omega)\frac{\partial}{\partial z_s}G(\mathbf{r}|\mathbf{r}_s, \omega)\ldots \\ \ldots\frac{\partial}{\partial z'_s}G^*(\mathbf{r}'|\mathbf{r}'_s, \omega)\,\mathrm{d}x_s\,\mathrm{d}y_s\,\mathrm{d}x'_s\,\mathrm{d}y'_s.$$

For the predictions of the acoustic radiation, we compute the pressure jump response of the flat plate to a single vortical gust, with the gust amplitude obtained from the von Karman model (Eq. 3.44). If multiple gusts are being considered, the surface pressure cross-spectrum is calculated from each gust response, and the cross-spectra are summed. The radiated acoustic field is then calculated using an acoustic analogy approach, where the pressure jump at each point in the aerofoil surface is treated as the complex amplitude of an infinitesimal point dipole source. We then calculate the acoustic pressure or the acoustic cross-power spectrum at the desired observer locations by numerically integrating the contributions of each point dipole.

From this analysis, we identified three near-field mechanisms of the aerofoil radiation: the hydrodynamic near-field of the fundamental dipole sources; the geometric near-field; and the aerofoil acoustic response to subcritical gusts. We then analyse their acoustic radiation characteristics and discuss the conditions where they will influence acoustic measurements of aerofoils.

4.1 Single-Gust Acoustic Radiation

We now present some predictions of near- and far-field radiation at a single frequency $k_0 c = 5$, at which non-compactness effects are expected to be significant. The aerofoil geometry and flow characteristics follow the description given in Section 3.2.

We look into four separate single-gust cases:

1. Normal incidence gust: $k_\psi = 0$ (supercritical response);
2. Oblique incidence gust, $k_\psi = 0.35 k_\psi^{crit}$ (supercritical response);
3. Oblique incidence gust, $k_\psi = 0.75 k_\psi^{crit}$ (supercritical response);
4. Oblique incidence gust, $k_\psi = 1.25 k_\psi^{crit}$ (subcritical response).

Since a flat-plate aerofoil is symmetric over the $z = 0$ plane, its directivity patterns are identical in the $+z$ and $-z$ directions; hence, we will show only the radiation corresponding to the $+z$ directions.

As previously stated, these directivity patterns are associated with the wavenumber transform of the surface pressure jump evaluated inside the radiation ellipse, multiplied by the dipole windowing function $W_{dip}(k_x, k_y, \omega)$ (Eq. 2.112). The chordwise directivity (over the plane $y = 0$) is related to the wavenumber spectrum over the $k_y = 0$ line, while the spanwise directivity (over the plane $x = 0$) is related to the wavenumber spectrum over the $k_x = -k_{x1}$ line. For this particular frequency, the wavenumber spectrum is shown in Figure 3.10; one can then observe the correspondence between the number and location of the main lobe, nulls and sidelobes in the directivity plots shown in this Section and their corresponding entries in Figure 3.10.

4.1.1 Normal Incidence Gust, $k_\psi = 0$

For a normal-incidence harmonic gust, $k_\psi = 0$ and hence the aerofoil response is supercritical. The variation in pressure jump over the aerofoil surface is shown on Figure 4.1, with the real part shown on the left-hand side and the normalised magnitude shown in decibels on the right-hand side. As the aerofoil surface pressure jump has its spanwise variations determined by the spanwise gust wavenumber k_ψ, there are no spanwise variations in this case.

Figure 4.2 shows the acoustic pressure radiated near the aerofoil in the $y = 0$ and $x = 0$ planes; some non-compactness effects can be observed in the chordwise radiation, where the radiated field is clearly not uniform with angle. The sinc-like directivity in the spanwise direction ($x = 0$ plane) is also evident, indicating a strong radiation in the $x = 0$ plane and weaker radiation towards other spanwise directions. Note as well the dipole directivity effect, superimposing a null on the $z = 0$ plane in both images.

Figure 4.3 shows the flat plate far-field directivity obtained on these same planes, normalised against the maximum chordwise directivity value. Note that the directivity plots in the next sections will also be normalised against this value. The directional behaviour of the aerofoil radiation is easily observable, particularly the slightly stronger chordwise acoustic radiation in the downstream direction (i.e. towards the $+x$ direction). The shape of the spanwise directivity (the sinc function) is also clearly observable, with distinct main lobe, sidelobes and nulls.

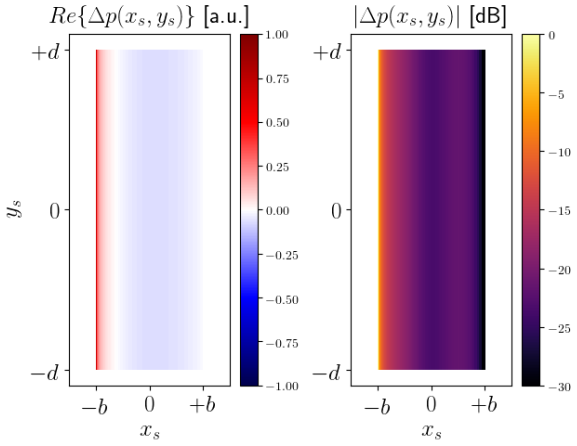

Figure 4.1: Surface pressure jump of a flat-plate aerofoil caused by a normal-incidence ($k_\psi = 0$) harmonic gust; real part (left-hand side), in arbitrary units, and absolute value (right-hand side), in normalised decibels.

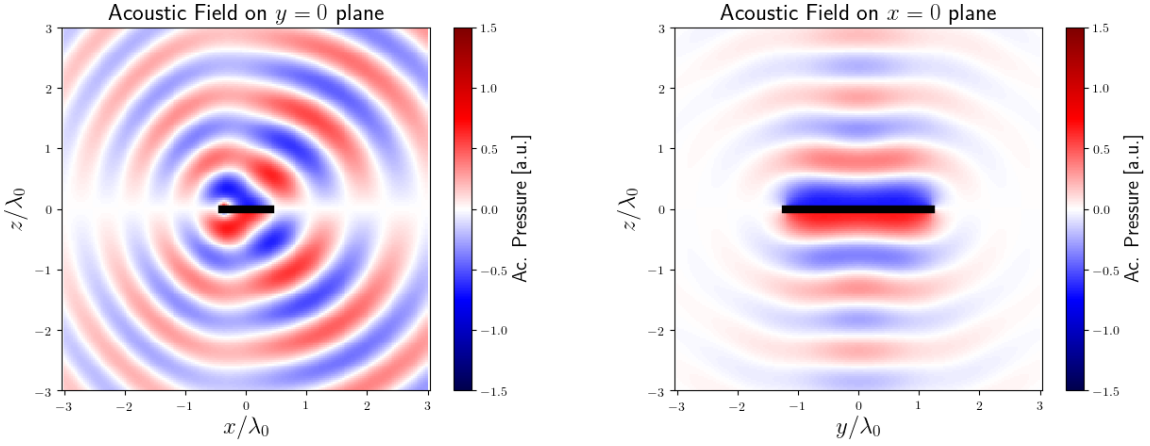

(a) **(b)**

Figure 4.2: Acoustic field simulation from leading edge radiation for a normal-incidence ($k_\psi = 0$) harmonic gust; (a) acoustic field on $y = 0$ plane; (b) acoustic field on $x = 0$ plane.

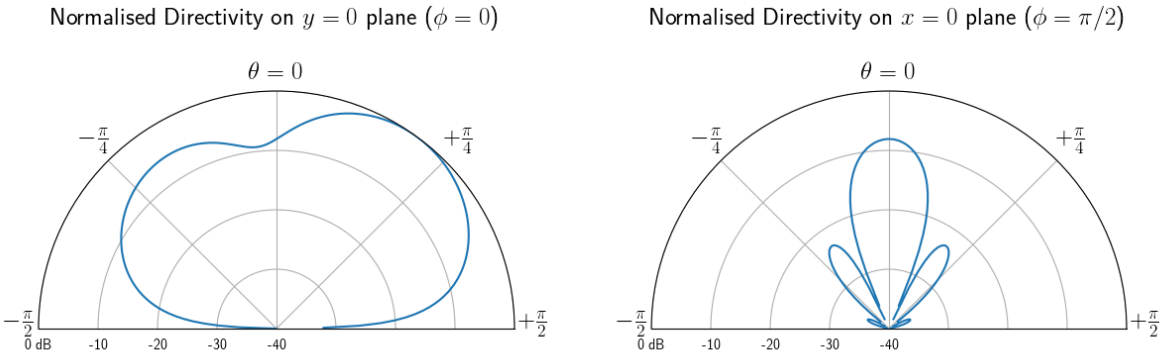

(a) **(b)**

Figure 4.3: Normalised far-field directivity simulation from leading edge radiation for a normal-incidence ($k_\psi = 0$) harmonic gust; (a) directivity on $y = 0$ plane; (b) directivity on $x = 0$ plane.

4.1.2 Oblique Incidence Gust, $k_\psi = 0.35 k_\psi^{crit}$

We now consider an oblique gust with spanwise wavenumber $k_\psi \approx 0.35 k_\psi^{crit}$, where the aerofoil response will be supercritical. The surface pressure jump over the aerofoil is shown in Figure 4.4, with the real part shown on the left-hand side and the normalised magnitude in decibels in the right-hand side. Note that now the aerofoil surface pressure jump spanwise variation follows the spanwise gust wavenumber component (of the form $e^{-jk_\psi y_s}$), as described before.

Figure 4.5 shows the acoustic pressure radiated around the aerofoil in the $y = 0$ and $x = 0$ planes. The general structure of the acoustic field over the $y = 0$ plane (left-hand side) is similar to the one shown for the normal-incidence case, despite the smaller amplitude; however, the acoustic field over the $x = 0$ plane (right-hand side) is quite different, with pronounced beaming effect towards an angle oblique to the aerofoil surface normal.

Figure 4.6 shows the flat plate far-field directivity obtained on these same planes, normalised by the maximum value for the $k_\psi = 0$ case. Note that the chordwise directivity now appears much smaller, since for this particular gust wavenumber the aerofoil directivity presents a null close to the $x = 0$ plane. The spanwise directivity, which is still similar to a sinc function, is now inclined and pointing at an angle $\theta > 0$; this is a direct consequence of the chosen spanwise wavenumber value $k_\psi > 0$. Due to symmetry, a spanwise wavenumber $k_\psi < 0$ would induce a sinc function-like directivity pointing at an angle $\theta < 0$.

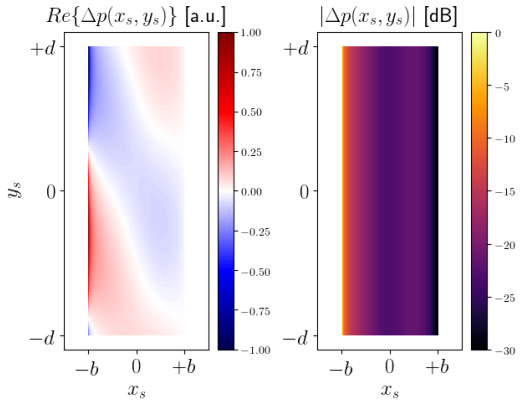

Figure 4.4: Surface pressure jump of a flat-plate aerofoil caused by an oblique-incidence ($k_\psi = 0.35k_\psi^{crit}$), supercritical harmonic gust; real part (left-hand side), in arbitrary units, and absolute value (right-hand side), in normalised decibels.

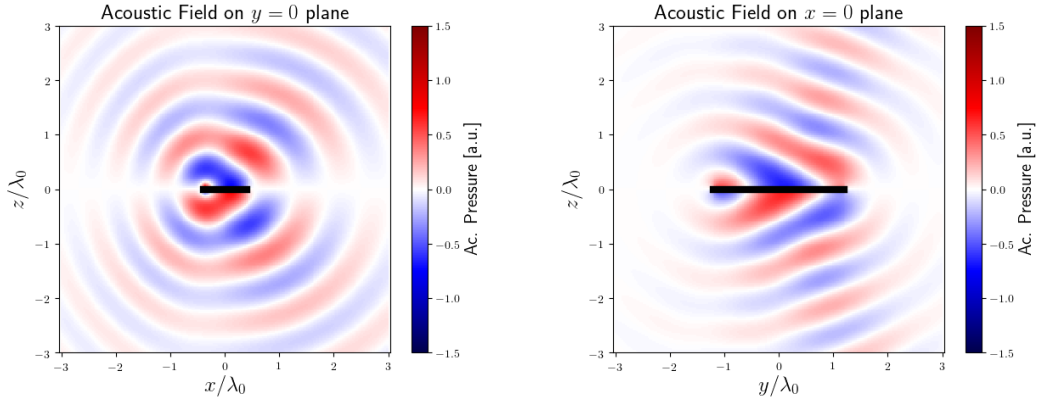

(a) **(b)**

Figure 4.5: Acoustic field simulation from leading edge radiation for an oblique-incidence ($k_\psi = 0.35k_\psi^{crit}$), supercritical harmonic gust; (a) acoustic field on $y = 0$ plane; (b) acoustic field on $x = 0$ plane.

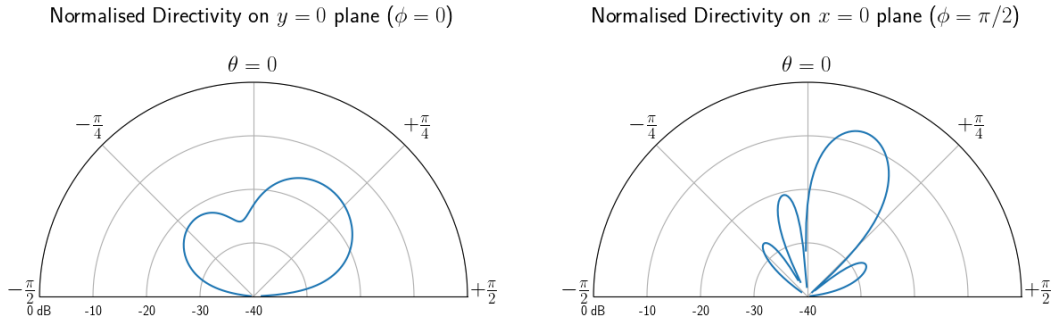

(a) **(b)**

Figure 4.6: Normalised far-field directivity simulation from leading edge radiation for an oblique-incidence ($k_\psi = 0.35k_\psi^{crit}$), supercritical harmonic gust; (a) directivity on $y = 0$ plane; (b) directivity on $x = 0$ plane.

4.1.3 Oblique Incidence Gust, $k_\psi = 0.75k_\psi^{crit}$

For the third case, we consider an oblique-incidence harmonic gust with spanwise wavenumber $k_\psi = 0.75k_\psi^{crit}$; hence, this gust is supercritical, but close to criticality.

The surface pressure jump over the aerofoil is now shown on Figure 4.7, with the real part shown on the left-hand side and the magnitude shown in decibels on the right-hand side. Note that again the aerofoil surface pressure jump spanwise variation follows the spanwise gust wavenumber component, of the form $e^{-jk_\psi y_s}$, as discussed before.

Figure 4.8 shows the acoustic pressure radiated around the aerofoil in the $y = 0$ and $x = 0$ planes, and Figure 4.9 shows the flat plate far-field directivity obtained on these same planes, normalised by the maximum value for the $k_\psi = 0$ case. We can now observe a greater difference between this case and the previous cases; the aerofoil is radiating towards a larger spanwise angle, with a few narrow sidelobes radiating towards the other directions on the $x = 0$ plane. There is once again a null close to the $y = 0$ plane, and thus the chordwise radiation is reduced in amplitude.

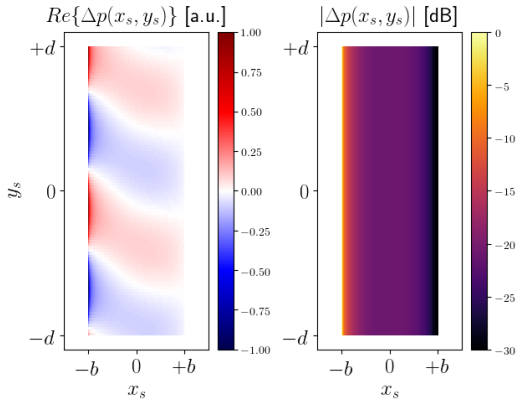

Figure 4.7: Surface pressure jump of a flat-plate aerofoil caused by an oblique-incidence ($k_\psi = 0.75k_\psi^{crit}$), supercritical harmonic gust; real part (left-hand side), in arbitrary units, and absolute value (right-hand side), in normalised decibels.

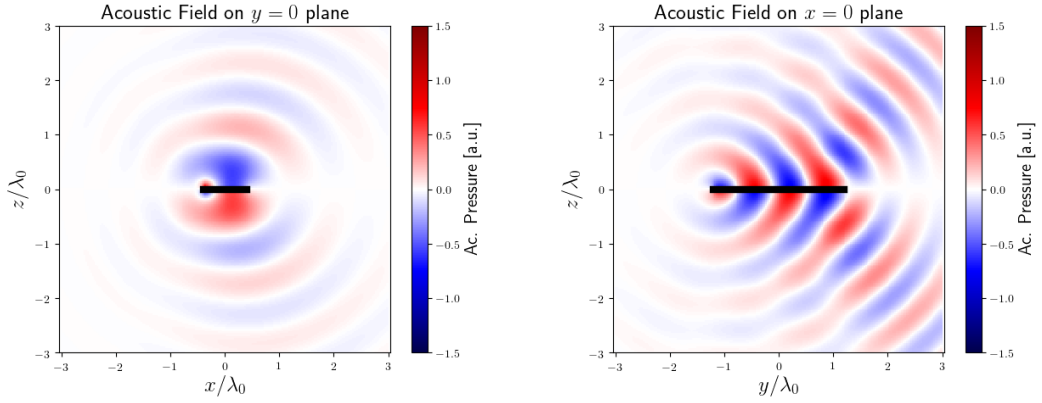

(a) **(b)**

Figure 4.8: Acoustic field simulation from leading edge radiation for an oblique-incidence ($k_\psi = 0.75k_\psi^{crit}$), supercritical harmonic gust; (a) acoustic field on $y = 0$ plane; (b) acoustic field on $x = 0$ plane.

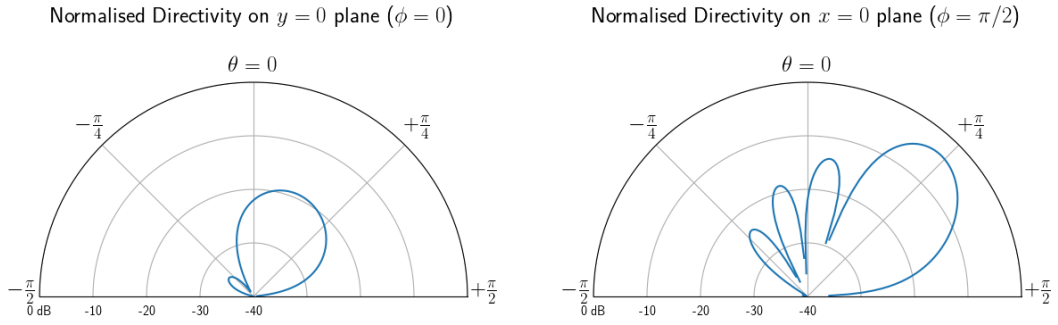

(a) **(b)**

Figure 4.9: Normalised far-field directivity simulation from leading edge radiation for an oblique-incidence ($k_\psi = 0.75k_\psi^{crit}$), supercritical harmonic gust; (a) directivity on $y = 0$ plane; (b) directivity on $x = 0$ plane.

4.1.4 Oblique Incidence Gust, $k_\psi = 1.25k_\psi^{crit}$

For the last case, we now consider an oblique-incidence harmonic gust with spanwise wavenumber $k_\psi = 1.25k_\psi^{crit}$; this gust response is subcritical.

The surface pressure jump over the aerofoil is shown in Figure 4.10, with the real part shown on the left-hand side and the magnitude shown in decibels on the right-hand side. As described before, the aerofoil surface pressure jump spanwise variation follows the spanwise gust wavenumber component, of the form $e^{-jk_\psi y}$; the behaviour of the pressure jump in the chordwise direction, however, presents an exponential decay towards the trailing edge, with a strong attenuation of the aerofoil response magnitude.

Figure 4.11 shows the residual acoustic pressure in the $y = 0$ and $x = 0$ planes. The aerofoil acoustic radiation is now much weaker compared to the previous cases, with the acoustic pressure negligible due to the exponential decay of the chordwise pressure jump coupled with the cancellation effects between adjacent spanwise regions of opposite phase. However, some weak acoustic radiation is still observed near the leading edge and near the span ends. As previously discussed, a finite-span aerofoil will have a radiating (and not evanescent) response to a subcritical gust, due to the incomplete cancellation effects at the span ends.

Figure 4.12 shows the flat plate far-field directivity obtained on these same planes, normalised by the maximum value for the $k_\psi = 0$ case. The chordwise directivity has significantly lower magnitude than previous cases at all chordwise angles, and the spanwise directivity displays a series of small, narrow sidelobes over the spanwise angles. Both directivities thus indicate this gust is an inefficient source of far-field sound.

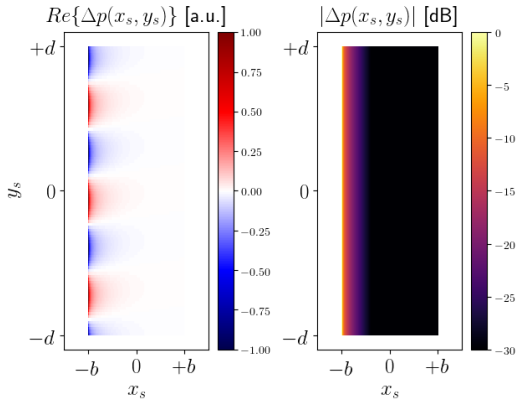

Figure 4.10: Surface pressure jump of a flat-plate aerofoil caused by an oblique-incidence ($k_\psi = 1.25k_\psi^{crit}$), subcritical harmonic gust; real part (left-hand side), in arbitrary units, and absolute value (right-hand side), in normalised decibels.

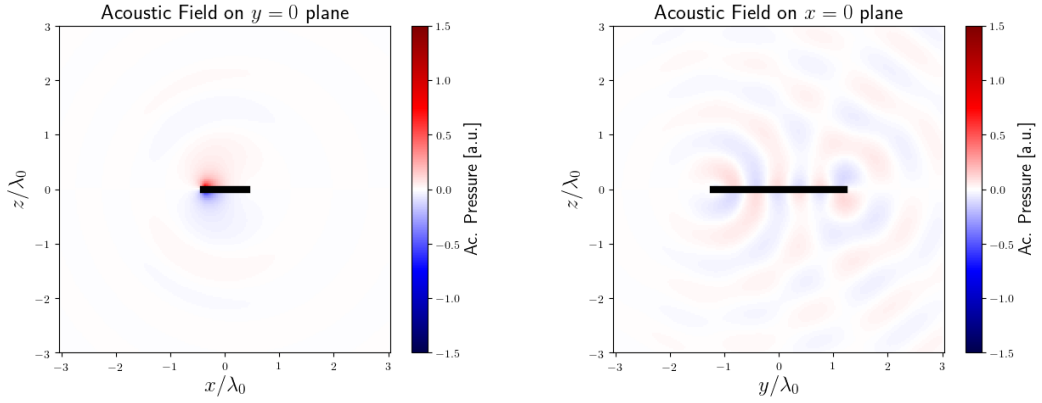

(a) **(b)**

Figure 4.11: Acoustic field simulation from leading edge radiation for an oblique-incidence ($k_\psi = 1.25k_\psi^{crit}$), subcritical harmonic gust; (a) acoustic field on $y = 0$ plane; (b) acoustic field on $x = 0$ plane.

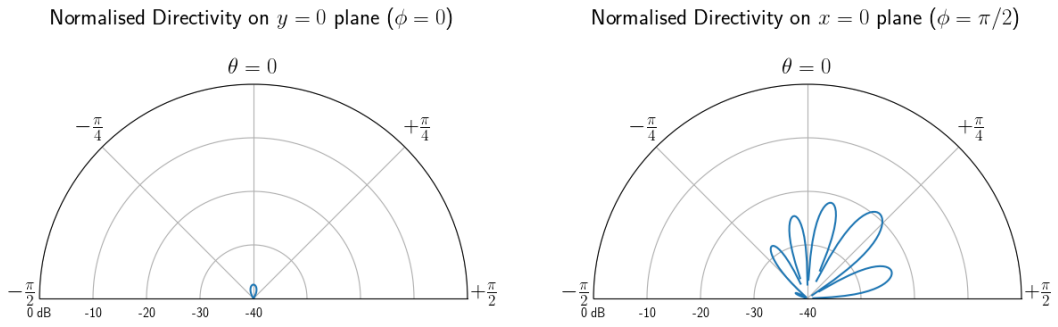

(a) **(b)**

Figure 4.12: Normalised far-field directivity simulation from leading edge radiation for an oblique-incidence ($k_\psi = 1.25k_\psi^{crit}$), subcritical harmonic gust; (a) directivity on $y = 0$ plane; (b) directivity on $x = 0$ plane.

4.2 Multiple-Gusts Acoustic Radiation

Simulation results are now presented for aerofoil radiation in response to multiple vortical gusts. We will adopt the same configuration (i.e. aerofoil geometry and flow properties) as described in Section 4.1 for single-gust radiation; however, we now integrate the contributions of gusts over a range of spanwise wavenumbers to calculate the surface pressure cross-spectrum, according to Eq. 3.10.

4.2.1 Gust Integration Limit for Acoustic Pressure Calculations

As we are now interested in the *acoustic* radiation of the aerofoil, it is not necessary to integrate the contributions of gusts up to the previously proposed wavenumber limit $k_\psi^{[-20]}$, as for the surface pressure calculations. This value, being reference-dependent and assuming values well above the critical gust limit k_ψ^{crit} for many conditions, includes the contributions of many gusts that are acoustically insignificant and is deemed excessive for acoustic radiation predictions.

In Section 3.2.3, it was shown that subcritical gusts are significant contributors to the acoustic radiation at low frequencies but cease to contribute at higher frequencies, where supercritical gusts are the main contributors to the radiated field. We can then consider a *low frequency* region, in which supercritical and subcritical gusts must be taken into account for predicting the acoustic field, and a *high frequency* region, in which only supercritical gusts are necessary. These regions are separated by a critical frequency f_{crit}, which we establish below.

In Section 3.1.3.1, the flat plate acoustic far-field was shown to have a sinc function-like dependence on the gust spanwise wavenumber k_ψ. The sinc function is shown in Figure 4.13 for an observer at mid-span, with its frequency-independent null locations indicated. We propose that gusts with wavenumbers in the range $k_\psi \in [-2\pi/d, +2\pi/d]$ (i.e. located within the sinc function main lobe and first sidelobes for an observer at mid-span) are significant contributors to the acoustic field and must be considered at all frequencies; these are indicated by the shaded region in Figure 4.13.

We can now determine the transition frequency f_{crit} by considering how the frequency-dependent critical gust wavenumber k_ψ^{crit} compares to the sinc function nulls:

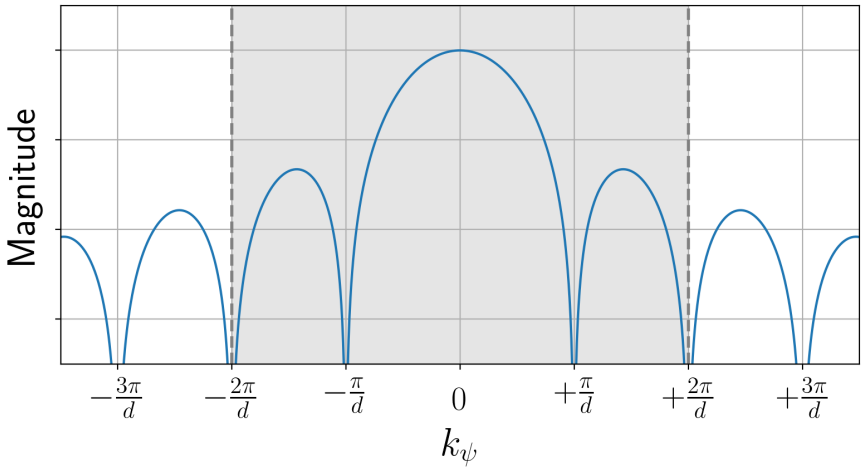

Figure 4.13: Spanwise sinc function in k_ψ domain, with region of significant gust responses shaded in grey; d is the aerofoil semi span.

- In the *low frequency region*, $k_\psi^{crit} < 2\pi/d$. Some wavenumbers in the proposed range will be subcritical in nature but still acoustically significant, and must be included in the predictions. The gust wavenumber integration limit will be $k_\psi^{max} = 2\pi/d$;
- At *high* frequencies, $k_\psi^{crit} \geq 2\pi/d$. All wavenumbers within the proposed range are supercritical, and there is satisfactory convergence considering supercritical gusts only. The gust wavenumber integration limit will be $k_\psi^{max} = k_\psi^{crit}$.

From Eq. 3.28, the transition frequency f_{crit} between the low- and high-frequency regions can be determined as where $k_\psi^{crit} = 2\pi/d$, which simplifies to

$$f_{crit} = \frac{c_0 \beta}{d}. \tag{4.1}$$

For the proposed conditions ($M_x \approx 0.17$ and $L = 2d = 0.45$ m), the transition frequency is $f_{crit} \approx 1487.4$ Hz, which is equivalent to $k_0 c \approx 4.12$.

4.2.2 Multiple-Gusts Normalised Directivities

Figures 4.14 to 4.16 show the chordwise (left-hand side) and spanwise (right-hand side) directivity patterns at frequencies $k_0 c \in [0.5, 5, 20]$ obtained when integrating the contributions of multiple gusts according to the above proposed rule. The plots were obtained from the

acoustic power spectral density $S_{pp}(\mathbf{r}, \omega)$ in Eq. 3.14, and are normalised against the largest magnitude observed in Figure 4.15a.

Figure 4.14 demonstrates the aerofoil radiates similarly to a point dipole source at low frequency $k_0 c = 0.5$, even when considering the contributions of multiple gusts. This indicates compactness effects of low-frequency radiation, as expected from the low normalised frequency value.

At medium frequency $k_0 c = 5$, Figure 4.15 begins to demonstrate non-compactness effects in both chordwise and spanwise directions. The chordwise directivity is very similar to the normal-incidence single-gust directivity shown in Figure 4.3a. This is expected, since it was shown that all other gusts will be beaming at different spanwise angles and thus will have very weak radiation in this plane. On the other hand, the spanwise directivity now contains the contributions of many different gusts radiating at different angles. The sum of all gust contributions yields a very different directivity pattern than those previously observed, with slightly stronger radiation towards angles slightly above $\theta = \pm\pi/4$ and very defined spanwise symmetry.

At high frequency $k_0 c = 20$, Figure 4.16 shows strong non-compactness effects, with both chordwise and spanwise directivity plots showing multiple lobes in a number of directions. The chordwise directivity is strongly asymmetric, while the spanwise directivity is symmetric.

Note that these far-field directivities are associated with the wavenumber-domain power spectrum shown in Figure 3.18. By considering the variations in the wavenumber spectrum magnitude inside the radiation ellipse across the $k_y = 0$ line, we can obtain the chordwise directivities (left-hand side of Figures 4.14 to 4.16), and by considering the variatins across the $k_x = -k_{x1}$ line, we can obtain the spanwise directivities (right-hand side of Figures 4.14 to 4.16).

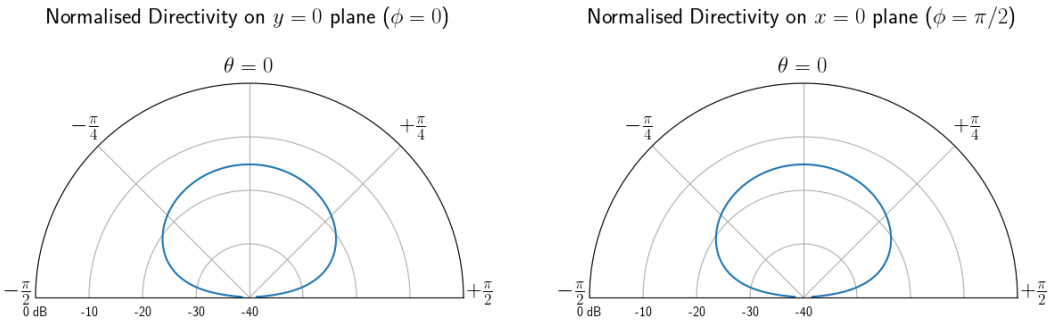

(a) **(b)**

Figure 4.14: Normalised far-field directivity simulation from leading edge radiation for multiple harmonic gusts at low ($k_0 c = 0.5$) frequency; (a) directivity in XZ plane; (b) directivity in YZ plane.

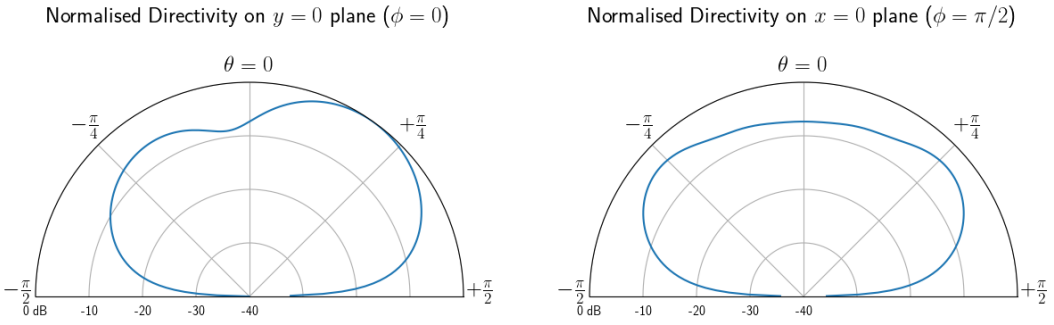

(a) **(b)**

Figure 4.15: Normalised far-field directivity simulation from leading edge radiation for multiple harmonic gusts at medium ($k_0 c = 5$) frequency; (a) directivity in XZ plane; (b) directivity in YZ plane.

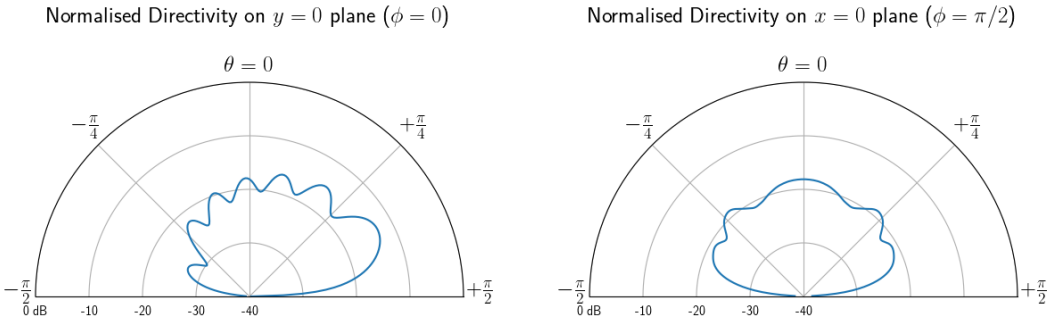

(a) **(b)**

Figure 4.16: Normalised far-field directivity simulation from leading edge radiation for multiple harmonic gusts at high ($k_0 c = 20$) frequency; (a) directivity in XZ plane; (b) directivity in YZ plane.

4.3 Comparing the Different Amiet Formulations for Near-Field Effects

We would now like to compare the different formulations for interaction noise predictions presented in Chapters 3 and 4 regarding their near-field effects, and investigate whether near-field effects should be expected for typical experimental conditions used in the ISVR anechoic wind tunnel.

4.3.1 Experimental Setup Description

The experimental setup for measuring aerofoil leading edge noise is described in more detail in Chapter 5, so we will briefly describe the main features of the experimental setup. A flat-plate aerofoil with chord $c = 0.15$ m and span $L = 0.45$ m is situated in a turbulent flow, with a mid-span, "far-field" microphone arc positioned at $R = 1.2$ m for chordwise directivity measurements, and a planar, "near-field" microphone array positioned at $z = -0.5$ m for beamforming measurements; see Figure 4.17. The mean flow speed is $U_x = 60$ m/s ($M_x \approx 0.17$). A turbulence-generating grid is installed at the wind tunnel nozzle, yielding a turbulence intensity of $T_i = 0.025$ and an integral length scale of $\Lambda = 0.007$ m. The von Karman spectrum for isotropic turbulence was found to adequately represent the observed velocity spectrum.

Let us compare the *predicted* acoustic power spectral density for an observer at mid-span, mid-chord at two distances, $R = 8c$ (1.2 m) and $R = 100c$ (15 m), with the *measured* acoustic PSD as seen by a mid-span, mid-chord microphone in the far-field arc (at $R = 1.2$ m). We compare three prediction formulations:

- the near-field, multiple-gust formulation (Eq. 3.14), which evaluates the integration over the spanwise wavenumber k_ψ and takes into account the effects of *multiple* gusts interacting with a *finite*-span aerofoil at each frequency;
- the far-field, single-gust formulation (Eq. 3.26), which considers the effect of a *single* gust interacting with an *infinite*-span aerofoil at each frequency;
- and a near-field, single-gust model, obtained by evaluating Eq. 3.14 at zero spanwise wavenumber ($k_\psi = 0$) only, which considers the effect of a *single* gust interacting with a *finite*-span aerofoil at each frequency.

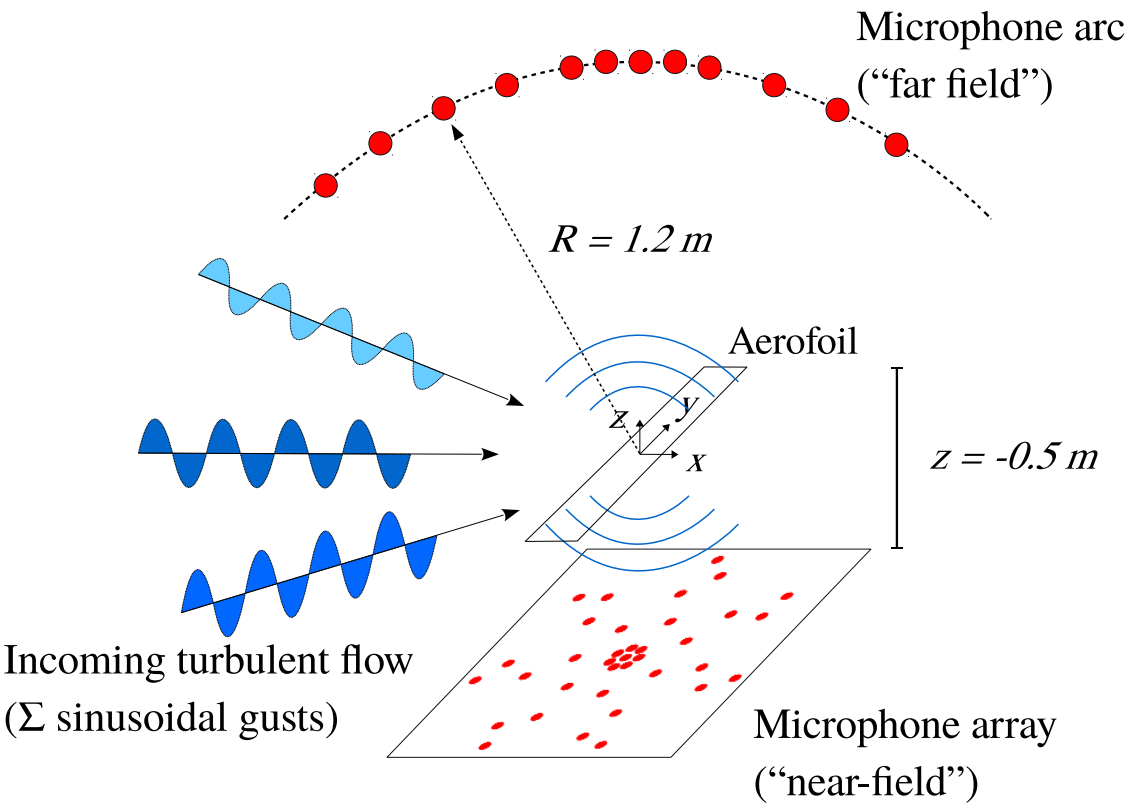

Figure 4.17: Typical experimental setup for interaction noise measurements: an aerofoil is exposed to a turbulent flow, with a mid-span, "far-field" microphone arc used for chordwise directivity measurements and a planar, "near-field" microphone array used for beamforming.

According to the flat plate radiation model presented in Chapter 3, gusts with $k_\psi = 0$ are the main contributors to the acoustic radiation for observers at mid-span ($y = 0$). Comparing the second and the third models allow us therefore to evaluate the validity of the geometric far-field approximation for the chosen measurement conditions.

As proposed by Clair et al. [15], an extra factor of $2\pi/(2d)$ is added when numerically evaluating the zero-spanwise-wavenumber spectrum $\Phi_{ww}(k_\chi, 0)$ (in Equation 3.14) for the single-gust, finite-span model. We can then obtain equivalent levels between single-gust and multiple-gust predictions.

It has been established in Section 3.1.3.1 that the far-field formulations for interaction noise prediction rely on the Fraunhofer far-field approximation, extensively discussed in Section 2.3. In order to evaluate whether these formulations are valid for the proposed measurement setup, we define the *Fraunhofer far-field distance limit* as

$$R_{FF} = \frac{2L^2}{\lambda}, \tag{4.2}$$

where L is the aerofoil span, and use it to determine whether the observer is in the geometric far-field or not.

4.3.2 Comparison of Measured and Predicted Results

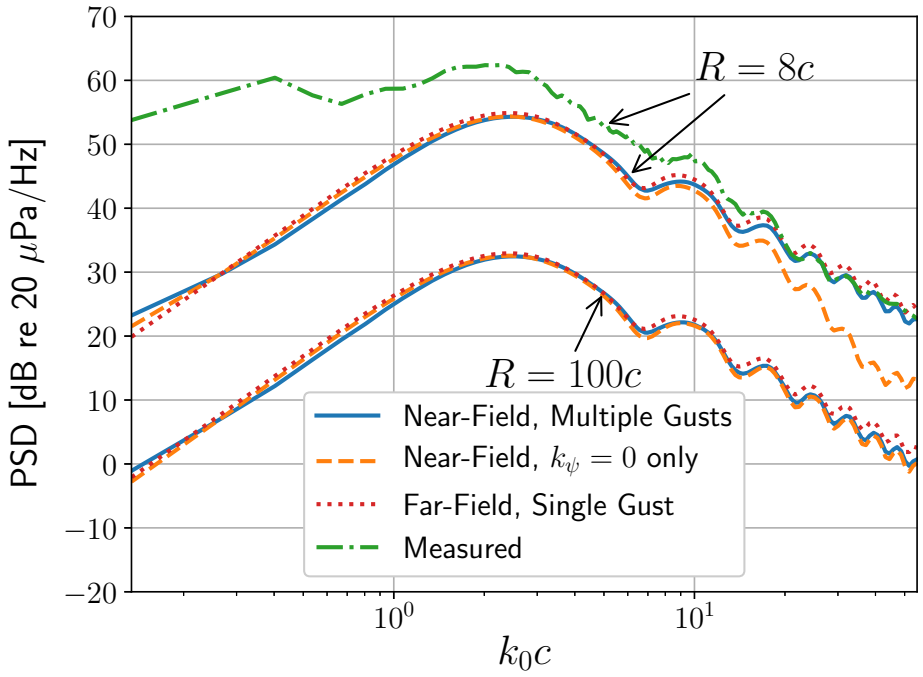

Figure 4.18: Prediction of acoustic PSD for mid-span microphone using different formulations: near-field, multiple-gust formulation (solid lines); near-field, $k_\psi = 0$ gust only formulation (dashed lines); and far-field, infinite-span approximation (dotted lines), for observers at $R = 8c$ (1.2 m) and $R = 100c$ (15 m) from the aerofoil. The measured PSD for an observer at $R = 8c$ is also shown (dash-dotted line) for reference. The frequency range shown in the Figure is approximately 50 Hz to 20 kHz.

The predicted PSD results for the three formulations are shown in Figure 4.18 for both observer distances, together with the measured PSD for the observer at $R = 8c$. The frequency range shown in the Figure is approximately 50 Hz to 20 kHz.

There is excellent agreement between all prediction models for the observer at $100c$ (15 m), with the near-field and far-field models collapsing well. However, according to Eq. 2.81, far-field conditions can be assumed at this distance for frequencies up to approximately 12.6 kHz ($k_0c \approx 35$), so in principle true geometric far-field conditions cannot be assuemd at the highest

frequencies of interest. Strikingly, the models still converge to very similar results at these frequencies, an indication that strict adherence to the Fraunhofer distance/frequency limit might not be necessary for adopting the far-field approximation.

For the observer at $8c$ (1.2 m), there are more significant differences between the predictions. A small discrepancy between the prediction models at low frequencies can be observed, where the far-field approximation underpredicts the PSD level by a few decibels when compared to the near-field models. This difference is likely to be due to the dipole hydrodynamic near field effect: the lowest frequency shown in Figure 4.18 is approximately 50 Hz, which is comparable to the $k_0\bar{r} = 1$ transition frequency given by Equation 2.99 (approximately 45 Hz). Note, however, how the measured PSD level is significantly above all prediction models at such low frequencies; it is known that wind tunnel measurements are often plagued by large levels of background noise at low frequencies, hence we assume such small level differences between the prediction methods at this frequency region are not significant for experimental purposes.

At middle and high frequencies the predictions and measurements display a much better agreement, with the "humps and dips" typical of aerofoil measurements visible on all curves. Note, for example, that the first two dips occur near $k_0c = 2\pi$ and $k_0c = 4\pi$ [7]. However, the near-field, single-gust ("$k_\psi = 0$ only") model diverges significantly from the far-field models at high frequencies, decreasing in amplitude as frequency increases. The level difference is seen to reach 3 dB at approximately $k_0c = 16.6$ ($f = 6$ kHz), indicating source non-compactness and possible near-field effects. A similar decrease in amplitude at high frequencies has been noted by Clair et al. [15] for the near-field, single-gust prediction model, who also pointed out possible near-field effects as a likely cause.

The frequency limit of the Fraunhofer approximation (Eq. 2.81) evaluated at the observer distance $R = 8c$ (1.2 m) yields a high frequency limit of approximately $f = 1$ kHz ($k_0c \approx 2.8$). The differences pointed out above could then be attributed to the observer entering the geometric near-field limit. However, as discussed above for the distant observer case, no apparent differences can be seen for frequencies near this limit, only significantly above it; this reinforces the idea of the Fraunhofer limit being useful as a general guideline, and not a strict rule.

Despite the far-field approximation yielding convergent results even when the Fraunhofer limit is not strictly obeyed, it must be noted that near-field effects are still apparent over a wide range of frequencies - even for an experimental setup designed to measure far-field directivities,

as the microphone arc described above. Therefore, it is recommended that experimenters be aware of near-field effects in measurements, especially above the Fraunhofer approximation frequency limit.

Strikingly, this near-field-related decrease in level is not observed when multiple gusts are included in the prediction. In fact, the multiple-gusts model presents very similar results to the far-field, infinite-span model and to the experimental measurements. Our hypothesis is that contributions from oblique ($k_\psi \neq 0$) gusts add up to the observed PSD level at mid-span, raising it to levels similar to the far-field, infinite-span PSD. However, this hypothesis has not been verified.

4.4 Acoustic Near-Field Effects from a Flat Plate

The previous section indicates that near-field effects should be expected for flat plate interaction noise over a wide frequency range, even for supposedly "far-field" measurement conditions. A more thorough investigation of when near-field effects occur and what are their consequences is therefore required.

As discussed in Section 2.3, we can assume an observer is in the *far-field* of a source when the sound field radiated by the source is locally perceived by the observer as a plane wave. However, the acoustic *near-field* can have more varied characteristics; these are summarised in Dowling and Ffowcs Williams [28], Kinsler et al. [32], Fahy [67], for example, from where we cite:

- The acoustic near-field presents an amplitude decay proportional to $1/R^2$, or higher inverse power;
- Acoustic energy can move between adjacent source regions instead of propagating towards the far-field, with the acoustic intensity vector often exhibiting circulatory patterns;
- The acoustic pressure and particle velocity are not in phase, and can be nearly in quadrature near vibrating surfaces;
- The acoustic impedance magnitude is lower than that of a plane wave due to larger particle velocities.

Hence, for our purposes, we choose to define the acoustic near-field of a source as *the region around the source, at a given frequency, where the far-field assumption is not applicable.* As one source can have multiple forms of near-field effects, there might be different spatial and frequency ranges for each type of near-field.

From the above definition, we identified three possible sources of near-field effects in the Amiet model for aerofoil leading edge noise. These are:

1. The fundamental dipole sources hydrodynamic near field, which affect the measurement results at very low frequencies;
2. The effect of subcritical gusts, which behave as "cut-off modes" of the aerofoil radiation and will yield an evanescent acoustic field in the infinite-span limit;
3. The geometric near-field effects, which can be observed at distances and frequencies where the Fraunhofer approximation is not valid.

We will now investigate how these effects might affect acoustic measurements of the aerofoil near-field radiation. We choose the centre microphone in the planar microphone array as the observer for this analysis. This microphone is located at a vertical distance of $R = 0.5$ m (approx. $3c$) below the aerofoil centre, as seen in Figure 4.17. Note that this distance is comparable to the aerofoil span ($L = 0.45$ m), which in principle invalidates the adoption of the Fraunhofer far-field approximation. With this observation in mind, we aim to investigate if R_{FF} can nevertheless function as a criterion for determining when the geometric far-field approximation can be successfully used.

4.4.1 Hydrodynamic Dipole Near-Field

The dipole hydrodynamic near-field was briefly discussed in Section 2.3.3. This source of near-field imposes a low-frequency limit on the far-field approximation, given by Equation 2.99. For typical wind tunnel experimental conditions, however, it is probably not a significant source of error, as it only affects very low frequencies - approximately 100 Hz for the observer at 0.5 m - where the signal-to-noise ratio is often already very poor due to the measurement rig background noise.

The hydrodynamic dipole near-field could significantly affect the results when using measurements techniques which benefit from very short distances from the aerofoil surface, such as Near-field Acoustical Holography and its variations.

4.4.2 Subcritical Gusts and Finite Span Effects

We now discuss the effects of subcritical gusts on the aerofoil acoustic radiation. The analysis by Graham [65] points towards subcritical gusts being minor contributors to the far-field sound, given their evanescent nature in the infinite-span approximation, and hence perhaps significant contributors to the aerofoil near-field sound. However, we will discuss how *finite*-span aerofoils do not generate a fully evanescent acoustic field. Indeed, in some frequency ranges, subcritical gusts might contribute significantly to the acoustic field and must be taken into consideration.

In order to analyse the overall behaviour of different gusts, we plot the relative PSD at the centre microphone of the near-field array, at 0.5 m. We use the near-field model of Equation 3.14, but evaluated at each single oblique gust k_ψ/k_ψ^{crit} separately.

Figures 4.19, 4.20 and 4.21 show the single-gust PSD magnitude as a function of spanwise gust wavenumber k_ψ at normalised frequencies $k_0c = 0.5$, $k_0c = 5$ and $k_0c = 20$, respectively. To illustrate our analysis, we also plot a series of spanwise cross-sections ($x = 0$ plane, distances normalised to the half span d) of the amplitude-normalised acoustic pressure at the spanwise wavenumbers $k_\psi = 0$ (supercritical), $k_\psi = 0.5k_\psi^{crit}$ (supercritical), $k_\psi = 0.9k_\psi^{crit}$ (supercritical, close to critical) and $k_\psi = 2k_\psi^{crit}$ (subcritical). These spanwise wavenumbers are marked in the plot with triangles, and each acoustic pressure cross-section plot is linked to its respective marker by an arrow.

4.4.2.1 Low Normalised Frequency ($k_0c = 0.5$)

The results shown in Figure 4.19 demonstrate that the aerofoil behaves as a compact source at this frequency. The different gusts can be seen to generate very similar acoustic fields, with no apparent preferred radiation direction. The PSD magnitude displays a slow variation as a function of k_ψ, with subcritical gusts generating PSD levels at the observer location that are comparable to those generated by supercritical gusts, despite their fundamentally different aerodynamic responses.

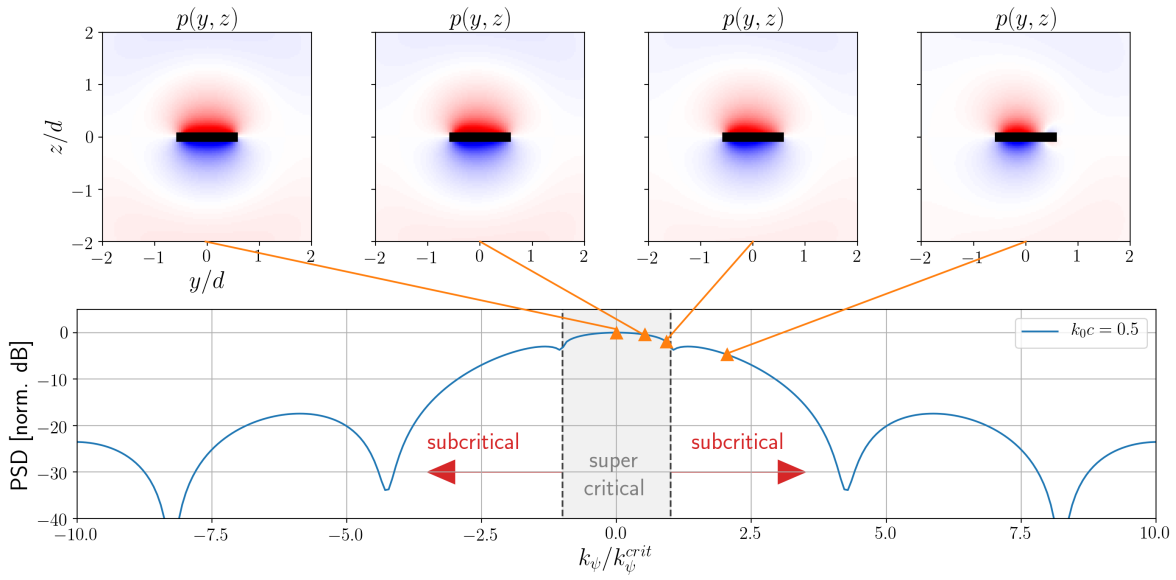

Figure 4.19: Bottom: prediction of acoustic PSD for observer at mid-span, $R = 0.5$ m, normalised chordwise frequency $k_0c = 0.5$, as a function of spanwise wavenumber k_ψ (normalised to k_ψ^{crit}, vertical dashed lines); PSD magnitudes have been normalised to their maximum value. Top: cross-section of the radiated acoustic field in the $x = 0$ plane for single-gust excitation at spanwise wavenumbers $k_\psi = 0$, $k_\psi = 0.5k_\psi^{crit}$, $k_\psi = 0.9k_\psi^{crit}$ and $k_\psi = 2k_\psi^{crit}$; spatial coordinates are normalised to the half-span d, and the acoustic field is shown in arbitrary units.

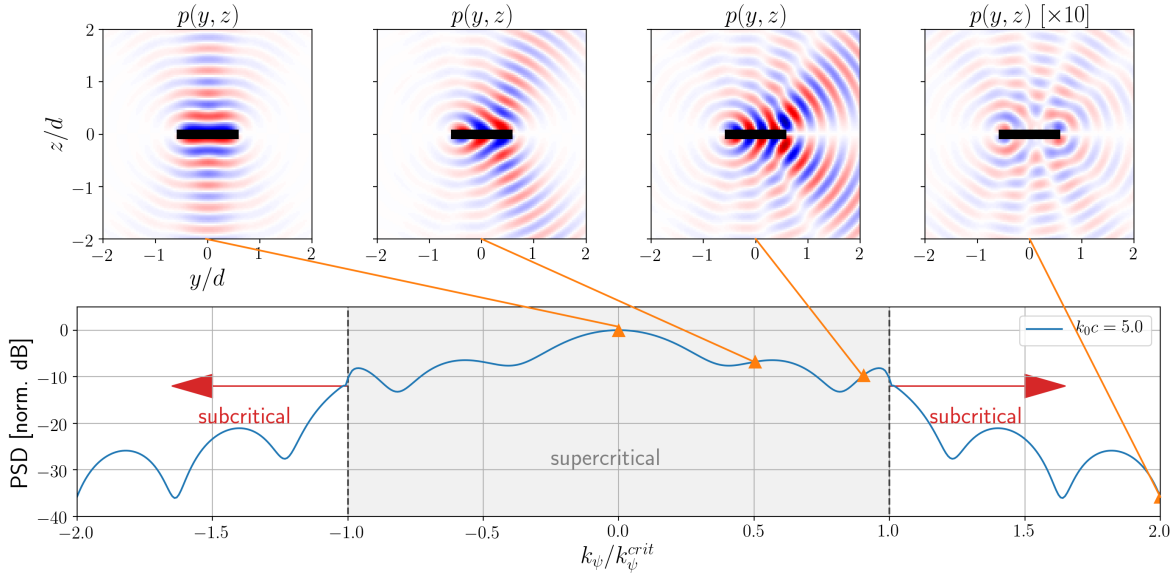

Figure 4.20: Bottom: prediction of acoustic PSD for observer at mid-span, $R = 0.5$ m, normalised chordwise frequency $k_0c = 5$, as a function of spanwise wavenumber k_ψ (normalised to k_ψ^{crit}, vertical dashed lines); PSD magnitudes have been normalised to their maximum value. Top: cross-section of the radiated acoustic field in the YZ plane for single-gust excitation at spanwise wavenumbers $k_\psi = 0$, $k_\psi = 0.5k_\psi^{crit}$, $k_\psi = 0.9k_\psi^{crit}$ and $k_\psi = 2k_\psi^{crit}$; spatial coordinates are normalised to the half-span d, and the acoustic field is shown in arbitrary units; the acoustic pressure amplitude in the rightmost plot has been increased ten times for better visibility.

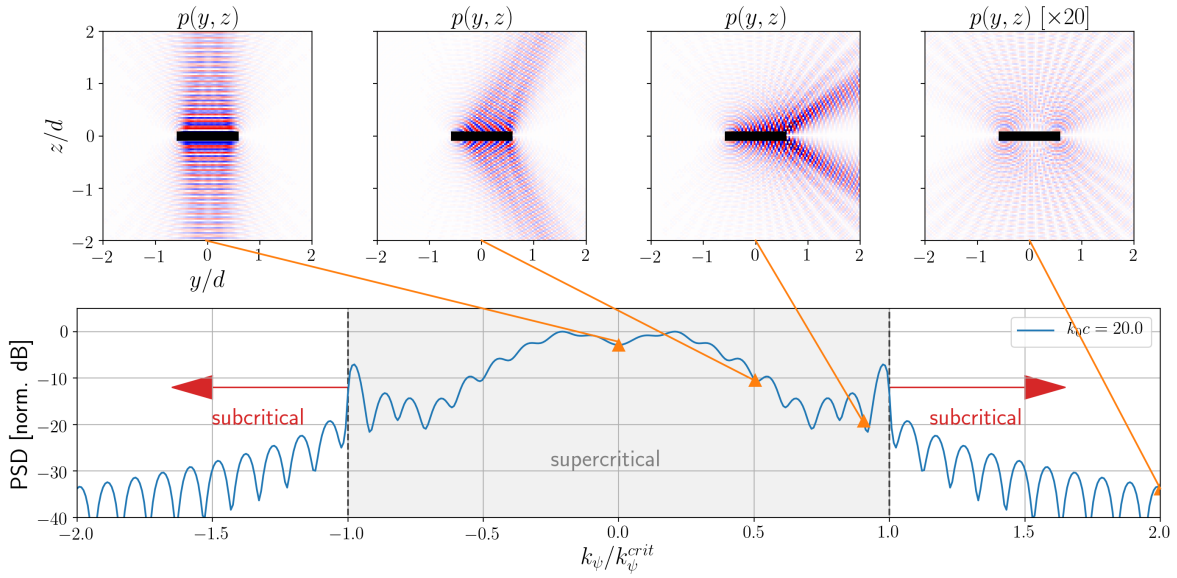

Figure 4.21: Bottom: prediction of acoustic PSD for observer at mid-span, $R = 0.5$ m, normalised chordwise frequency $k_0c = 20$, as a function of spanwise wavenumber k_ψ (normalised to k_ψ^{crit}, vertical dashed lines); PSD magnitudes have been normalised to their maximum value. Top: cross-section of the radiated acoustic field in the YZ plane for single-gust excitation at spanwise wavenumbers $k_\psi = 0$, $k_\psi = 0.5k_\psi^{crit}$, $k_\psi = 0.9k_\psi^{crit}$ and $k_\psi = 2k_\psi^{crit}$; spatial coordinates are normalised to the half-span d, and the acoustic field is shown in arbitrary units; the acoustic pressure amplitude in the rightmost plot has been increased twenty times for better visibility.

Despite the geometric far-field approximation not being strictly applicable at distances comparable to the aerofoil span, the observer is beyond the Fraunhofer far-field distance limit $R_{FF} \approx 0.21$ m (Eq. 4.2) at this frequency and we will therefore use the far-field formulation to interpret some of the general trends in the results. The plot of the PSD versus k_ψ clearly presents the expected sinc-like behaviour, with the $k_\psi = 0$ being the largest contributor to the radiated sound. However, at this frequency, the sinc function main lobe width is much wider than the far-field "visible region" determined by $[-k_\psi^{crit}, +k_\psi^{crit}]$, and some subcritical wavenumbers can be seen to contribute significantly to the acoustic PSD at the observer - even reaching levels comparable to that of supercritical gusts.

When evaluating multiple-gust acoustic radiation at low frequencies, we proposed in Section 4.2.1 to consider the contributions of all gusts located within the main lobe and the first sidelobes of the sinc function (i.e. $|k_\psi/k_\psi^{crit}| < 8$ in Fig. 4.19, approximately). Here it can be seen that gust wavenumbers beyond this limit will contribute less than -20 dB to the PSD at the observer (relative to the maximum level), and therefore can be safely ignored.

4.4.2.2 Medium Normalised Frequency ($k_0 c = 5$)

Figure 4.20 shows the same plots for $k_0 c = 5$ (approx. 1.8 kHz), where now the aerofoil begins to show non-compactness effects. The Fraunhofer far-field limit at this frequency is $R_{FF} \approx 2.1$ m, so the observer at 0.5 m is technically in the geometric near-field region. The sinc-like behaviour of the PSD over k_ψ is still apparent, and the $k_\psi = 0$ gust is still the largest contributor to the observed PSD. However, the nulls between the lobes are not as pronounced - an indicator of increasing near-field effects.

Another feature of this Figure are the small "peaks" observed near the critical hydrodynamic wavenumbers $\pm k_\psi^{crit}$. This type of behaviour is often present when acoustic sources transition between radiating and non-radiating behaviours [67]. It appears to indicate that, despite the far-field aerofoil response for such gusts present stronger acoustic radiation away from an observer at mid-span, near-critical gusts are still significant contributors to the acoustic radiation at mid-span.

The acoustic pressure cross-sections show interference effects between adjacent areas of the aerofoil, which lead to the formation of beams and nulls in the acoustic field at specific spanwise angles, as predicted by the sinc-function-like directivity in the far-field model. It is visible how different gusts "beam" towards and contribute more strongly in certain spanwise observer locations, and how the range between $[-k_\psi^{crit}, +k_\psi^{crit}]$ corresponds to radiation angles in the range $[-90°, 90°]$ - i.e. the "visible" region. Note, however, that the dipole directivity cancels out most of the acoustic radiation for spanwise angles close to $\pm 90°$, creating nulls in the acoustic field at these directions.

The acoustic pressure cross-section for the subcritical gust response ($k_\psi = 2k_\psi^{crit}$, rightmost plot) show significant cancellation effects across the entire aerofoil span, and its induced PSD is shown to be almost 40 dB lower than that of the $k_\psi = 0$ gust. In fact, the acoustic pressure amplitude shown in the figure is increased ten times relative to the other plots in order to improve visibility. One striking feature of this plot is the strong cancellation effects around the aerofoil centre, but not at the edges. This incomplete cancellation effect is responsible for the decreasing but fundamentally non-evanescent (i.e. propagating) character of the finite-span aerofoil response to subcritical gusts, where most of the radiation is generated at the tips of the distributed source.

4.4.2.3 High Normalised Frequency ($k_0c = 20$)

Figure 4.21 shows a normalised frequency of $k_0c = 20$ (approx. 7.2 kHz). At this frequency, the aerofoil is a non-compact source, and the observer is well below the Fraunhofer distance $R_{FF} \approx 8.6$ m at this frequency. The PSD does not display a sinc-like behaviour in k_ψ any longer, the supercritical region is now almost completely smeared, and gusts other than $k_\psi = 0$ have become the largest contributors to the PSD. These are strong indicators that the observer is located within the source near-field.

The peaks near the critical wavenumbers k_ψ^{crit} are now more prominent. We have found that these peaks determine the largest spanwise wavenumber k_ψ that still contribute significantly to the acoustic radiation at higher frequencies, with gusts $k_\psi > k_\psi^{crit}$ not being significant contributors of sound at the observer location any more.

The overall beaming behaviour of the single-gust response can again be seen in the acoustic pressure cross-sections, with even stronger beaming effects. For the subcritical gust, the cancellation effect is severe enough that the acoustic pressure amplitude shown in the figure is increased twenty times relative to the other plots to improve visibility in the Figure. However, the response is again showing incomplete cancellation effects at the tips. This tip radiation is clearly non-evanescent and will eventually reach an observer in the far-field, although likely at insignificant levels.

4.4.3 Geometric Near-Field Effects

We will now consider how the acoustic field predicted with the near-field, multiple-gust model and with the far-field, single-gust model behave as a function of observer distance R. We will calculate the acoustic pressure PSD over a vertical line at mid-chord, mid-span, over distances between $0.001R_{FF}$ and $100R_{FF}$.

Figure 4.22 shows the PSD decay with distance for the near-field, multiple-gust formulation in Equation 3.14 (thick lines) and for the far-field, single-gust formulation of Equation 3.26 (thin lines), at the three chordwise normalised frequencies $k_0c = 0.5$, $k_0c = 5$ and $k_0c = 20$ previously considered. Note that the Fraunhofer distance R_{FF} is frequency-dependent, therefore the absolute distances are not directly comparable between the different frequencies.

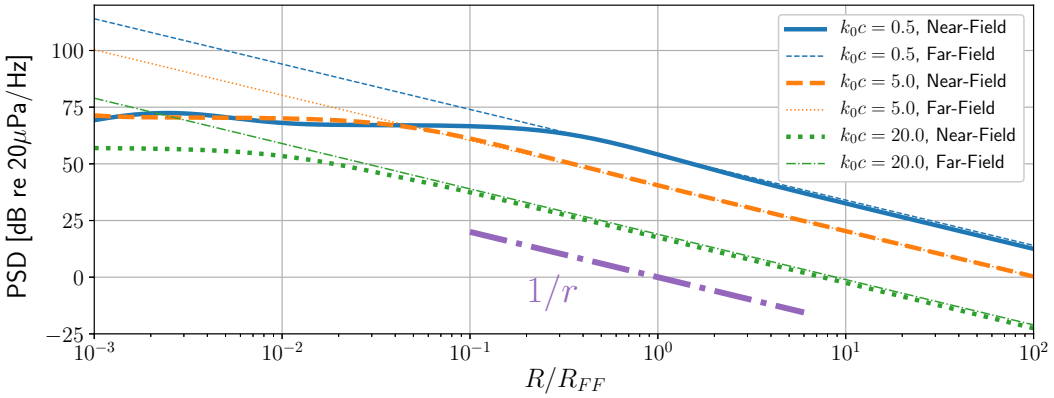

Figure 4.22: Acoustic PSD magnitude decay as a function of vertical distance R from aerofoil with far-field approximations (thin lines) and without far-field approximations (thick lines), at normalised frequencies $k_0c = 0.5$ (solid, thick and dashed, thin blue lines), $k_0c = 5$ (dashed, thick and dotted, thin orange lines) and $k_0c = 20$ (dotted, thick and dash-dotted, thin green lines). Distances are normalised to the Fraunhofer far-field distance $R_{FF} = 2L^2/\lambda$; note that R_{FF} is frequency dependent, and thus the absolute distances are different for each normalised frequency.

As expected, the acoustic PSD decays proportionally to $1/R$ for observer distances larger than R_{FF}, displaying good agreement with the far-field, infinite-span model; as distance becomes much shorter than R_{FF}, the far-field and the near-field models diverge, with the far-field model maintaining its $1/R$ slope. Contrary to the descriptions of near-field in the literature presented above, however, the magnitude decay of the near-field model does not follow a $1/R^2$ or higher inverse-power decay close to the source. Instead, the magnitudes appear to converge to a roughly constant level independent of distance. The relative distance at which the PSD behaviour transition from stationary to decaying also appears to change with frequency.

Figure 4.23 extends the above analysis for single-gust responses at the spanwise wavenumbers $k_\psi = 0$, $k_\psi = 0.5k_\psi^{crit}$, $k_\psi = 0.9k_\psi^{crit}$ and $k_\psi = 2k_\psi^{crit}$, evaluated at the same three normalised frequencies. Since the observer is at mid-span, the $k_\psi = 0$ gust is expected to be the main contributor to the pressure field. The microphone array height relative to the aerofoil ($R = 0.5$ m) is also marked in the Figures with a black arrow for reference.

For the low frequency case ($k_0c = 0.5$) in Figure 4.23a, both supercritical and subcritical gust responses present similar levels and distance decay behaviour, in agreement with the previous discussions for compact, finite-span aerofoils. Each individual response presents a $1/R$ decay for distances above R_{FF}, but ceases to decay at distances smaller than R_{FF} and converge to a steady level. None of the gust responses present regions with $1/R^2$ or higher inverse-power decay. As previously discussed, although the observer distance is greater than the Fraunhofer distance limit R_{FF}, it is also comparable to the source length, so it is not clear whether the

approximation is indeed valid. Nevertheless, the results seem to indicate that the Fraunhofer distance limit is an adequate estimate of far-field behaviour threshold at this frequency range, at least regarding the aerofoil response pressure decay.

For the medium frequency case ($k_0 c = 5$) in Figure 4.23b, a different behaviour can be observed in the supercritical oblique ($k_\psi = 0.5k_\psi^{crit}$ and $k_\psi = 0.9k_\psi^{crit}$) gusts responses. Their PSD curves change from a constant level in the near-field to an inverse-power decay higher than $1/R$ (but under $1/R^2$) below the Fraunhofer distance R_{FF}, and then change to a $1/R$ rate further away. The supercritical, oblique gust responses levels are similar to the parallel gust response in the near-field, although their responses reach a lower level in the far-field. Similarly, the subcritical gust ($k_\psi = 2k_\psi^{crit}$) presents a much lower PSD than the supercritical gusts over all distances, despite not presenting $1/R^2$ decay trends. The actual observer distance is now below R_{FF}, indicating the far-field approximation might be innacurate.

For the high frequency case ($k_0 c = 20$) in Figure 4.23c, the parallel gust response now presents some magnitude oscillations in the near-field. There is now a distinct near-field region where the oblique, supercritical gust responses present a level decay with a higher inverse-power than $1/R$ - and for the $k_\psi = 0.5k_\psi^{crit}$ case, higher than $1/R^2$ over a short region - before reaching a constant region at shorter ranges. Again, it can be expected that oblique gusts might contribute significantly to the aerofoil acoustic near-field. The subcritical gust does not reach a steady level at short distances, but instead its PSD appears to decay proportionally to R. The actual observer distance is below R_{FF}, and therefore the far-field approximation is not valid for this distance and frequency.

As a final observation, note that all subcritical gust responses exhibit a $1/R$ decay in the far-field, although at very low levels for medium and high frequencies; an exponential decay with distance, as would be expected from an infinite-span aerofoil, is not observed in any of the plots. Therefore, one can conclude that finite-span aerofoils responding to subcritical gusts do not exhibit exponentially decaying acoustic fields, but instead exhibit propagating acoustic fields that reach the far-field [7]. The relative importance of subcritical gusts responses to the overall sound level is clearly frequency-dependent, and the results presented above indicate that they are not significant contributors of sound at medium and high frequencies.

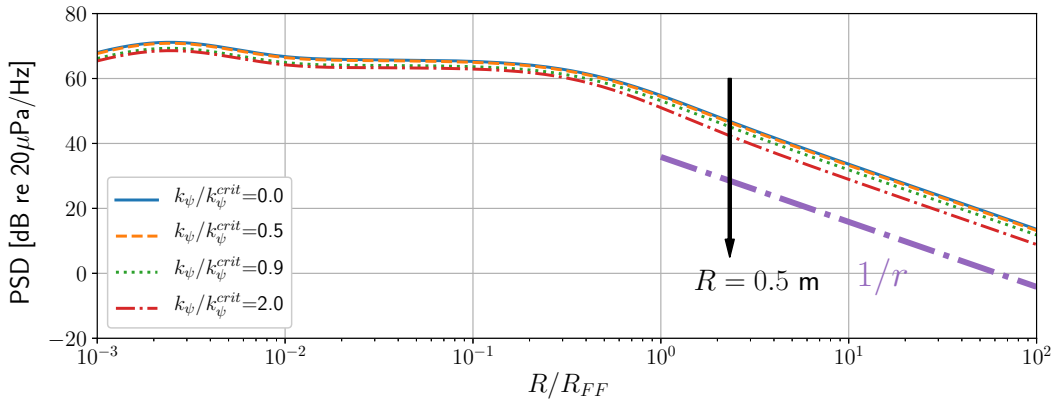

(a)

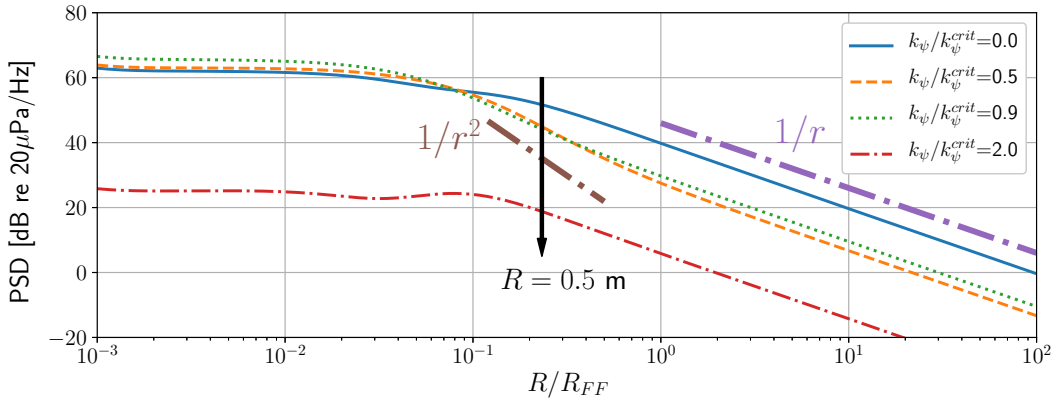

(b)

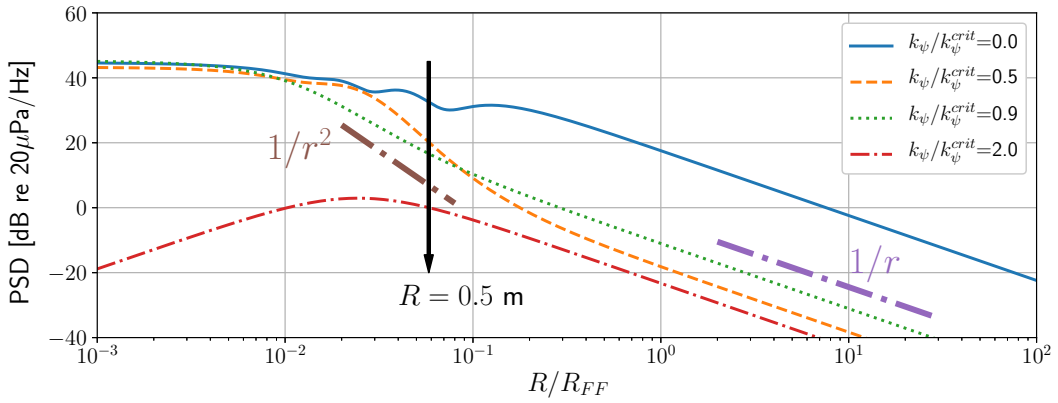

(c)

Figure 4.23: Acoustic PSD magnitude decay as a function of vertical distance R from aerofoil for different gusts; distances are normalised to the Fraunhofer far-field distance $R_{FF} = 2L^2/\lambda$.(a) Normalised frequency $kc = 0.5$; (b) normalised frequency $kc = 5$; (c) normalised frequency $kc = 20$.

Chapter 5

Experiments

This chapter describes the experiments aimed at validating the interaction noise prediction models presented in Chapter 4. A diagram of the experimental setup can be seen in Figure 4.17 (repeated here from p. 116). A flat-plate aerofoil is situated in a turbulent flow, and its radiated acoustic pressure is measured with two microphone array systems: a mid-span, "far-field" microphone arc positioned at $R = 1.2$ m, and a planar, "near-field" microphone array positioned at $z = -0.5$ m.

5.1 Wind Tunnel Experimental Setup

5.1.1 The Wind Tunnel

The measurements were performed in the ISVR Large Anechoic Chamber using the DARP Open Jet Facility. The ISVR Large Anechoic Chamber [68] is a box-within-a-box construction, and its internal walls, floor and ceiling are covered in 0.91 m-long glass-fibre cored wedges. The wedges allow for free-field conditions inside the chamber above 80 Hz, and result in internal usable dimensions of $7.33 \times 7.33 \times 5.50$ m. A grid of metal floor panels is generally used above the floor wedges to provide mechanical support with minimum acoustic disturbance of the sound field.

The DARP Open Jet Facility [69] is a low-noise, low-turbulence wind tunnel, with its working section located inside the ISVR Large Anechoic Chamber. It was originally designed to facilitate aerofoil trailing edge self-noise measurements by providing a very low level of background

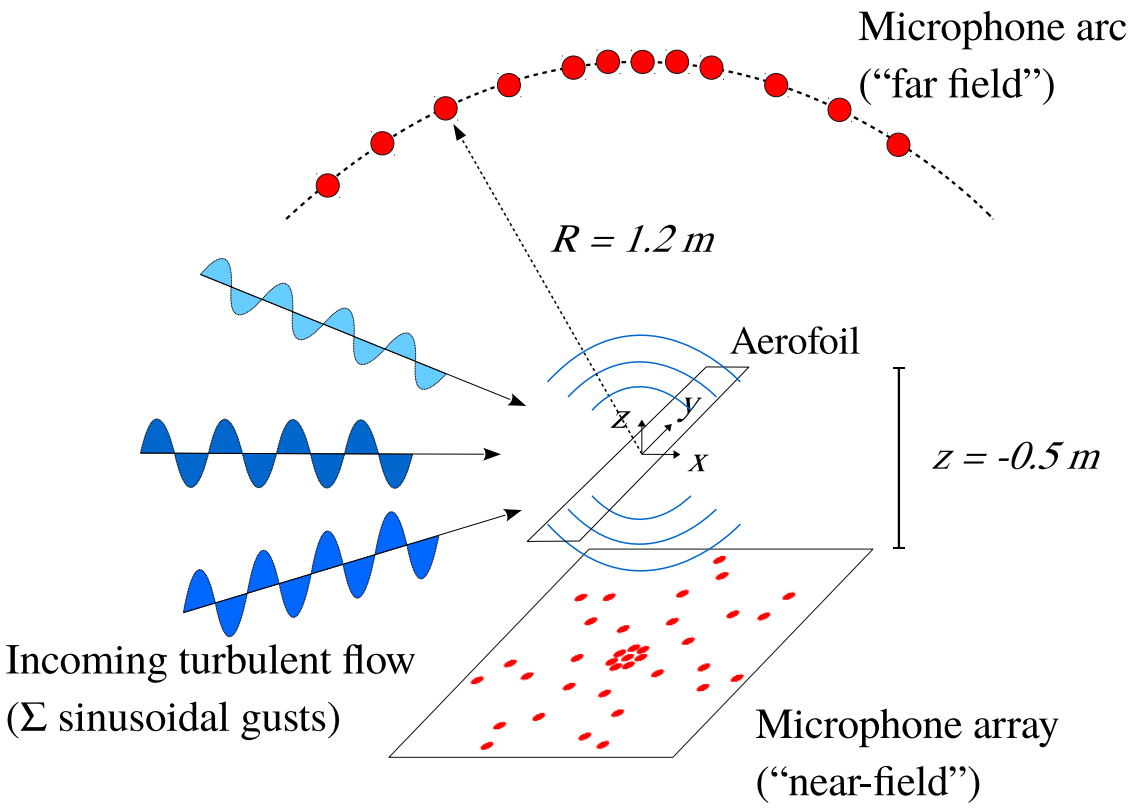

Figure 4.17 (repeated from p. 116): Typical experimental setup for interaction noise measurements: an aerofoil is exposed to a turbulent flow, with a mid-span, "far-field" microphone arc used for chordwise directivity measurements and a planar, "near-field" microphone array used for beamforming.

noise, while at the same time providing a very low turbulence flow so the noise generated by the interaction of the aerofoil leading edge with turbulent incoming flow is eliminated.

Turbulent flows can also be achieved by introducing a turbulence-generating grid in the nozzle. Aerofoil noise predictions were performed using a flow speed of $U_x = 60$ m/s. The turbulence intensity and integral length scale were measured using hot-wire anemometry and found to be $T_i = 0.025$ and $\Lambda = 0.007$ m, respectively [70]. The turbulence wavenumber spectrum for the noise prediction methods was modelled using the von Karman model for isotropic turbulence (previously introduced in Section 3.1.5), using the parameters described above as input.

The wind tunnel nozzle, with dimensions of 0.15 x 0.45 m, also holds two sideplates used to fix the aerofoil within the mean flow. Figure 5.1 shows a photograph taken during the experiments showing the setup described above.

The air temperature T_C was measured inside the chamber with a thermometer, and used to calculate the speed of sound $c_0(T_C)$ using Eq. 2.2.

Figure 5.1: Photograph of the experimental setup; the aerofoil is attached to the wind tunnel nozzle, and the near-field microphone array is visible underneath it.

5.1.2 The Aerofoils

The aerofoils tested were a a metal flat plate, a NACA651210 aerofoil, and a NACA0012 aerofoil, all with $L = 0.45$ m span. All aerofoils were tested at 20 m/s, 40 m/s and 60 m/s flow speed, at different angles of attack and with either straight or serrated leading edges attached. All aerofoils had their boundary layer tripped using a strip of rough sandpaper attached near the leading edge on both sides of the aerofoils to ensure a turbulent boundary layer, which would cause trailing edge noise. The full list of measurement cases and air temperatures is shown in Table 5.1.

5.1.3 The Far-Field Microphone Arc

The open jet wind tunnel was equipped with a mid-span, "far-field" microphone arc positioned above the aerofoil at 1.2 m and used to observe chordwise spectra and directivity of the aerofoils under study. This array is not visible in Figure 5.1, but is indicated in Figure 4.17.

The microphones are B&K Type 4189, with 1/2" diameter and are arranged in a circular arc at 1.2 m from the centre of the aerofoil, covering a range of emission angles between

Table 5.1: List of measurement cases for aerofoil noise measurement.

Case Number	Aerofoil	Angle of Attack	LE Type	Turbulence Grid	Temp. [°C]
01	NACA651210	5°	Straight	Yes	14.9
02	NACA651210	0°	Straight	Yes	14.5
03	NACA651210	0°	Serrated	Yes	13.7
04	NACA651210	5°	Serrated	Yes	13.6
05	NACA0012	0°	Straight	Yes	13.5
06	NACA0012	10°	Straight	Yes	13.5
07	Flat plate	0°	Straight	Yes	13.5
08	Flat plate	0°	Serrated	Yes	13.4
09	NACA651210	5°	Serrated	No	12.0
10	NACA651210	0°	Serrated	No	12.0
11	NACA0012	0°	Straight	No	12.2
12	NACA651210	0°	Straight	No	12.2
13	NACA651210	5°	Straight	No	12.3
14	Flat plate	0°	Straight	No	12.3
15	Flat plate	0°	Serrated	No	12.3

40° and 140° relative to the flow direction. The microphones were connected to a National Instruments acquisition card and sampled at $f_s = 50$ kHz. The microphone signal amplitudes were calibrated using a 1 kHz, 1 Pa RMS reference signal from a B&K Type 4231 calibrator. Only a small part of this data will be presented in this Thesis.

5.2 Near-Field Microphone Array Measurements

In addition to the typical wind tunnel experimental setup described above, we also included a planar microphone array for measuring the aerofoil acoustic "near-field" and apply beamforming methods to estimate the aerofoil source distribution. The array was positioned at 0.5 m below the aerofoil, with the centre microphone visually aligned with the aerofoil mid span. The array can be seen in the experiment diagram (Fig. 4.17) and in the photograph of the experimental setup (Fig. 5.1).

The array geometry was an Underbrink multi-arm spiral array with 36 electret microphones, comprising 7 spiral arms with 5 microphones each, plus one extra microphone added at the centre of the array. The Underbrink design [27, 71] is a modified multi-arm spiral array: an odd number of logarithmic spirals are traced over the array plane with uniform angular separation, and the microphones are then positioned at specific arc lengths over each spiral so that each microphone samples an equal-area aperture. This design results in a denser packing of sensors at larger radii when compared to an equal-arc-length sampling, effectively weighting

this region of the array more heavily than the smaller radii. This type of spatial weighting is known to decrease the maximum sidelobe level while slightly increasing the main lobe width, which tends to produce arrays with better broadband performance [27].

An Underbrink array can be designed from the maximum and minimum microphone radii r_{max} and r_0, the number of spiral arms N_a (odd by definition), the number of microphones per spiral N_m (excluding the extra central microphone), and the spiral angle α. The circular area containing the microphones is divided into $N_m - 1$ equal area annuli, which are further subdivided into N_a equal area segments each. The microphones are then positioned at the centre of these segments, and an extra inner circle of microphones is added at the minimum radius r_0 to improve the high frequency behaviour.

Following the formulation described in Prime and Doolan [71], the polar coordinates $(r_{m,n}, \theta_{m,n})$ over the array surface for the m-th microphone positioned over the n-th spiral are given by

$$r_{m,1} = r_0, \tag{5.1}$$

$$r_{m,n} = r_{max}\sqrt{\frac{2n-3}{2N_m-3}}, \tag{5.2}$$

for $m = 1, \ldots, N_a$ and $n = 2, \ldots, N_m$, and

$$\theta_{m,n} = \frac{\ln\left(r_{m,n}/r_0\right)}{\cot(\alpha)} + \frac{m-1}{N_a}2\pi, \tag{5.3}$$

for $m = 1, \ldots, N_a$ and $n = 1, \ldots, N_m$. As mentioned above, we have also added one extra microphone at the origin of the coordinate system in the centre of the array.

The parameter values adopted to design the array are shown on Table 5.2, and the resulting microphone positions are given in Table 5.3. A diagram of the full microphone array, with its spirals traced for visual reference, can be seen on Figure 5.2.

It should be noted that there was an error in the code to transform the microphone positions from polar to Cartesian coordinates, and thus the array shown here has its spirals "rotating" in the clockwise direction, in opposition to the ones commonly shown in the literature which

Table 5.2: Microphone array design parameters

Min. radius [m]	r_0	0.025
Max. radius [m]	r_{max}	0.25
No. of arms	N_a	7
Mics per arm	N_m	5
Spiral angle [rad]	α	$6\pi/14$

Table 5.3: Microphone coordinates (in centimetres)

Mic Number	x-coord	y-coord	Mic Number	x-coord	y-coord	Mic Number	x-coord	y-coord
01	0	0	13	2.184	-9.193	25	-21.072	-1.553
02	2.5	0	14	8.124	-14.208	26	-24.318	-5.799
03	8.477	4.175	15	6.203	-20.198	27	-0.556	2.437
04	12.044	11.082	16	11.065	-22.418	28	-5.957	7.335
05	18.311	10.542	17	-2.252	-1.085	29	-13.484	9.276
06	19.394	15.776	18	-5.825	-7.44	30	-14.352	15.506
07	1.559	-1.955	19	-6.043	-15.21	31	-19.696	15.397
08	8.549	-4.024	20	-11.924	-17.443	32	1.559	1.955
09	16.173	-2.507	21	-10.628	-22.628	33	2.021	9.231
10	19.659	-7.743	22	-2.252	1.085	34	-1.155	16.326
11	24.426	-5.327	23	-9.449	-0.084	35	3.174	20.889
12	-0.556	-2.437	24	-15.659	-4.759	36	-0.242	24.999

"rotate" in the counter-clockwise direction. This minor mistake has no influence on the array performance.

The array was built on a 60 × 60 cm, 1 cm-thick plywood board. The microphones positions were marked on the board surface, which was then drilled manually creating 1 cm-diameter holes. The microphones used in this array were *OBO Pro.2* model *OBO-04FP-0A-1F0* electret condenser capsules, which were mounted flush to the plywood board surface and fixed using hot melt adhesive. The capsules were connected to 3 m-long coaxial cables with added heat-shrink tubing, polarised via 10 kΩ resistors and connected to a custom-made multi-channel microphone amplifier providing a polarising voltage of 5 V. The amplifiers were set to a gain of 20 dB ref 1 V/V on all channels.

The amplifier outputs were then connected via balanced cables to a rack of five *RME ADI-8 DS* analog-to-digital converters. The converters were connected via ADAT cables to an *RME ADI-648* MADI/ADAT converter, which was in turn connected via MADI cables to an *RME MADIface USB* interface. The interface was connected via USB cable to a laptop computer running *Adobe Audition 3.0* to record the microphone signals at a chosen sampling frequency of 48 kHz. Each measurement was made over 30 s.

The planar array microphone signal amplitudes were calibrated using a 1 kHz, 1 Pa RMS reference signal from a B&K Type 4230 calibrator positioned above each microphone. It

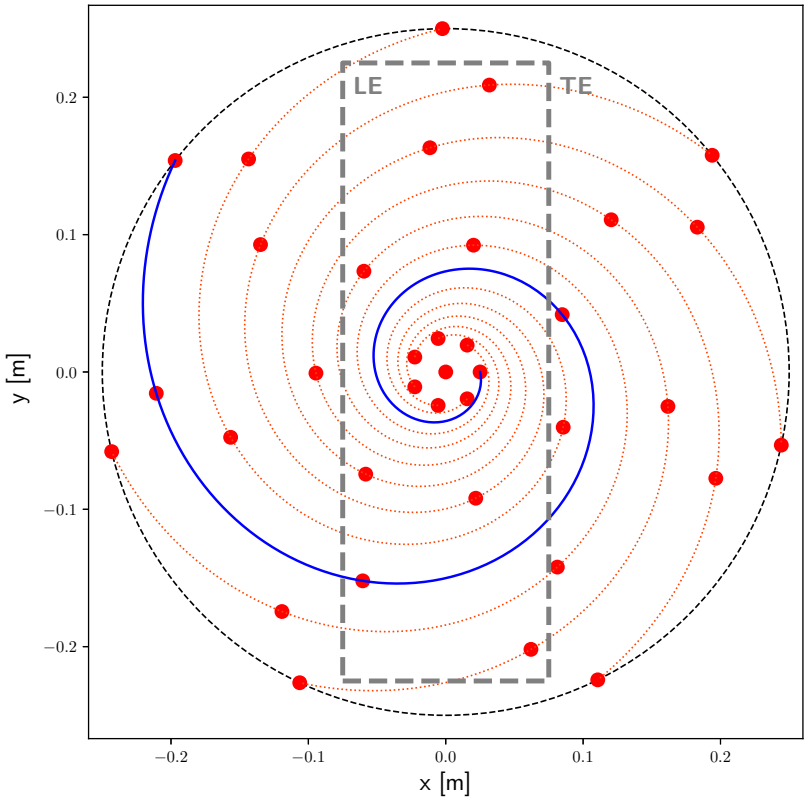

Figure 5.2: Top-down view of Underbrink multiarm spiral array, with its spirals traced for visual reference. The aerofoil position is indicated with the thick, dashed lines.

should be noted that the microphone capsules were *not* inserted into the calibrator cavity for recording the reference signals, as is standard procedure; instead, the calibrator was positioned on the array baffle, on top of each microphone at a time. This calibration is therefore not expected to be very accurate, and errors of a few decibels should be expected.

5.3 Acoustic Cross-Spectral Density Results

The array was used to measure the cross-spectral characteristics of the acoustic pressure at the different microphone locations. We choose to investigate the microphones numbered 32 to 36: these microphones are positioned at increasing spanwise coordinate y, as shown in Figure 5.3, and can be used to determine whether the spanwise behaviour of the radiated near-field also follows the far-field characteristics described by the Amiet model in Chapter 3. We investigate their power spectral density magnitude, and cross-spectral density phase and coherence - the latter two using the centre microphone as the phase reference.

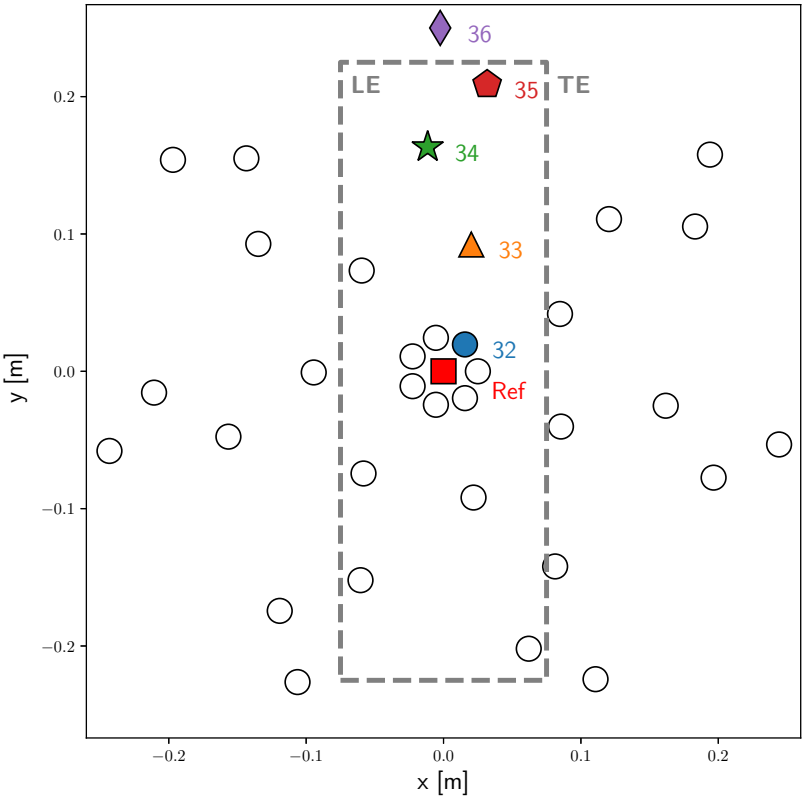

Figure 5.3: Selected microphones in planar array for spanwise (y direction) acoustic field analysis. The aerofoil position is indicated with the thick, dashed lines.

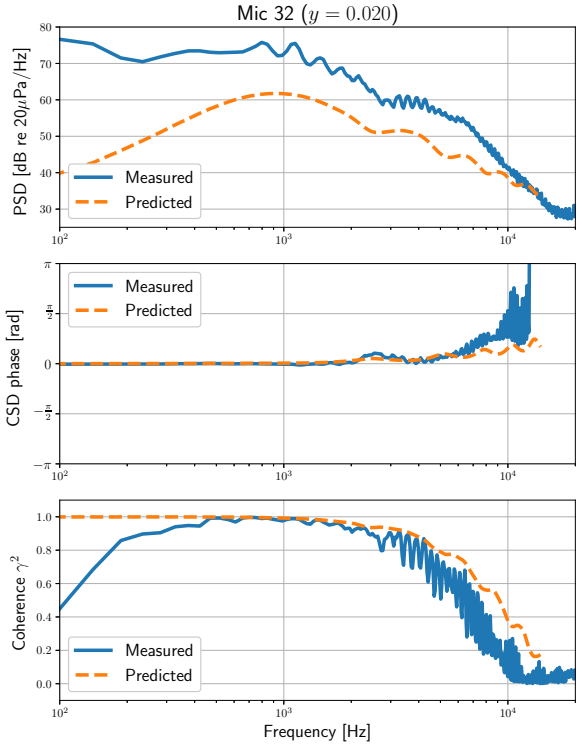

Figure 5.4: Predicted and measured PSD magnitude (dB re 20μPa/Hz), unwrapped CSD phase (rad) and coherence γ^2 (ref mic 1) as a function of frequency for microphone 32 ($y = 0.020$ m).

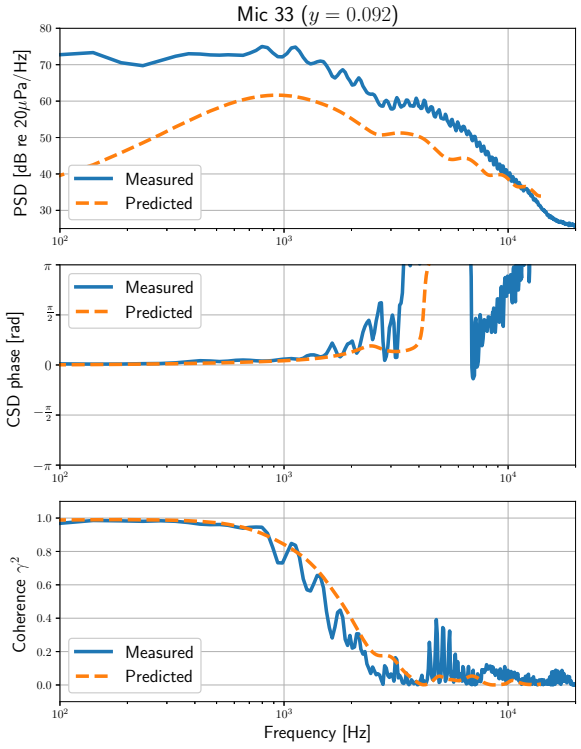

Figure 5.5: Predicted and measured PSD magnitude (dB re 20μPa/Hz), unwrapped CSD phase (rad) and coherence γ^2 (ref mic 1) as a function of frequency for microphone 33 ($y = 0.092$ m).

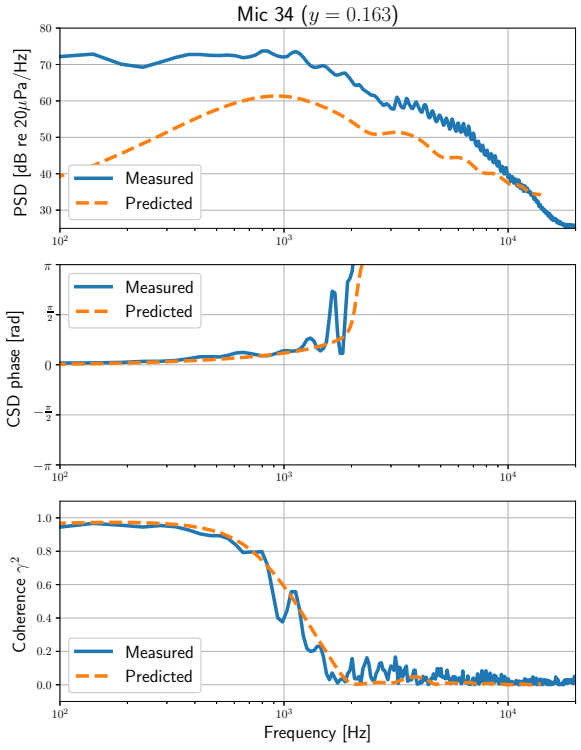

Figure 5.6: Predicted and measured PSD magnitude (dB re 20μPa/Hz), unwrapped CSD phase (rad) and coherence γ^2 (ref mic 1) as a function of frequency for microphone 34 ($y = 0.163$ m).

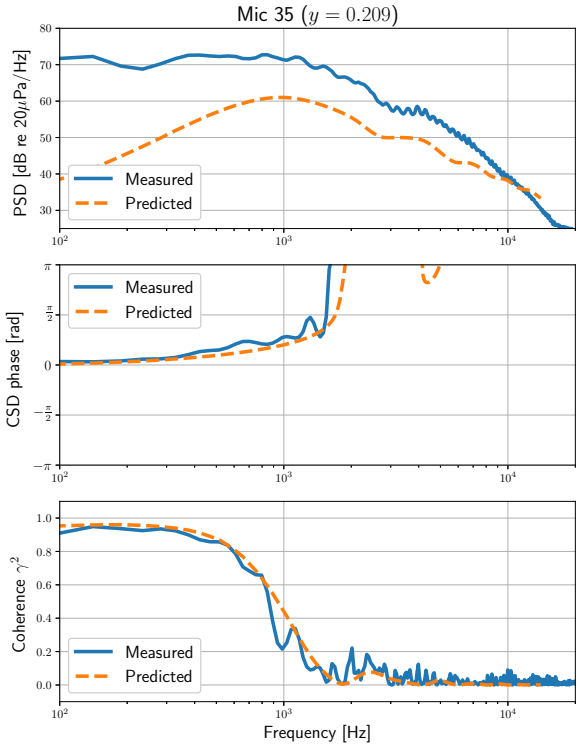

Figure 5.7: Predicted and measured PSD magnitude (dB re 20μPa/Hz), unwrapped CSD phase (rad) and coherence γ^2 (ref mic 1) as a function of frequency for microphone 35 ($y = 0.209$ m).

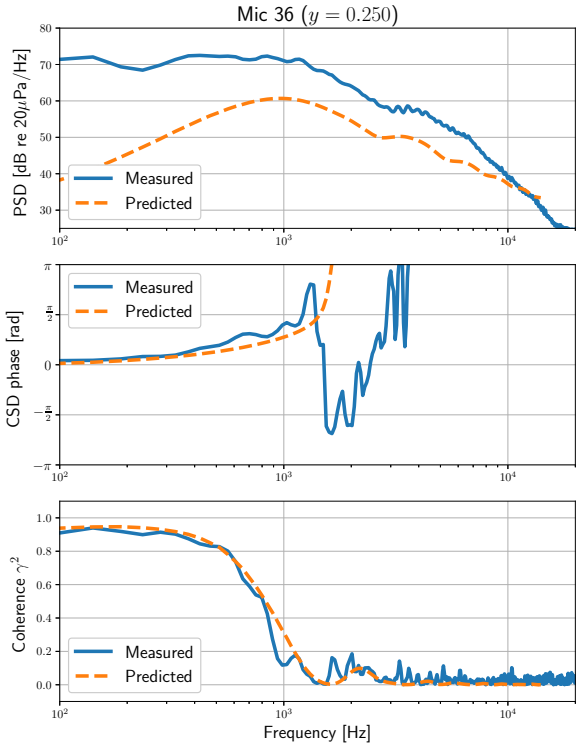

Figure 5.8: Predicted and measured PSD magnitude (dB re 20μPa/Hz), unwrapped CSD phase (rad) and coherence γ^2 (ref mic 1) as a function of frequency for microphone 36 ($y = 0.25$ m).

Figures 5.4 to 5.8 show a comparison of the predicted and measured PSD in dB re 20μPa/Hz, the unwrapped phase (in radians) and coherence function γ^2 for the selected near-field planar array microphones, ordered in increasing spanwise distance y from the array centre. The cross-spectra were calculated from the calibrated microphone signals using the Welch method [66]. The spectra were obtained using $N_{DFT} = 1024$ samples, 50% overlap and used a Hann window for each window. We compare the experimental data with predictions made using the Amiet model, and include shear layer refraction effect as described in Section 2.4.

5.3.1 PSD levels

The above spectra display slight oscillations in all measured data, in a manner similar to a "comb filter" effect, with peaks at approximately every 340 Hz. This was identified as a standing wave effect between the flat plate aerofoil and the planar microphone array baffle. This effect is clearly undesirable, since it might obscure actual features of the acoustic field; hence, we recommend the use of acoustically transparent microphone arrays when possible.

All power spectral density plots in Figures 5.4 to 5.8 show significant differences between the predictions and the measurements, both in level and in general shape of the spectra. Differences of more than 10 dB are visible over a wide range of frequencies for all plots. The rate of decay is slightly different between the predictions and measurements, and the oscillations seen in the predicted spectra at high frequencies are not visible in the measurements. This result can be contrasted with Figure 4.18, which showed a good agreement between prediction and measurement for the PSD as seen by a "far-field" observer, particularly at higher frequencies.

A few reasons for these discrepancies are:

- Measured data are contaminated by wind tunnel jet noise, which is particularly prominent at low frequencies;
- The planar array is significantly closer to the wind tunnel shear layer than the far-field array, and thus might be more affected by shear layer hydrodynamic near-field noise, particularly at low frequencies;
- The measurements of the turbulence characteristics (turbulence intensity and integral length scale) might be in error, leading to a poor estimation of the turbulent wavenumber energy spectrum - and consequently, a poor estimation of the radiated noise spectra;

- The wind tunnel turbulent velocity field might not be isotropic, as is assumed when adopting the von Karman model;
- The shear layer amplitude correction model presented in Section 2.4 and adopted for the prediction calculations might be inaccurate and lead to errors in the noise spectra.

5.3.2 CSD phase and Coherence

Figures 5.4 to 5.8 show the (unwrapped) cross-spectrum phase and the coherence of microphones 32 (closest to the array centre) to 36 (furthest from the array centre), relative to microphone 01 at the array centre. These plots can be broadly divided into two frequency zones based on the coherence function: a low-frequency zone is present where the coherence rolls off from approximately unity to zero, and a high frequency zone, where the coherence remains very close to zero, with some minor oscillations.

At the lower range of the low frequency region, it is expected that the aerofoil response to single gusts will not exhibit a very directional radiation. Every gust will thus induce a sound field that is fully coherent at different spanwise observer locations. The acoustic field seen at all microphones will therefore be highly coherent with respect to the phase reference (microphone 1). This effect is observed in both predictions and measurements with the exception of microphone 32, whose measured coherence decays for very low frequencies as well. The comb-filtering effect pointed out above is not present at this frequency range, possibly because the array baffle is not large enough (compared to the acoustic wavelength) to be a significant reflector of sound. In general, the phase and coherence predictions agree well within this region.

At the higher range of the low frequency region, where the coherence roll-off frequency is more apparent in the semi-logarithmic plots of Figures 5.4 to 5.8, there is still a good agreement between the predicted and the measured phase and coherence. Small differences are visible at the higher range, where the coherence curves first reach zero; this frequency will be used in the next Section to propose an explanation for the origin of the coherence decay. The comb-filtering effects also become more prominent in this zone, possibly because the array baffle dimensions become comparable to the acoustic wavelength. However, the predicted trend is still correctly observed in the measured curves.

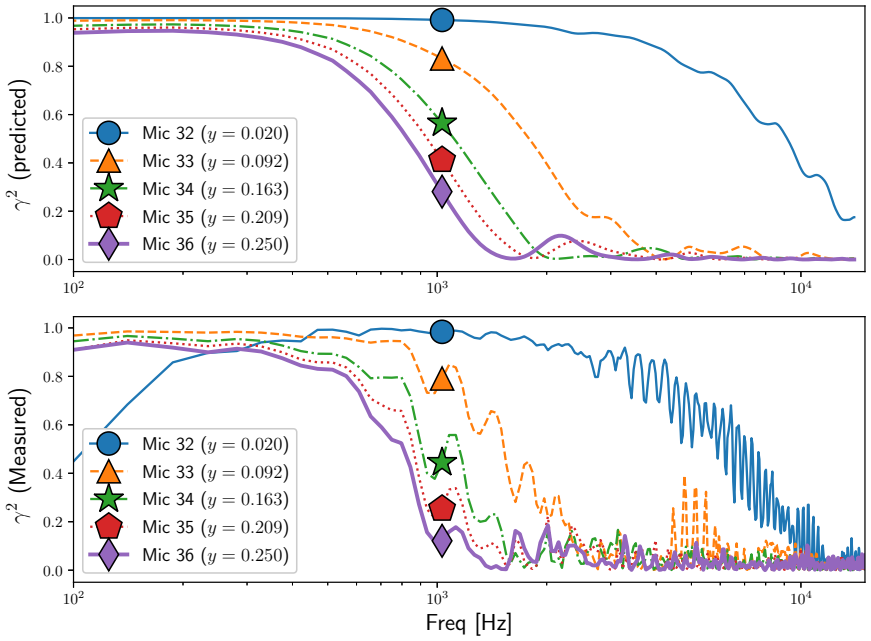

Figure 5.9: Predicted (top) and measured (bottom) coherence function γ^2 evaluated between selected planar array microphones with reference to microphone 1 (array centre).

As a consequence of the loss of coherence, the measured phase difference diverges significantly from the predictions at higher frequencies (not visible in all plots). This effect is to be expected, since incoherent signals by definition do not have a well-defined phase difference. Another possible cause for the divergence between predicted and measured phase is the effect of noise on the phase unwrapping algorithm, which might also lead to significant "jumps" in the unwrapped phase.

Figure 5.9 provides a comparison of the predicted coherence (top) and the measured coherence (bottom) for microphones 32 to 36. Each curve is marked with the symbol corresponding to its microphone number, as used in Figure 5.3. The difference in the frequency at which the coherence begins to decay is clearly visible, with microphones further away from the array centre (e.g. microphone 36) rolling off at lower frequencies than microphones that are closer to the array centre (e.g. microphone 32). It is also apparent how the measured coherence curves follow the predicted trends.

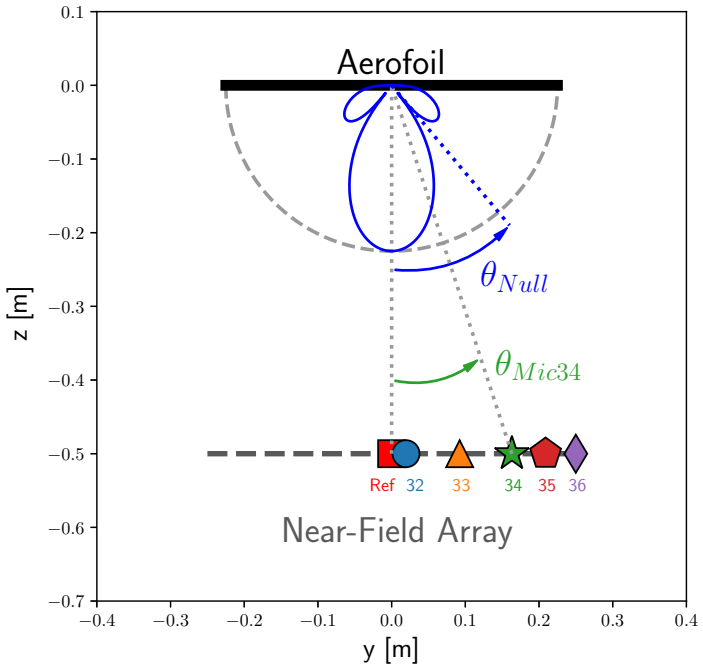

Figure 5.10: Diagram demonstrating the peak-to-null width angle for normal-incidence ($k_\psi = 0$) gust responses and spanwise microphone angles over the plane $x = 0$. The mean flow direction is perpendicular to the page and towards the reader.

5.3.3 Relationship between Main Lobe Width and Coherence for $k_\psi = 0$ Gusts

We now propose an explanation for the observed coherence drop as a function of frequency and spanwise microphone location. In the plane $x = 0$, we denote θ_{Null} the first null angle of the aerofoil spanwise directivity in response to the $k_\psi = 0$ gust; we also denote θ_{MicXX} the spanwise angle of the XX-th microphone. Both angles are indicated in Figure 5.10.

We propose that the coherence between the XX-th microphone and the centre microphone will first reach zero at the frequency where $\theta_{Null} = \theta_{MicXX}$ - i.e. when the aerofoil spanwise directivity angle becomes equal to the microphone spanwise angle.

The rationale for this explanation is as follows. As the aerofoil tends to beam its acoustic radiaton at well-determined spanwise directions for each gust (as shown in Section 4.1), different microphones will be acoustically "illuminated" by different, incoherent gusts, and would show zero coherence for an infinite-span aerofoil. Therefore, a non-zero coherence between a pair of microphones indicates that both microphones are being exposed to the same single-gust response; in particular, the coherece will be high when both microphones are located within the aerofoil spanwise directivity main lobe. This will occur when the aerofoil spanwise main

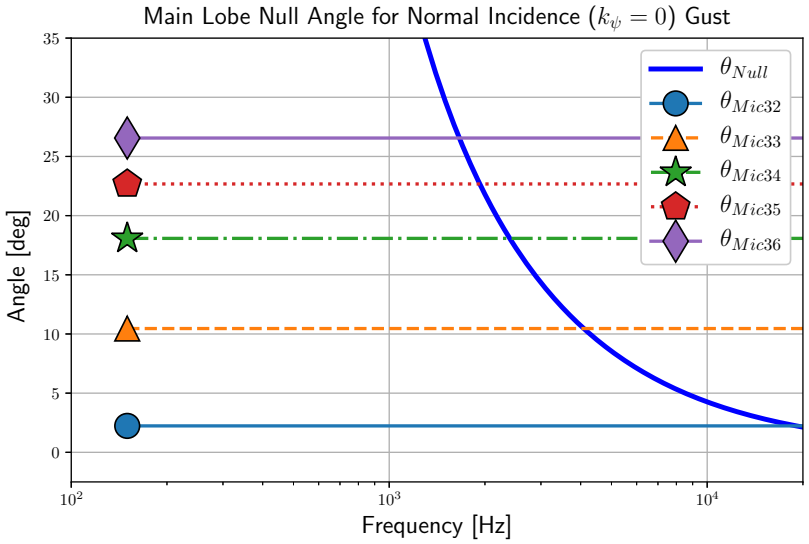

Figure 5.11: Spanwise radiation null angle θ_{Null} for $k_\psi = 0$ gusts as a function of frequency, with microphone angles θ_{MicXX} indicated as horizontal lines.

lobe covers a broad angular range (i.e. at low frequencies), or when the microphone pairs are closely spaced in the spanwise direction.

In order to test this hypothesis, we calculate the null angle θ_{Null} as a function of frequency for a normal-incidence ($k_\psi = 0$) gust, shown in Figure 5.11. This particular gust was chosen as the reference microphone in the array centre is always exposed to its maximum spanwise directivity. We then mark on top of this plot the spanwise angles corresponding to the microphones under analysis. It has been discussed in Section 3.1.3.1 that the main lobe null-to-null width in the wavenumber domain is $\Delta k_\psi^{ML} = 2\pi/d$, and hence the null must be located at $k_\psi^{null} = \Delta k_\psi^{ML}/2 = \pi/d$. From Eq. 2.88, this wavenumber corresponds to a flow-corrected spanwise angle $y/\sigma = k_\psi/k_0$. In the $x = 0$ plane, this simplifies to

$$\frac{y}{r} = \beta \frac{k_\psi}{k_0}, \tag{5.4}$$

from which we obtain the frequency where the two angles coincide as

$$f(\theta_{Mic} = \theta_{Null}) = \frac{c_0 \beta}{2d} \left(\frac{r}{y} \right), \tag{5.5}$$

where y and r correspond to the microphone spanwise coordinate and radius, respectively.

Table 5.4: Approximate frequencies for zero microphone coherence (ref mic 01) and spanwise radiation null angle, and relative difference.

Mic number	$f(\gamma^2_{pred} = 0)$ [Hz]	$f(\theta_{Mic} = \theta_{Null})$ [Hz]	Rel. difference
32	*not observed	19060	-
33	4230	4092	-3.3%
34	2110	2394	13.5%
35	1840	1927	4.7%
36	1620	1661	2.5%

We compare the frequencies where the predicted coherence function γ^2 first reaches zero, as visually identified from Figure 5.9 (top), with the frequencies where the null angle and the microphone angle coincide, as seen in Figure 5.11 and obtained from Eq. 5.5.

The comparison is shown in Table 5.4, together with the relative difference between the frequencies (ref $f(\gamma^2_{pred} = 0)$). As can be seen, the frequencies are fairly close to each other, indicating that the two phenomena are consistent. The agreement is not perfect, however; this might be because the calculation of the zero predicted coherence frequency $f(\gamma^2_{pred} = 0)$ takes into account shear layer refraction effects, while the null angle frequency $f(\theta_{Null} = \theta_{Mic})$ does not.

Another possible explanations for this difference is that we are using a *far-field* characteristic of the aerofoil - its directivity pattern - as a proposed mechanism to describe a coherence drop phenomenon in the *near-field*. It is possible that the acoustic radiation nulls are not fully developed at these distances and frequencies, thus causing the above mentioned differences. Nevertheless, there is a satisfactory agreement between the values - which perhaps illustrates once again how the borders between the near- and the far-field are not clearly defined.

5.3.4 Coherence Between Array Microphones

We now consider how the acoustic field coherence varies as a function of frequency over the array microphones, and investigate how it changes when choosing different reference microphones. For this analysis, we calculate the pairwise coherence over each microphone and a reference microphone, and linearly interpolate the coherence in the space between the microphones for visualisation purposes.

Figure 5.12 show the predicted (left) and measured (right) coherence function for frequencies close to 200 Hz (top), 400 Hz (middle) and 800 Hz (bottom), and Figure 5.13 for frequencies

close to 1600 Hz (top), 3200 Hz (middle) and 6400 Hz (bottom). Both Figures use microphone 1 at the centre of the planar array (marked with a blue square) as the phase reference. Figures 5.14 and 5.15 show the same analysis, but using microphone 34, located off-centre, as the phase reference.

In these Figures, the expected coherence behaviour of the radiated sound field is clearly visible: all microphones are highly coherent at low frequencies, and the spanwise coherence decreases with increasing frequency, as the aerofoil single-gust response begins to become more directional. It is also noteworthy that, since the chordwise radiation is always fully coherent, the coherence is preserved over a larger range of frequencies for microphones aligned in the chordwise direction. These effects are observed regardless of which microphone is chosen as the phase reference.

The agreement displayed in these Figures is noteworthy. To the best of our knowledge, this is the first time the radiated acoustic field power spectral density, cross-spectrum phase and coherence are measured and compared against an analytical model for observers in the aerofoil near-field and out of the mid-span plane.

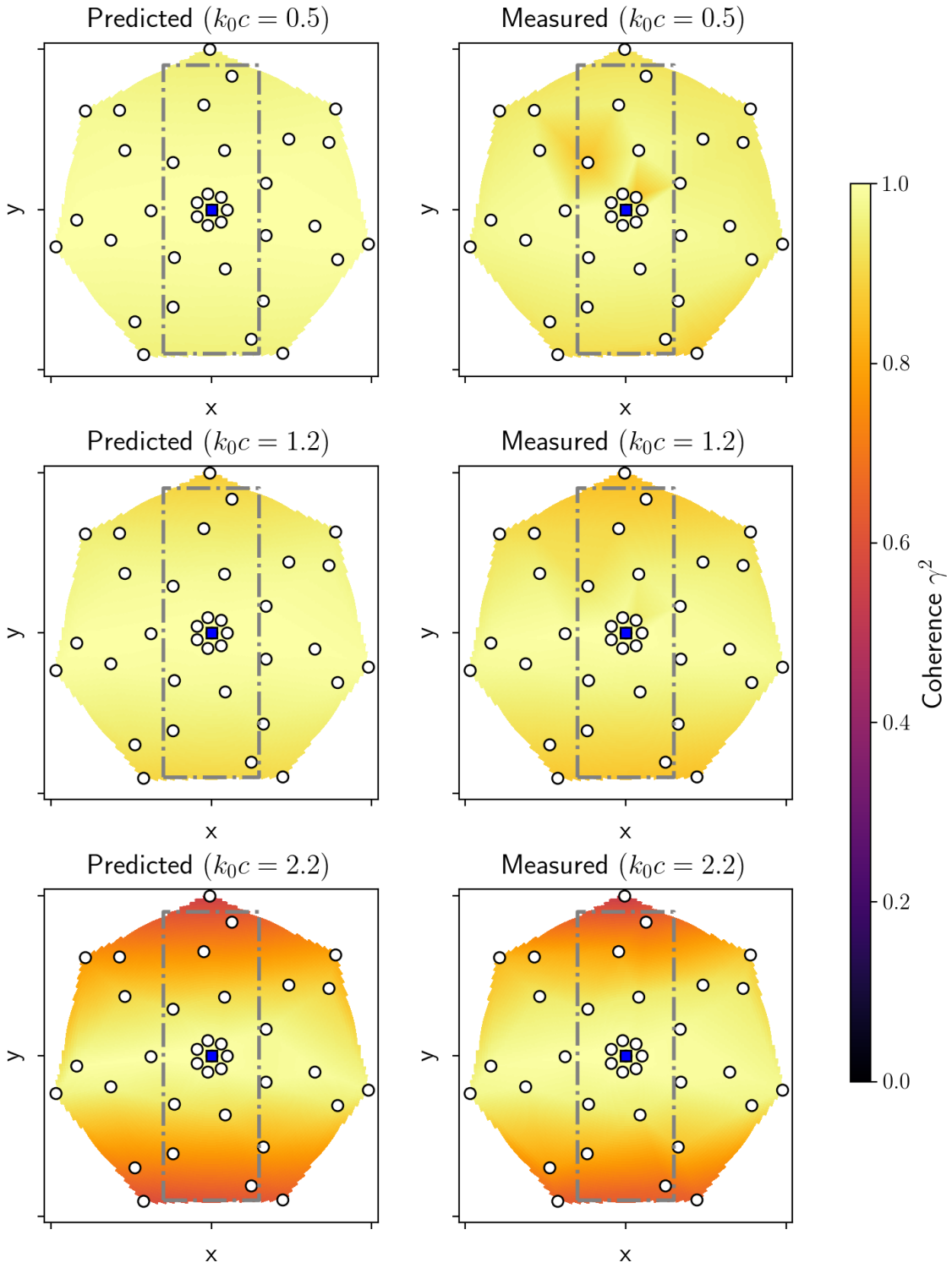

Figure 5.12: Predicted (left) and measured (right) coherence function γ^2 evaluated over the planar array face with reference to microphone 1 (array centre, square marker); values are interpolated from pairwise coherences at approximate narrowband frequencies $k_0c = 0.5$ (200 Hz - top), $k_0c = 1.2$ (400 Hz - middle) and $k_0c = 2.2$ (800 Hz - bottom).

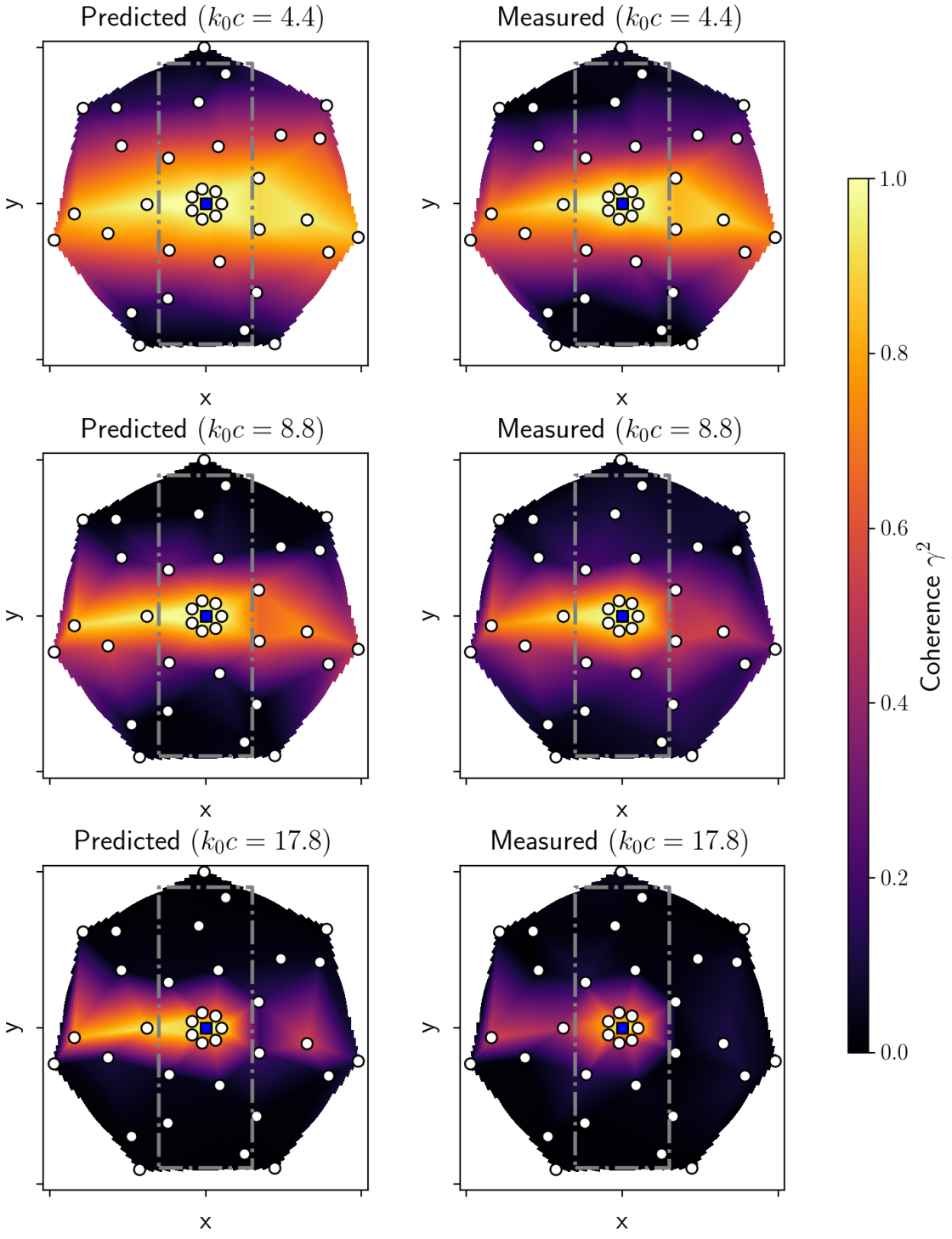

Figure 5.13: Predicted (left) and measured (right) coherence function γ^2 evaluated over the planar array face with reference to microphone 1 (array centre, square marker); values are interpolated from pairwise coherences at approximate narrowband frequencies $k_0c = 4.4$ (1600 Hz - top), $k_0c = 8.8$ (3200 Hz - middle) and $k_0c = 17.8$ (6400 Hz - bottom).

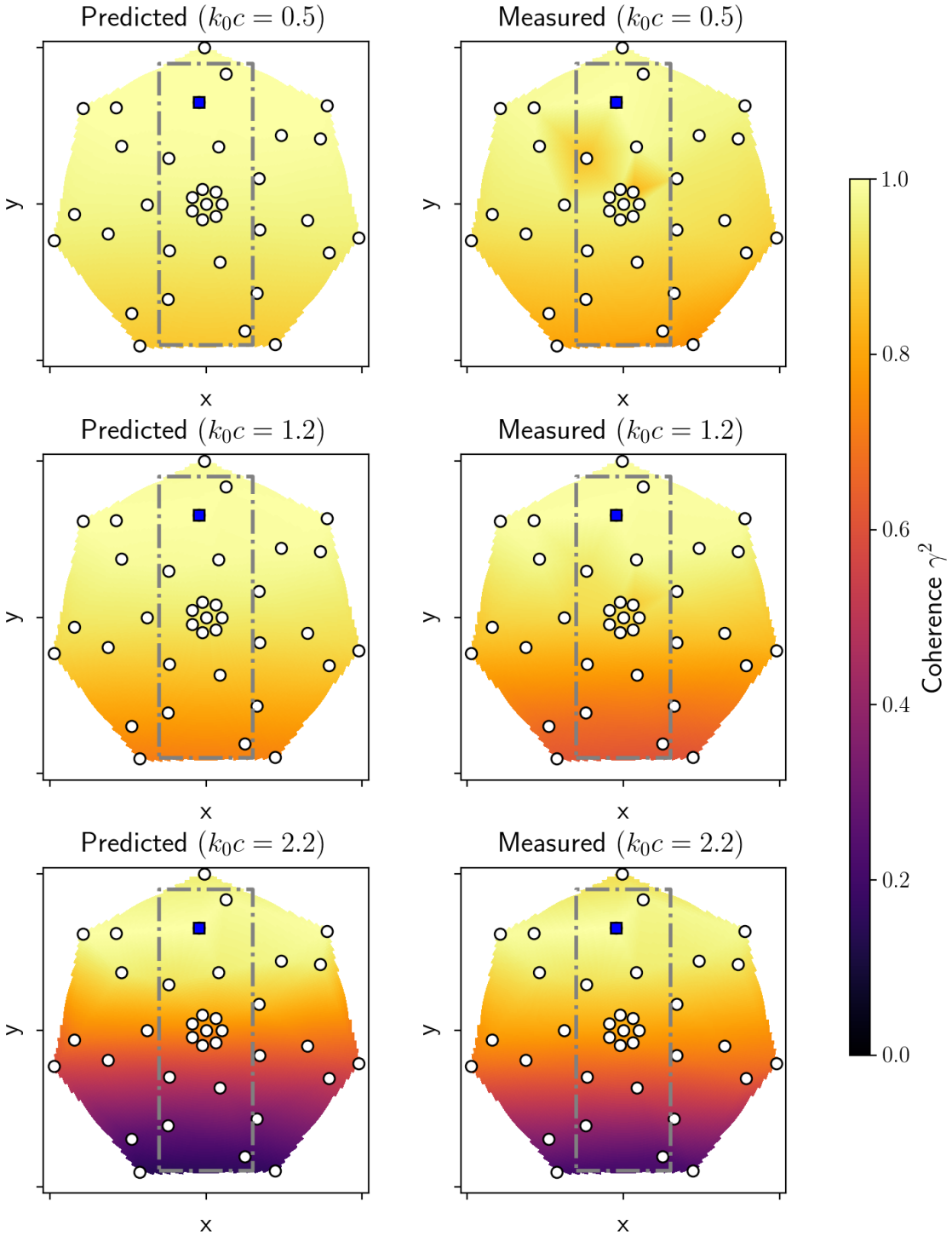

Figure 5.14: Predicted (left) and measured (right) coherence function γ^2 evaluated over the planar array face with reference to microphone 34 (off centre, square marker); values are interpolated from pairwise coherences at approximate narrowband frequencies $k_0c = 0.5$ (200 Hz - top), $k_0c = 1.2$ (400 Hz - middle) and $k_0c = 2.2$ (800 Hz - bottom).

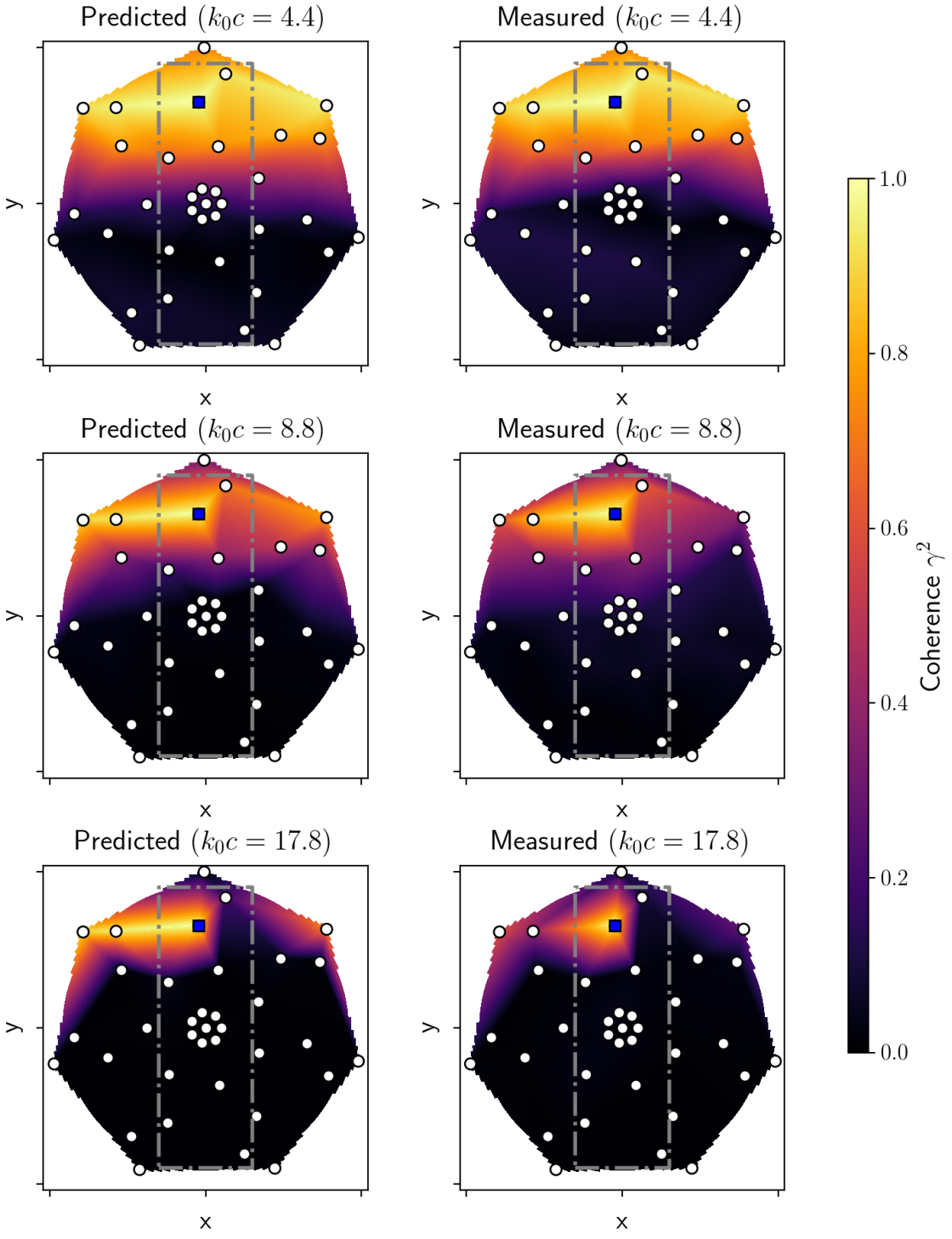

Figure 5.15: Predicted (left) and measured (right) coherence function γ^2 evaluated over the planar array face with reference to microphone 34 (off centre, square marker); values are interpolated from pairwise coherences at approximate narrowband frequencies $k_0c = 4.4$ (1600 Hz - top), $k_0c = 8.8$ (3200 Hz - middle) and $k_0c = 17.8$ (6400 Hz - bottom).

Chapter 6

Source Reconstruction via Conventional Beamforming

In this Chapter we review frequency-domain beamforming [1] from a source reconstruction perspective. Beamforming is by far the most popular signal processing strategy employed in the microphone array literature, with a large number of references from the radar and sonar array communities as well. It is perhaps the simplest and most robust array processing method, and as such its advantages and limitations are well understood.

Despite the importance of conventional beamforming, its shortcomings have driven deconvolution algorithms to become the new standard for aeroacoustic measurements. These methods generally attempt to analyse a source map originally obtained by conventional beamforming and deconvolve the array response from it. Our review will focus on covering the algorithms CLEAN-PSF and CLEAN-SC [3], which are some of the most popular deconvolution algorithms in current use.

6.1 Conventional Beamforming

All analyses here are assumed to be in the frequency domain. We first define an ensemble of acoustic sources at $\mathbf{r}_n$, $n = 1, \ldots, N$ with $\mathbf{q} = [q_1, q_2, \ldots, q_N]^T$ being the column vector of complex source strengths. The acoustic pressure generated by these sources and observed at the M array element positions $\mathbf{r}_m$, $m = 1, \ldots, M$ can be written as a column vector $\mathbf{p} = [p_1, p_2, \ldots, p_M]^T$. The forward radiation problem is then expressed as [72]

$$\mathbf{p} = \sum_{n=1}^{N} q_n \mathbf{g}_n \tag{6.1}$$

$$= \begin{bmatrix} | & | & & | \\ \mathbf{g}_1 & \mathbf{g}_2 & \cdots & \mathbf{g}_N \\ | & | & & | \end{bmatrix} \begin{bmatrix} q_1 \\ q_2 \\ \vdots \\ q_N \end{bmatrix} \tag{6.2}$$

$$= \mathbf{G}\mathbf{q}. \tag{6.3}$$

We define $\mathbf{g}_n = [g_{(1,n)}, g_{(2,n)}, \ldots, g_{(M,n)}]^T$ as the *transfer vector*[1]; it contains the transfer function elements between the n-th source and all M microphones, arranged in vector form. We can also interpret the transfer vector as containing the complex pressures induced at the microphone locations by a unitary-amplitude source located at $\mathbf{r}_n$ [50]; every source will induce a multiple of its associated transfer vector at the array elements, scaled by the source complex amplitude [72]. The matrix $\mathbf{G}$ groups all transfer vectors $\mathbf{g}_n$ and can be defined as the *transfer matrix*.

The transfer vector elements describe the acoustic source radiation and wave propagation inside the medium of interest. Different radiation and propagation models were described in Chapter 2 and are possible candidates for transfer vector elements: for example, monopole or dipole transfer functions, with or without convection, and with or without shear layer refraction. For the remainder of the current Chapter, however, we will assume an appropriate wave propagation model has been adopted, and we will deal with the transfer vector components as arbitrary elements $g_{(m,n)}$.

A common interest in array processing is to find an estimate of the n-th complex source strength $\tilde{q}_n$ through a linear combination of the array signals. This result is often called the *array output*, and it has the general form

$$\tilde{q}_n = \sum_{m=1}^{M} w^*_{(m,n)} p_m = \mathbf{w}_n^H \mathbf{p}, \tag{6.4}$$

[1] It should be pointed out that many authors in the literature call the vector $\mathbf{g}_n$ as the *steering vector*; however, we have decided not to adopt this nomenclature since it can be confusing when discussing the act of steering the array to estimate a given sound source using a weights vector, as is described below.

where the asterisk superscript $\{.\}^*$ denotes complex conjugation, the superscript $\{.\}^H$ denotes complex conjugate (Hermitian) transpose, and $\mathbf{w}_n = [w_{(1,n)}, w_{(2,n)}, \ldots, w_{(M,n)}]^T$ is a vector of weighting coefficients, generally obtained by optimising the array response for a given metric. It is then said that, by applying the complex-conjugated weights vector $\mathbf{w}_n^H$ to the microphone signals to estimate the n-th source amplitude, we are *steering* the array towards the n-th source location; hence, this vector is often named the *steering vector*.

We now formally introduce *conventional beamforming* as the combination of array signals that minimizes the difference $\|\mathbf{p} - \tilde{q}_n \mathbf{g}_n\|^2$ [50]. The estimated source strength that minimizes this cost function is given by

$$\tilde{q}_n = \frac{\mathbf{g}_n^H}{\|\mathbf{g}_n\|^2}\mathbf{p}, \tag{6.5}$$

from which we obtain the following formulation for the steering vector $\mathbf{w}_n$:

$$\mathbf{w}_n = \frac{\mathbf{g}_n}{\|\mathbf{g}_n\|^2}. \tag{6.6}$$

Alternatively, we can obtain the entire vector of source strength estimates $\tilde{\mathbf{q}}$ by multiplying the vector of acoustic pressures $\mathbf{p}$ by the Hermitian transpose of a matrix $\mathbf{W}$ containing all steering vectors:

$$\tilde{\mathbf{q}} = \mathbf{W}^H \mathbf{p} \tag{6.7}$$

$$= \begin{bmatrix} - & \mathbf{w}_1^H & - \\ - & \mathbf{w}_2^H & - \\ & \vdots & \\ - & \mathbf{w}_N^H & - \end{bmatrix} \begin{bmatrix} p_1 \\ p_2 \\ \vdots \\ p_M \end{bmatrix}. \tag{6.8}$$

Note that steering vector formulations other than Eq. 6.6 are available, which usually provide a trade-off between correct source localisation and correct source strength estimation [73]. It is shown below that Eq. 6.6 provides the correct source strength in a single-source case.

In practice, a grid of candidate source locations is defined a priori over a region of interest, and the array is successively steered towards each point in the grid, effectively *scanning* it. The

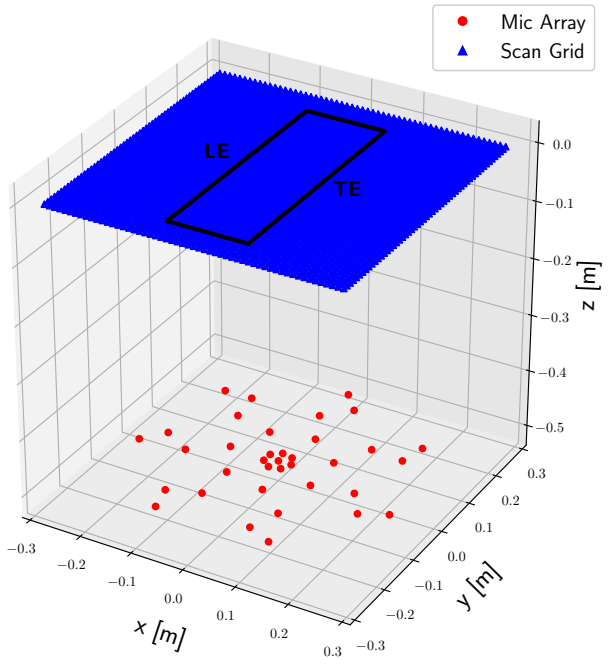

Figure 6.1: Diagram demonstrating the beamforming scan grid elements over the aerofoil plane ($z = 0$) and the near-field microphone array elements. The wind tunnel mean flow is in the $+x$ direction.

beamforming algorithm will estimate the source strength complex amplitude at each point, and the resulting estimated source strength distribution as a function of grid point location is called the *beamforming map*.

As an example, let us consider the setup used to analyse the measurement results described in Chapter 5: we define a planar scan grid with dimensions 0.55×0.55 m at a height $z = 0$, where the aerofoil is located, with grid points spaced 0.01 m apart in both directions. The near-field planar microphone array described in Section 5.2 is positioned below and parallel to the scan plane, at a vertical distance of 0.5 m, as shown in Figure 6.1. For the moment, we will not consider shear layer effects; instead, we will assume the entire medium is subject to a mean flow of $U_x = 60$ m/s.

6.1.1 Array Point Spread Function

Let us define a single point source located at the k-th position in the scan plane and with amplitude q_k. The microphone signals induced by this source are

$$\mathbf{p} = q_k \mathbf{g}_k. \tag{6.9}$$

We can now use conventional beamforming to estimate the source amplitude seen by the array at the n-th position. From Eq. 6.4, we have:

$$\begin{aligned}
\tilde{q}_n &= \mathbf{w}_n^H \mathbf{p} && (6.10)\\
&= \mathbf{w}_n^H \left(q_k \mathbf{g}_k\right) && (6.11)\\
&= q_k \mathbf{w}_n^H \mathbf{g}_k && (6.12)\\
&= q_k \ \mathrm{PSF}_{n,k}. && (6.13)
\end{aligned}$$

We define the array *point spread function*, denoted $\mathrm{PSF}_{n,k}$, as the array output when it is steered at the n-th location and exposed to a unitary-amplitude source at the k-th location.

When using the steering vector formulation defined in Equation 6.6, the point spread function is unitary when the array is steered towards the correct source location. If only one source is present at the steering location, the array estimate will yield its correct source strength:

$$\begin{aligned}
\tilde{q}_k &= \mathbf{w}_k^H \mathbf{p} && (6.14)\\
&= \left(\frac{\mathbf{g}_k}{\|\mathbf{g}_k\|^2}\right)^H \left(q_k \mathbf{g}_k\right) && (6.15)\\
&= q_k \frac{\mathbf{g}_k^H \mathbf{g}_k}{\|\mathbf{g}_k\|^2} && (6.16)\\
&= q_k. && (6.17)
\end{aligned}$$

Note that due to the PSF, a source at the k-th location can affect the estimation of a source at the n-th location; the point spread function thus describes the beamformer limited spatial resolution, and as such it depends on frequency, problem geometry (including the microphone array design) and choice of steering vector formulation. An ideal PSF would be an infinitesimally thin beam with unitary amplitude at the source location, and zero everywhere else (i.e. a Dirac Delta function); in practice, it normally contains a *main lobe* around the source location with an associated width, which limits the array resolution, and many smaller *sidelobes* elsewhere, which limit the array dynamic range.

We can also consider the PSF in matrix form. Let us rewrite Eq. 6.4 as

$$\tilde{\mathbf{q}} = \begin{bmatrix} - & \mathbf{w}_1^H & - \\ - & \mathbf{w}_2^H & - \\ & \vdots & \\ - & \mathbf{w}_N^H & - \end{bmatrix} \mathbf{p} \tag{6.18}$$

$$= \mathbf{W}^H \mathbf{p} \tag{6.19}$$

$$= \left(\mathbf{W}^H \mathbf{G}\right) \mathbf{q}. \tag{6.20}$$

Note that the PSF is now expressed in the columns of the matrix $\mathbf{W}^H\mathbf{G}$, as they describe the estimated source strength distribution when exposed to a unitary point source. In this formulation, the ideal PSF would have $\mathbf{W}^H\mathbf{G} = \mathbf{I}_{N\times N}$ - i.e. the ideal matrix of beamforming steering vectors is the inverse of the matrix of transfer functions, so that each source estimate would depend only on its corresponding source strength. However, most times $\mathbf{W}^H\mathbf{G}$ will not be diagonal, and a given source estimate will be contaminated by adjacent sources, as previously described.

Figure 6.2 illustrates the PSF for the planar near-field array at frequencies ranging from 500 Hz to 16 kHz, obtained by applying conventional beamforming to a point monopole source in the middle of the scan plane. The main lobe width can be seen to dominate the entire scan grid at low frequencies, demonstrating that conventional beamforming suffers from poor resolution at low frequencies and will not be able to separate closely spaced sources. At mid to high frequencies, the main lobe becomes narrower and a series of sidelobes appear around the main lobe, which in turn will disturb the identification of lower-amplitude sources close to a large amplitude source. The main lobe width and the sidelobes location and level are directly linked to the microphone array geometry, and careful array design can mitigate these limitations to a certain extent [27, 74].

One common assumption in array processing is that a given beamforming map is composed of PSFs scaled by their respective source strengths. This assumption implies that all occuring sources must be mutually incoherent point sources, and that the chosen steering vectors are calculated from the correct transfer vectors. This might not always be the case, as: sources can have their acoustic radiation properties differing from the transfer functions used to calculate the steering vectors (for example, the sources might present dipole characteristics while the

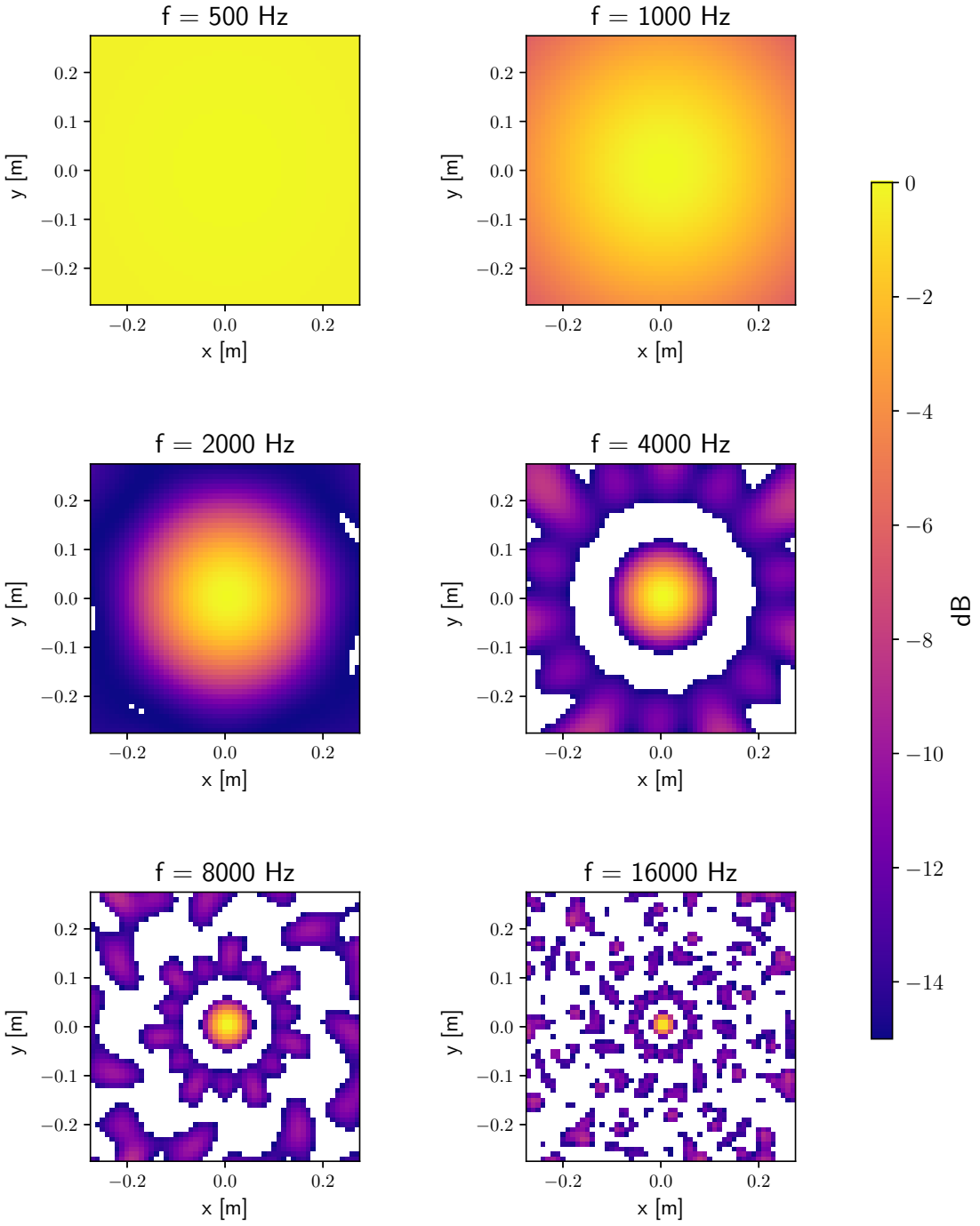

Figure 6.2: Microphone array point spread function for the near-field array at frequencies between 500 Hz and 16 kHz.

steering vectors were calculated with monopole transfer functions); sources can be distributed instead of point-like; and multiple sources can have varying degrees of coherence with one another. These assumptions should be taken into consideration when interpreting a source map [60], and might also affect the performance of deconvolution algorithms.

6.1.2 Cross-Spectral Matrix and Source Power Estimation

In aeroacoustics experiments, the noise sources under analysis are generally broadband, and thus require analysis in the cross-power spectral domain [30]. Let us denote the expected values of the source auto-powers by $\mathrm{E}\left\{|q_n|^2\right\} = Q_n$ to simplify the notation; the estimated expected value of the n-th source power is given by [72, 75]

$$\begin{aligned}
\tilde{Q}_n &= \mathrm{E}\left\{|\mathbf{w}_n^H \mathbf{p}|^2\right\} && (6.21)\\
&= \mathrm{E}\left\{\left(\mathbf{w}_n^H \mathbf{p}\right)\left(\mathbf{w}_n^H \mathbf{p}\right)^H\right\} && (6.22)\\
&= \mathbf{w}_n^H \mathrm{E}\left\{\mathbf{p}\mathbf{p}^H\right\}\mathbf{w}_n && (6.23)\\
&= \mathbf{w}_n^H \mathbf{C} \mathbf{w}_n. && (6.24)
\end{aligned}$$

We now define the microphone array *cross-spectral matrix* $\mathbf{C}$ (CSM - alternatively called *spatial covariance matrix*, *cross-power matrix* or *spatial correlation matrix*) as [60]

$$\begin{aligned}
\mathbf{C} &= \mathrm{E}\left\{\mathbf{p}\mathbf{p}^H\right\} && (6.25)\\
&= \mathrm{E}\left\{\begin{bmatrix} p_1 p_1^* & p_1 p_2^* & \cdots & p_1 p_M^* \\ p_2 p_1^* & p_2 p_2^* & \cdots & p_2 p_M^* \\ \vdots & \vdots & \ddots & \vdots \\ p_M p_1^* & p_M p_2^* & \cdots & p_M p_M^* \end{bmatrix}\right\}. && (6.26)
\end{aligned}$$

The CSM is akin to the correlation matrix of a temporal signal [76], but contains information about the *spatial* correlation characteristics of the observed signal instead of *temporal* correlation. Since it only contains the relative phase between different microphones, the phase difference given by the wave propagation from the source to the centre of the array is ignored, as is the phase difference from evaluating the CSM at increasing time origins for different STFT blocks [1].

The CSM is usually computed using the Welch's method for spectral density estimation. A set of digitised recordings of the microphone signals are separated into temporal blocks called *frames*, and a Short-Time Fourier Transform is performed for each frame. The frame duration must be much larger than the difference between the shortest and the longest propagation time from any grid point to each microphone [60]. For each frame, a CSM is computed for each frequency using the corresponding complex microphone coefficients, and the resulting CSMs are averaged across different frames; the temporal frames can be windowed and overlapped as desired. As with any temporal averaging processes, the implicit assumption is that the sources are wide-sense stationary during the interval of observation [75].

For a single source at the n-th location, the CSM takes the form

$$\mathbf{C} = \mathrm{E}\left\{\mathbf{p}\mathbf{p}^H\right\} \tag{6.27}$$

$$= \mathrm{E}\left\{(q_n\mathbf{g}_n)(q_n\mathbf{g}_n)^H\right\} \tag{6.28}$$

$$= \tilde{Q}_n\mathbf{g}_n\mathbf{g}_n^H. \tag{6.29}$$

6.1.2.1 Noise and the Diagonal Elements of the CSM

Let us consider what happens at the CSM when uncorrelated noise is added at the microphone signals. The noisy microphone output vector is written

$$\mathbf{p}_{noisy} = \mathbf{p} + \mathbf{n}, \tag{6.30}$$

where $\mathbf{n}$ is a vector of M random uncorrelated noise signals. The ratio of the signal power to the noise power at the microphones is defined as the *signal-to-noise ratio* (SNR), usually expressed in decibels as

$$SNR = 10\log_{10}\left(\frac{\frac{1}{M}\left\|\mathbf{p}\right\|^2}{\frac{1}{M}\left\|\mathbf{n}\right\|^2}\right). \tag{6.31}$$

It is assumed the elements of $\mathbf{n}$ are statistically uncorrelated with one another, such that a CSM obtained from the noise signal alone would be purely diagonal:

$$\mathbf{C_n} = \mathrm{E}\left\{\mathbf{n}\mathbf{n}^H\right\} \tag{6.32}$$

$$= \mathrm{E}\left\{\begin{bmatrix} n_1 n_1^* & 0 & \dots & 0 \\ 0 & n_2 n_2^* & \dots & 0 \\ \vdots & \vdots & \ddots & \vdots \\ 0 & 0 & \dots & n_M n_M^* \end{bmatrix}\right\}. \tag{6.33}$$

It is also assumed $\mathbf{n}$ is statistically uncorrelated to $\mathbf{p}$, such that

$$\mathrm{E}\left\{\mathbf{p}\mathbf{n}^H\right\} = \mathrm{E}\left\{\mathbf{n}\mathbf{p}^H\right\} = \mathbf{0}_{M\times M}. \tag{6.34}$$

The CSM calculated from a noisy microphone array recording is then expressed as

$$\mathbf{C}_{noisy} = \mathrm{E}\left\{\mathbf{p}_{noisy}\ \mathbf{p}_{noisy}^H\right\} \tag{6.35}$$

$$= \mathrm{E}\left\{(\mathbf{p}+\mathbf{n})(\mathbf{p}+\mathbf{n})^H\right\} \tag{6.36}$$

$$= \mathrm{E}\left\{\mathbf{p}\mathbf{p}^H\right\} + \underbrace{\mathrm{E}\left\{\mathbf{p}\mathbf{n}^H\right\}}_{=\mathbf{0}_{M\times M}} + \underbrace{\mathrm{E}\left\{\mathbf{n}\mathbf{p}^H\right\}}_{=\mathbf{0}_{M\times M}} + \mathrm{E}\left\{\mathbf{n}\mathbf{n}^H\right\} \tag{6.37}$$

$$= \mathbf{C_p} + \mathbf{C_n}. \tag{6.38}$$

Hence, the noise CSM will load only the diagonal terms of the noisy microphone array CSM; this raises the background noise level of the beamforming map, and decreases even further the beamformer dynamic range.

When performing array measurements in poor signal-to-noise conditions, such as in closed-walls wind tunnels, it is usual to replace the diagonal elements of the CSM with zeros to reduce the effects of noise and improve the dynamic range of the beamforming map [60]. This procedure is justified by noting that most sources of microphone noise, such as turbulent boundary layer perturbations at the microphones, and electrical noise in the microphone capsules and preamplifier circuits, are uncorrelated between different microphone pairs and will "enter" the CSM through the diagonal terms, as shown above. Meanwhile, sound waves radiated from the aeroacoustic sources towards the array will be correlated between pairs of microphones and will "enter" the CSM through the non-diagonal terms as well.

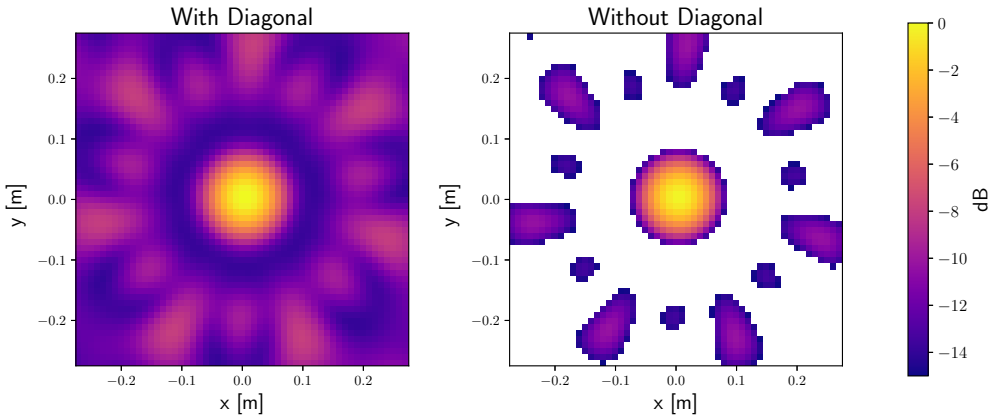

Figure 6.3: Beamforming maps obtained via conventional beamforming with (left) and without (right) the CSM diagonal elements at $f = 5$ kHz.

As an example, let us simulate a beamforming map with a unitary amplitude point source in the middle of the scan grid, and add noise to the microphone signals such that a SNR of 0 dB is obtained - i.e. the uncorrelated noise at the microphones contains as much energy as the acoustic signals of interest. A noise vector $\mathbf{n}$ that satisfies a desired SNR for a given microphone signal vector $\mathbf{p}$ can be obtained via the expression [77]

$$\mathbf{n} = \frac{10^{-\frac{SNR}{20}} \|\mathbf{p}\| \, e^{j\phi_M}}{\sqrt{M}}, \tag{6.39}$$

where ϕ_N is a vector of M randomly distributed phase angles.

For visualisation purposes, we consider a temporal frequency of 5 kHz. Figure 6.3 shows the resulting source maps for conventional beamforming by using the noisy CSM (left), and by applying diagonal removal (right); note the improvement in the background noise level. However, this procedure is not always recommended, since beamforming without the diagonal can sometimes lead to negative source power estimations; these are obviously non-physical results, and might interfere with techniques such as source map integration. We refer the reader to Dougherty [60] for a more in-depth discussion on the justifications for diagonal removal.

6.1.2.2 Multiple Sources and Source Coherence

Let us consider how the coherence between a pair of sources will influence the microphone CSM. Let two sources i and j, with their respective amplitudes q_i and q_j, radiate sound towards the microphone array; from Equation 6.3, these sources will induce a vector of pressure amplitudes $\mathbf{p}$ at the microphones of the form

$$\mathbf{p} = \mathbf{p}_i + \mathbf{p}_j \tag{6.40}$$

$$= q_i \mathbf{g}_i + q_j \mathbf{g}_j. \tag{6.41}$$

The total microphone CSM will be given by

$$\mathbf{C}_{i+j} = \mathrm{E}\left\{(\mathbf{p}_i + \mathbf{p}_j)(\mathbf{p}_i + \mathbf{p}_j)^H\right\} \tag{6.42}$$

$$= \mathrm{E}\left\{\mathbf{p}_i\mathbf{p}_i^H + \mathbf{p}_i\mathbf{p}_j^H + \mathbf{p}_j\mathbf{p}_i^H + \mathbf{p}_j\mathbf{p}_j^H\right\} \tag{6.43}$$

$$= \mathrm{E}\left\{\mathbf{p}_i\mathbf{p}_i^H\right\} + \mathrm{E}\left\{\mathbf{p}_i\mathbf{p}_j^H\right\} + \mathrm{E}\left\{\mathbf{p}_j\mathbf{p}_i^H\right\} + \mathrm{E}\left\{\mathbf{p}_j\mathbf{p}_j^H\right\} \tag{6.44}$$

$$= \mathbf{C}_i + \mathrm{E}\left\{q_i q_j^*\right\}\mathbf{g}_i\mathbf{g}_j^H + \mathrm{E}\left\{q_j q_i^*\right\}\mathbf{g}_j\mathbf{g}_i^H + \mathbf{C}_j. \tag{6.45}$$

Therefore, the CSM obtained for two sources will be given by the sum of the individually induced CSMs plus two cross-terms that depends on the expected value of the cross-power between the sources.

From classical signal processing, it is known that *incoherent* sources will not have a stable phase relationship along time, and therefore the expected value of their cross-powers will tend to zero. Meanwhile, *coherent* sources do have a stable phase relationship, and hence the expected value of their cross-powers will not tend to zero [1]. If the sources are incoherent, their cross-terms will average to zero and the microphone array CSM can be written as

$$\mathbf{C}_{i+j} = \mathbf{C}_i + \mathbf{C}_j. \tag{6.46}$$

This property is explored in the CLEAN-PSF deconvolution method, where incoherent acoustic sources are separated based on estimating and subtracting each individually induced CSM from the measured CSM. However, if the sources are coherent (or partially coherent), it will not be

possible to directly subtract the individual CSMs, and a different approach is required; this case is explored in the CLEAN-SC deconvolution method. Both methods are further detailed below.

6.1.3 Power PSF

We can then extend the concept of the point spread function to the broadband case. Assuming a single source at the k-th location and the array steered at the n-th location, we can express Equation 6.24 as

$$\begin{aligned}
\tilde{Q}_n &= \mathbf{w}_n^H \mathbf{C} \mathbf{w}_n && (6.47)\\
&= \mathbf{w}_n^H \mathrm{E}\left\{\mathbf{p}\mathbf{p}^H\right\} \mathbf{w}_n && (6.48)\\
&= \mathbf{w}_n^H \mathrm{E}\left\{ \left(q_k \mathbf{g}_k\right) \left(q_k \mathbf{g}_k\right)^H \right\} \mathbf{w}_n && (6.49)\\
&= \mathrm{E}\left\{q_k q_k^*\right\} \ \mathbf{w}_n^H \mathbf{g}_k \mathbf{g}_k^H \mathbf{w}_n && (6.50)\\
&= Q_k \ \mathrm{PSF}_{n,k}^2, && (6.51)
\end{aligned}$$

from where we define the point spread function squared - or power PSF - as

$$\begin{aligned}
\mathrm{PSF}_{n,k}^2 &= \left\| \mathbf{w}_n^H \mathbf{g}_k \right\|^2 && (6.52)\\
&= \left(\mathbf{w}_n^H \mathbf{g}_k\right) \left(\mathbf{w}_n^H \mathbf{g}_k\right)^H && (6.53)\\
&= \mathbf{w}_n^H \mathbf{g}_k \mathbf{g}_k^H \mathbf{w}_n. && (6.54)
\end{aligned}$$

As with the amplitude PSF, the magnitude of the power PSF is unitary when the steering direction n and the source location k coincide.

As previously pointed out, when the acoustic sources are incoherent, the microphone array CSM will be composed of the sum of the individually induced CSMs from each source. The beamforming source powers estimation will be composed of a sum of squared PSFs scaled by its corresponding source power, which is akin to a spatial convolution of the real source location and power with the array power PSF. In theory, if the experimenter has knowledge of the PSFs induced by each source and of the source locations, it should be possible to subtract

the PSF effect from the beamforming map; this is the basis for deconvolution algorithms, described in the next Section.

6.2 Deconvolution Algorithms

In recent years, deconvolution algorithms such as DAMAS, CLEAN-PSF and CLEAN-SC became widely used to reduce misinterpretation and improve accuracy of beamforming maps, and likely are the *de facto* tools for modern array signal processing in aeroacoustic applications. Their aim is to remove the effects of the PSF on the source map and thus arrive at the "true" source strength distribution; their rationale and performance, however, vary considerably amongst different methods, and therefore each method deserves a separate description.

6.2.1 CLEAN-PSF

We begin by describing the CLEAN-PSF algorithm, sometimes termed simply CLEAN, originally developed for astronomy and later adapted to acoustics [3]. In broad terms, this algorithm takes a beamforming map (called the "dirty" map) as input, locates the highest peak on the map, subtracts a scaled PSF from the map, and adds a "clean beam" - i.e. an artificially created narrow beam with no sidelobes - at the corresponding peak location and level to a "clean map". The process is repeated iteratively until a stop condition is met. The "clean" map, populated by clean beams at the estimated source locations and levels, is presented as a final output.

The main assumption for the CLEAN algorithm is that all sources are incoherent and point-like, and that peaks in the source map are due to single sources. Each source will then induce a PSF on the beamforming map equal to the theoretical PSF of the array, and the beamforming map can be expressed as a finite sum of individual PSFs. Note that this algorithm requires knowledge - or at least assumption - of the transfer vectors $\mathbf{g}_n$ from the scan points to the microphones in order to build the theoretical PSFs for each source.

The CLEAN algorithm is initialized by defining a "degraded" CSM $\mathbf{D}^{(i)}$ and initialising its iteration $i = 0$ with the original array CSM $\mathbf{C}$:

$$\mathbf{D}^{(0)} = \mathbf{C}. \tag{6.55}$$

The initial source power "dirty map" is obtained from conventional beamforming using the initial CSM:

$$\tilde{Q}_n^{(0)} = \mathbf{w}_n^H \mathbf{D}^{(0)} \mathbf{w}_n = \mathbf{w}_n^H \mathbf{C} \mathbf{w}_n, \tag{6.56}$$

and the source power "clean map" is initialised with zeros:

$$\tilde{Q}_{n\ CLEAN}^{(0)} = 0, \quad \forall n. \tag{6.57}$$

For $i \geq 1$, we apply the following algorithm:

- Find the location $\mathbf{r}_k$ containing the peak on the "dirty" map $\tilde{Q}_n^{(i-1)}$ and determine the peak power $\tilde{Q}_k^{(i-1)}$;
- Define the CSM $\mathbf{C}_k^{(i)}$ induced by the source at $\mathbf{r}_k$ as

  $$\mathbf{C}_k^{(i)} = \tilde{Q}_k^{(i-1)} \mathbf{g}_k \mathbf{g}_k^H \tag{6.58}$$

  and remove ("clean") its contribution from the beamforming map:

  $$\tilde{Q}_n^{(i)} = \tilde{Q}_n^{(i-1)} - \varphi \mathbf{w}_n^H \mathbf{C}_k^{(i)} \mathbf{w}_n, \tag{6.59}$$

  where φ is a "loop gain", with $0 < \varphi \leq 1$;
- Add a clean beam Φ_k (with specified width, no side lobes and maximum value $\Phi_0 = 1$) centred at the peak location $\mathbf{r}_k$ and scaled by the peak power level $\tilde{Q}_k^{(i-1)}$ to the clean map:

  $$\tilde{Q}_{n\ CLEAN}^{(i)} = \tilde{Q}_{n\ CLEAN}^{(i-1)} + \varphi \tilde{Q}_k^{(i-1)}\ \Phi_k; \tag{6.60}$$

- Subtract the source-induced CSM $\mathbf{C}_k^{(i)}$ from the previous degraded CSM to obtain the new degraded CSM:

  $$\mathbf{D}^{(i)} = \mathbf{D}^{(i-1)} - \varphi \mathbf{C}_k^{(i)}; \tag{6.61}$$

- Alternatively to Equation 6.59, the new "dirty" map can also be calculated using the new degraded CSM:

  $$\tilde{Q}_n^{(i)} = \mathbf{w}_n^H \mathbf{D}^{(i)} \mathbf{w}_n. \tag{6.62}$$

The above loop is repeated until a stop criterion is reached. One suggested stop criterion is

$$\left\|\mathbf{D}^{(i+1)}\right\|_1 \geq \left\|\mathbf{D}^{(i)}\right\|_1, \tag{6.63}$$

where $\|.\|_1$ is the 1-norm of the degraded CSM; quoting Sijtsma [3], it makes sense to stop if the current degraded CSM contains more "information" than the previous iteration.

After I iterations, the clean map is written as a sum of the clean beams and the remaining dirty map:

$$\tilde{Q}_{n\ CLEAN}^{(I)} = \sum_{i=1}^{I} \tilde{Q}_k^{(i)} \Phi_i + \tilde{Q}_n^{(I)}. \tag{6.64}$$

Note that it is not necessary to know the number of sources in advance. However, the conventional beamforming step requires the user to define a grid of candidate source positions, which in practice limits the number of possible sources the CLEAN algorithm can identify. This is usually of no concern, since usual beamforming grids will often have hundreds or thousands of points, while the number of real sources in an aeroacoustic context is generally much smaller.

6.2.2 CLEAN-SC

The assumption used for CLEAN can become impractical for aeroacoustic applications: sources can be distributed instead of point-like; they can have different acoustic radiation properties, and thus the source map will not be composed of a sum of theoretical PSFs; and we might not have a model for the steering vector $\mathbf{g}$ for a non-point source. In such cases, CLEAN will fall short.

In order to overcome these disadvantages, Sijtsma [3] developed an adaptation of CLEAN based on spatial Source Coherence, named CLEAN-SC, which is described below. The driving idea for CLEAN-SC is that the sidelobes of a source must be coherent with its main lobe, since they originate from the same physical source; thus, they can be empirically identified from the beamforming map, regardless of the source being point-like or not.

First, let us define what is meant by spatial source coherence. For a source at the k-th location and with amplitude q_k, we define the estimate of the expected value of its auto-power $\tilde{Q}_{kk}$ as

$$\tilde{Q}_{kk} = \mathrm{E}\left\{\tilde{q}_k \tilde{q}_k^*\right\} = \mathrm{E}\left\{|\tilde{q}_k|^2\right\} \tag{6.65}$$

$$= \mathbf{w}_k^H \mathbf{C} \mathbf{w}_k, \tag{6.66}$$

and we define the cross-power $\tilde{Q}_{jk}$ between sources at $\mathbf{r}_j$ and $\mathbf{r}_k$ as

$$\tilde{Q}_{jk} = \mathrm{E}\left\{\tilde{q}_j \tilde{q}_k^*\right\} = \mathbf{w}_j^H \mathbf{C} \mathbf{w}_k. \tag{6.67}$$

The expected value of the source auto power is also denoted $\tilde{Q}_k$ (with a single subscript index) in previous sections for convenience, but here it is denoted as $\tilde{Q}_{kk}$ (with a double subscript index) for clarity.

The coherence function γ^2 presented in Eq. 3.57 can be applied in the present context as the ratio between two sources' cross-powers squared and the product of the sources auto-powers:

$$\gamma_{jk}^2 = \frac{|\tilde{Q}_{jk}|^2}{\tilde{Q}_{jj}\tilde{Q}_{kk}} \tag{6.68}$$

$$= \frac{|\mathbf{w}_j^H \mathbf{C} \mathbf{w}_k|^2}{\left(\mathbf{w}_j^H \mathbf{C} \mathbf{w}_j\right)\left(\mathbf{w}_k^H \mathbf{C} \mathbf{w}_k\right)}. \tag{6.69}$$

The coherence function γ_{jk}^2 measures the degree of linear association between two sources, and can assume values $0 \leq \gamma_{jk}^2 \leq 1$ [66]. Thus, for a given beamforming map, we can define one point k as a reference - for example, a main lobe peak - and calculate the coherence between the reference k and all other source points j, thus identifying all other points that are coherent with the given reference. We will call the combination of the reference scan point k and all other points coherent with k as a *coherent source component*; in principle, such source components will contain all sidelobes associated with the chosen main lobe.

Once identified, these coherent components can be subtracted from the source map, similarly to the CLEAN-PSF algorithm:

$$\tilde{Q}_{jj}^{(i)} = \tilde{Q}_{jj}^{(i-1)}\left(1 - \gamma_{jk}^2\right). \tag{6.70}$$

However, this method is not robust to diagonal removal of the CSM, since this procedure can induce negative source autopowers and thus becomes unstable due to a coherence function $\gamma_{jk}^2 \notin [0,1]$ [78].

An alternative approach consists of identifying a "coherent component" $\mathbf{h}_k$, with unitary magnitude and containing the pressures induced at the microphone array by a single coherent source distribution with peak autopower $\tilde{Q}_k$. The CSM induced by this coherent component is then

$$\mathbf{C}_{kk} = \tilde{Q}_k \mathbf{h}_k \mathbf{h}_k^H, \tag{6.71}$$

and it is assumed the source cross-powers $\tilde{Q}_{jk}$ with reference to the source peak $\tilde{Q}_k$ is entirely defined from the coherent component $\mathbf{h}_k$ and its induced CSM $\mathbf{C}_{kk}$ only:

$$\tilde{Q}_{jk} = \mathbf{w}_j^H \mathbf{C} \mathbf{w}_k = \mathbf{w}_j^H \mathbf{C}_{kk} \mathbf{w}_k. \tag{6.72}$$

This source component can then be written as [3]

$$\mathbf{h}_k = \frac{\mathbf{C}\mathbf{w}_k}{\tilde{Q}_k}, \tag{6.73}$$

which allow us to fully determine its induced CSM $\mathbf{C}_{kk}$ and subtract it from the observed CSM $\mathbf{C}$, in the same spirit of the original CLEAN algorithm.

When the observed CSM has had its diagonal elements removed, however, the estimation of the coherent component becomes slightly different: we now define the diagonal-removed induced CSM $\mathbf{C}_{kk}$ as

$$\mathbf{C}_{kk} = \tilde{Q}_k \left(\mathbf{h}_k \mathbf{h}_k^H - \mathbf{H}_k \right), \tag{6.74}$$

where the matrix $\mathbf{H}_k$ contains the diagonal elements of the matrix $\mathbf{h}_k \mathbf{h}_k^H$:

$$\mathbf{H}_k = \operatorname{diag}\left(\mathbf{h}_k \mathbf{h}_k^H \right). \tag{6.75}$$

We then define the coherent component $\mathbf{h}_k$ as [50, 79]

$$\mathbf{h}_k = \frac{1}{\left(1 + \mathbf{w}_k^H \mathbf{H}_k \mathbf{w}_k\right)^{1/2}} \left(\frac{\mathbf{C}\mathbf{w}_k}{\tilde{Q}_k} + \mathbf{H}_k \mathbf{w}_k \right). \tag{6.76}$$

This is not an explicit expression for $\mathbf{h}_k$, since $\mathbf{H}_k$ depends on $\mathbf{h}_k$. We can, however, use the above Equation iteratively if we initialise the coherent component as $\mathbf{h}_k = \mathbf{g}_k$, and then compute its diagonal matrix $\mathbf{H}_k$. This allow us to estimate the coherent component $\mathbf{h}_k$ once again and thus repeat the loop. According to Sijtsma [3], only a few iterations are required for convergence. Our implementation of the algorithm confirms the quick convergence of this approximation.

Once $\mathbf{h}_k$ is identified and its CSM $\mathbf{C}_{kk}$ estimated, it can then be removed from the observed CSM $\mathbf{C}$ as described in the original CLEAN algorithm. The same stop condition can be applied here as well.

6.2.3 Deconvolution Example: Point Sources and Line Source

In order to illustrate the performance of the above mentioned deconvolution algorithms, we simulate a test case consisting of two point monopole sources and one line source. The line source has a length of 20 cm, and is modelled as a distribution of fully coherent monopole sources, all radiating with the same amplitude and phase. The point sources and the line source are incoherent with respect to one another.

We assume an operating frequency of 5 kHz and a mean flow of $U_x = 60$ m/s. The two point monopoles have unitary source power (i.e. $Q_n = 1$), and the line source amplitude was adjusted until the resulting beamforming map displayed similar peak levels for all three sources. The beamforming maps show the estimated auto-powers of the sources in decibels. The levels are normalised with respect to the maximum power observed in each plot, and the dynamic range is limited to 15 dB.

Figure 6.4 compares the results obtained for conventional beamforming (6.4a), CLEAN-PSF (6.4b) and CLEAN-SC (6.4c) when dealing with the proposed source arrangement; the real source locations are indicated with small black stars, and the sources identified by the CLEAN methods are marked with large red stars. Conventional beamforming correctly indicates the three sources as bright zones in the source map, and presents the correct levels for the point

sources; however, the background of the source map contains many sidelobes, and it is difficult to determine whether there might be other low-level sources.

In Figure 6.4b, we can see that CLEAN-PSF has successfully identified all sources and their respective levels as well. Note, however, how CLEAN-PSF "interprets" the line source as a distribution of point sources, and how it also incorrectly locates lower-level sources elsewhere in the map. The final source map background shows some residues, possibly due to the line source sidelobes that were not correctly removed; the final map is not very "clean" and it does not provide much information about the line source characteristics.

Figure 6.4c shows the final CLEAN-SC map. We can observe that CLEAN-SC managed to correctly identify all three sources, while also "cleaning" the source map background of all residues. Figure 6.5 compares the final CLEAN-SC map with the first three coherent source components identified by the method, allowing for a more detailed analysis. The first component, corresponding to the line source, is shown in Figure 6.5b; while the source location has been defined at the source map peak, the coherent component structure correctly accounts for the extended length of this particular source, while also considering all its sidelobes. Figures 6.5c and 6.5d show the next two components, corresponding to the two point sources; their location and peak levels have been correctly identified as well, and some of their sidelobe structure is very similar to that of the PSFs previously shown in Figure 6.2.

Let us also compare the source powers identified by CLEAN-PSF and CLEAN-SC. Figure 6.6 plots the peak source powers as a function of source index for both methods. It can be observed how CLEAN-PSF successively identifies point sources in a slowly decreasing fashion. This is an indication of how CLEAN-PSF tries to account for the line source (and possibly its sidelobes) by using a sequence of incoherent point sources over the actual source location. Still, despite identifying 10 point sources, the remaining "dirty" map still contains a significant amount of sidelobes, indicating a poor performance of this method when dealing with distributed, coherent sources.

On the other hand, CLEAN-SC identifies five sources, with the first three displaying levels similar to the first three sources found by CLEAN-PSF. However, the remaining two sources identified by CLEAN-SC have significantly lower levels than the others, and can be ignored. Hence, CLEAN-SC can deal with the distributed nature of the line source much more gracefully than CLEAN-PSF.

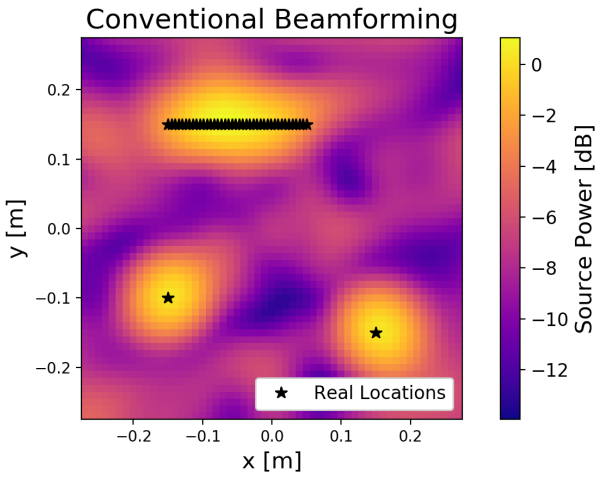

(a)

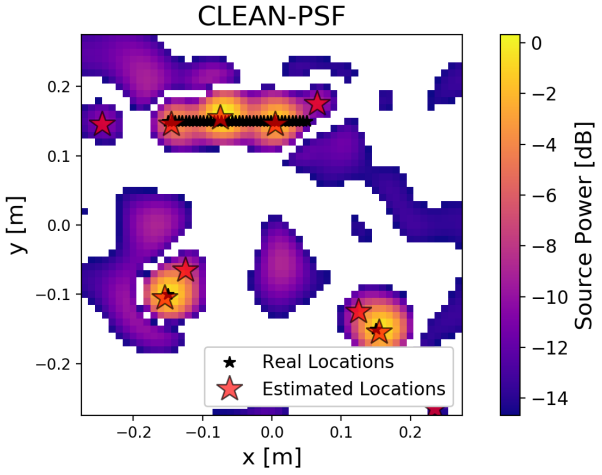

(b)

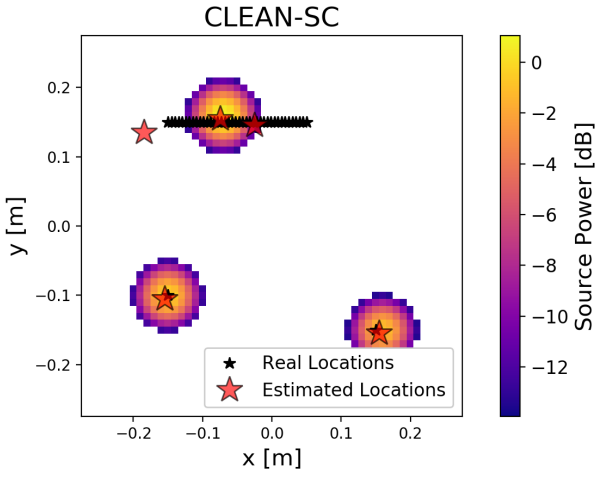

(c)

Figure 6.4: Beamforming maps of two point sources and a line source, at narrowband frequency of 5 kHz and plotted in normalised decibels; mean flow direction is left to right. (a) conventional beamforming; (b) deconvolution using CLEAN-PSF; (c) deconvolution using CLEAN-SC.

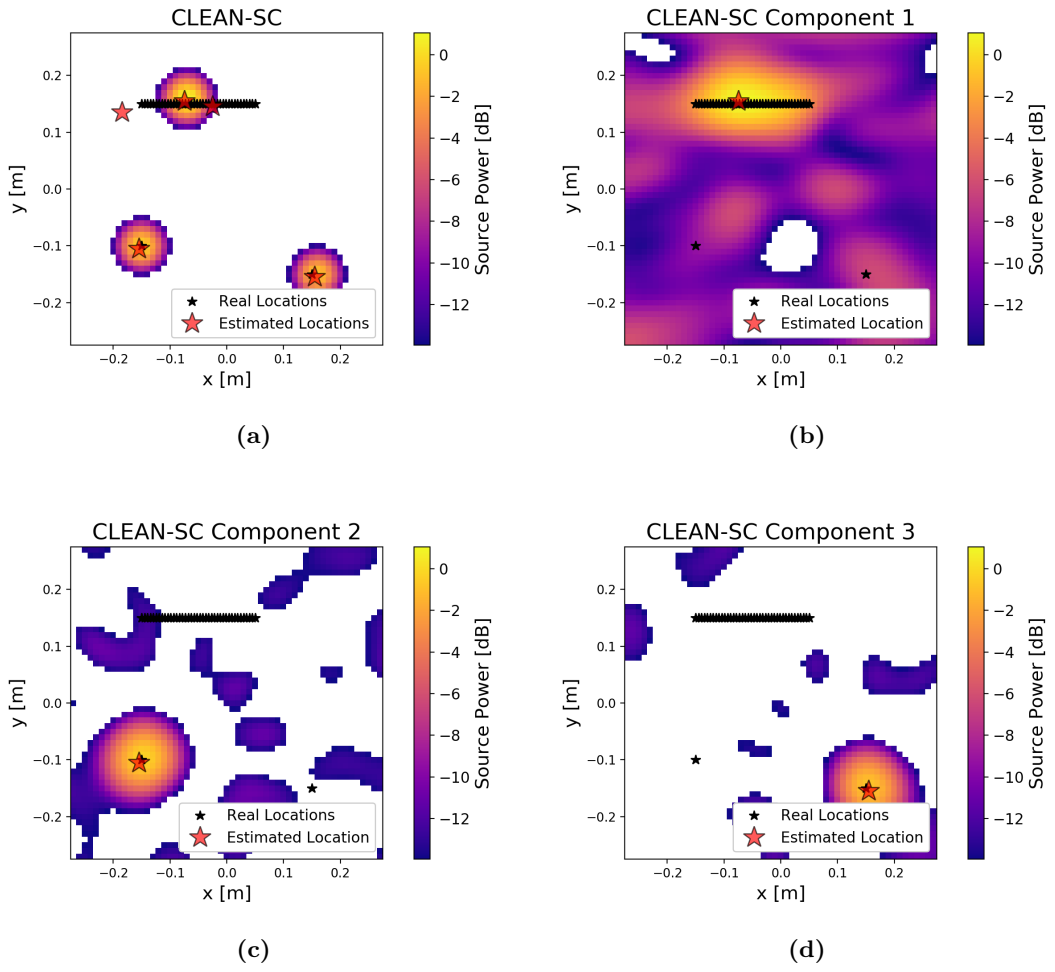

Figure 6.5: CLEAN-PSF map of two point sources and a line source, at narrowband frequency of 5 kHz and plotted in normalised decibels; mean flow direction is left to right. (a) "clean" map; (b) coherent source component 1; (c) coherent source component 2; and (d) coherent source component 3.

6.3 Beamforming Results for Aerofoil Interaction Noise

6.3.1 Simulated Conventional Beamforming Results

We now use the turbulence-aerofoil interaction model developed in Chapters 3 and 4 to simulate the performance of the near-field microphone array when observing leading edge noise. We use the geometry shown in Figure 6.1, but we now include shear layer refraction effects to model the ISVR open jet wind tunnel and allow for a more direct comparison between the simulated and the experimental results. As described in Section 5.1.1, the aerofoil is positioned in the jet core at the plane $z = 0$, and the planar shear layer is located at $z_l = -7.5$ cm. The temporal freuency is $f = 5$ kHz (approx. $k_0 c = 13.8$), and the mean flow velocity is $U_x = 60$ m/s. The

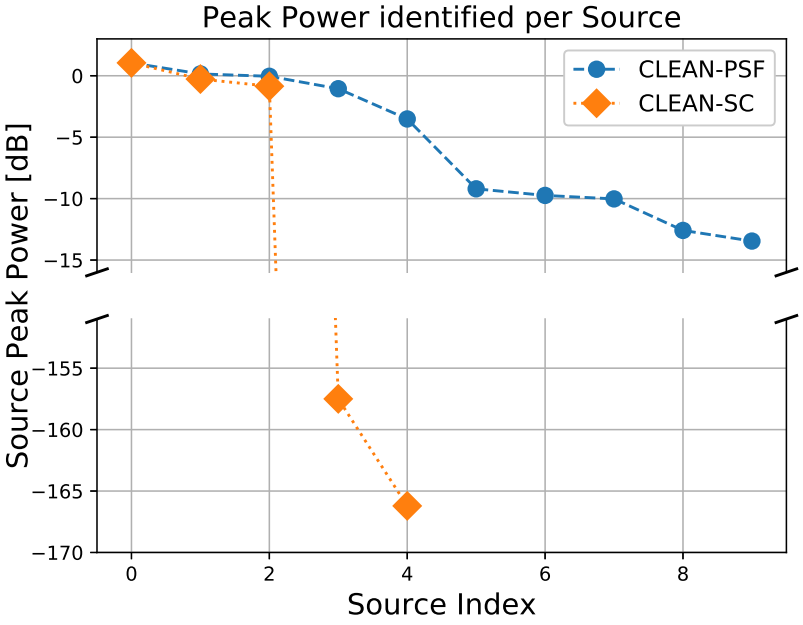

Figure 6.6: Peak source power identified via CLEAN-PSF and CLEAN-SC deconvolution methods as a function of source index. Vertical axis has been "cut" to show the discrepancy between the first three and the last two source powers identified via CLEAN-SC.

shear layer effects are modelled using the dipole transfer function defined in Eq. 2.144, and this same transfer function is used to compute the conventional beamforming steering vectors.

In Section 4.2.1, we discussed the gust integration limits for aerofoil acoustic predictions. It was proposed that at high frequencies, only supercritical gusts are acoustically relevant and should be integrated when predicting leading edge acoustic radiation. Let us now compare the effect of adding subcritical gusts to conventional beamforming source maps: Figure 6.7 shows the simulated conventional beamforming maps obtained when integrating the acoustic contributions of supercritical gusts only ($k_\psi \in [-k_\psi^{crit}, +k_\psi^{crit}]$, Fig. 6.7a) and when doubling the gust integration range and integrating both supercritical and subcritical gusts ($k_\psi \in [-2k_\psi^{crit}, +2k_\psi^{crit}]$, Fig. 6.7b). Both source maps are essentially identical, so it can be concluded that subcritical gusts do not play a significant role for beamforming at these frequencies.

From a more general perspective, the beamforming maps present an almost uniform source strength distribution over the aerofoil leading edge, as expected. Some low-level structures can be observed near the trailing edge and downstream of the aerofoil, possibly due to sidelobes; given the extended nature of the source under consideration, these sidelobe structures cannot be directly compared to the sidelobes seen in the array PSF.

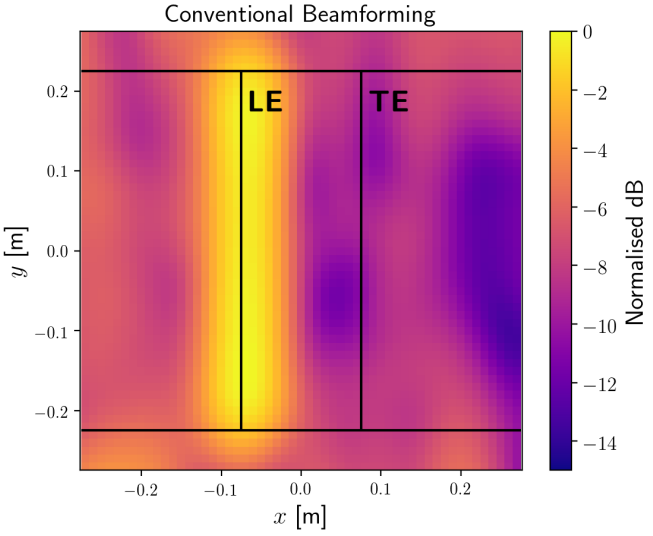

(a)

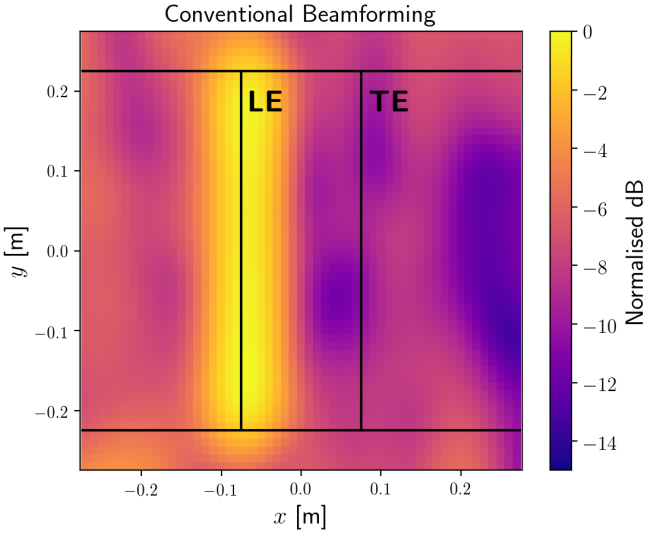

(b)

Figure 6.7: Simulated Conventional Beamforming source map obtained from turbulence-flat plate interaction noise model at narrowband frequency 5 kHz; (a) using supercritical gusts only; (b) using supercritical and subcritical gusts.

6.3.2 Simulated CLEAN-SC Results

Let us now apply CLEAN-SC to the simulated beamforming maps. Figure 6.8a shows the CLEAN-SC map for the supercritical-only case, with the first ten coherent source components indicated as red stars; of these, the three largest coherent source components are shown individually in Figs. 6.8b to 6.8d. The results for the supercritical-plus-subcritical case are essentially identical and are not shown. As expected, the CLEAN-SC method identifies a series of sources more or less uniformly spread along the aerofoil leading edge, all displaying similar levels.

It is interesting to observe how CLEAN-SC deals with the simulated aerofoil, which bears some similarities to a partially-coherent line source. The first coherent source component, shown in Fig. 6.8b, contains a main lobe near the lower span end, but it also displays an extended sidelobe in the spanwise direction, along the aerofoil leading edge. This could indicate that sections of the leading edge at mid-span are partially coherent with the peak. This behaviour is observed in a weaker manner for the second source component (Fig. 6.8c), but not observed for the third source component (Fig. 6.8d).

In Section 3.2.4, it was shown that the aerofoil surface pressure jump has a very short coherence length near the leading edge at these frequencies; see, for example, Figs. 3.15 and 3.16. On the other hand, the CLEAN-SC coherent source components appear to indicate a much longer coherence length for leading edge sources. We propose two possible explanations to this difference: the short coherence lengths arise from the integrating a wide range of subcritical gusts, which are by nature acoustically weak and might not be "seen" by the microphone array. Alternatively, this result can also be due the finite resolution capabilities of the microphone array, which would naturally "smear out" short coherence lengths into wider regions, in a similar manner to how a point source is smeared out into a PSF when seen by a microphone array. At the moment, it is unknown whether one of the two explanations - or a combination of both - is the main cause of this effect.

6.3.3 Experimental Beamforming Results

We now use the experimental data presented in Chapter 5 to estimate the source strength distribution over the aerofoils using the conventional beamforming algorithm and the CLEAN-SC

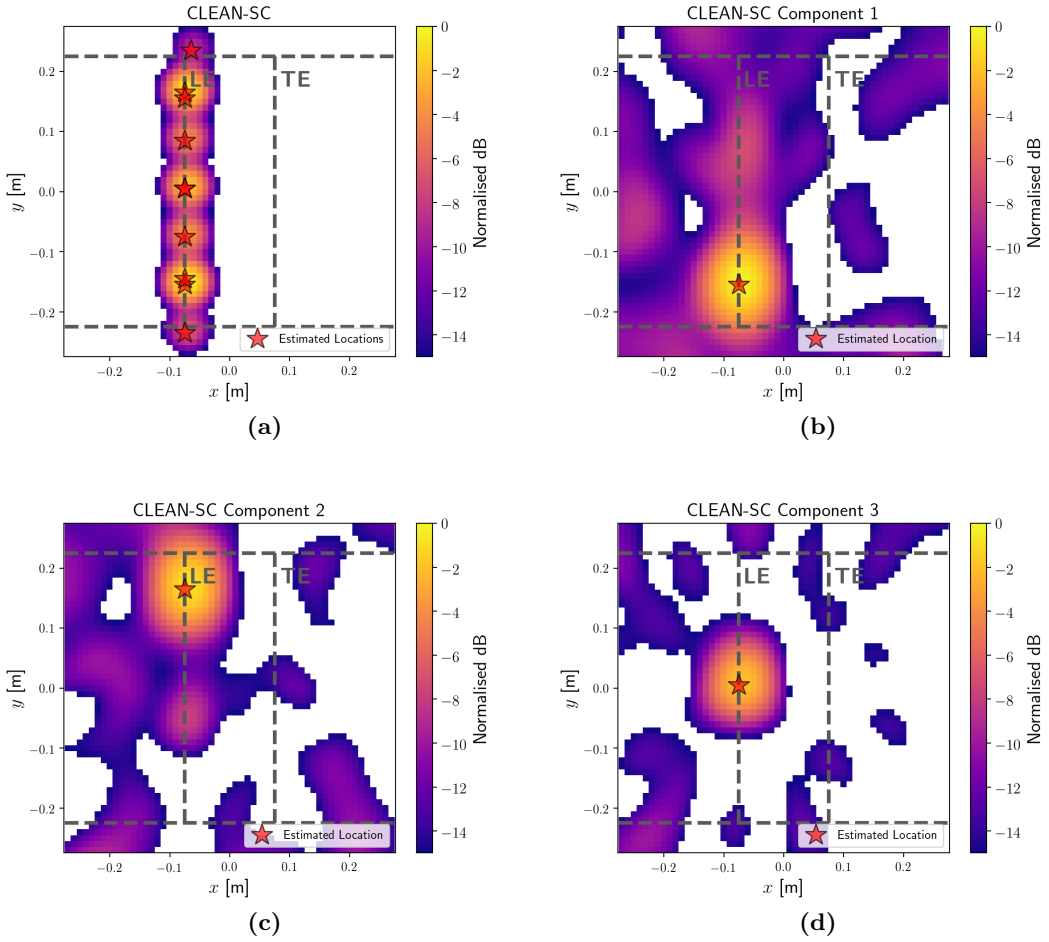

Figure 6.8: Simulated CLEAN-SC results for turbulence-flat plate interaction simulation using supercritical gusts only: (a) "clean" map; (b) coherent source component 1; (c) coherent source component 2; and (d) coherent source component 3.

deconvolution algorithm. The goal for this section is to present some typical results of conventional beamforming array processing and compare them with the predicted results shown in the previous section.

For the sake of brevity, we will focus on the results of a small selection of aerofoils with straight leading edge at 0° angle of attack, 60 m/s flow speed and at a narrowband temporal frequency of $f = 5$ kHz. The turbulence grid was installed at the tunnel nozzle, and should induce leading edge noise on all aerofoils, although some level of trailing edge noise is known to be present from previous experiments. The aerofoils to be shown are a flat plate, a NACA651210 aerofoil and a NACA0012 aerofoil.

As previously mentioned, the steering vectors are calculated using in-flow, dipole transfer functions, and also take into account the shear layer propagation correction presented in Eq.

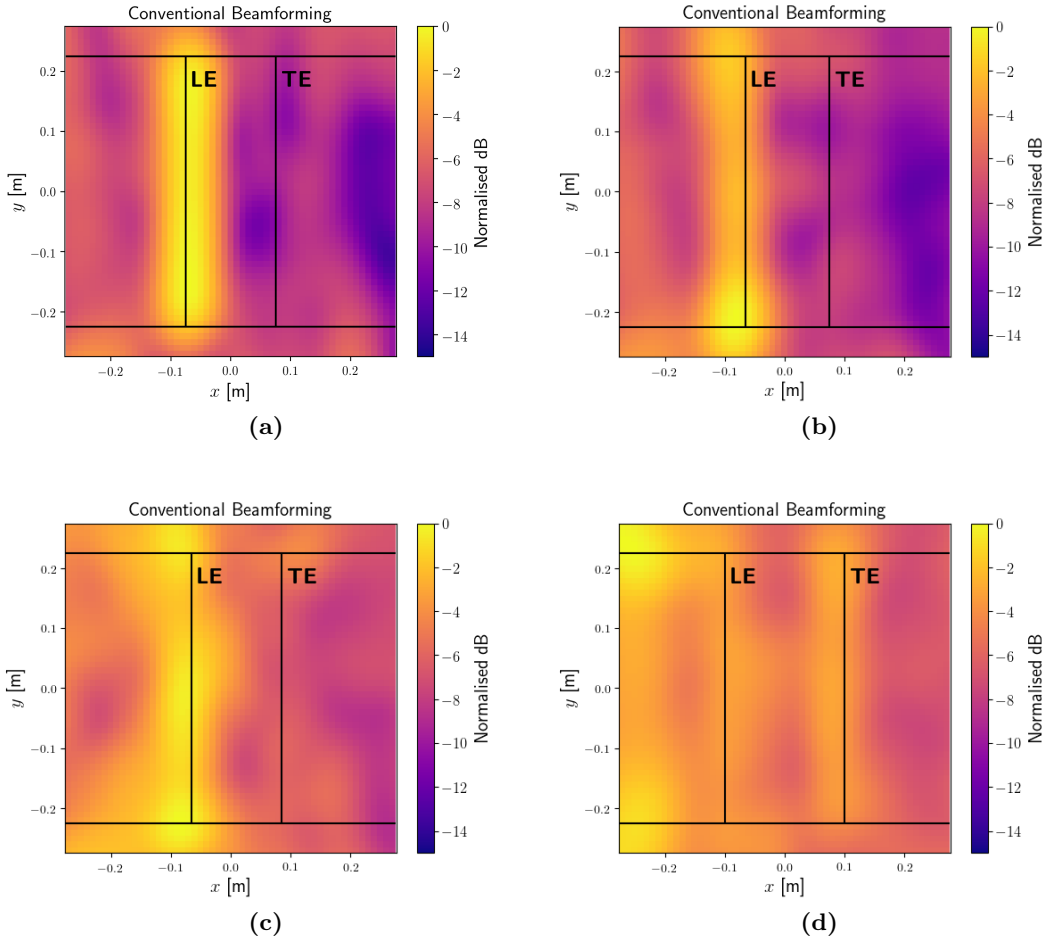

Figure 6.9: Experimental Conventional Beamforming source maps for different aerofoils at narrowband frequency of 5 kHz and plotted in normalised decibels; mean flow direction is left to right. (a) Simulated flat plate aerofoil; (b) measured flat plate aerofoil; (c) measured NACA651210 aerofoil; (d) measured NACA0012 aerofoil.

2.144. As the levels are normalised with respect to the maximum power observed in each plot, the different beamforming plots are not comparable amongst each other.

Figure 6.9a shows the beamforming map for the simulated flat plate, while Figure 6.9b shows the measured flat plate beamforming map. A good agreement can be observed between the two maps, particularly at the sidelobe structure downstream of the trailing edge. The leading edge can be clearly seen as the dominant source, with an approximately uniform span distribution, but the aerofoil span ends show high acoustic power in the experimental map. Such "corner sources" have been previously reported in the literature [79, 80], and are associated with turbulent flow at the junction of the aerofoil to the sideplates. Trailing edge sources are not visible in this map, and neither are sources located outside the aerofoil surface.

Figure 6.9c shows the beamforming map for the NACA651210 aerofoil. This beamforming map shows a less uniform distribution of sources over the leading edge span when compared to the flat plate case, but the leading edge region still appears to be the dominant source region. The beamforming map in general appears to be "noisier", with more "hot spots" near the trailing edge than the flat plate.

Figure 6.9d shows the beamforming map for the NACA0012 aerofoil. The leading edge radiation is relatively weaker compared to the previous cases, and the trailing edge radiation is now significantly stronger, with a clear source distribution observable near that region. The plot also shows two point-like sources appearing upstream of the aerofoil leading edge, at the same direction as the aerofoil span tips; the origin of these sources has not been identified.

In order to verify the relative strength of leading versus trailing edge noise observed in the beamforming maps, we compare the PSD seen by the mid-span, far-field microphone at 90° for measurements performed with and without the turbulence-generating grid in the wind tunnel nozzle: measurements performed without the grid should display trailing edge noise only, while measurements performed with the grid should exhibit leading and trailing edge noise.

These are shown in Figure 6.10 for the three aerofoils under consideration: the vertical dotted line marks the 5 kHz frequency at which we applied beamforming, and the wind tunnel background noise level is shown as a dash-dotted line. Note the significant level difference at 5 kHz for the flat plate case (Fig. 6.10a - approx. 10 dB), indicating a dominance of leading edge noise. A smaller level difference can be observed for the NACA651210 aerofoil (Fig. 6.10b - approx. 4 dB), and an even smaller difference for the NACA0012 aerofoil (Fig. 6.10c - approx. 2 dB), indicating a relative increase in the trailing edge noise contribution for the two latter aerofoils and validating the beamforming results. Note as well how the NACA0012 levels are very close to the wind tunnel background noise level, indicating a poor signal-to-noise ratio at the frequency of interest.

6.3.4 Experimental CLEAN-SC Results

We now apply the CLEAN-SC deconvolution algorithm to the measured results, using a loop gain of $\varphi = 0.95$. The ten first coherent source component locations are indicated with stars on the "clean map", and the three first components are also shown individually for a more in-depth investigation.

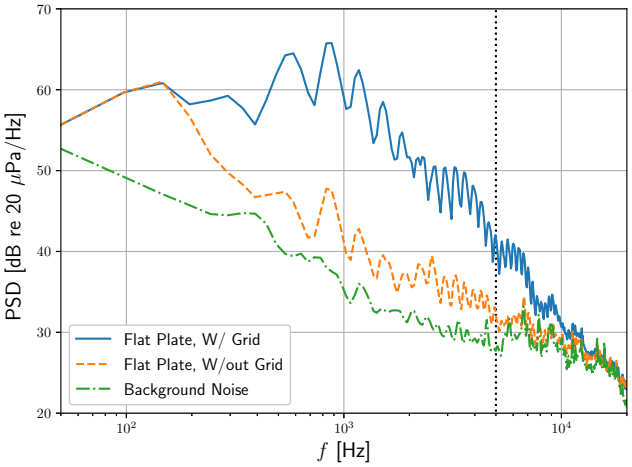

(a)

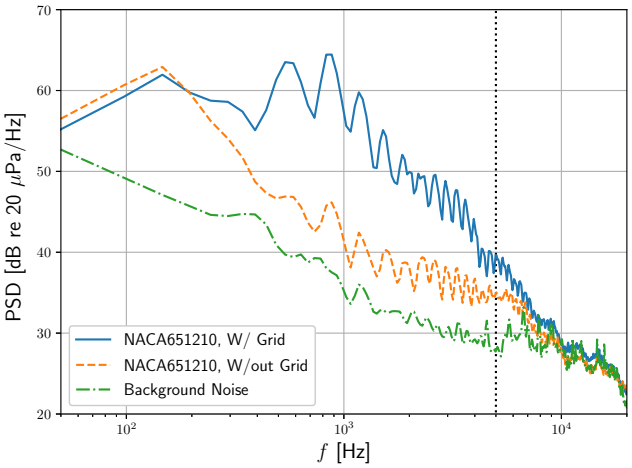

(b)

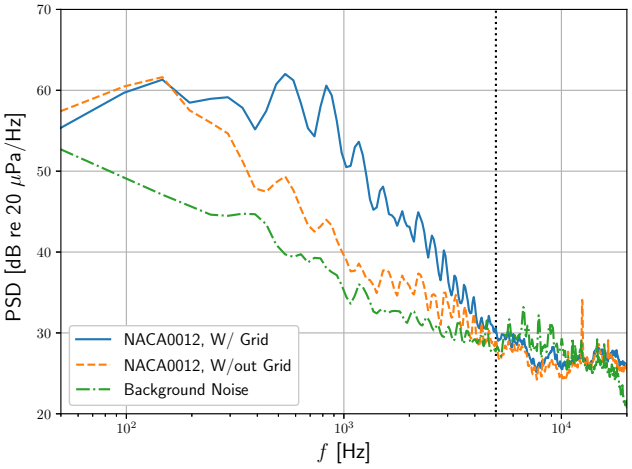

(c)

Figure 6.10: Measured aerofoil acoustic PSD for observer at mid-span, 90°, for measurements performed with (solid line) and without (dashed line) a turbulence-generating grid at the wind tunnel nozzle: (a): flat plate aerofoil; (b): NACA651210 aerofoil; (c): NACA0012 aerofoil. The vertical dotted line marks the 5 kHz frequency used in the beamforming plots, and the wind tunnel background noise level is shown as a dash-dotted line.

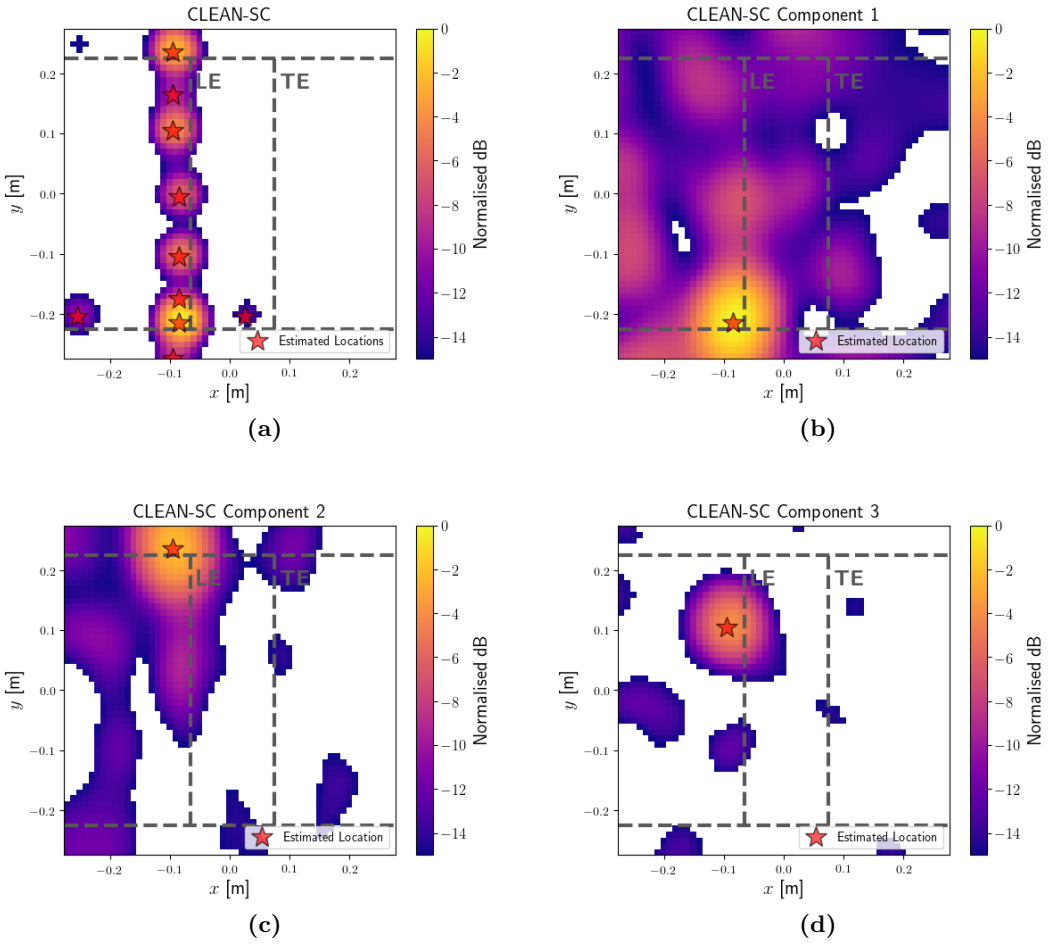

Figure 6.11: CLEAN-SC results for flat plate beamforming measurements: (a) "clean" map; (b) coherent source component 1; (c) coherent source component 2; and (d) coherent source component 3.

6.3.4.1 Flat Plate Aerofoil

Figure 6.11 shows the CLEAN-SC results for the flat plate aerofoil. The sources are almost all evenly spaced over the aerofoil leading edge, with a few low-amplitude sources located away from the leading edge.

When compared to the simulation results in Fig. 6.8, there is a very good qualitative agreement between the resulting source maps. In particular, the first two coherent source components in both cases display extended sidelobes towards the leading edge at mid-span, which as previously discussed might be an indication of significant coherence between different span regions. The sidelobe structure is also similar, although some slight differences can be noted.

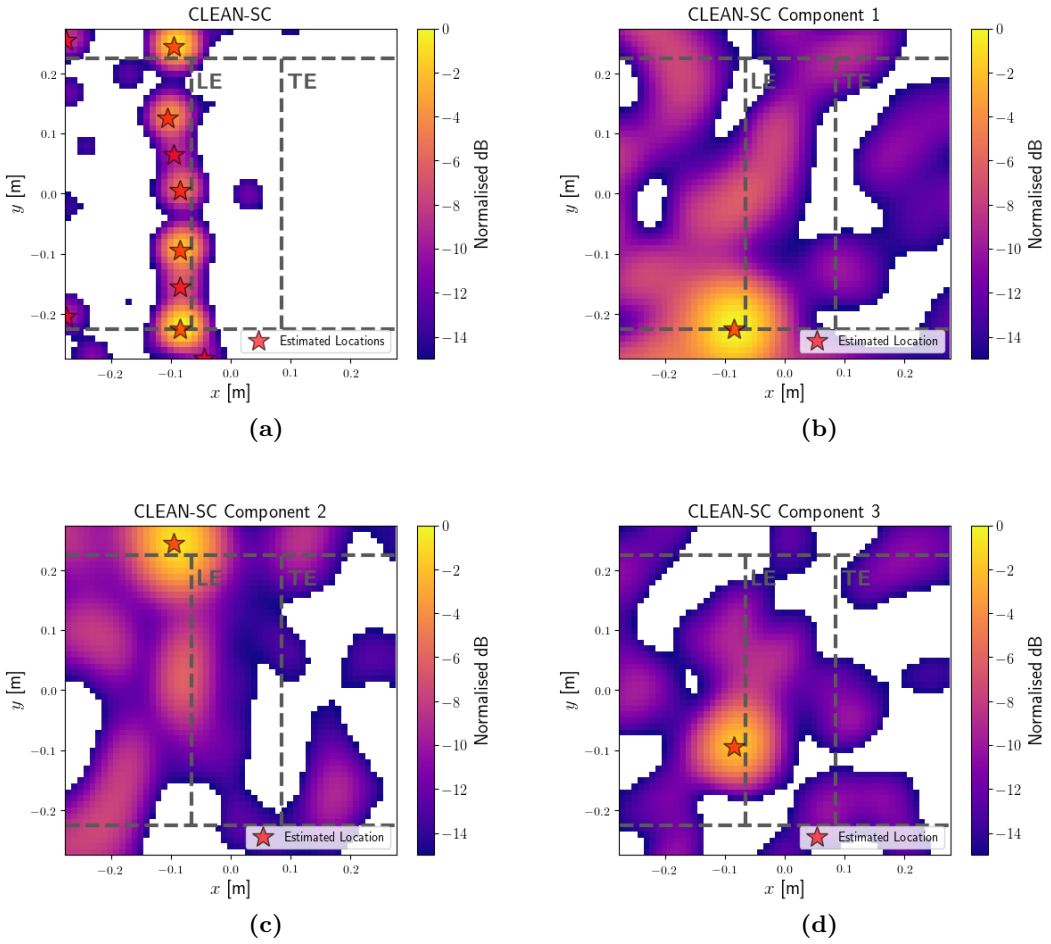

Figure 6.12: CLEAN-SC results for NACA651210 beamforming measurements: (a) "clean" map; (b) coherent source component 1; (c) coherent source component 2; and (d) coherent source component 3.

6.3.4.2 NACA651210 Aerofoil

Figure 6.12 shows the CLEAN-SC result for the NACA651210 aerofoil. Once again, a series of source components were identified along the leading edge, with the two dominant sources located at the span ends and the third source located near mid-span. The individual source components appear to show a more complex sidelobe structure in this case when compared to the flat plate aerofoil, and is still different from the array PSF. However, the source components again display extended sidelobes towards the leading edge mid-span.

6.3.4.3 NACA0012 Aerofoil

Figure 6.13 shows the CLEAN-SC result for the NACA0012 aerofoil. In this case, the deconvolution algorithm was unable to identify the leading edge sources; instead, it identified two strong point-like sources upstream of the aerofoil leading edge and two small sources at the aerofoil span ends. While not shown here, conventional beamforming maps for this same test case at different frequencies show the same point sources upstream of the aerofoil, indicating these are possibly parasitic sources from the wind tunnel apparatus.

While the beamforming map shows that these parasitic sources appear stronger than the leading edge sources, we expected the CLEAN-SC algorithm would be able to identify acoustic sources at the leading edge or at the trailing edge after removing the parasitic sources. Its failure in doing so could have been caused by the poor signal-to-noise ratio obtained for this particular aerofoil at this frequency range, as previously mentioned.

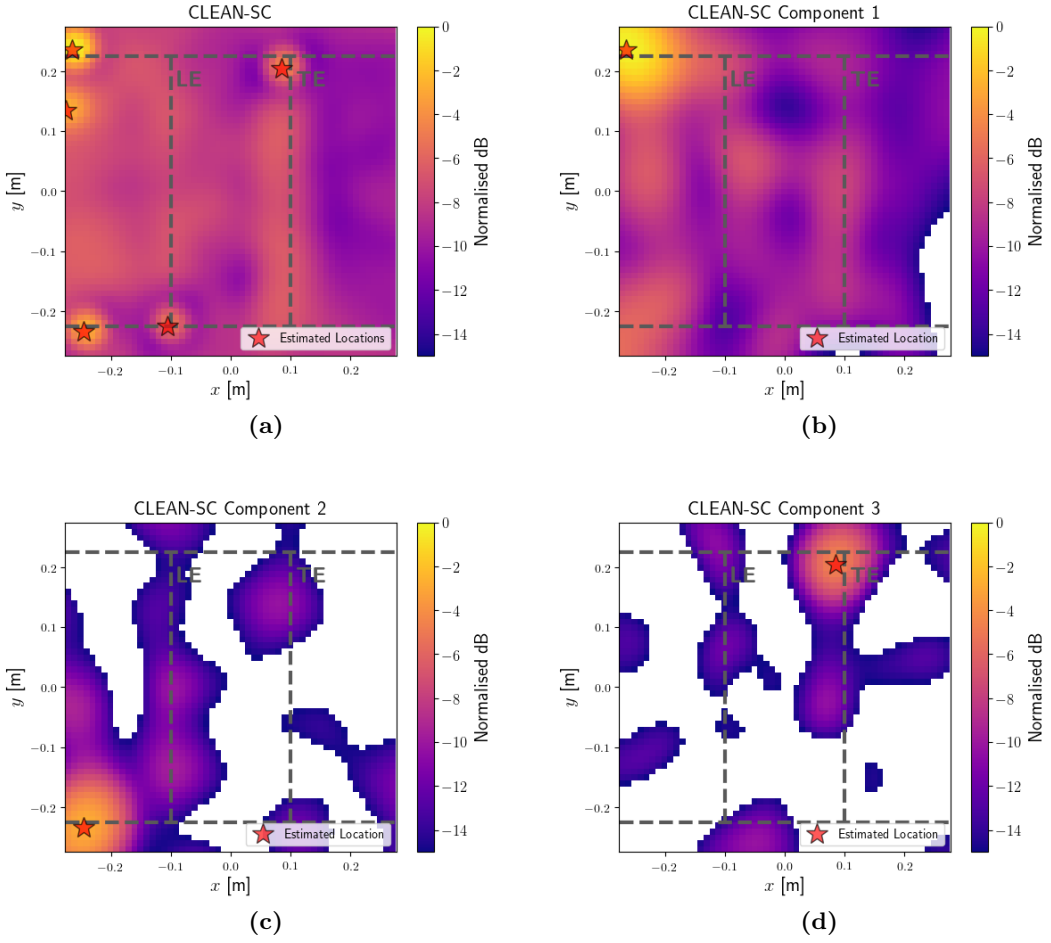

Figure 6.13: CLEAN-SC results for NACA0012 beamforming measurements: (a) "clean" map; (b) coherent source component 1; (c) coherent source component 2; and (d) coherent source component 3.

Chapter 7

Far-Field Inversion for Planar Sources in Flow

In this Chapter, we invert the relationship between the aerofoil surface pressure wavenumber spectrum and its radiated far-field, described in Chapter 2, and introduce a Fourier-based method for estimating the aerofoil surface pressure distribution from far-field acoustic pressure measurements.

We first discuss the consequences of using far-field data only for estimating a planar source distribution in flow. As only wavenumbers within the radiation ellipse are "visible" in the far-field, any source reconstruction method based on far-field data is bandlimited to these wavenumbers only. The lack of high spatial frequencies imposes a degree of smoothness in the estimated source distribution, as fine spatial details cannot be recovered.

We present two implementations of this method. The first assumes an arbitrary far-field microphone array layout. As no constraints are placed on the microphone locations, the equivalent wavenumber sampling might be non-uniform, and the Inverse Spatial Fourier Transform must take this into account. We simulate the performance of this method for estimating the aerofoil surface pressure jump cross-spectrum using a hemispherical array, discuss the estimated source power spectral density, phase and coherence characteristics, and compare them to the original aerofoil characteristics.

In the second implementation, we first impose a uniform sampling in the bandlimited wavenumber domain, and consider a Nyquist-type source sampling in the spatial domain. The Inverse Spatial Fourier Transform is shown to become an Inverse Discrete Fourier Transform (IDFT) under these assumptions, and the microphone array geometry can be obtained from the wavenumber-domain samples. We use this method to recover the complex source strength of a simplified one-dimensional source, and analyse whether the far-field-estimated source distribution can correctly describe the far-field radiation of the original source.

Finally, we have identified from the optics literature a super-resolution source estimation method that could possibly be applied in tandem with our proposed framework [81]. We briefly discuss the basis and some limitations of this method, but leave an in-depth feasibility investigation for future work.

7.1 Fourier Approach for Far-Field Source Reconstruction

It is well known that conventional beamforming, presented in Chapter 6, allows for a great degree of flexibility regarding the microphone array configuration, as it does not impose any special requirements for the spatial sampling of the sound field and can be used with arbitrary microphone array geometries. However, source estimation via beamforming can be inaccurate due to its finite spatial resolution and sidelobes, as discussed in Section 6.1.1 and expressed by a non-diagonal PSF matrix $\mathbf{W}^H\mathbf{G}$ (Eq. 6.20) relating the original and the estimated source strength vectors.

In Section 2.3.4 we have shown that by restricting the observer locations to a hemisphere in the far field, the acoustic field seen by a distant observer is directly related to the source strength wavenumber spectrum evaluated at a single wavenumber inside the radiation ellipse. This relationship can be said to *diagonalise* the radiation integral operator, as each observer is dependent on a single wavenumber component. Diagonal operators are of special interest for being easier to analyse and, especially, easy to invert. It is then natural to consider inverting the above described relationship and obtain expressions for source strength estimation from far-field acoustic data.

Assuming a distribution of dipole sources, it is possible to invert Equation 2.109 to estimate the source strength at a single wavenumber $\hat{\mathbf{k}} = (\hat{k}_x, \hat{k}_y)$ inside the radiation ellipse from the observed acoustic far-field at the observer location $\mathbf{r}$:

$$\tilde{Q}\left(\hat{\mathbf{k}},\omega\right) \approx \frac{1}{(2\pi)^2}\left(jk_0\frac{z}{\sigma_{\mathbf{r}}}\frac{e^{-j\hat{\mathbf{k}}\cdot\mathbf{r}}}{4\pi\sigma_{\mathbf{r}}}\right)^{-1} p(\mathbf{r},\omega). \tag{7.1}$$

If one would know the acoustic far-field $p(\mathbf{r},\omega)$ over the entire (continuous) hemisphere, it would be possible to estimate the source strength spatial distribution via an Inverse Spatial Fourier Transform (Eq. 2.29) of the estimated source strength wavenumber spectrum evaluated at all wavenumbers inside the radiation ellipse:

$$\tilde{q}(\mathbf{r}_s,\omega) = \int_{k_x}\int_{k_y} \tilde{Q}(\mathbf{k},\omega)e^{-j\mathbf{k}\cdot\mathbf{r}_s}\,\mathrm{d}k_x\,\mathrm{d}k_y, \qquad (k_x,k_y)\in \text{Rad Ellipse}. \tag{7.2}$$

In practice, measurements of an acoustic far-field must be performed with an array of discrete microphones, and hence the wavenumber domain is necessarily sampled and the Fourier Transform must be discretized.

The problem can then be approached from two perspectives. One is by fixing the microphone array geometry and obtaining its equivalent wavenumber sampling, as discussed in Section 7.2. The second is by fixing the wavenumber sampling and obtaining the equivalent microphone array geometry, as discussed in Section 7.3.

7.1.1 Source Estimation from Limited Wavenumber-Domain Information

Before introducing the proposed methods, we discuss the effects of source reconstruction from far-field data. Equation 7.2 illustrates one limitation of the proposed framework: even from knowledge of the entire radiated far-field in all directions, the "visible" information in wavenumber domain is limited to the "acoustic domain" [51] inside the radiation ellipse. That is, only wavenumber components that correspond to propagating plane waves are observable; wavenumbers outside of the radiation ellipse represent evanescent waves, which are by definition "invisible" in the far-field and cannot be included in the inversion process. This effective "wavenumber windowing" has severe consequences for source estimation, as we describe below.

Real acoustic sources, such as an aerofoil, have finite dimensions - i.e. are spatially *bounded*. From the properties of the Fourier Transform, its source wavenumber spectrum must then be: *unbounded*, i.e. extend to infinity [82]; and it must be an *analytic function*, i.e. infinitely

differentiable [81]. By estimating the source strength from far-field data only, we are essentially taking the Inverse Fourier Transform of a windowed version of the original wavenumber spectrum, as described in Eq. 7.2. As such, the estimated source strength distribution is forced to become *band-limited*, as the estimated spectrum is now *bounded*.

However, by ignoring the wavenumbers outside the radiation ellipse, the estimated source strength distribution becomes spatially low-passed, and exhibits a lower spatial resolution than the original source. This "spatial smearing" effect is solely determined by observing the source from the far-field, as high spatial frequency phenomena are not efficient far-field sources and cannot be observed. Note that a similar but distinct "spatial smearing" effect when estimating a source arises from a microphone array point spread function (PSF), previously discussed in Section 6.1.1, which describes the finite resolution capability of a given microphone array. Despite having similar consequences for source estimation, both effects have different origins and should be interpreted separately.

It must be noted that bandpassing the source spectrum also forces the source distribution to become spatially *unbounded* [81]. As such, the estimated source distribution becomes smeared over all space, beyond the physical limits of the real source. While in principle one could simply ignore the "extra" source distribution as physically insignificant and consider only the source terms that fall within the real aerofoil dimensions, we describe further below that these extra terms are important to accurately describe the acoustic source radiated far-field.

7.2 Far-Field Inversion with Arbitrary Wavenumber Sampling

We now return to the proposed far-field inversion method for arbitrary distributions of microphones in far-field, hemispherical array geometries. Let us consider an arbitrary sampling of the far-field hemisphere - and thus, of the wavenumber space as well. Figure 7.1 shows a far-field hemispherical array covering the entire angular space above the source as an example, and its corresponding wavenumber-domain sampling.

The two-dimensional wavenumber integration in Eq. 7.2 is discretised and expressed as a single sum over the M microphone elements:

$$\tilde{q}(x_s, y_s, \omega) \approx \sum_{m=1}^{M} \tilde{Q}_m \left(\hat{k}_{xm}, \hat{k}_{ym}, \omega\right) e^{-j\hat{k}_{xm}x_s} e^{-j\hat{k}_{ym}y_s} \; \Delta S_m, \tag{7.3}$$

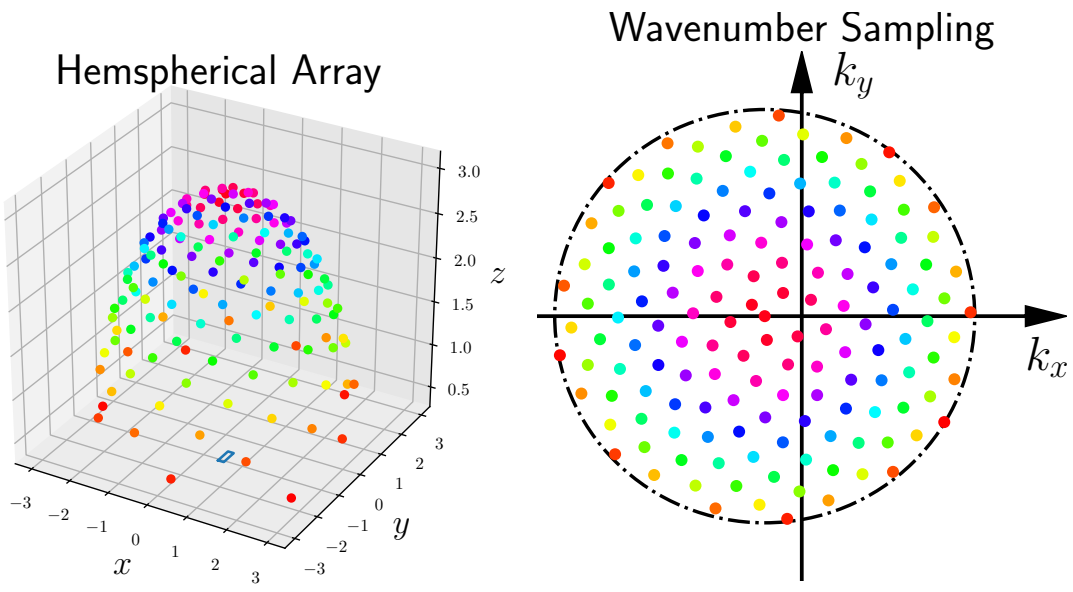

Figure 7.1: Full hemispherical microphone array (left) and corresponding wavenumber-domain sampling (right).

where $\tilde{Q}_m\left(\hat{k}_{xm}, \hat{k}_{ym}, \omega\right)$ is the estimated wavenumber spectrum corresponding to the m-th microphone, and ΔS_m is an equivalent area in the two-dimensional wavenumber domain associated with the m-th sample. These area terms are further explained in section 7.2.1 below.

The above expression for the source wavenumber spectrum can be rewritten as a function of the acoustic pressure $p(\mathbf{r}_m)$ measured at the array microphones. By applying the far-field approximation in Eq. 7.1 to the Inverse Fourier Transform in Eq. 7.3, we obtain

$$\tilde{q}(x_s, y_s, \omega) \approx \frac{1}{(2\pi)^2} \sum_{m=1}^{M} \left[\left(jk_0 \frac{z_m}{\sigma_m} \frac{e^{-j\hat{\mathbf{k}}_m \cdot \mathbf{r}_m}}{4\pi\sigma_m} \right)^{-1} p(\mathbf{r}_m, \omega) \right] e^{-j\hat{\mathbf{k}}_m \cdot \mathbf{r}_s} \, \Delta S_m \tag{7.4}$$

$$= \frac{1}{(2\pi)^2} \sum_{m=1}^{M} \left(jk_0 \frac{z_m}{\sigma_m} \frac{e^{-j\hat{\mathbf{k}}_m \cdot (\mathbf{r}_m - \mathbf{r}_s)}}{4\pi\sigma_m} \right)^{-1} p(\mathbf{r}_m, \omega) \, \Delta S_m \tag{7.5}$$

$$= \frac{1}{(2\pi)^2} \sum_{m=1}^{M} \left(\frac{\partial}{\partial z_s} G_{FF}(\mathbf{r}_m | \mathbf{r}_s, \omega) \right)^{-1} p(\mathbf{r}_m, \omega) \, \Delta S_m, \tag{7.6}$$

where $\partial G_{FF}/\partial z_s$ is the far-field approximation to the convected dipole transfer function between a given source point $\mathbf{r}_s$ and the m-th observer location $\mathbf{r}_m$, previously presented in Eq. 2.98.

One can interpret the procedure outlined in Eq. 7.6 as back-propagating the plane waves seen by the far-field observers, while also compensating for the dipole directivity and amplitude

decay over distance. Each back-propagated plane wave is then projected over the source points $\mathbf{r}_s$, and the sum of all projections constitutes the estimated source strength distribution.

Note that the proposed inversion method in Equation 7.6 is very similar to the frequency-domain delay-and-sum beamforming algorithm [1], where the proposed steering vector elements $w_{(m,n)}$ (as per Eq. 6.4) are proportional to the element-wise inverse of the transfer matrix elements:

$$w_{(m,n)} = \frac{1}{(2\pi)^2}\left[\frac{\partial}{\partial z_s} G^*_{FF}(\mathbf{r}_m|\mathbf{r}_n,\omega)\right]^{-1} \Delta S_m. \tag{7.7}$$

7.2.1 Wavenumber-Domain Equivalent Areas

In order to consider a possibly uneven sampling of the array visibility region, we propose calculating the areas ΔS_m using a modified Voronoi diagram of the wavenumber samples, as shown in Figure 7.2 for the full hemispherical array shown in Figure 7.1.

A Voronoi diagram is a division of a plane into Voronoi cells from a set of seeds, where the m-th cell is a convex polygon around the m-th seed and contains all points that are closer to the m-th seed than to any other seed [83]. This diagram is calculated using the Python package *scipy.spatial.Voronoi* [57], where the seeds are the wavenumber samples of the microphone array. The cells are denoted by their corresponding vertices, from which the cell areas ΔS_m can be calculated. In addition, to avoid allocating a disproportionately large area to microphones at the edges of the diagram, vertices located out of the radiation ellipse are scaled and repositioned close to the ellipse.

7.2.2 Inverse Equation for Source Cross-Spectrum

As aeroacoustic sources are often broadband in nature, we now obtain expressions for estimating the source cross-power spectral density. From Eq. 3.58, we can express the source cross-power spectral density in spatial domain from the cross-power spectral density in the wavenumber domain as

$$S_{qq'}(\mathbf{r}_s,\mathbf{r}'_s,\omega) = \int\int S_{QQ'}(\mathbf{k},\mathbf{k}',\omega) e^{-j(\mathbf{k}\cdot\mathbf{r}_s - \mathbf{k}'\cdot\mathbf{r}'_s)}\,\mathrm{d}\mathbf{k}\,\mathrm{d}\mathbf{k}'. \tag{7.8}$$

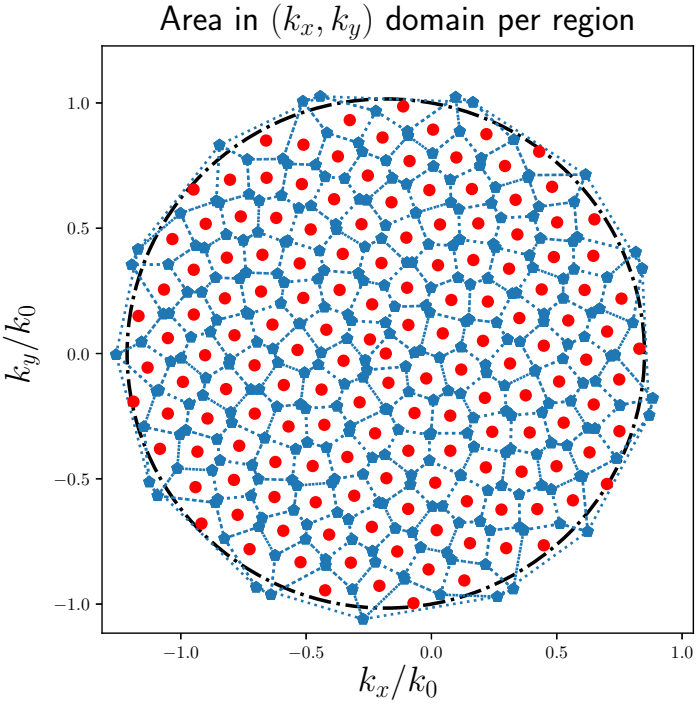

Figure 7.2: Modified Voronoi diagram denoting the equivalent area ΔS_m of each microphone in wavenumber domain for the full hemispherical microphone array shown in Figure 7.1. Microphone wavenumber-domain samples (seeds) are shown as red circles, Voronoi cells are shown as dashed lines and Voronoi vertices are shown as blue pentagons.

The estimation of the source wavenumber spectrum from far-field acoustic measurements (Eq. 7.1) can be generalised to the estimation of the source wavenumber cross-spectrum from measurements of the acoustic far-field cross-spectrum:

$$\widetilde{S}_{QQ'}(\hat{\mathbf{k}}_m, \hat{\mathbf{k}}_{m'}, \omega) = \lim_{T\to\infty}\left[\frac{\pi}{T}\mathrm{E}\left\{\widetilde{Q}\left(\hat{\mathbf{k}}_m, \omega\right)\widetilde{Q}^*\left(\hat{\mathbf{k}}_{m'}, \omega\right)\right\}\right] \tag{7.9}$$

$$= \frac{1}{(2\pi)^4}\left[(jk_0)\left(\frac{z_m}{\sigma_m}\right)\frac{e^{-j\hat{\mathbf{k}}_m\cdot\mathbf{r}_m}}{4\pi\sigma_m}\right]^{-1}\cdots$$

$$\cdots\left[(jk_0)^*\left(\frac{z_{m'}}{\sigma_{m'}}\right)\left(\frac{e^{-j\hat{\mathbf{k}}_{m'}\cdot\mathbf{r}_{m'}}}{4\pi\sigma_{m'}}\right)^*\right]^{-1} S_{pp'}(\mathbf{r}_m, \mathbf{r}_{m'}, \omega) \tag{7.10}$$

By inserting the expression for the wavenumber-domain source cross-spectrum (Eq. 7.10) in the expression for the spatial-domain source cross-spectrum (Eq. 7.8), we obtain

$$\widetilde{S}_{qq'}(\mathbf{r}_s, \mathbf{r}'_s, \omega) = \sum_m \sum_{m'} \frac{1}{(2\pi)^4} \left[\frac{\partial}{\partial z_s} G_{FF}(\mathbf{r}_m | \mathbf{r}_s, \omega) \right]^{-1} \dots$$
$$\dots \left[\frac{\partial}{\partial z_s} G^*_{FF}(\mathbf{r}_{m'} | \mathbf{r}'_s, \omega) \right]^{-1} S_{pp'}(\mathbf{r}_m, \mathbf{r}_{m'}, \omega) \left[\Delta S_m \Delta S_{m'} \right]. \quad (7.11)$$

Equation 7.11 is the discrete approximation to the cross-power spectral density of the source strength distribution from the cross-power spectral density of the acoustic far-field measurements.

7.2.3 Full Hemispherical Array Simulation

We now consider the simulated performance of the proposed far-field source reconstruction method when applied to a flat plate. We first investigate the performance of the full hemispherical array shown in Figure 7.1 to discuss the main characteristics of the proposed method, and then consider the effects of using a smaller, more practical microphone array design in the next section.

We consider a setup similar to the experimental conditions typically found in the ISVR open-jet wind tunnel. However, it is assumed that the flow is everywhere the same, and no shear layer effects are considered. The flow speed is $U_x = 60$ m/s ($M_x \approx 0.17$), and the wavenumber spectral density of the turbulent velocity field is calculated from the von Karman model.

We compare three types of source descriptions:

- The source distribution obtained from the Amiet model in Chapter 3;
- A source distribution obtained from the Amiet model, but with its spectra set to zero for all wavenumber components outside of the radiation ellipse. This bandlimited source is an approximation to Eq. 7.2, and describes the best outcome that can theoretically be obtained from far-field measurements;
- The source distribution estimated from the proposed far-field method, presented in Eq. 7.11.

In these examples, we will only consider the acoustic source strength estimated over the aerofoil surface. It must be kept in mind, however, that truncating a function in the frequency domain

has the effect of extending it in the spatial domain, as previously described, so the actual estimated source is actually "smeared" over all space beyond the physical limits of the aerofoil.

7.2.3.1 Surface Pressure Chordwise PSD

Figure 7.3 shows the chordwise surface pressure power spectral density magnitude at frequencies $k_0c = 0.5$, $k_0c = 5$ and $k_0c = 20$. We can observe that the proposed source estimation method and the wavenumber-bandlimited source agree qualitatively well, with a disagreement of approximately 3 dB at high frequencies. The reason for this disagreement is unclear at the moment. The proposed method can be seen to successfully estimate the source wavenumber spectrum within the radiating region for low and medium frequencies.

In all cases, the leading edge singularity is removed. This seems to indicate that as the far-field is concerned, the aerofoil can be described as an extended acoustic source without the leading edge singularity. The Kutta condition of zero pressure at the trailing edge is also absent, possibly due to the spatial low-passing effect.

In the $k_0c = 0.5$ case, the estimated level is significantly lower than the original. As previously discussed in Section 3.2.4.2, the area of the radiation ellipse is proportional to k_0, and at low frequencies it will be relatively small and contain only a small portion of the total power in wavenumber space. Note in Figure 3.18a that wavenumber components outside of the ellipse contain levels identical to those inside the ellipse.

At higher frequencies, when $k_0c = 5$ and $k_0c = 20$, the original and the estimated source display a better agreement in the aft sections of the aerofoil, indicating that these regions are significant contributors to the aerofoil far-field sound. The leading edge singularity is again not prominent in the estimated source distribution.

7.2.3.2 Surface Pressure Cross-Spectrum Phase and Coherence

Figure 7.4 shows the estimated surface pressure cross-spectrum phase for three mid-span reference points (1% chord, 10% chord and 50% chord). There is some loss of fine detail in the bandlimited and in the estimated phase distribution. As the wavenumber-bandlimited version and the estimated version again display a good agreement, this indicates the lack of detail is likely due to the missing high spatial frequency wavenumbers. The proposed method can thus correctly recover the information available in the far-field.

Similarly, Figure 7.5 shows the surface pressure coherence for the same three reference points. The original source coherence is very short near the leading edge due to the presence of subcritical gusts. As these gusts are acoustically inefficient, however, the coherence as seen from the far-field is significantly broader. The wavenumber-bandlimited coherence is similarly broader, indicating the smearing effect due to the removal of the high spatial frequencies.

For the reference point at mid-chord, however, the coherence is almost identical across the three plots, indicating that the aft sections of the aerofoil are not as contaminated by high spatial frequency wavenumbers due to subcritical gusts.

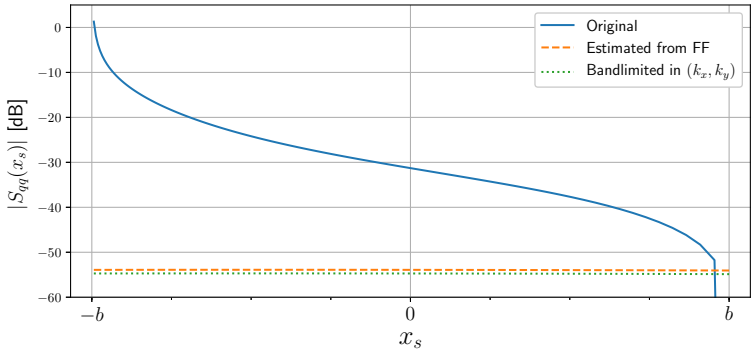

(a)

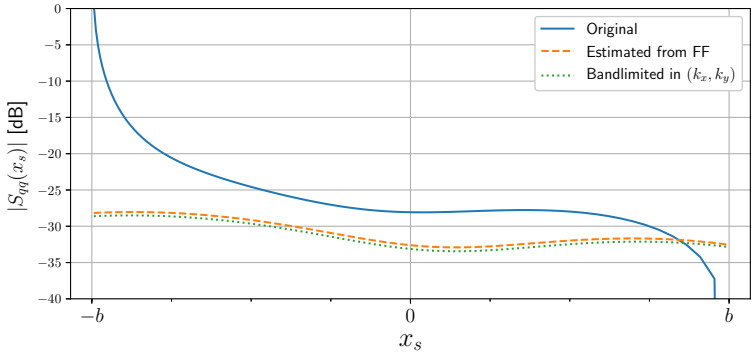

(b)

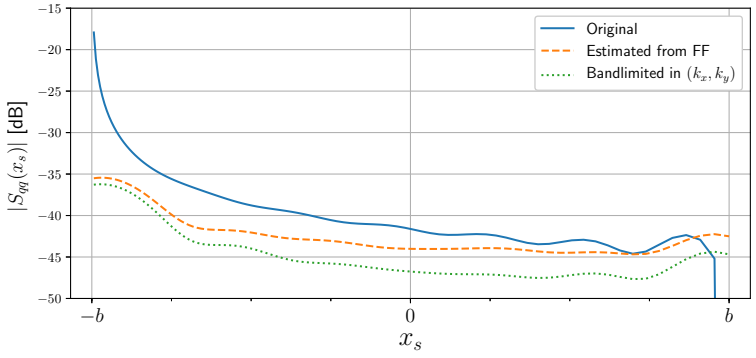

(c)

Figure 7.3: Original and estimated chordwise surface pressure jump power spectral density for full hemispherical array: (a) low frequency ($k_0 c = 0.5$); (b) medium frequency ($k_0 c = 5$); (c) high frequency ($k_0 c = 20$).

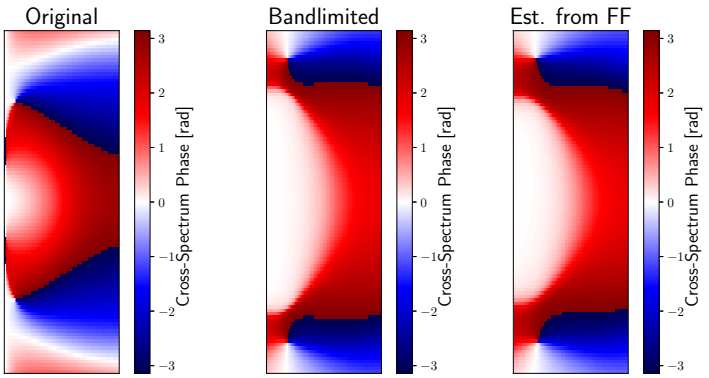

(a)

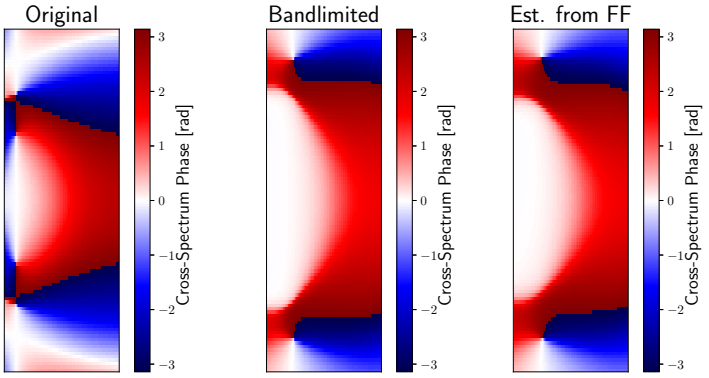

(b)

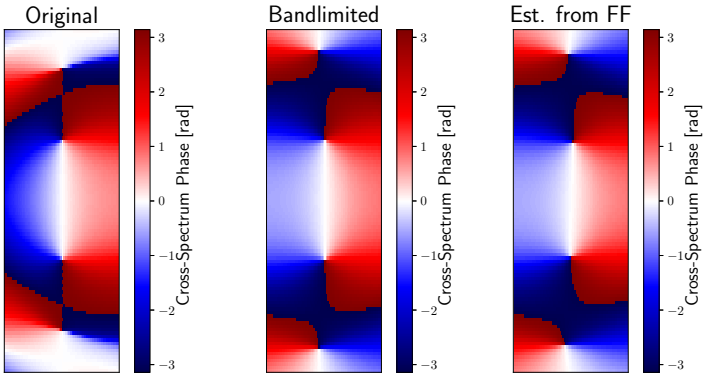

(c)

Figure 7.4: Original (left), wavenumber-domain bandlimited (middle) and estimated using full hemispherical array (right) cross-spectral density phase at medium frequency ($k_0 c = 5$): (a) reference point at 1% chord; (b) reference point at 10% chord; (c) reference point at 50% chord.

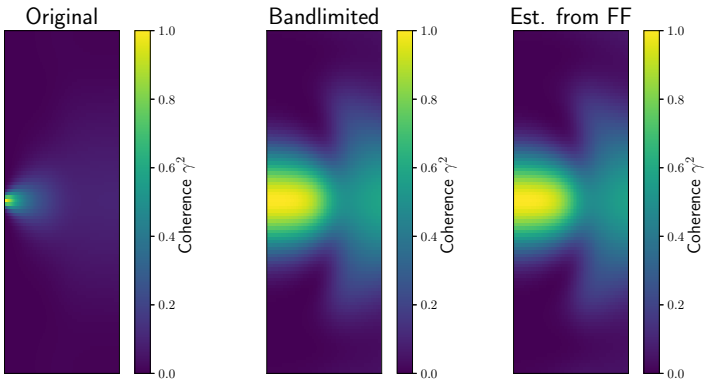

(a)

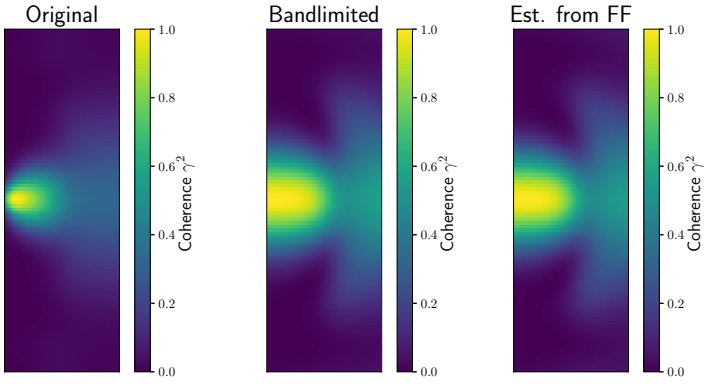

(b)

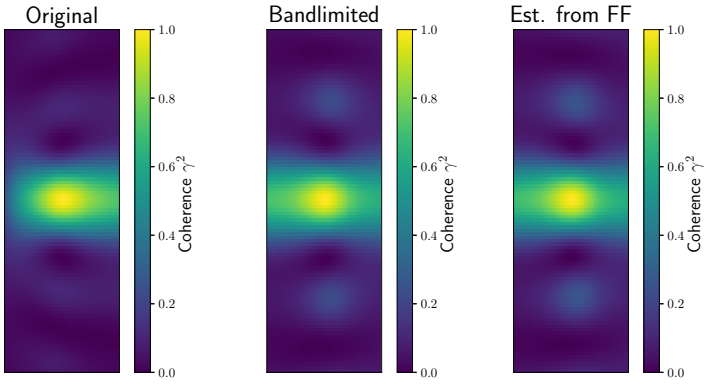

(c)

Figure 7.5: Original (left), wavenumber-domain bandlimited (middle) and estimated using full hemispherical array (right) coherence at medium frequency ($k_0 c = 5$): (a) reference point at 1% chord; (b) reference point at 10% chord; (c) reference point at 50% chord.

7.2.4 Hemispherical Cap Array Simulation

The hemispherical far-field array used in the previous example provides an optimistic scenario for the source reconstruction, as the entire acoustic domain in wavenumber space is sampled by the array. However, this is an impractical setup for real experiments, given the spatial distribution of the sensors was chosen to cover the entire hemisphere over the source.

Practical arrays often sample only a portion of the hemispherical angular space, and as such have an even more limited "visibility region" in the wavenumber domain. Let us consider a hemispherical cap array positioned above the aerofoil. Its geometrical sensor arrangement and equivalent wavenumber sampling are shown in Figure 7.6. As this array only samples a limited region in the wavenumber domain, its Voronoi diagram has its vertices restricted to a smaller region near the ellipse centre, so all microphones have similar wavenumber-domain areas ΔS_m, as shown in Figure 7.7.

This design is more representative of typical microphone arrays used in the literature, but is only able to observe wavenumbers close to the radiation ellipse centre. As this array is "blind" to a significant range of wavenumbers, even those that are efficient radiators to the far-field, it is not surprising that its performance will be worse than that of the full hemispherical array, as its source estimation will not include wavenumbers it cannot observe.

Its chordwise surface pressure PSD distribution is shown in Figure 7.8, and the estimated phase and coherence for the three reference points are shown in Figures 7.9 and 7.10. The estimated source distribution PSD is significantly underestimated when compared to the original or to the wavenumber-bandpassed sources. The phase and the coherence plots have lost major spatial features and look very similar regardless of which reference points are taken. Overall, the estimated source characteristics bear little resemblance to the original sources.

From the results presented herein and considering the similarities between the proposed far-field estimation method and frequency-domain delay-and-sum beamforming, we hypothesize that delay-and-sum beamforming might also benefit from using microphone arrays that cover a wide angular region of the source radiation. However, while our method proposes a clear explanation on why large aperture arrays present better performance, it is currently not clear how much this improvement carries on to near-field source estimation methods.

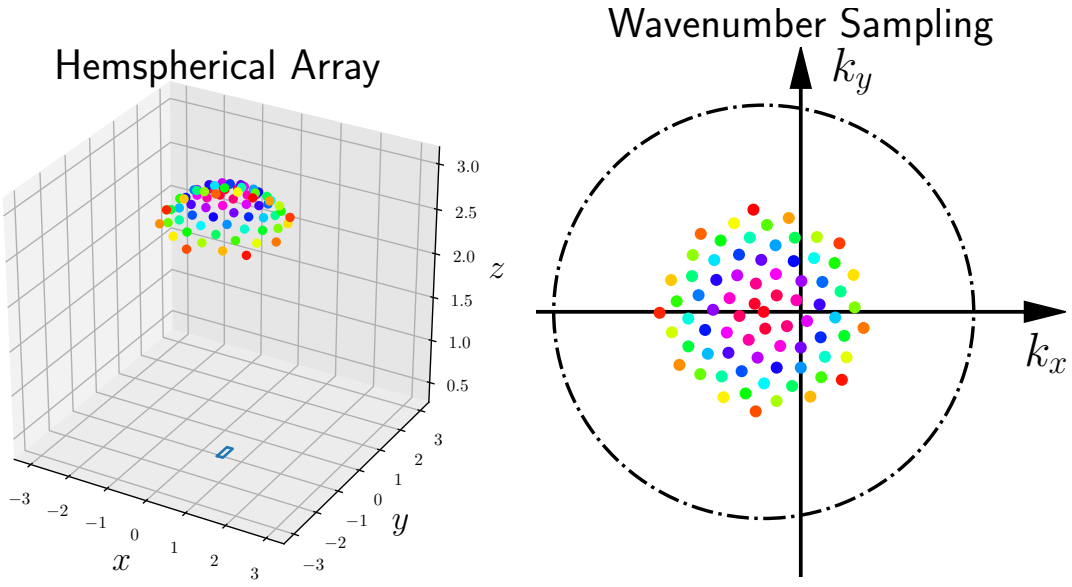

Figure 7.6: Hemispherical cap microphone array (left) and corresponding wavenumber-domain sampling (right).

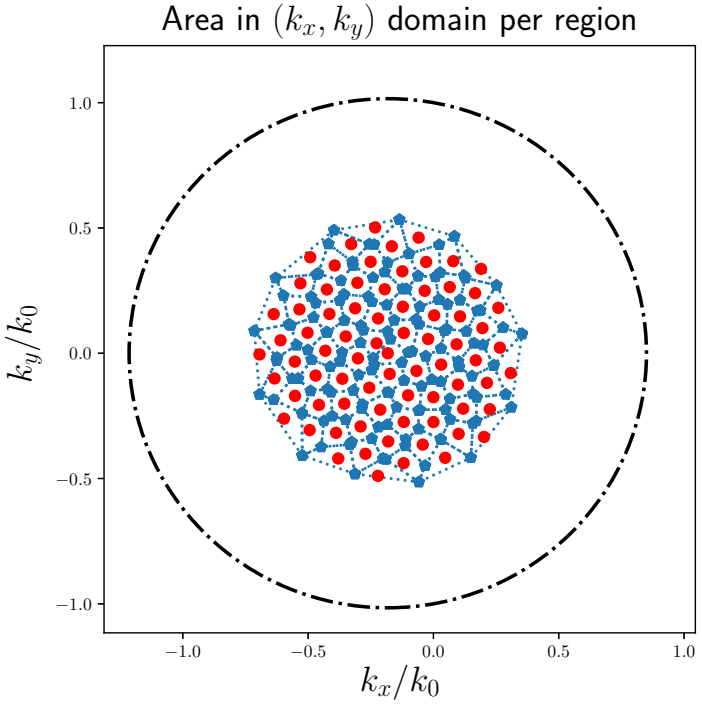

Figure 7.7: Modified Voronoi diagram denoting the equivalent area ΔS_m of each microphone in wavenumber domain for the hemispherical cap microphone array shown in Figure 7.6.

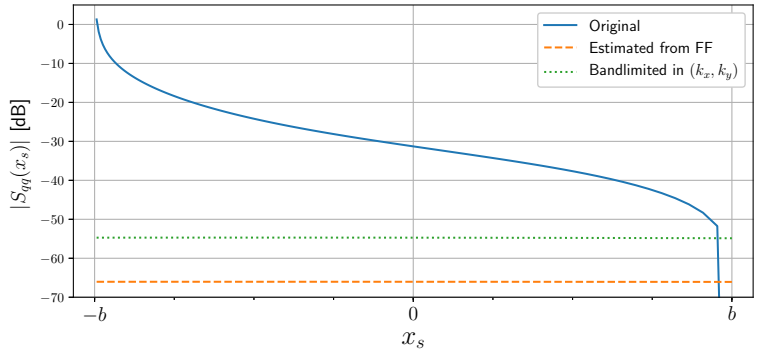

(a)

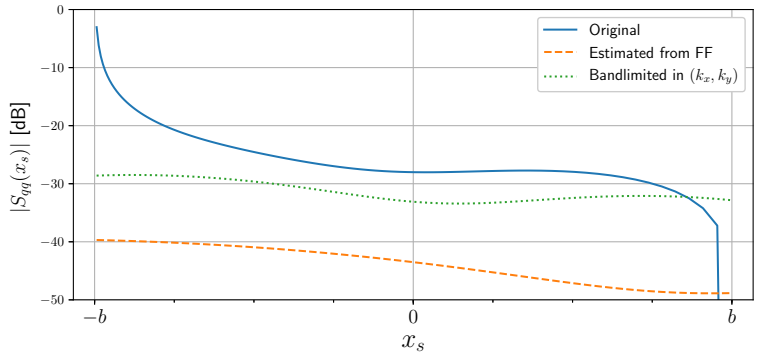

(b)

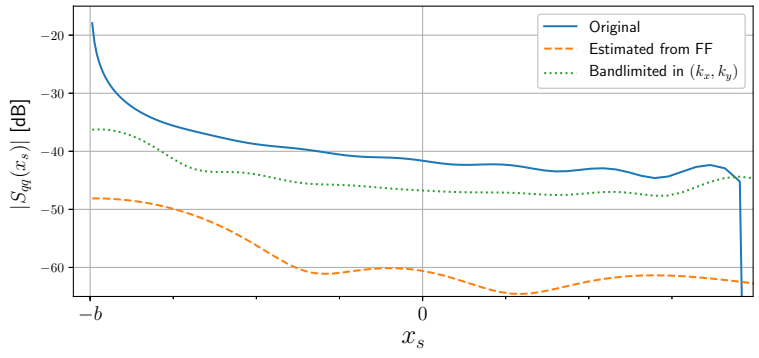

(c)

Figure 7.8: Original and estimated chordwise surface pressure jump power spectral density for hemispherical cap array: (a) low frequency ($k_0 c = 0.5$); (b) medium frequency ($k_0 c = 5$); (c) high frequency ($k_0 c = 20$).

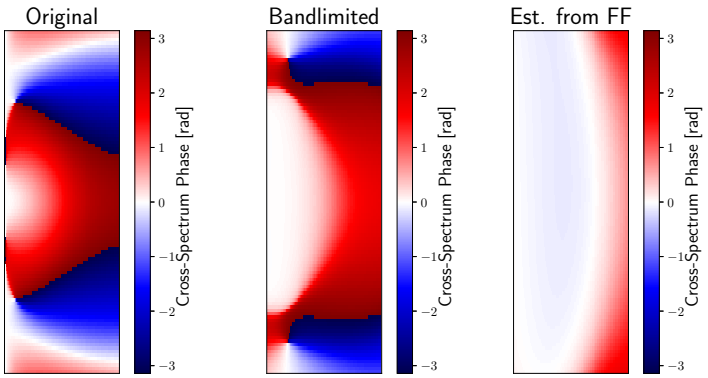

(a)

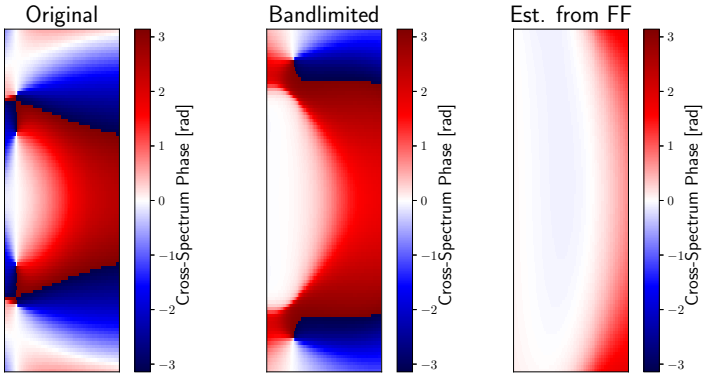

(b)

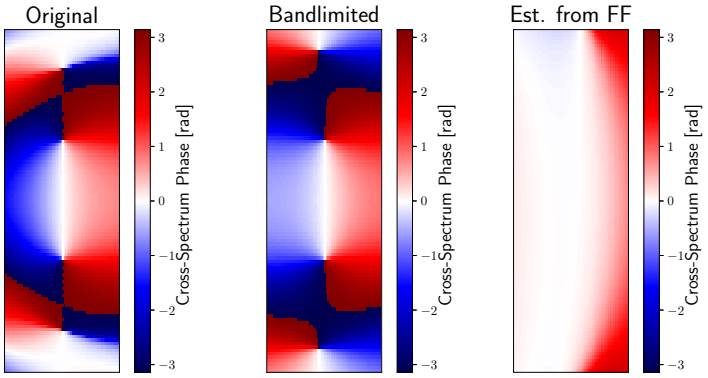

(c)

Figure 7.9: Original (left), wavenumber-domain bandlimited (middle) and estimated using hemispherical cap array (right) cross-spectral density phase at medium frequency ($k_0 c = 5$): (a) reference point at 1% chord; (b) reference point at 10% chord; (c) reference point at 50% chord.

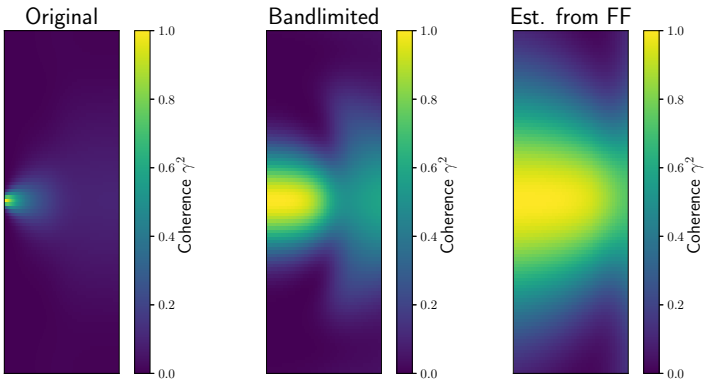

(a)

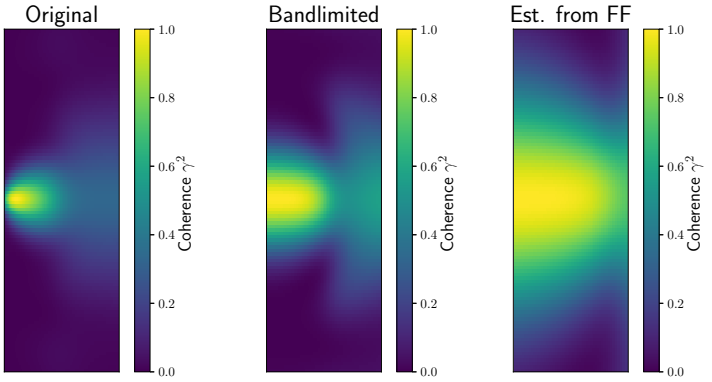

(b)

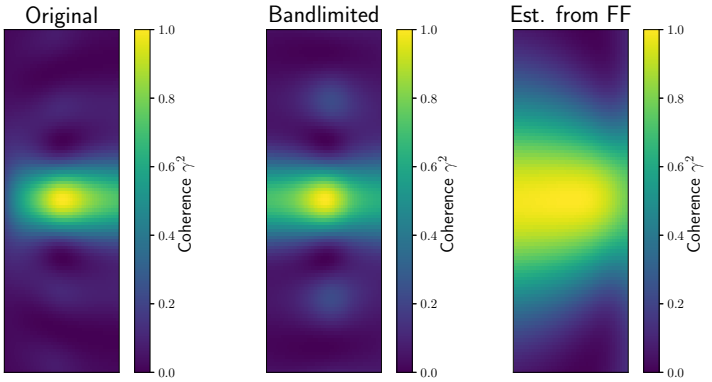

(c)

Figure 7.10: Original (left), wavenumber-domain bandlimited (middle) and estimated using hemispherical cap array (right) coherence at medium frequency ($k_0 c = 5$): (a) reference point at 1% chord; (b) reference point at 10% chord; (c) reference point at 50% chord.

7.3 Far-Field Inversion with Uniform Wavenumber Sampling

We now consider the far-field inversion problem using a uniform sampling of the source spectrum in the wavenumber domain. From Fourier Transform theory, a uniform sampling of N points in the frequency domain is associated with an equivalent uniform sampling of N points in the time domain - or in our case, in the spatial domain - via the Nyquist-Shannon Sampling Theorem [66, 82]. This theorem states that a bandlimited signal must be sampled at a rate at least two times its bandwidth in order to avoid aliasing of its high frequency components.

As we have discussed in this Thesis, the acoustic far-field is associated with the source wavenumber spectrum within a pass-band, which defines a bandwidth for the acoustic source as seen from the far-field. We can then apply the Sampling Theorem in the spatial domain, and obtain an equivalent sampling in the wavenumber domain - and its equivalent microphone array design in the acoustic far-field. In principle, this array is optimal from the standpoint of being able to recover the bandlimited equivalent source distribution with a minimum number of microphones. However, we will see that there are other factors involved in this analysis.

The relationship between the DFT of an acoustic source strength and its radiated far-field has been previously identified and investigated by Kim and Nelson [31] in a medium at rest. We propose a formulation for dipole-type sources in a uniformly moving medium and discuss the necessary changes in the wavenumber-domain sampling strategy. Although we have extensively explored planar acoustic radiators in a three-dimensional space, the method will be demonstrated for a one-dimensional acoustic source, which is simpler to analyse.

In the previous section, it was established that the source distribution estimated from far-field data will contain less fine spatial details when compared to the original source due to the lack of high spatial frequencies. In this Section, we propose to investigate whether the estimated source distribution can adequately describe the far-field behaviour of the original source or, in other words, whether the estimated source distribution will radiate the same far-field as the original source.

7.3.1 One-Dimensional Case: Line Source in x_s

We present the uniform-sampling method with a line source example. This case, being simpler to analyse, helps illustrate the sampling strategy and the method results.

We consider a continuous linear distribution of point dipole sources over $x_s \in [-L_x/2, L_x/2]$, with a complex source strength distribution $q(x_s, \omega)$ and its associated Spatial Fourier Transform $Q(k_x, \omega)$. This source region is sampled at N points, as shown in Figure 7.11a. The inter-sample distance is $\Delta x_s = L_x/N$, and we assume for simplicity that N is even. The source samples are indexed as $n \in [-(N/2), (N/2) - 1]$, so the x_s coordinate of the n-th sample is

$$x_s[n] = n\Delta x_s. \tag{7.12}$$

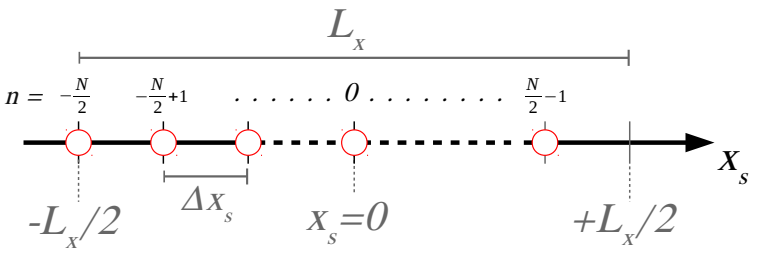

(a)

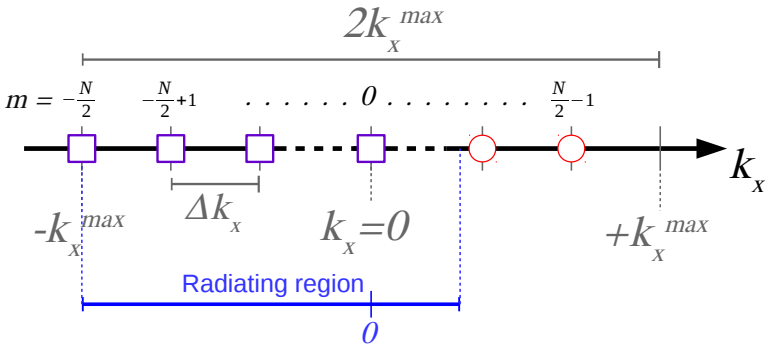

(b)

Figure 7.11: Sampling scheme for one-dimensional acoustic source in a convected medium: (a) sampling in spatial domain; (b) sampling in wavenumber domain. Samples marked with a square are within the radiating region and correspond to disturbances visible in the far-field. For illustration purposes, the DFT length N is assumed to be even.

It was extensively discussed in this Thesis that only wavenumber components within the radiation ellipse can contribute to the far-field. From this argument, there will be a maximum streamwise wavenumber k_x^{max} that represents the highest spatial frequency of interest, and its associated minimum wavelength $\lambda_x^{min} = 2\pi/k_x^{max}$ on the source surface. We can apply the Shannon-Nyquist Sampling Theorem and determine the minimum sampling interval Δx_s to correctly sample the maximum radiating wavenumber k_x^{max} as a function of its wavelength as

$$\Delta x_s = \frac{L_x}{N} \leq \frac{\lambda_x^{min}}{2}, \tag{7.13}$$

from which the minimum number of samples N is expressed as

$$N \geq \frac{2L_x}{\lambda_x^{min}} = \frac{L_x k_x^{max}}{\pi}. \tag{7.14}$$

For simplicity, we assume the source length L_x is an integer multiple of $\lambda_x^{min}/2$, so Eq. 7.14 becomes an equality and N is an integer. The wavenumber domain will contain N samples in the region $k_x \in [-k_x^{max}, +k_x^{max} - \Delta k_x]$, as shown in Figure 7.11b, where Δk_x is a wavenumber interval obtained from the previous equations as

$$\Delta k_x = \frac{2\pi}{L_x}, \tag{7.15}$$

and therefore the wavenumber-domain resolution is inversely proportional to the source length. We will explore this fact later on when considering methods to increase the accuracy of the estimated acoustic far-field.

The wavenumber samples are indexed as $m \in [-N/2, (N/2) - 1]$, and the k_x coordinate of the m-th sample is

$$k_x[m] = m\Delta k_x = m\left(\frac{2\pi}{N\Delta x_s}\right). \tag{7.16}$$

As discussed in Section 2.1.2 and shown in Figure 2.3, the radiation region is a circle of radius k_0 for $M_x = 0$, but becomes progressively wider and more skewed towards negative wavenumbers as the Mach number increases. Consequently, larger magnitude wavenumbers become visible in the far-field and the source requires a denser sampling in the spatial domain

as the flow velocity increases. To illustrate this phenomenon, consider that for $M_x = 0.5$, the largest magnitude wavenumber is $k_x^{max} = |-k_{r1} - k_{x1}| = 2k_0$. A Mach number of 0.5 will therefore double the minimum number of samples required compared to the quiescent medium case.

Note as well that the DFT frequency sampling is *symmetric* around $k_x = 0$, but for non-zero Mach numbers the wavenumber-domain radiation region is *asymmetric* around the origin. In this case, there will inevitably be wavenumber samples that fall outside the radiating region, particularly around positive wavenumbers. These are indicated in Figure 7.11b as red circles. Hence, of the N possible samples in wavenumber domain, only a subset of $M \leq N$ samples will be observable from far-field data and correspond to physical observer locations in the far-field.

7.3.1.1 Matrix Formulation - Direct Problem

Let us now consider the formulation of the direct problem and of the inverse problem in matrix form. For simplicity, we first consider a linear distribution of dipole sources in a medium at rest, where all wavenumber samples fall within the radiation circle and $M = N$. We then consider the special case of a medium with non-zero Mach number and how it affects the original problem formulation.

We use a similar formulation for the direct problem to the one shown in Eq. 6.3, where a vector of $M(= N)$ acoustic pressures $\mathbf{p}$, where $m \in [M_{min}, M_{max}](= [N_{min}, N_{max}])$, is linked to a vector of N source strengths $\mathbf{q}$, where $n \in [N_{min}, N_{max}]$, via a matrix $\mathbf{G}$ of transfer function elements. However, to keep the units consistent, we multiply the source strengths $\mathbf{q}$ by the spatial sampling interval Δx_s, effectively defining a numerical evaluation of the radiation integral. The final expression reads

$$\mathbf{p} = \mathbf{G}(\mathbf{q}\Delta x_s) \tag{7.17}$$

$$= \begin{bmatrix} | & | & & | \\ \mathbf{g}_{N_{min}} & \mathbf{g}_{N_{min}+1} & \dots & \mathbf{g}_{N_{max}} \\ | & | & & | \end{bmatrix} (\mathbf{q}\Delta x_s). \tag{7.18}$$

Each vector $\mathbf{g}_n = [g_{M_{min},n}, \dots, g_{M_{max},n}]^T$ contains the transfer functions from the n-th source to all N observers and describes the acoustic radiation and propagation from source to receiver.

By assuming dipole-type radiation in a moving medium and the observers in the far-field, the matrix elements $g_{m,n}$ can be approximated by the far-field dipole transfer function of Eq. 2.98:

$$g^{FF}_{m,n} = \frac{\partial}{\partial z_n} G_{FF}(\mathbf{r}_m|\mathbf{r}_n, \omega) \tag{7.19}$$

$$= \left(jk_0 \frac{z_m}{\sigma_m} \frac{e^{-j\hat{\mathbf{k}}_m \cdot \mathbf{r}_m}}{4\pi\sigma_m} \right) \left(e^{j\hat{\mathbf{k}}_m \cdot \mathbf{r}_n} \right) \tag{7.20}$$

$$= d_m \; e^{j\hat{\mathbf{k}}_m \cdot \mathbf{r}_n}, \tag{7.21}$$

where we can isolate the term d_m, containing the phase and attenuation effects that depend solely on the observer location $\mathbf{r}_m$, from the complex exponential $e^{j\hat{\mathbf{k}}_m \cdot \mathbf{r}_n}$, that depends on both the source location $\mathbf{r}_n$ and on the observer location via $\hat{\mathbf{k}}_m$.

As the transfer function elements can be separated as in Eq. 7.21, we can write the far-field-approximated transfer function matrix as

$$\mathbf{G}^{FF} = \begin{bmatrix} | & | & & | \\ \mathbf{g}^{FF}_{N_{min}} & \mathbf{g}^{FF}_{N_{min}+1} & \cdots & \mathbf{g}^{FF}_{N_{max}} \\ | & | & & | \end{bmatrix} \tag{7.22}$$

$$= \begin{bmatrix} d_{M_{min}} & \dots & 0 \\ \vdots & \ddots & \vdots \\ 0 & \dots & d_{M_{max}} \end{bmatrix} \begin{bmatrix} e^{j\hat{\mathbf{k}}_{M_{min}} \cdot \mathbf{r}_{N_{min}}} & \dots & e^{j\hat{\mathbf{k}}_{M_{min}} \cdot \mathbf{r}_{N_{max}}} \\ \vdots & \ddots & \vdots \\ e^{j\hat{\mathbf{k}}_{M_{max}} \cdot \mathbf{r}_{N_{min}}} & \dots & e^{j\hat{\mathbf{k}}_{M_{max}} \cdot \mathbf{r}_{N_{max}}} \end{bmatrix} \tag{7.23}$$

$$= \mathbf{DE}. \tag{7.24}$$

Thus, the far-field transfer matrix can be written as the product of a diagonal matrix $\mathbf{D}$ containing the phase shifts and amplitude attenuation related to the observer location, including the dipole directivity effect, and a Fourier-like matrix $\mathbf{E}$ mapping the source strength at $\mathbf{r}_n$ to an observer-dependent wavenumber $\hat{\mathbf{k}}_m$.

Note that the (m, n)-th element of the matrix $\mathbf{E}$ is

$$e^{j\hat{\mathbf{k}}_m \cdot \mathbf{r}_n} = e^{jk_x[m]x_s[n]} \tag{7.25}$$

$$= e^{j\left[m\left(\frac{2\pi}{N\Delta x_s}\right)\right][n\Delta x_s]} \tag{7.26}$$

$$= e^{jmn\left(\frac{2\pi}{N}\right)}, \tag{7.27}$$

which is identical to the entries in a DFT matrix. It is known that the DFT matrix has the property $\mathbf{E}\mathbf{E}^H = \mathbf{E}^H\mathbf{E} = N\mathbf{I}$, and therefore $\mathbf{E}^{-1} = (1/N)\mathbf{E}^H$. The DFT matrix is also known for having unitary condition number, indicating an optimal conditioning of the acoustic problem [31].

The direct problem can then be re-expressed as

$$\mathbf{p} \approx \mathbf{G}^{FF}(\mathbf{q}\Delta x_s) \tag{7.28}$$

$$= \mathbf{D}\mathbf{E}(\mathbf{q}\Delta x_s) \tag{7.29}$$

$$= 2\pi\mathbf{D}\mathbf{q}_k, \tag{7.30}$$

where $\mathbf{q}_k = [Q[M_{min}], \ldots, Q[M_{max}]]^T$ is a vector of source strength Spatial Fourier Transform samples evaluated at the discrete wavenumbers $k_x[m]$.

However, as previously discussed, some wavenumber samples will fall outside the radiating region when the Mach number is non-zero. In such cases, only $M < N$ observer locations are available in the far-field, and therefore the matrix $\mathbf{E}$ will be rectangular ($M \times N$). Since "invisible" samples can occur either at the leftmost or rightmost ends of the wavenumber spectrum (see Figure 7.11b), the matrix $\mathbf{D}$ then takes the form

$$\mathbf{D}_{M\times N} = \begin{bmatrix} d_{M_{min}} & 0 & \ldots & 0 & 0 & \ldots & 0 \\ 0 & d_{M_{min}+1} & \ldots & 0 & 0 & \ldots & 0 \\ \vdots & \vdots & \ddots & 0 & 0 & \ldots & 0 \\ 0 & 0 & \ldots & d_{M_{max}} & 0 & \ldots & 0 \end{bmatrix}. \tag{7.31}$$

Only the diagonal is populated with non-zero terms, and the $N_{max} - M_{max}$ rightmost columns will be identically zero. All $N - M$ wavenumbers located outside of the radiating region will be within the matrix $\mathbf{D}$ nullspace, and will not have a corresponding element in the vector of microphone pressures $\mathbf{p}$.

7.3.1.2 Matrix Formulation - Inverse Problem

Our objective is to obtain an estimate $\tilde{\mathbf{q}}$ of the source strength vector $\mathbf{q}$ from the far-field pressures $\mathbf{p}$. A first step is to obtain an estimate $\tilde{\mathbf{q}_k}$ of the source strength Spatial Fourier Transform from the vector of microphone complex pressures:

$$\tilde{\mathbf{q}_k} = \frac{1}{2\pi}\mathbf{D}^{\dagger}\mathbf{p}, \tag{7.32}$$

where $\mathbf{D}^{\dagger} = \mathbf{D}^H(\mathbf{D}\mathbf{D}^H)^{-1}$ is the right pseudoinverse of $\mathbf{D}$, and contains the element-wise inversion of the non-zero entries of the main diagonal of $\mathbf{D}$:

$$\mathbf{D}^{\dagger}_{N\times M} = \begin{bmatrix} (d_{M_{min}})^{-1} & 0 & \dots & 0 \\ 0 & (d_{M_{min}+1})^{-1} & \dots & 0 \\ \vdots & \vdots & \ddots & \vdots \\ 0 & 0 & \dots & (d_{M_{max}})^{-1} \\ 0 & 0 & 0 & 0 \\ \vdots & \vdots & \vdots & \vdots \\ 0 & 0 & 0 & 0 \end{bmatrix}. \tag{7.33}$$

Since the matrix $\mathbf{D}$ only contains the attenuations and phase shifts related to the microphone positions, it element-wise inverse is numerically stable[1]. Note that wavenumber samples in $\tilde{\mathbf{q}}_k$ that are outside the radiating region cannot be estimated and are automatically set to zero.

Finally, from $\tilde{\mathbf{q}_k}$, we can compute the source distribution estimate $\tilde{\mathbf{q}}$ via an Inverse Discrete Fourier Transform by multiplying by $\mathbf{E}^H$. The apparently missing factor $1/N$ is explained below. Here we perform the same modification as we did in Eq. 7.17, and multiply the

[1] A possible exception occurs for microphones placed in the $z = 0$ plane, where the dipole directivity presents a null in the acoustic radiation and $d_m = 0$. However, as microphones placed in this plane would not record any acoustic pressure from a dipole-like source, this situation most likely would not occur in practice.

estimated source strength wavenumber spectrum $\tilde{\mathbf{q}}_k$ by the wavenumber-domain sampling interval Δk_x:

$$\tilde{\mathbf{q}} = \mathbf{E}^H(\tilde{\mathbf{q}}_k \Delta k_x) \tag{7.34}$$

$$= \frac{1}{2\pi}\mathbf{E}^H\left(\mathbf{D}^\dagger \mathbf{p}\right)\Delta k_x \tag{7.35}$$

$$= \begin{bmatrix} e^{-j\hat{\mathbf{k}}_{M_{min}}\cdot\mathbf{r}_{N_{min}}} & \dots & e^{-j\hat{\mathbf{k}}_{M_{max}}\cdot\mathbf{r}_{N_{min}}} \\ \vdots & \ddots & \vdots \\ e^{-j\hat{\mathbf{k}}_{M_{min}}\cdot\mathbf{r}_{N_{max}}} & \dots & e^{-j\hat{\mathbf{k}}_{M_{max}}\cdot\mathbf{r}_{N_{max}}} \end{bmatrix} \begin{bmatrix} (d_{M_{min}})^{-1} & \dots & 0 \\ \vdots & \ddots & \vdots \\ 0 & \dots & (d_{M_{max}})^{-1} \\ 0 & \dots & 0 \\ \vdots & \vdots & \vdots \\ 0 & \dots & 0 \end{bmatrix} \mathbf{p}\Delta k_x. \tag{7.36}$$

Here, we define the $N \times M$ matrix $\mathbf{E}^H\mathbf{D}^\dagger$ appearing in Eq. 7.35 as $\mathbf{W}^H$, and write its (n,m)-th element as

$$w^*_{n,m} = e^{-j\hat{\mathbf{k}}_m\cdot\mathbf{r}_n}(d_m)^{-1} \tag{7.37}$$

$$= e^{-j\hat{\mathbf{k}}_m\cdot\mathbf{r}_n}\left(jk_0\frac{z_m}{\sigma_m}\frac{e^{-j\hat{\mathbf{k}}_m\cdot\mathbf{r}_m}}{4\pi\sigma_m}\right)^{-1} \tag{7.38}$$

$$= \left(jk_0\frac{z_m}{\sigma_m}\frac{e^{-j\hat{\mathbf{k}}_m\cdot(\mathbf{r}_m-\mathbf{r}_n)}}{4\pi\sigma_m}\right)^{-1} \tag{7.39}$$

$$= \left(\frac{\partial}{\partial z_n}G_{FF}(\mathbf{r}_m|\mathbf{r}_n,\omega)\right)^{-1}, \tag{7.40}$$

The elements of $\mathbf{W}^H$ are the element-wise inverse of the far-field-approximated transfer matrix $\mathbf{G}^{FF}$ (Eq. 7.19). Therefore, the n-th source estimate can be written as

$$\tilde{q}(\mathbf{r}_n,\omega) = \frac{1}{2\pi}\mathbf{w}_n^H\mathbf{p}\Delta k_x \tag{7.41}$$

$$= \frac{1}{2\pi}\sum_{m=M_{min}}^{M_{max}}\left(\frac{\partial}{\partial z_n}G_{FF}(\mathbf{r}_m|\mathbf{r}_n,\omega)\right)^{-1}p(\mathbf{r}_m,\omega)\Delta k_x. \tag{7.42}$$

We note here that the one-dimensional source estimation in Equation 7.42 for a uniform wavenumber-domain sampling has a similar form to the two-dimensional source estimation

presented in Equation 7.6 for arbitrary wavenumber-domain sampling, and both are similar to classical frequency-domain delay-and-sum beamforming [1].

Finally, we observe that, despite explicitly lacking the usual $1/N$ factor, the proposed formulation is identical to the definition of the Discrete Fourier Transform. Observe that the two added sampling intervals Δx_s and Δk_x, when considered in combination with the extra $1/(2\pi)$ factor in the definition of the Spatial Fourier Transform, result in the apparently missing $1/N$ factor:

$$\frac{\Delta x_s \Delta k_x}{2\pi} = \frac{(L_x/N)(2\pi/L_x)}{2\pi} = \frac{1}{N}. \tag{7.43}$$

Therefore, including the sampling intervals Δx_s and Δk_x, and the $1/(2\pi)$ factor in the DFT definition is equivalent to applying the usual DFT/IDFT formulations with the $1/N$ term. As an advantage, our proposed formulation maintains the variable values consistent with their physical entities, thus allowing a direct comparison between the original and the sampled variables, as shown below.

7.3.1.3 Sinc Interpolation of Bandlimited Functions

It is known that if the Nyquist-Shannon sampling theorem is satisfied, the original continuous signal can be recovered from its samples via a sinc interpolation [66]. As our far-field-estimated source distribution $\tilde{q}$ is bandlimited in wavenumber to the radiation region, and our sampling scheme is defined accordingly, the - now bandpassed - continuous source distribution can be estimated as

$$\tilde{q}(x_s) = \sum_{n=-\infty}^{\infty} \tilde{q}_n \operatorname{sinc}\left(\frac{(x_s - x_n)\pi}{\Delta x_s}\right), \tag{7.44}$$

where the unnormalised sinc function is defined as $\operatorname{sinc}(x) = \sin(x)/x$.

Similarly, we can apply the same theorem for wavenumber-domain sampling. If a function is spatially-limited, its continuous wavenumber spectrum can also be reconstructed from its samples via a sinc interpolation:

$$\tilde{Q}(k_x) = \sum_{m=-\infty}^{\infty} \tilde{Q}_m \,\mathrm{sinc}\left(\frac{(k_x - k_m)\pi}{\Delta k_x}\right). \tag{7.45}$$

However, as the sinc function interpolator presents an infinite number of decreasingly small sidelobes between the samples, correctly evaluating the continuous functions between pairs of samples require knowledge of samples over the entire wavenumber domain, into the evanescent region and up to infinity. Note that even samples that are distant from the region of interest will contribute to the interpolation.

Equations 7.44 and 7.45 indicate that wavenumber samples in the evanescent region will contribute to the acoustic field inside the radiation region. Therefore, lack of knowledge of samples in the evanescent region will in principle lead to errors in the estimated spectrum within the radiation region, and hence to errors in the estimated radiated far-field as well. This limitation is observed in the examples shown in the next section.

7.3.1.4 Example: Nyquist-type Sampling in the Wavenumber Domain

Let us now consider an example of the proposed source reconstruction method with uniform wavenumber-domain sampling. We consider a linear distribution of point dipole sources in x_s, with a source strength distribution given by a typical flat plate chordwise surface pressure jump $\Delta p(x_s, \omega)$, as described in Chapter 3.

We assume a Mach number $M_x = 0.5$, and a frequency where the aerofoil chord is $c = 2\lambda_0$. As a result, $k_x^{max} = 2k_0$, and the Nyquist sampling criterion will require 8 samples over the aerofoil chord. The chordwise normalised frequency is $k_0 c \approx 12.5$. Figure 7.12 shows the resulting wavenumber-domain sampling, indicating which samples are inside the radiation region, and the equivalent far-field microphone array.

The acoustic field at the far-field microphone array is calculated using a standard radiation integral for distributed dipole sources. The sampled source wavenumber spectrum is estimated from these far-field pressures using Eq. 7.32, and the source strength distribution in the spatial domain is estimated from the sampled wavenumber spectrum using Eq. 7.34. Finally, we compute the acoustic far-field radiated by the estimated source strengths, and compare it with the original far-field directivity.

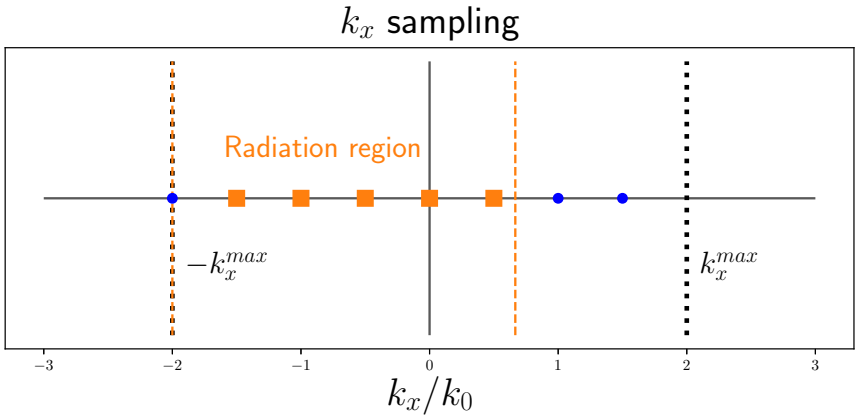

(a)

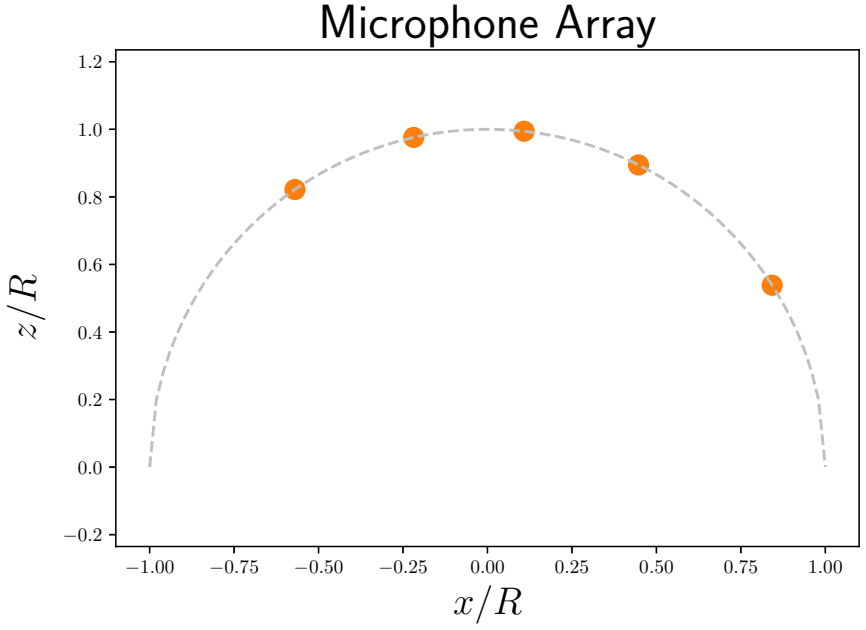

(b)

Figure 7.12: Uniform wavenumber-domain sampling and associated far-field microphone arc for Nyquist-type wavenumber sampling: (a) Samples in wavenumber domain k_x; samples marked with squares are inside the radiation region, while samples marked with circles are outside; (b) Far-field microphone arc design corresponding to wavenumber-domain samples within tha radiation region.

The normalised far-field directivity of the original and of the estimated source are shown in Figure 7.13, together with the acoustic pressure magnitudes observed by the far-field microphone array. The original and the estimated far-field directivities present a similar general structure, with a stronger radiation in the downstream direction and the presence of multiple sidelobes and nulls. Because the Nyquist-Shannon theorem has been satisfied, both curves agree exactly at the microphone locations.

However, it can also be observed that the curves don't agree well in the angles between microphone positions. Significant differences can be observed, reaching approximately 10 dB at some upstream angles. As discussed in the previous section, this inaccuracy in the observed directivity between the microphone positions is associated with a lack of samples outside of the radiation region, coupled with a relatively sparse wavenumber-domain sampling.

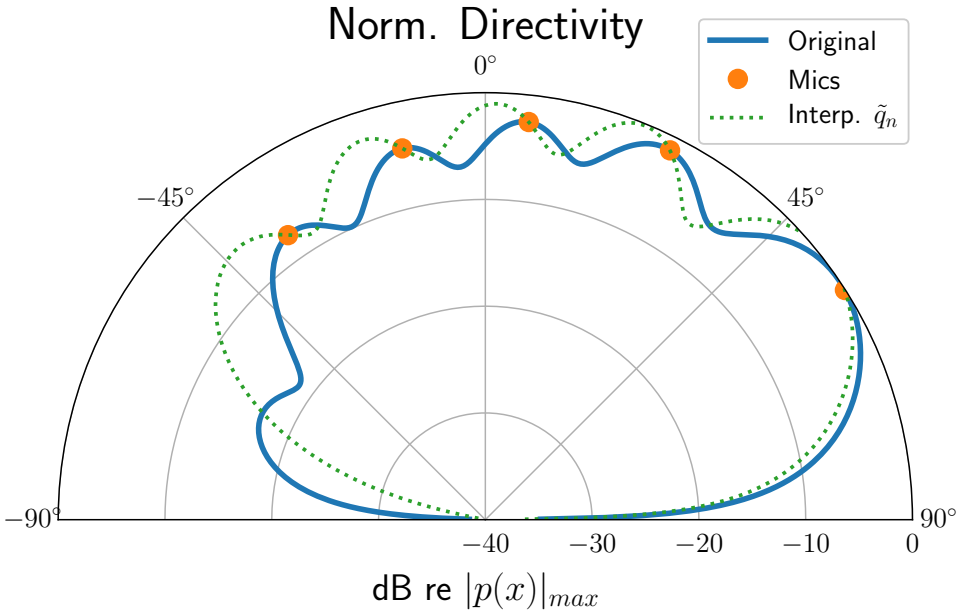

Figure 7.13: Chordwise normalised far-field directivity for Nyquist-type wavenumber sampling. The original source directivity is plotted with a solid line; the acoustic pressure observed by the microphone array are indicated with circles; and the far-field-estimated source directivity is plotted with a dash-dotted line.

We now show in Figures 7.14 and 7.15 the estimated source distribution in the wavenumber and in the spatial domains, plotted as continuous lines. For comparison, we include the wavenumber band-passed source distribution, as we did for the arbitrary wavenumber sampling formulation. The bandpassed source is shown using dashed lines.

In the wavenumber domain, shown in Fig. 7.14, we compare the sampled wavenumber spectrum estimated from the far-field, shown as circles, and a continuous estimated source

wavenumber spectrum obtained from interpolating the wavenumber-domain samples, shown as a dotted line. The estimated wavenumber samples can be seen to correctly estimate the original source spectrum. The wavenumber-interpolated spectrum also agrees with the original spectrum at the microphone positions, but diverges from it in the regions between samples. Observe also how the interpolated spectrum is able to estimate part of the spectrum within the evanescent region, due to the sinc function sidelobes.

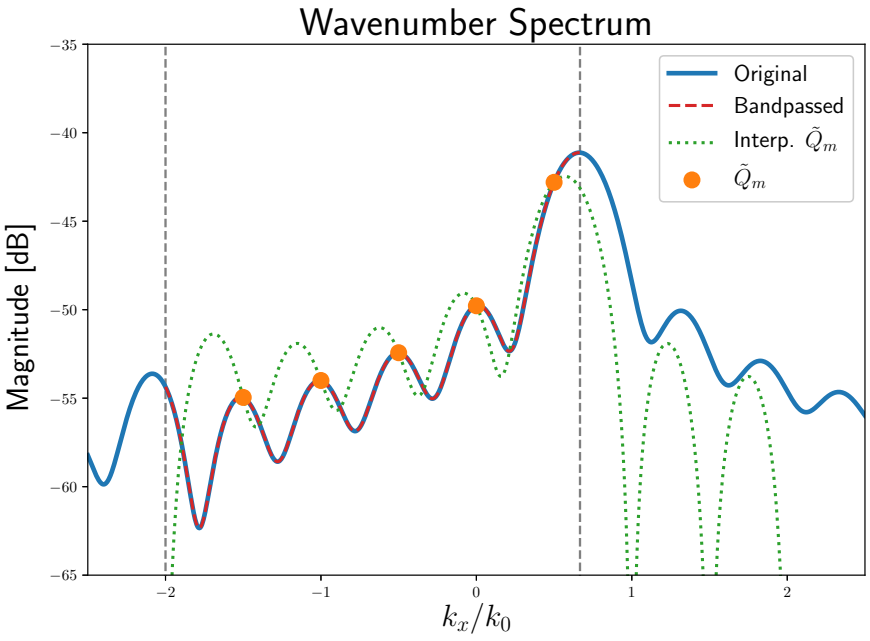

Figure 7.14: Original and far-field-estimated source wavenumber spectrum for Nyquist-type wavenumber sampling. The original source is plotted with a solid line; the wavenumber-bandpassed source is indicated with a dashed line; the far-field-estimated source is indicated with circles; and the interpolated source (from the far-field-estimated samples) is plotted with a dashed-dotted line.

In the spatial domain, Fig. 7.15, we compare the real part (Fig. 7.15a) and the magnitude (Fig. 7.15b) of the sampled source strength, as estimated from the proposed far-field inversion method, and the continuous estimated source strength obtained from spatial interpolation, shown as a dotted line. The wavenumber-bandpassed source distribution is not very prominent at the leading edge, and it is now spread beyond the source physical limits. It displays a quickly decaying, oscillatory behaviour outside of the source length, but agrees reasonably well with the original source within the source limits. The sampled estimated source follows the same trends as the original and bandpassed sources, but presents very different details to the previous two. The sampled source also displays a similarly reduced leading edge peak when compared to the bandpassed source.

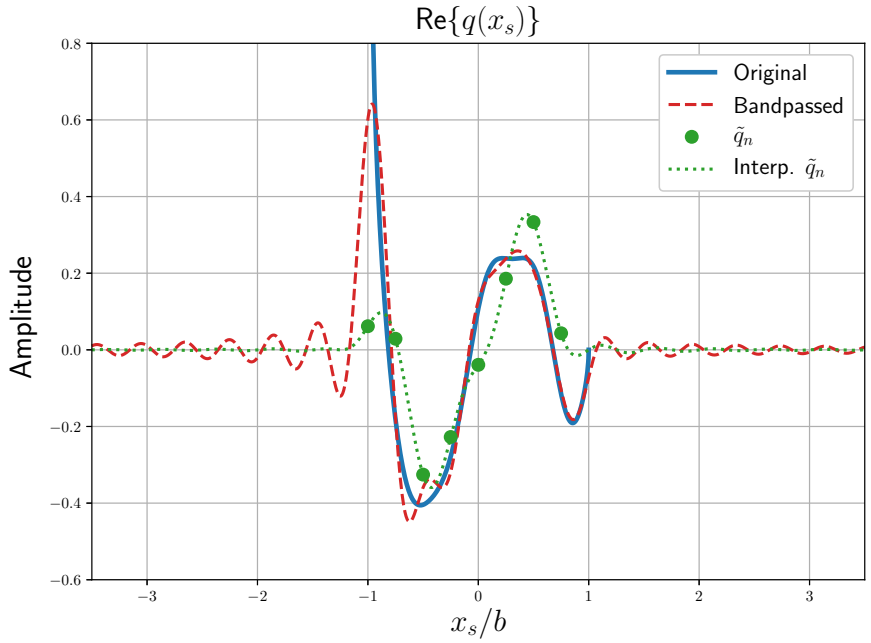

(a)

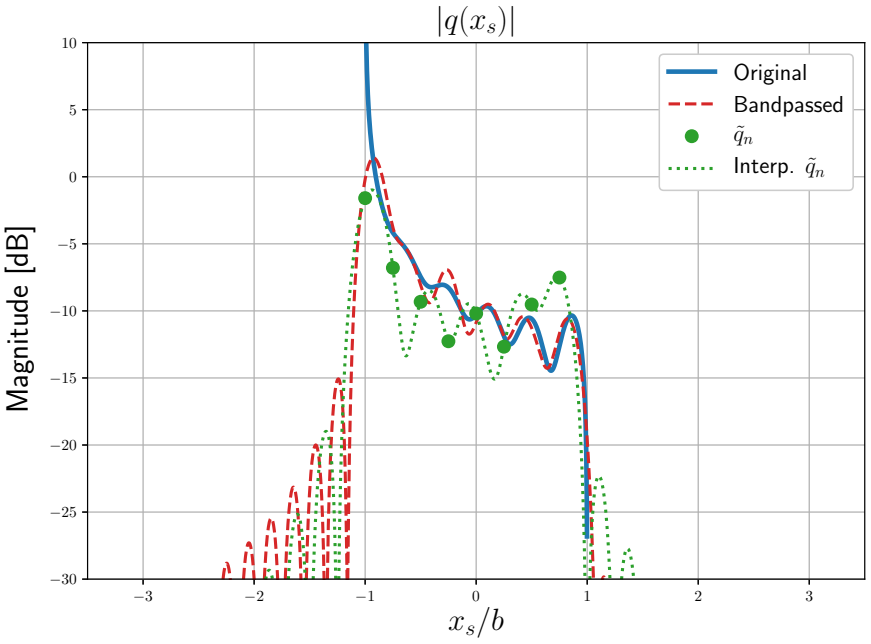

(b)

Figure 7.15: Original and far-field-estimated source spatial distribution for Nyquist-type wavenumber sampling: (a) real part of estimated source strength spatial distribution; (b) magnitude of estimated source strength spatial distribution. The original source is plotted with a solid line; the wavenumber-bandpassed source is indicated with a dashed line; the far-field-estimated source is indicated with circles; and the interpolated source (from the far-field-estimated samples) is plotted with a dashed-dotted line.

7.3.1.5 Example: Oversampling in the Wavenumber Domain

As the wavenumber-domain resolution is dependent on the source length L, one method of improving the wavenumber resolution - and hence, the estimated far-field resolution - is to artificially increase the estimated source length. We now assume that the source is three times larger than its physical dimensions, and estimate the source strength distribution on those samples beyond its physical limits as well. This will increase the DFT length in the spatial domain while maintaining the spatial sampling interval, thus increasing the number of points - and hence, the resolution - within the passband in the frequency domain, as shown in Figure 7.16a.

The denser sampling in the wavenumber domain is equivalent to increasing the sensor count in the microphone array, shown in Figure 7.16b. Since the proposed uniform sampling framework is able to identically recover the sampled acoustic pressures, the larger number of observations reduces the error when predicting the acoustic far-field from the estimated source distribution. Regarding the source spatial distribution, we can conclude that the "extra" source samples, located outside the source physical dimensions, become significant contributors to the accuracy of the reconstructed far-field pressures.

The larger number of far-field sensors allow us to increase the number of wavenumber samples, shown in Figures 7.17 and 7.18. Because of the denser wavenumber sampling, the interpolated far-field directivity and the interpolated wavenumber spectrum are now significantly closer to their original values.

Figure 7.19 shows the real part (Fig. 7.19a) and the magnitude (Fig. 7.19b) of the source strength spatial distribution. Both the sampled and the interpolated estimated sources display a reduced magnitude at the leading edge, and non-zero values outside of the source physical limits. Note that the estimated source does not agree well with the bandpassed source outside of the source limits, although both have very similar wavenumber spectra. The origin for this difference is not currently understood.

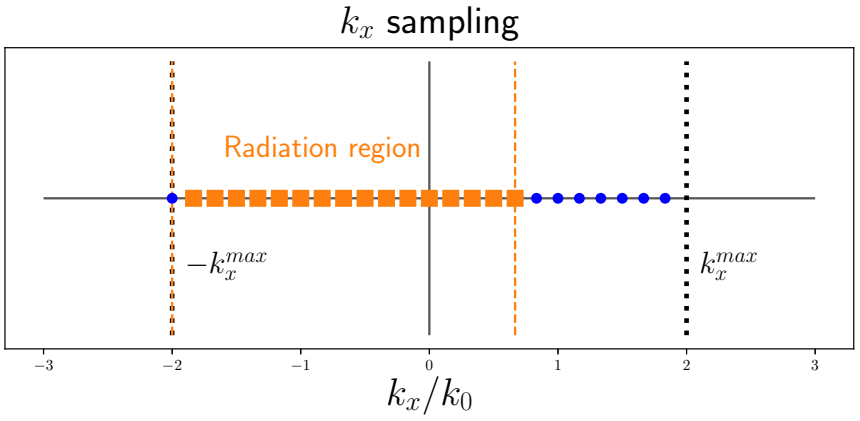

(a)

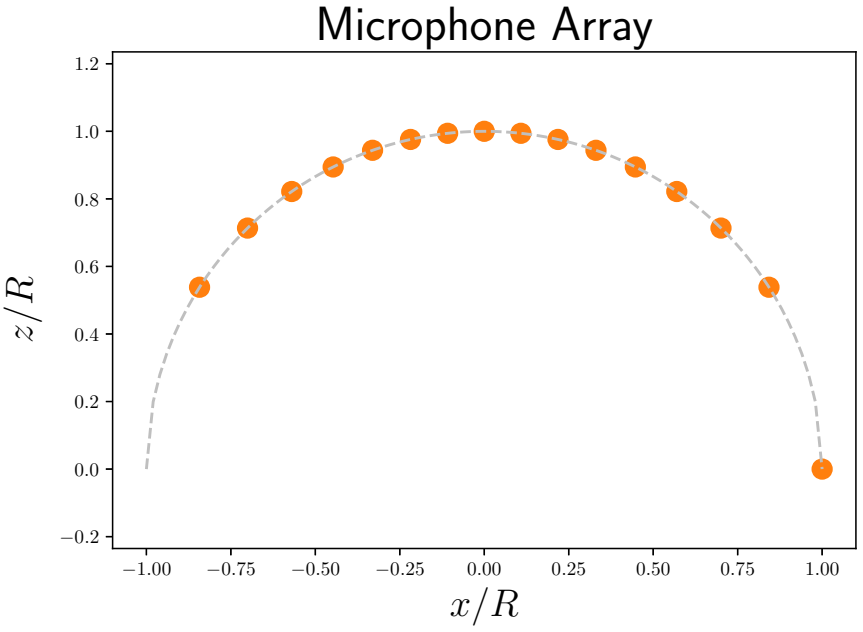

(b)

Figure 7.16: Uniform wavenumber-domain sampling and associated far-field microphone arc for wavenumber-domain oversampling: (a) Samples in wavenumber domain k_x; samples marked with squares are inside the radiation region, while samples marked with circles are outside; (b) Far-field microphone arc design corresponding to wavenumber-domain samples within tha radiation region.

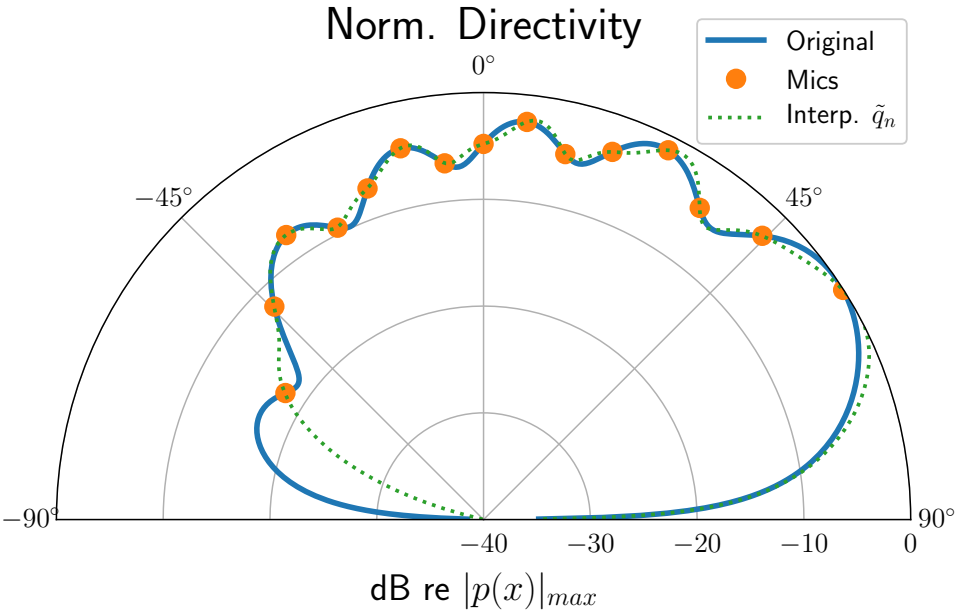

Figure 7.17: Chordwise normalised far-field directivity for wavenumber-domain oversampling. The original source directivity is plotted with a solid line; the acoustic pressure observed by the microphone array are indicated with circles; and the far-field-estimated source directivity is plotted with a dash-dotted line.

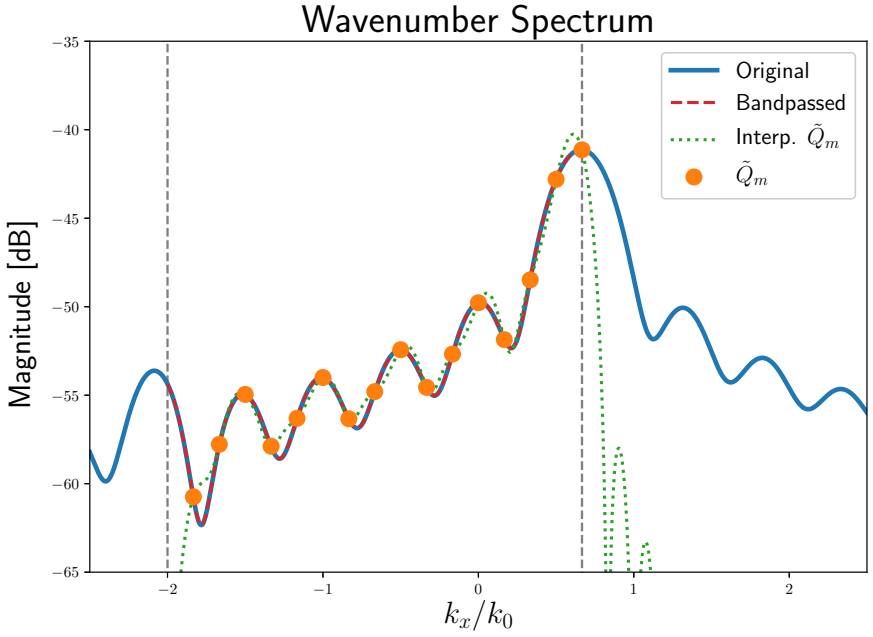

Figure 7.18: Original and far-field-estimated source wavenumber spectrum for wavenumber-domain oversampling. The original source is plotted with a solid line; the wavenumber-bandpassed source is indicated with a dashed line; the far-field-estimated source is indicated with circles; and the interpolated source (from the far-field-estimated samples) is plotted with a dashed-dotted line.

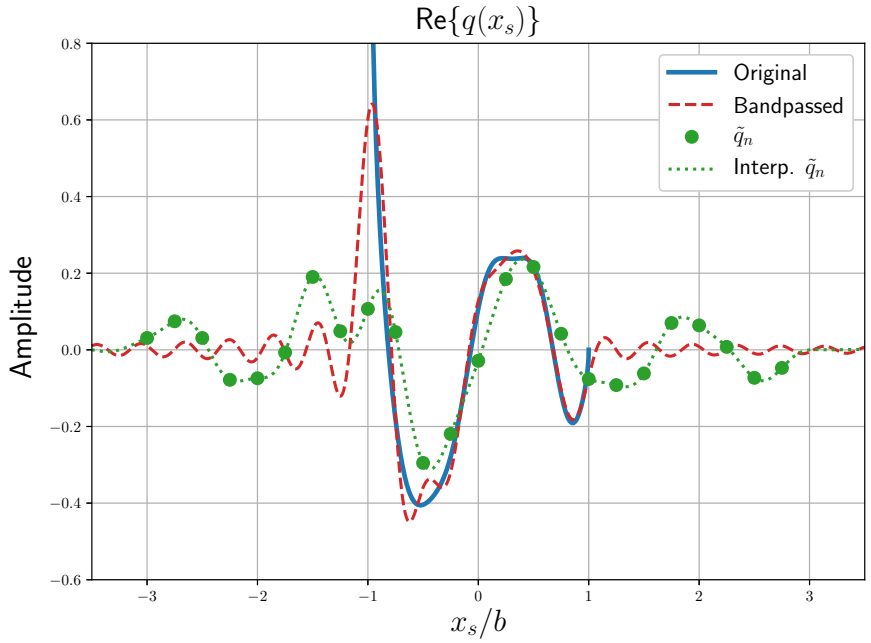

(a)

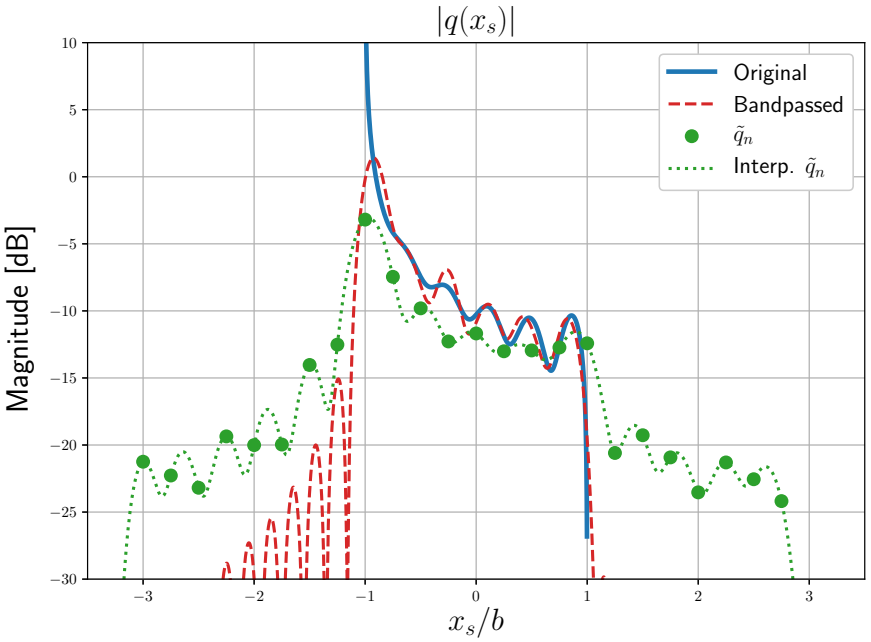

(b)

Figure 7.19: Original and far-field-estimated source spatial distribution for wavenumber-domain oversampling: (a) real part of estimated source strength spatial distribution; (b) magnitude of estimated source strength spatial distribution. The original source is plotted with a solid line; the wavenumber-bandpassed source is indicated with a dashed line; the far-field-estimated source is indicated with circles; and the interpolated source (from the far-field-estimated samples) is plotted with a dashed-dotted line.

7.4 Super Resolution Methods

Although the proposed far-field inversion method outlined in this Chapter is able to recover the radiating source distribution, it is in theory possible to further process the results to obtain super-resolution. We briefly outline this super-resolution method below, and discuss some of its limitations.

The spatial bandlimiting effect on far-field data is analogous to the Rayleigh resolution limit, which states that two point sources spaced by less than half of the wavelength cannot be clearly separated [84]. This limitation can be contrasted with Nearfield Acoustic Holography, for example, where the acoustic field is sampled very close to the source in order to acquire the evanescent components and obtain resolution beyond the Rayleigh limit [31, 85]. Methods that exceed the Rayleigh limit are often termed *super-resolution methods* [81].

We have identified a super-resolution method which could be applied to our far-field results. It is based on the principle of *analytic continuation* [81] . It is known that, in the absence of noise, an analytic function can be perfectly reconstructed over its entire domain from knowledge of its values over a finite domain. As the original source wavenumber spectrum is analytic, then in principle its evanescent components can be correctly estimated from knowledge of its radiating components only.

Working in the context of diffraction-limited optical signals, Castleman [81] describes the "Successive Energy Reduction" method: the estimated source spatial distribution is Inverse Fourier Transformed from spectrally-limited data, and as such it is spatially unbounded; the source is enforced to be spatially limited again, which in turn makes its spectrum unbounded; the spectrum within the system passband is then imposed to be identical to the original band-limited data; and the source distribution is again estimated from Inverse Fourier Transforming the new estimated spectrum, now available a wider bandwidth. This process is iterative, and each step yields a slightly better approximation for the "invisible" parts of the spectrum.

Although some extension of the observable bandwidth is obtained, in practice such superresolution methods require considerable oversampling of the original signal and very low noise conditions to obtain significant bandwidth extension. Moreover, in order to obtain a fine spectral resolution, the Fourier Transforms must be computed over a domain much larger than the original signal. Given the strict demands that this method imposes, it has rarely been reported in practice [81].

Chapter 8

Conclusions

8.1 Summary of Thesis Contributions

This Thesis investigated the acoustic characteristics of flat plate aerofoils interacting with turbulent flows, and the use of microphone array methods to experimentally assess these characteristics. The main findings of this work are summarised below.

A systematic Fourier-based framework linking the far-field acoustic radiation of planar sources in a convected medium to the Spatial Fourier Transform of its source strength distribution has been presented. It was shown, via the Fraunhofer geometric far-field approximation, that a distant observer will perceive the incoming sound field as a plane wave. The wavenumber vector of this plane wave is uniquely associated with the observer location, and its magnitude is determined by the source strength spectrum evaluated at its wavenumber vector within the radiation ellipse. This framework is applicable for distributions of monopole or dipole sources, in flows with Mach number $0 \leq M_x < 1$, and is valid up to a distance-dependent high frequency limit.

The analytical model by Amiet for a flat plate interacting with a turbulent flow was presented, and discussed from a wavenumber-domain perspective. Single-gust supercritical responses were shown to have a principal wavenumber component located over the radiation ellipse in wavenumber domain, corresponding to an acoustic wave propagating over the aerofoil surface. Subcritical responses, on the other hand, were shown to have a principal wavenumber component located outside the radiation ellipse, corresponding to an evanescent wave on the

aerofoil surface. An empirical rule for determining the gust integration limit for surface pressure calculations was proposed, and the aerofoil surface pressure characteristics for single- and multiple-gust responses were discussed in both spatial and wavenumber domains.

The acoustic radiation characteristics of a flat plate for single- and multiple-gust responses were discussed, and an empirical rule for determining the gust integration limit for acoustic radiation calculations was proposed. From these analyses, three near-field effects were identified for the flat plate acoustic radiation: the hydrodynamic dipole near-field, considered a significant contributor to low-frequency radiation; the geometric near-field, considered significant at high frequencies for single-gust responses but not observed in multiple-gust responses; and the subcritical gust response, considered significant at low frequencies for finite-span aerofoils. Frequency and distance limits for all three near-field effects were identified: the dipole near-field imposes a low frequency limit to the far-field approximation, while the geometric near-field imposes a high frequency limit to the approximation.

The acoustic field of a real flat plate interacting with a turbulent flow was measured with a planar microphone array in the ISVR wind tunnel. A good agreement was observed between the flat plate measurements and the prediction model, particularly regarding the coherence between array microphones as a function of microphone location and frequency. A good agreement was also observed when applying array signal processing methods to the predicted and measured acoustic fields, both when using conventional beamforming and CLEAN-SC deconvolution.

A far-field inversion method for planar sources in flow was proposed by inverting the previously discussed Fourier framework linking the acoustic far-field and the source wavenumber spectrum. Two formulations for the inversion method were shown: the first formulation considered an arbitrary microphone array geometry, where an equivalent irregular wavenumber-domain sampling is calculated from the microphone positions. This formulation was evaluated with a broadband aerofoil simulation using a full hemispherical microphone array. The estimated aerofoil source distribution was shown to be almost identical to a wavenumber-domain bandpassed source distribution: both versions lack fine spatial detail in general, and the leading edge singularity is not prominent anymore. It was also shown that arrays that do not cover the entire far-field hemisphere, as is the case in typical experimental setups, have their source estimates even further bandpassed, and their spatial resolution is further decreased. This

formulation was shown to be analytically very similar to frequency-domain delay-and-sum beamforming

The second formulation considered a Nyquist-type spatial sampling criterion and an associated uniform wavenumber-domain sampling, from which the microphone array geometry is obtained. This formulation was shown to be directly related to the Discrete Fourier Transform of the source strength, and as such it represents an optimal conditioning of the plant matrix. This formulation was evaluated with a narrowband, one-dimensional aerofoil model using a microphone arc; it was shown that the equivalent source is able to describe the original far-field pressures at the microphones, but the acoustic field between the microphones might be in error due to missing wavenumber-domain samples. We showed that it is possible to improve the far-field reconstruction by considering a wider source length, which in turn takes into account the source smearing due to the bandpassing effect in wavenumber domain and increases the number of microphone sensors in the far-field. This formulation was also shown to be very similar to frequency-domain delay-and-sum beamforming, although slightly different to the first formulation.

8.2 General Remarks and Open Questions

In general, this research has achieved a better understanding of the acoustic characteristics of a flat plate aerofoil in terms of its spatial source distribution, wavenumber spectrum and radiated near-field and far-field. We have also proposed methods to assess these characteristics from far-field microphone arrays, and simulated their performance at a few single-frequency cases.

We have extensively applied the Spatial Fourier Transform to relate the spatial source distribution and its wavenumber spectrum, and the wavenumber spectrum to the acoustic far-field radiated by the source. This relationship has been described in a systematic manner, allowing its applications to a variety of sources and medium conditions. Although we have established what are the theoretical limits to the Fraunhofer far-field approximation, we have also shown that in practice this limit is not very well defined, and must be taken as a general indicator of validity only.

The proposed Fourier framework currently assumes a uniform convected medium encompassing both source and observers. However, in many aeroacoustics experiments the medium is not

uniform, such as in the open-jet wind tunnel experiments described in Chapter 5. Further work is required to determine whether the proposed framework can be extended to include inhomogeneities in the flow, such as shear layer refraction effects.

Detailed investigations of the flat plate surface pressure distribution in the spatial domain and in the wavenumber domain have been performed. However, it is currently unknown whether these results can be validated by experimental surface pressure measurements. Hence, an experimental verification and possible validation of these results would provide a strong argument to their importance. It is known, however, that such measurements are very difficult to perform due to the difference in magnitude between the acoustic surface pressure fluctuations and the boundary layer pressure fluctuations, and would require a data acquisition system with a very high dynamic range.

Results regarding the acoustic near-field behaviour of an aerofoil were presented for the first time. As their mechanisms and frequency ranges were also established, it is now feasible to consider which near-field behaviours might affect a particular measurement setup and must be taken into account, and which ones can be safely ignored via a far-field approximation. Surprisingly, such behaviours were more easily observable when considering single-gust responses, but not multiple-gust responses. The reason for this difference is not known at the moment, and is recommended as further investigation.

We have applied beamforming methods to simulated microphone array data generated from the Amiet flat plate model, and obtained qualitatively very similar results to those of a real experiment, using both conventional beamforming and deconvolution with CLEAN-SC. This is the first time this comparison has been performed. It is still necessary to extend this comparison and perform a quantitative analysis as well over multiple frequencies, which is suggested as future work.

If further investigations confirm the viability of achieving realistic microphone array results with the Amiet model, we propose adopting this prediction model as a benchmark case for assessing microphone array performance, both in terms of array design and signal processing strategy. Such model would present a higher level of complexity than the usual point sources or incoherent line sources generally used, and it would allow comparing beamforming results regarding source characteristics with the "ground truth"known from the analytical model.

It must be noted that the deconvolution method CLEAN-SC was originally formulated to separate distinct, incoherent sources, and it is currently unknown how CLEAN-SC performs when observing a single distributed, partially-coherent source, such as a flat plate aerofoil. Although some results presented here indicate that CLEAN-SC might be able to separate coherent regions on the source surface, it is now known how the source coherence length or the microphone array design might play a role in this separation. This investigation is left for future work.

The proposed source estimation methods from far-field data describes a "line-of-sight" relationship between the microphone locations and their observable wavenumber components. As these methods assume formulations that are very similar to classical delay-and-sum beamforming, there is a strong possibility that this "line of sight" relationship is also applicable to classical beamforming. This hypothesis requires further investigation, but we believe this might be a novel interpretation of a well-known microphone array signal processing method, and might yield novel beamforming arrangements with more varied microphone array layouts.

In order to discuss the source estimation results in more depth, both formulations of the proposed far-field inversion method were simulated at a single frequency or at a few discrete frequencies. A natural next step would be to apply these methods over all frequencies and compare, for example, the estimated and the original PSD of the aerofoil surface pressure at some points on the aerofoil surface.

The far-field inversion method in the uniform wavenumber-domain sampling formulation requires an extension to two-dimensional sources and to the broadband case - i.e. to estimate the source cross-spectral density matrix from the acoustic far-field cross-spectral density matrix measurements. As the resulting microphone array layout is frequency-dependent, in practice one would likely design the array for the highest frequency of interest; in this case, the source domain would be oversampled at lower frequencies, and thus an adapted formulation would be required to use all microphones. These tasks are also suggested as future work.

Appendix A

Defining Dirac Delta Functions

This Appendix describes a method used by Osgood [82] to obtain a Dirac Delta function $\delta(x)$ from a starting - or "nascent" - function $f(x)$.

A.1 Defining $\delta(x)$

At first, we must define what is meant by a Dirac Delta function $\delta(x)$. Following Osgood [82], it is better to define a Delta function by describing its behaviour when inside integrals, instead of its values in a point-wise manner. This is often easier when considering a limiting process: we say that a function $f(x,p)$ will tend towards a Delta function $\delta(x)$ in the limit

$$\lim_{p\to\infty} f(x,p) \to \delta(x), \tag{A.1}$$

if the function $f(x,p)$ presents the behaviour

$$\lim_{p\to\infty} \int_{-\infty}^{+\infty} f(x,p)\psi(x)\,\mathrm{d}x = \psi(0). \tag{A.2}$$

Such a function will then present the following properties:

- $\lim_{p\to\infty} f(x,p) = 0, \quad x \neq 0;$
- $\lim_{p\to\infty} f(x=0,p) = \infty;$

- and $\int_{-\infty}^{+\infty} f(x,p)\,\mathrm{d}x = 1,$

which are often cited as properties of the Delta function $\delta(x)$.

A.2 Obtaining $\delta(x)$

We will now describe a procedure to obtain a Delta function $\delta(x)$ from a starting function $f(x)$ taken to a limit. Let us first define $f(x)$ such that

$$\int_{-\infty}^{\infty} f(x)\,\mathrm{d}x = 1. \tag{A.3}$$

We must then form a scaled version of $f(x)$, defined as

$$f_p(x) = pf(px), \quad p > 0. \tag{A.4}$$

Informally, one might interpret that the original function $f(x)$ becomes compressed by a factor p in the x axis, while becoming "taller" by the same amount. From this interpretation, it is trivial to observe that

$$\int_{-\infty}^{\infty} f_p(x)\,\mathrm{d}x = \int_{-\infty}^{\infty} f(px)\,\mathrm{d}px = 1. \tag{A.5}$$

As a consequence, we have that

$$\lim_{p\to\infty} \int_{-\infty}^{+\infty} f(x,p)\psi(x)\,\mathrm{d}x = \psi(0), \tag{A.6}$$

which is our definition of the Delta function $\delta(x)$. We can then write

$$\lim_{p\to\infty} f_p(x) \to \delta(x). \tag{A.7}$$

A.3 The $\mathrm{sinc}(x)$ as a nascent Delta Function

We will now explore two different "nascent" Delta functions: the $\mathrm{sinc}(x)$ and the $\mathrm{sinc}^2(x)$. First, let us define the unnormalised sinc function $\mathrm{sinc}(x)$ as

$$\mathrm{sinc}(x) = \frac{\sin(x)}{(x)}. \tag{A.8}$$

We will assume it is known that $\int_{-\infty}^{+\infty} \mathrm{sinc}(x)\,\mathrm{d}x = \pi$; therefore, we must consider a function $f(x)$ such that

$$f(x) = \frac{1}{\pi}\,\mathrm{sinc}(x) \quad \rightarrow \quad \int_{-\infty}^{+\infty} f(x)\,\mathrm{d}x = 1. \tag{A.9}$$

Let us now define a modified function $f_p(x)$ as

$$f_p(x) = pf(px) \tag{A.10}$$

$$= \frac{p}{\pi}\frac{\sin(px)}{(px)}. \tag{A.11}$$

We then have that

$$\lim_{p\to\infty} f_p(x) = \lim_{p\to\infty} \frac{p}{\pi}\frac{\sin(px)}{(px)} \tag{A.12}$$

$$= \lim_{p\to\infty} \frac{\sin(px)}{x\pi} \rightarrow \delta(x). \tag{A.13}$$

The above limit can be shown, with small modifications, to be equivalent to Equation 3.22.

On a side note, it is also known that

$$\int_{-d}^{d} e^{jkx}\,\mathrm{d}x = \frac{1}{jk}\left(e^{jkd} - e^{jk(-d)}\right) = \frac{(2d)\sin(kd)}{kd}. \tag{A.14}$$

Taking the limit of $d \rightarrow \infty$, it can be seen that

$$\lim_{d\to\infty}\int_{-d}^{+d} e^{jkx}\,\mathrm{d}x = \lim_{d\to\infty}\frac{(2d)\sin(kd)}{kd} \to 2\pi\delta(k), \tag{A.15}$$

which we now denote as

$$\int_{-\infty}^{+\infty} e^{jkx}\,\mathrm{d}x = 2\pi\delta(k). \tag{A.16}$$

A.4 The $\mathrm{sinc}^2(x)$ as a nascent Delta Function

We can now apply the same analysis to the sinc squared function:

$$\mathrm{sinc}^2(x) = \frac{\sin^2(x)}{x^2}. \tag{A.17}$$

First, it is necessary to evaluate $\displaystyle\int_{-\infty}^{+\infty}\mathrm{sinc}^2(x)\,\mathrm{d}x$; this improper integral can be calculated via the limit of an integration by parts:

$$\int_{-\infty}^{+\infty}\mathrm{sinc}^2(x)\,\mathrm{d}x = \lim_{t\to\infty}\int_{-t}^{+t}\sin^2(x)\frac{1}{x^2}\,\mathrm{d}x. \tag{A.18}$$

Let

$$u = \sin^2(x) \quad \to \quad \mathrm{d}u = \underbrace{2\sin(x)\cos(x)}_{=\sin(2x)}\,\mathrm{d}x, \tag{A.19}$$

$$\mathrm{d}v = x^{-2}\,\mathrm{d}x \quad \to \quad v = (-1)x^{-1}. \tag{A.20}$$

We can then write

$$\lim_{t\to\infty}\int_{-t}^{+t}\sin^2(x)\frac{1}{x^2}\,\mathrm{d}x = \lim_{t\to\infty}\left[(-1)\frac{\sin^2(x)}{x}\right]_{x=-t}^{+t} - \lim_{t\to\infty}\left[\int_{-t}^{+t}(-1)\frac{\sin(2x)}{x}\,\mathrm{d}x\right]. \tag{A.21}$$

Let us analyse the first term on the right-hand side of Eq. A.21:

$$\lim_{t\to\infty}\left[(-1)\frac{\sin^2(x)}{x}\right]_{x=-t}^{+t} = \lim_{t\to\infty}\left[(-1)\frac{\sin^2(+t)}{+t} - (-1)\frac{\sin^2(-t)}{-t}\right]. \tag{A.22}$$

Note that $\sin^2(x)/x$ is the product of a monotonically decaying function ($1/t \to 0$ as $t \to \pm\infty$) and a bounded function ($\sin^2(t) \in [0,1]$), and must converge to zero in the limit $t \to \pm\infty$.

Back to Eq. A.21, we are left with

$$\lim_{t\to\infty}\int_{-t}^{+t}\frac{\sin^2(x)}{x^2}\,\mathrm{d}x = 0 + \lim_{t\to\infty}\left[\int_{-t}^{+t}\frac{\sin(2x)}{x}\,\mathrm{d}x\right] \tag{A.23}$$

$$= \lim_{t\to\infty}\int_{-t}^{+t}\frac{\sin(2x)}{2x}\,\mathrm{d}2x \tag{A.24}$$

$$= \lim_{t\to\infty}\int_{-t}^{+t}\frac{\sin(u)}{u}\,\mathrm{d}u. \tag{A.25}$$

We can now evaluate the limits and reach the interesting conclusion that

$$\int_{-\infty}^{+\infty}\mathrm{sinc}^2(x)\,\mathrm{d}x = \int_{-\infty}^{+\infty}\mathrm{sinc}(x)\,\mathrm{d}x = \pi. \tag{A.26}$$

In order to generate a Delta function $\delta(x)$, we must thus define a function $f(x)$ such that

$$f(x) = \frac{1}{\pi}\mathrm{sinc}^2(x) \quad \to \quad \int_{-\infty}^{+\infty} f(x)\,\mathrm{d}x = 1. \tag{A.27}$$

Let us now define a modified function $f_p(x)$ as

$$f_p(x) = pf(px) \tag{A.28}$$

$$= \frac{p}{\pi}\frac{\sin^2(px)}{(px)^2}. \tag{A.29}$$

We then have that

$$\lim_{p\to\infty} f_p(x) = \lim_{p\to\infty}\frac{p}{\pi}\frac{\sin^2(px)}{(px)^2} \tag{A.30}$$

$$= \lim_{p\to\infty}\frac{\sin^2(px)}{x^2 p\pi} \to \delta(x). \tag{A.31}$$

This last limit is equivalent to Eq. 3.24, and is the limit originally used by Amiet [8].

Bibliography

[1] Don Johnson and Dan Dudgeon. *Array Signal Processing.* Prentice-Hall, New Jersey, USA, 1993.

[2] Thomas Brooks and William Humphreys. A deconvolution approach for the mapping of acoustic sources (damas) determined from phased microphone arrays. *Journal of Sound and Vibration*, Vol. 294:856–879, 2006.

[3] Pieter Sijtsma. Clean based on spatial source coherence. Technical Report NLR-TP-2007-345, National Aerospace Laboratory (NLR) - the Netherlands, 2007.

[4] Benshuai Lyu, Mahdi Azarpeyvand, and Samuel Sinayoko. Noise prediction for serrated leading-edges. In *22nd AIAA/CEAS Aeroacoustics Conference*, 2016. AIAA Paper 2016-2740.

[5] William Devenport, Joshua Staubs, and Stewart Glegg. Sound radiation from real airfoils in turbulence. *Journal of Sound and Vibration*, 329:3470–3483, 2010.

[6] Leandro D. Santana, Christophe Schram, and Wim Desmet. Low-frequency extension of amiet's theory for compact airfoil noise predictions. *Journal of Sound and Vibration*, 372 (23):342–356, 2016.

[7] Michel Roger. Broadband noise from lifting surfaces: Analytical modeling and experimental validation. In Roberto Camussi, editor, *Noise Sources in Turbulent Shear Flows: Fundamentals and Applications.* Springer-Verlag Wien, 2013.

[8] R. K. Amiet. Acoustic radiation from an airfoil in a turbulent stream. *Journal of Sound and Vibration*, Vol. 41, No. 4:407–420, 1975.

[9] Michel Roger and Stéphane Moreau. Extensions and limitations of analytical airfoil broadband noise models. *International Journal of Aeroacoustics*, 9(3):273–305, 2010.

[10] Roy Amiet. Noise produced by turbulent flow into a rotor: Theory manual for noise calculation. Technical Report NASA Contractor Report 181788, National Aeronautics and Space Administration (NASA) - USA, 1989.

[11] J. Christophe, J. Anthoine, P. Rambaud, and S. Moreau. Numerical issues in the application of an Amiet model for spanwise-varying incoming turbulence. In *14th AIAA/CEAS Aeroacoustics Conference*, 2008. AIAA Paper 2008-2865.

[12] Renato F. Miotto, William R. Wolf, and Leandro D. Santana. Numerical computation of gust aerodynamic response for realistic airfoils: Application of amiets theory. In *22nd AIAA/CEAS Aeroacoustics Conference*, 2016. AIAA Paper 2016-2737.

[13] Leandro D. Santana, Julien Christophe, Christophe Schram, and Wim Desmet. A rapid distortion theory modified turbulence spectra for semi-analytical airfoil noise prediction. *Journal of Sound and Vibration*, 383:349–363, 2016.

[14] Michel Roger, Christophe Schram, and Leandro De Santana. Reduction of airfoil turbulence-impingement noise by means of leading-edge serrations and/or porous materials. In *19th AIAA/CEAS Aeroacoustics Conference*, 2013. AIAA Paper 2013-2108.

[15] Vincent Clair et al. Experimental and numerical investigation of turbulence-airfoil noise reduction using wavy edges. *AIAA Journal*, Vol. 51(11):2695–2713, 2013.

[16] Christopher Bahr et al. An analysis of different measurement techniques for airfoil trailing edge noise. In *14th AIAA/CEAS Aeroacoustics Conference*, 2008. AIAA Paper 2008-2957.

[17] Stefan Oerlemans and Paul Migliore. Aeroacoustic wind tunnel tests of wind turbine airfoils. In *10th AIAA/CEAS Aeroacoustics Conference*, 2004. AIAA Paper 2004-3042.

[18] Danielle Moreau, Zebb Prime, Ric Porteous, Con Doolan, and Vincent Valeau. Flow-induced noise of a wall-mounted finite airfoil at low-to-moderate reynolds number. *Journal of Sound and Vibration*, 333:6924–6941, 2014.

[19] Kyle A. Pascioni and Louis N. Cattafesta. Aeroacoustic measurements of leading-edge slat noise. In *22nd AIAA/CEAS Aeroacoustics Conference*, 2016. AIAA Paper 2016-2960.

[20] Florence Hutcheson, Thomas Brooks, Casey Burley, and Daniel Stead. Measurement of the noise resulting from the interaction of turbulence with a lifting surface. In *17th AIAA/CEAS Aeroacoustics Conference*, 2011. AIAA Paper 2011-2907.

[21] Subramanian Narayanan et al. Airfoil noise reductions through leading edge serrations. *Physics of Fluids*, 27(025109), 2015.

[22] Pieter Sijtsma. Experimental techniques for identification and characterisation of noise sources. Technical Report NLR-TP-2004-165, National Aerospace Laboratory (NLR) - the Netherlands, 2004.

[23] Thomas Geyer, Ennes Sarradj, Jens Giesler, and Marcus Hobracht. Experimental assessment of the noise generated at the leading edge of porous airfoils using microphone array techniques. In *17th AIAA/CEAS Aeroacoustics Conference*, 2011. AIAA Paper 2011-2713.

[24] Vincent Fleury, Jean Bulté, Renaud Davy, Eric Manoha, and Michael Pott-Pollenske. 2d high-lift airfoil noise measurements in an aerodynamic wind tunnel. In *21st AIAA/CEAS Aeroacoustics Conference*, 2015. AIAA Paper 2015-2206.

[25] Thomas Geyer, Ennes Sarradj, and Jens Giesler. Application of a beamforming technique to the measurement of airfoil leading edge noise. *Advances in Acoustics and Vibration*, 2012(Article ID 905461), 2012. doi:10.1155/2012/905461.

[26] Thomas Geyer et al. Experimental investigation of leading edge hook structures for wind turbine noise reduction. In *22nd AIAA/CEAS Aeroacoustics Conference*, 2016. AIAA Paper 2016-2954.

[27] James R. Underbrink. Aeroacoustic phased array testing in low speed wind tunnels. In Thomas J. Mueller, editor, *Aeroacoustic Measurements*. Springer, September 2002.

[28] Ann Dowling and John Ffowcs Williams. *Sound and Sources of Sound*. Ellis Horwood, Chichester, UK, 1983.

[29] Earl Williams. *Fourier Acoustics: Sound Radiation and Nearfield Acoustical Holography*. Academic Press, London, UK, 1999.

[30] Stewart Glegg and William Devenport. *Aeroacoustics of Low Mach Number Flows*. Elsevier Academic Press, London, UK, 2017.

[31] Y. Kim and P. Nelson. Spatial resolution limits for the reconstruction of acoustic source strength by inverse methods. *Journal of Sound and Vibration*, Vol. 265:583–608, 2003.

[32] Lawrence Kinsler, Austin Frey, Alan Coppens, and James Sanders. *Fundamentals of Acoustics*. John Wiley and Sons, London, UK, 2000.

[33] Helene Parisot-Dupuis, Frank Simon, Estelle Piot, and Francis Micheli. Non-intrusive planar velocity-based nearfield acoustic holography in moving fluid medium. *Journal of the Acoustical Society of America*, Vol. 133:4087–4097, 2013.

[34] Pijush Kundu, Ira Cohen, and David Dowling. *Fluid Mechanics*. Elsevier Academic Press, Oxford, UK, 2012.

[35] Hyu-Sang Kwon, Yaying Niu, and Yong-Joe Kim. Planar nearfield acoustical holography in moving fluid medium at subsonic and uniform velocity. *Journal of the Acoustical Society of America*, Vol. 126:1823–1832, 2010.

[36] Gabriel Barton. *Elements of Green's Functions and Propagation*. Clarendon Press, Oxford, UK, 1989.

[37] Philip Morse and Herman Feshbach. *Methods of Theoretical Physics*. McGraw-Hill, New York, USA, 1953.

[38] Jens Ahrens. *Analytic Methods of Sound Field Synthesis*. Springer-Verlag, Berlin, Germany, 2012.

[39] Frank Fahy and Paolo Gardonio. *Sound and Structural Vibration*. Academic Press, Oxford, UK, 2007.

[40] Philip Nelson and Stephen Elliott. *Active Control of Sound*. Academic Press, London, UK, 1992.

[41] T. Wu and L. Lee. A direct boundary integral formulation for acoustic radiation in a subsonic uniform flow. *Journal of Sound and Vibration*, Vol. 175:51–63, 1994.

[42] Simone Mancini, R. Jeremy Astley, Samuel Sinayoko, Gwenael Gabard, and Michel Tournour. An integral formulation for wave propagation on weakly non-uniform potential flows. *Journal of Sound and Vibration*, Vol. 385:184–201, 2016.

[43] C. J. Chapman. Similarity variables for sound radiation in a uniform flow. *Journal of Sound and Vibration*, Vol. 233, No. 1:157–164, 2000.

[44] Finn Jacobsen and Peter Juhl. *Fundamentals of General Linear Acoustics*. Wiley, Chichester, UK, 2013.

[45] Joseph Goodman. *Introduction to Fourier Optics*. Roberts & Company, Colorado, USA, 2005.

[46] Warren Stutzman and Gary Thiele. *Antenna Theory and Design*. John Wiley and Sons, New Jersey, USA, 1998.

[47] Tapan Sarkar, Magdalena Salazar-Palma, and Eric Mokole. *Physics of Multiantenna Systems and Broadband Processing*. John Wiley and Sons, New Jersey, USA, 2008.

[48] Charles Capps. Near field or far field? EDN Magazine, Available online: https://m.eet.com/media/1140931/19213-150828.pdf, August 2001.

[49] Sjoerd Rienstra and Avraham Hirschberg. An introduction to acoustics. Technical Report Updated version of Report IWDE 01-03, May 2001, Eindhoven University of Technology, The Netherlands, 2012.

[50] Pieter Sijtsma. Phased array beamforming applied to wind tunnel and fly-over tests. Technical Report NLR-TP-2010-549, National Aerospace Laboratory (NLR) - the Netherlands, 2010.

[51] Stefan Haxter and Carsten Spehr. Infinite beamforming: Wavenumber decomposition of surface pressure fluctuations. In *5th Berlin Beamforming Conference*, 2014. BeBeC Paper BeBeC-2014-04.

[52] Roy Amiet. Refraction of sound by a shear layer. *Journal of Sound and Vibration*, Vol. 58, part 4:467–482, 1978.

[53] Ric Porteous, Thomas Geyer, Danielle Moreau, and Con Doolan. A correction method for acoustic source localisation in convex shear layer geometries. *Applied Acoustics*, Vol. 130:128132, 2018.

[54] Lars Koop, Klaus Ehrenfried, and Stefan Kröber. Investigation of the systematic phase mismatch in microphone-array analysis. In *11th AIAA/CEAS Aeroacoustics Conference*, 2005. AIAA Paper 2005-2962.

[55] Christopher Bahr et al. Shear layer correction validation using a non-intrusive acoustic point source. In *16th AIAA/CEAS Aeroacoustics Conference*, 2010. AIAA Paper 2010-3735.

[56] Chris Bahr, Nikolas Zawodny, Tarik Yardibi, Fei Liu, Drew Wetzel, Brandon Bertolucci, and Louis Cattafesta. Shear layer time-delay correction using a non-intrusive acoustic point source. *International Journal of Aeroacoustics*, 10(5&6):497–530, 2011.

[57] Eric Jones, Travis Oliphant, Pearu Peterson, et al. SciPy: Open source scientific tools for Python. Available online: http://www.scipy.org/, 2001. Accessed 31 July 2014.

[58] Christopher Morfey and Phillip Joseph. Shear layer refraction corrections for off-axis sources in a jet flow. *Journal of Sound and Vibration*, Vol. 239:819–848, 2001.

[59] Paul Soderman and Christopher Allen. Microphone measurements in and out of airstream. In Thomas J. Mueller, editor, *Aeroacoustic Measurements*. Springer, September 2002.

[60] Robert P. Dougherty. Beamforming in acoustic testing. In Thomas J. Mueller, editor, *Aeroacoustic Measurements*. Springer, September 2002.

[61] Gabriel Reboul. *Modélisation du bruit à large bande de soufflante de turboréacteur*. Phd thesis, Laboratoire de Mécanique des Fluides et d'Acoustique - École Centrale de Lyon, Lyon - France, 2010.

[62] Leandro de Santana. *Semi-analytical methodologies for airfoil noise prediction*. Phd thesis, Faculty of Engineering Sciences - Katholieke Universiteit Leuven, Leuven, Belgium, 2015.

[63] Michel Roger. Sound radiation by moving surfaces and the green's functions technique. In Roberto Camussi, editor, *Noise Sources in Turbulent Shear Flows: Fundamentals and Applications*. Springer-Verlag Wien, 2013.

[64] Robert Paterson and Roy Amiet. Acoustic radiation and surface pressure characteristics of an airfoil due to incident turbulence. Technical Report NASA Contractor Report CR-2733, National Aeronautics and Space Administration (NASA) - USA, 1976.

[65] John Graham. Similarity rules for thin aerofoils in non-stationary subsonic flows. *Journal of Fluid Mechanics*, Vol. 43, part 4:753–766, 1970.

[66] Kihong Shin and Joseph Hammond. *Fundamentals of Signal Processing for Sound and Vibration Engineers*. John Wiley and Sons, Chichester, UK, 2008.

[67] Frank Fahy. *Foundations of Engineering Acoustics*. Elsevier Academic Press, London, UK, 2001.

[68] ISVR Consulting. Large anechoic chamber. Available online: http://www.isvr.co.uk/faciliti/lg_anech.htm, 2015. Accessed 15 February 2016.

[69] Tze Pei Chong, Philip Joseph, and Peter Davies. Design and performance of an open jet wind tunnel for aero-acoustic measurement. *Applied Acoustics*, Vol. 70:605–614, 2009.

[70] Chaitanya Paruchuri. *Aerofoil geometry effects on turbulence interaction noise*. Phd thesis, Institute of Sound and Vibration Research - University of Southampton, Southampton, UK, 2017.

[71] Zebb Prime and Con Doolan. A comparison of popular beamforming arrays. In *Proceedings of ACOUSTICS 2013 - Victor Harbor*, 2013. Australian Acoustical Society, 17-20 November.

[72] Hamid Krim and Mats Viberg. Two decades of array signal processing research. IEEE Signal Processing Magazine, July 1996.

[73] Ennes Sarradj. Three-dimensional acoustic source mapping with different beamforming steering vector formulations. *Advances in Acoustics and Vibration*, Vol. 2012:1–12, 2012.

[74] Ennes Sarradj. A generic approach to synthesize optimal array microphone arrangements. In *6th Berlin Beamforming Conference*, 2016. BeBeC Paper BeBeC-2016-S4.

[75] Barry Van Veen and Kevin Buckley. Beamforming: A versatile approach to spatial filtering. IEEE ASSP Magazine, April 1988.

[76] Charles Therrien. *Discrete Random Signals and Statistical Signal Processing*. Prentice-Hall, New Jersey, USA, 1992.

[77] Fabrice Castres. *Mode Detection in Turbofan Inlets*. Phd thesis, Institute of Sound and Vibration Research - University of Southampton, Southampton, UK, 2006.

[78] Pieter Sijtsma. Clean based on spatial source coherence. In *2nd Berlin Beamforming Conference*, 2008. BeBeC Paper BeBeC-2008-11.

[79] Marthijn Tuinstra and Pieter Sijtsma. Supression of spurious noise sources in airfoil self-noise measurements. In *21st AIAA/CEAS Aeroacoustics Conference*, 2015. AIAA Paper 2015-2689.

[80] Roberto Merino-Martinez, Pieter Sijtsma, and Mirjam Snellen. Inverse integration method for distributed sound sources. In *8th Berlin Beamforming Conference*, 2018. BeBeC Paper BeBeC-2018-S07.

[81] Kenneth Castleman. *Digital Image Processing*. Prentice-Hall, Upper Saddle River, USA, 1996.

[82] Brad Osgood. The Fourier Transform and its Applications. Lecture notes for EE261, University of Stanford - USA, available online: http://see.stanford.edu/materials/lsoftaee261/book-fall-07.pdf, 2007. Accessed 27 August 2014.

[83] Franz Aurenhammer. Voronoi diagrams - a survey of a fundamental geometric data structure. *ACM Computing Surveys*, Vol. 23:345–405, 1991.

[84] Philip Nelson. Source identification and location. In Frank Fahy and John Walker, editors, *Advanced Applications in Acoustics, Noise and Vibration*. Spon Press, September 2004.

[85] J. D. Maynard, E. G. Williams, and Y. Lee. Nearfield acoustic holography: I. theory of generalized holography and the development of nah. *Journal of the Acoustical Society of America*, Vol. 78:1395–1413, 1985.